Jan Figgener

Data-driven battery aging analysis of home storage systems based on high-resolution field measurements

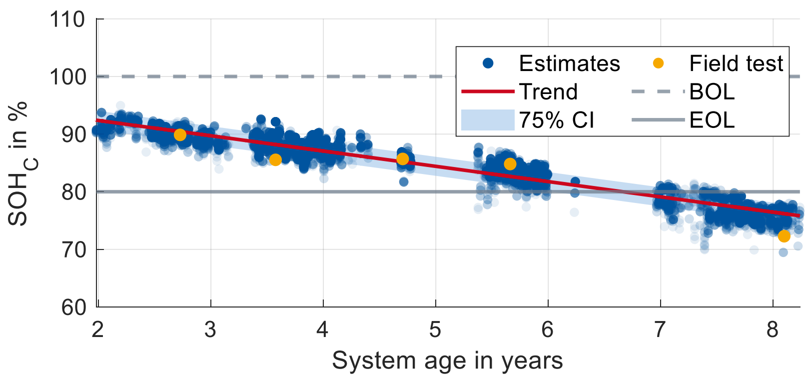

Aachener Beiträge des ISEA Band 177

Data-driven battery aging analysis of home storage systems based on high-resolution field measurements

Von der Fakultät für Elektrotechnik und Informationstechnik
der Rheinisch-Westfälischen Technischen Hochschule Aachen
zur Erlangung des akademischen Grades eines Doktors der
Ingenieurwissenschaften genehmigte Dissertation

vorgelegt von

Jan Figgener
Master of Science
aus Bocholt

Berichter:
Univ.-Prof. Dr. rer. nat. Dirk Uwe Sauer
Univ.-Prof. Dr. sc. Andreas Ulbig

Tag der mündlichen Prüfung: 19. Dezember 2023

AACHENER BEITRÄGE DES ISEA
Vol. 177

Editor:
Univ.-Prof. Dr. ir. Dr. h. c. Rik W. De Doncker
Director of the Institute for Power Electronics and Electrical Drives (ISEA)
RWTH Aachen University

ISSN 1437-675X

Institute for Power Electronics and Electrical Drives (ISEA)
RWTH Aachen University
Campus-Boulevard 89 • 52074 Aachen • Germany
Tel: +49 (0)241 80-96920
Fax: +49 (0)241 80-92203
post@isea.rwth-aachen.de

*“We have to learn to harness the energy that comes to us from the sun […].
But you have to be able to store that energy […]. So that is one
of the reasons you work on batteries [...]. But we have
to keep working hard on it to improve it, okay?”*

John Bannister Goodenough (1922 — 2023)
Nobel laureate in chemistry for his work on
developing lithium-ion batteries

Vorwort

Wir leben in einer Zeit, in der die ersten Folgen des Klimawandels durch gestiegene Temperaturen und gehäufte Naturkatastrophen deutlich sichtbar werden. Die nächsten Jahre werden entscheiden, inwieweit der Temperaturanstieg durch den Zubau von erneuerbaren Energien und die Senkung von Emissionen in allen Sektoren begrenzt werden kann. Damit liegt eine Aufgabe vor uns, die nur gesamtgesellschaftlich und durch internationale Kooperation zu bewältigen ist. Ich bin dankbar, dass ich in den letzten Jahren Teil dieser Bewegung sein durfte und einen kleinen Beitrag rund um Batteriespeicher erarbeiten konnte. Batteriespeicher stellen eine Schlüsselkomponente für die Energiewende dar. Sie können zum Beispiel das Stromnetz stützen, volatile Energieerzeugung aus erneuerbaren Energien optimieren und ermöglichen emissionsarme Mobilität.

Die vorliegende Dissertation entwickelt Methoden zur Alterungsanalyse von Batteriespeichern im Feldbetrieb. Der Fokus liegt dabei auf 21 Heimspeichersystemen, die in einem Zeitraum von bis zu acht Jahren durch unseren Lehrstuhl in Privathaushalten vermessen wurden. Die Erkenntnisse in Bezug auf die Batteriealterung im Feld und entwickelte Diagnosealgorithmen ermöglichen bedarfsgerechte Wartungseinsätze und damit eine möglichst lange Lebensdauer. Zudem könnten sie einen Beitrag für die Standards zur Batteriediagnostik leisten, die zurzeit auf europäischer Ebene erarbeitet werden.

Die Forschungsergebnisse entstanden in meiner Zeit am Lehrstuhl für Elektrochemische Energiewandlung und Speichersystemtechnik unter Professor Dirk Uwe Sauer. Ich bin ihm sehr dankbar, dass er mir die Möglichkeit zur Promotion gegeben hat. Trotz eines großen Lehrstuhls hat er sich immer Zeit für einen fachlichen Austausch genommen und wertvollen Input in zahlreichen Diskussionen geliefert. Sein Vertrauen in mich, die Abteilung Netzintegration und Speichersystemanalyse über drei Jahre leiten zu dürfen, weiß ich sehr zu schätzen. Auch die Unterstützung beim Umgang mit Medien- und Presseanfragen hat mich geprägt. Sie stellen meiner Meinung nach eine wichtige Aufgabe in der Wissenschaft dar, um Erkenntnisse von der Forschung in die Gesellschaft zu kommunizieren.

Herrn Professor Andreas Ulbig danke ich herzlich für die Übernahme des Korreferats meiner Arbeit und sein hilfreiches Feedback zu den Analysen. Zudem werde ich die inspirierenden Gespräche zur beruflichen Laufbahn in guter Erinnerung behalten. Ergänzend gibt es eine Vielzahl weiterer Personen aus dem Institutsumfeld, denen ich jeweils in der Danksagung individuelle Abschnitte für Ihre wertvolle Unterstützung gewidmet habe.

Ich freue mich, auch in den kommenden Jahren weiter an den Themen rund um die Energiewende zu arbeiten und habe die Hoffnung, dass die weitreichendsten Veränderungen aufgrund des Klimawandels durch gemeinsame Anstrengungen der Gesellschaft und zielgerichtete Politik begrenzt werden können.

Kurzfassung

Batteriespeicher sind eine Schlüsseltechnologie für die Energiewende. Sie können Energie flexibel in der Zeit verschieben und damit die Fluktuation im Dargebot von Sonne und Wind ausgleichen. In Deutschland, einem der weltweit führenden Märkte, machen Heimspeicher den größten Anteil der netzgekoppelten Speicherkapazität aus. In dem jungen Markt haben sich Garantiezeiten von etwa zehn Jahren etabliert. Es ist jedoch bisher unbekannt, ob diese Garantien aufrechterhalten werden können. Gegen Ende des Jahres 2022 sind die meisten der 650.000 in Betrieb befindlichen Speichersysteme erst wenige Jahre alt und daher noch nicht am Ende ihres Garantiezeitraums angelangt. Um Transparenz zu schaffen, fordert die Europäische Union die zukünftige Bereitstellung verlässlicher Informationen über den Alterungszustand von Batterien.

Im Labor sind die Methoden zur Bestimmung der Batteriealterung bereits weitgehend definiert, jedoch stellen Felddaten bisher einen größtenteils unerschlossenen Forschungsbereich dar. Als Beitrag zur Forschung entwickelt diese Dissertation neuartige datengetriebene Methoden zur Schätzung wichtiger garantierelevanter Parameter von Lithium-Ionen-Batterien wie der nutzbaren Kapazität oder des Innenwiderstands aus Betriebsdaten. Die entwickelten Methoden analysieren Feldmessungen von 21 Heimspeichersystemen in Privathaushalten über einen Zeitraum von bis zu acht Jahren. Dies entspricht rund 106 Systemjahren, 146 Gigabyte und 14 Milliarden Datenpunkten.

Die Methode zur Bestimmung der nutzbaren Kapazität verwendet Relaxationsphasen, um den genauen Ladezustand sowohl bei Vollladung als auch bei Vollentladung zu berechnen und daraus die Kapazität abzuleiten. Die untersuchten Speichersysteme zeigen einen Kapazitätsverlust von etwa zwei bis drei Prozentpunkten pro Jahr. Die Methode zur Quantifizierung des Innenwiderstands analysiert betriebsbedingte Leistungspulse oder Relaxationsphasen, um die elektrochemischen Widerstandskomponenten zu quantifizieren. Die Batterien zeigen eine systemspezifische Widerstandserhöhung von durchschnittlich einem bis zu 25 Prozentpunkten pro Jahr. Trotz teilweise hoher Widerstandsanstiege ist der Kapazitätsverlust der ausschlaggebende Parameter für den Energieverlust. Die Methode zur Identifizierung der Degradationsarten rekonstruiert die Leerlaufspannungskurve kontinuierlich über die Lebensdauer der Batterien. Sie überträgt die überwiegend aus Einzelzellenanalysen im Labor bekannten Methoden der inkrementellen Kapazitätsanalyse und der differentiellen Spannungsanalyse in einem neuartigen Ansatz auf Feldmessdaten der Gesamtsysteme. Die identifizierten Degradationsarten umfassen den Verlust des Lithiuminventars sowie den Verlust des Aktivmaterials an Anode und Kathode.

Im kommerziellen Maßstab können diese Methoden für die Online-Diagnose von Heimspeichern zur bedarfsgerechten Wartung eingesetzt werden. Die Forschung kann die Methoden erweitern und zur Modellparametrisierung nutzen. Im politischen Kontext ermöglicht eine erarbeitete Marktanalyse, legislative Ziele zu formulieren und die Energiewende mit fundierten Entscheidungen zu gestalten.

Abstract

Battery storage systems are a key technology for the energy transition. They can shift energy flexibly in time and thus balance out fluctuations in the presence of sun and wind. Home storage systems account for the largest share of grid-connected storage capacity in Germany, one of the pioneering markets worldwide. In the relatively young market, warranty periods of about ten years have become the norm. However, it is unknown whether these warranties can be maintained. Until the end of 2022, most of the 650,000 systems in operation are only a few years old and have not yet reached the end of their warranty. To increase transparency, the European Union requires the future provision of reliable information on the batteries' state of health.

In the laboratory, methods to determine battery aging have already been defined to a large extent, but field data represent a predominantly unexplored research field until now. As a contribution to research, this dissertation develops novel data-driven methods to estimate important warranty-relevant parameters of lithium-ion batteries, such as the remaining capacity or the internal resistance, based on operational data. The developed methods use the data generated during field measurements of 21 home storage systems in private households over a period of up to eight years. This corresponds to about 106 system years, 146 gigabytes, and 14 billion data points.

The method to track the usable capacity identifies relaxation phases to calculate the exact state of charge at both full charge and full discharge and computes the capacity with these values. The analyzed storage systems show a decreased usable capacity of around two to three percentage points per year. The method to quantify the internal resistance analyzes system dynamics, such as power pulses or relaxation phases during operation, to quantify the electrochemical resistance components. The batteries show an average system-specific resistance increase of around one to 25 percentage points per year. However, the capacity fade is still mainly responsible for the energy fade. The method to identify the degradation modes reconstructs the open circuit voltage curve continuously over the lifetime of the batteries. The innovative approach transfers the methods of incremental capacity analysis and differential voltage analysis, known predominantly from single-cell investigations in the laboratory, to system-level field data. The degradation modes observed are the loss of lithium inventory and the loss of active material on both anode and cathode.

The industry can employ these methods for the online diagnosis of home storage systems to enable demand-oriented maintenance. Researchers can extend the methods and use the results for model parametrization. In the political context, an additionally elaborated market analysis enables formulation of legislative objectives in order to shape the energy transition with substantiated decisions.

Content

1 Introduction

This chapter explains the dissertation's motivation in the context of the energy transition and defines objectives of battery aging analysis based on field data measurements. Afterward, it depicts the structure and content of the dissertation.

1.1 Motivation and objective

Climate change is one of the largest challenges that humanity ever had to face [1]. To limit the rising global temperature, it is essential to lower emissions by reducing energy and raw material use, and switching from a fossil-based to a renewable energy system [2]. However, renewable energies such as photovoltaic (PV) and wind show fluctuation in their generation. Furthermore, times of generation do not always match times of demand. Energy storage on all time scales, from short-term to long-term, offers a solution. It can store excess energy, shift it in time, and make it available when needed. For short-term storage, batteries are the most cost-efficient solution to date [3]. The market for stationary battery storage systems (BSSs) has been growing rapidly for years and is expected to continue this growth. The application areas for BSSs are diverse. They range from increasing PV self-consumption through home storage to grid stability and renewable energy integration through large-scale storage. Home storage systems (HSSs) account for the largest share of grid-connected storage capacity in Germany, one of the pioneering markets worldwide [4].

The market ramp-up leads to a large use of raw materials. For sustainable and efficient use in the context of a circular economy, a long operational life is a decisive factor in addition to the chosen materials and their recycling potential [5]. Reliable estimates of the state of health (SOH) are necessary for demand-oriented maintenance, enabling a prolonged operational life. In the young HSS market, warranty periods of about ten years have become the norm. However, it is questionable whether these warranties can be maintained. By the end of 2022, most of the around 650,000 systems in Germany, the leading HSS market in Europe, are only a few years old [6]. Thus, research lacks publicly available SOH evaluations based on long-term measurements to date. To establish transparency and material circularity, the future digital battery passport of the European Union requires reliable and transparent SOH estimations [7].

In the laboratory, methods to determine the SOH have already been defined to a large extent. Still, field data represent a predominantly uncharted research area, as only few field datasets are publicly available. Furthermore, the data quality is not comparable to controlled laboratory measurements. Therefore, methods are urgently needed to transfer laboratory-approved approaches to field data, establishing broadly accepted and standardized methods.

To contribute to battery research, this dissertation analyzes field data of 21 privately operated HSSs of the first product generation over up to eight years. The main scientific contribution of this dissertation is the development of novel data-driven methods to estimate important warranty-relevant parameters of lithium-ion batteries. These are the usable battery capacity and the internal resistance. In addition, it develops a method to investigate the underlying degradation modes responsible for capacity and power fade. The presented methods only use data generated during operation and do not require expensive and restrictive testing. The methods are validated through periodic field capacity tests.

This dissertation provides extensive knowledge of many aspects of HSS operation and aging, enabling various subsequent work. The industry can use the developed methods for the online diagnosis of three currently relevant lithium-ion battery chemistries. Within the last few years, battery analytic methods developed within the context of this dissertation have already been transferred to the industry. Researchers can extend the methods, for example, with safety analytics, as the large dataset gathered during this dissertation is published. This helps overcome the current lack of freely available datasets. In addition, the results can be used for model parametrization. In politics, decision-makers can use the comprehensive market analysis elaborated within this thesis. They can align their objectives with the current state of battery deployments and make informed decisions for the energy transition. In addition, the insights on battery aging and warranty periods can be used to plan HSS material circularity.

1.2 Structure and content

The structure of this dissertation is presented in Figure 1-1. After the introduction in **Chapter 1**, the following chapters are presented.

Chapter 2 summarizes the fundamentals from literature while focusing on HSSs and lithium-ion batteries. Besides the presentation of their principles, it gives important definitions and discusses battery aging.

Chapter 3 presents the market analysis conducted within the thesis. In Germany alone, 220,000 new HSSs were installed in 2022, showing a growth of 50 % compared to 2021. The large market growth motivates the further chapters of this thesis since there are still many open questions regarding life span and associated warranty periods.

Chapter 4 depicts the field measurement of 21 HSSs over a period of up to eight years in private households. The analyzed dataset corresponds to the system-level battery voltage, current, power, and temperature measurement. The dataset comprises 106 system years, 14 billion data points, and a size of 146 gigabytes. It includes three currently relevant lithium-ion battery chemistries: lithium iron phosphate (LFP), lithium nickel manganese cobalt oxide (NMC), and a blend of NMC and lithium manganese oxide (LMO). The data is analyzed to obtain key operational metrics, such as seasonal voltage and current distributions, to understand HSS operation. The HSSs differ in system design and battery chemistry, which makes the development of reliable state estimation methods a key challenge this thesis overcomes.

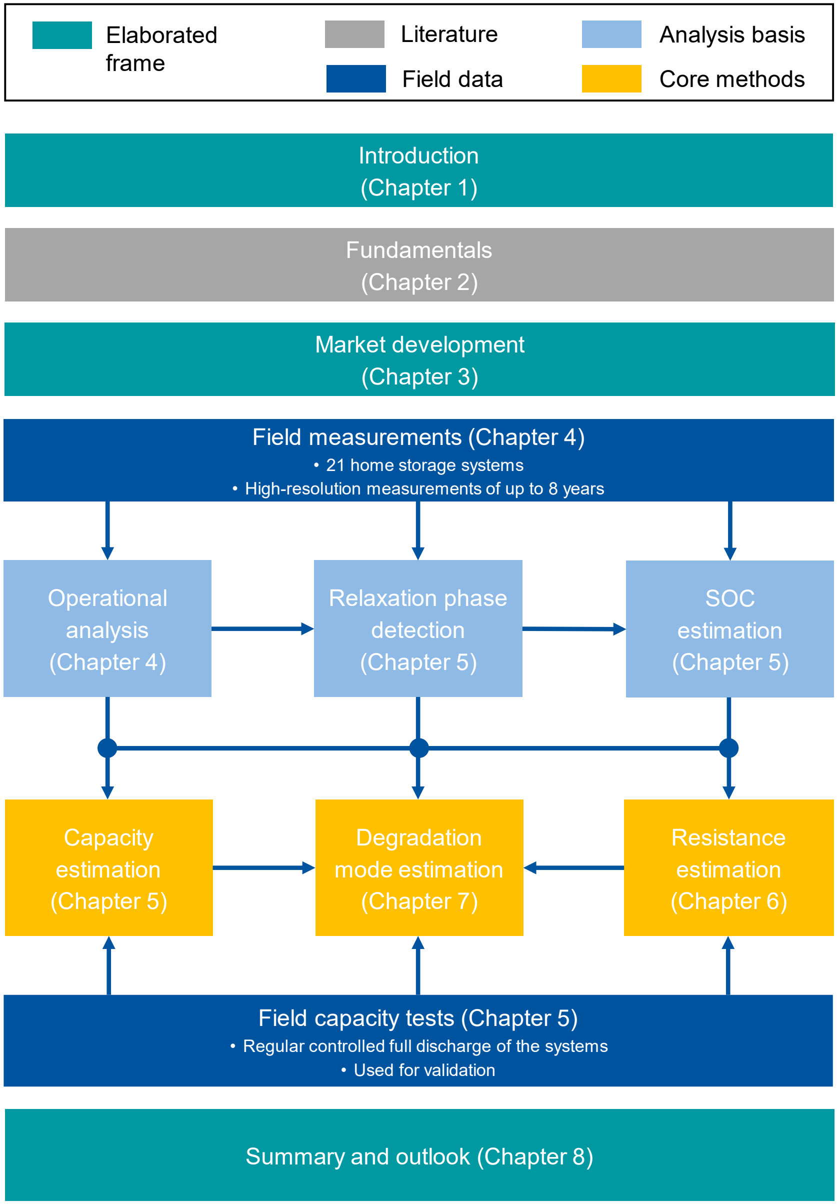

Figure 1-1: Structure of this dissertation.

Chapter 5 investigates the capacity and energy fade based on the field measurements. It describes the development of methods for SOH estimation while analyzing the remaining usable capacity and energy. The methods are based on detecting relaxation phases used to parameterize a second-order equivalent circuit model. These relaxation phases are the recalibration points for the developed state of charge (SOC) estimation based on ampere-hour counting. Periodic field capacity tests conducted over the measurement period validate the results.

Chapter 6 explains the calculation of the internal resistance, which is the second important aging criterion of a battery. It increases over time and leads to lower battery efficiency. The method identifies system dynamics, such as load-induced current peaks or relaxation phases, to estimate the direct current resistance while considering SOC and temperature. Furthermore, it analyzes the slow diffusion voltage derived from the second-order equivalent circuit model from Chapter 5. Linear regression and a neural network show that a prediction of the capacity fade is possible using relaxation parameters.

Chapter 7 reveals the occurring degradation modes responsible for the observed aging effects in Chapters 5 and 6. It presents a novel method for continuously reconstructing the open circuit voltage (OCV) curve using low-dynamic operational phases, such as the coverage of standby household electricity consumption. Based on this, the incremental capacity analysis and differential voltage analysis, known from the laboratory environment, are transferred to the field data to determine the degradation modes.

Chapter 8 concludes and showcases potential areas for future work, such as scaling the methods to a large storage population or transferring them to other applications and emerging battery technologies.

2 Fundamentals of home storage systems and batteries

This chapter presents the fundamentals essential to understand the developed methods within this dissertation. Parts of it are based on the publications [8,9] under the lead of the author.

2.1 Home storage systems

Home storage systems (HSSs) are combined with PV systems to save surplus energy during the day and make it available during evening and night. They consist of a battery and the required power electronics in the form of inverters.

2.1.1 Principle

PV energy production increases during morning hours, reaching its peak at midday, and then decreases toward the evening due to solar irradiation. However, a typical household consumes most of its energy in the morning and evening, with lower demands during the day. To address this imbalance, HSSs store excess PV energy generated during the day rather than feeding it directly into the public grid. This stored energy can be used later in the day when needed, reducing reliance on the grid for energy supply [8].

Both consumers and the grid benefit from HSS implementation [10]. In Germany, households with HSSs achieve approximately 60 % self-sufficiency and around 50 % self-consumption annually, depending on the component design [8]. On the grid side, HSSs play a crucial role in reducing the PV power fed into the grid, especially during periods of high solar irradiation [10]. This is particularly important as the increased number of PV systems can lead to local grid overloads, causing overvoltage and thermal issues with grid components [11].

2.1.2 Topologies

There are two main topologies to connect the HSS to the PV system [12], namely AC coupling and DC coupling. In AC-coupled systems, both the battery and PV system are connected to the household's AC network. In contrast, DC-coupled systems are connected to the PV system's DC side, sharing a hybrid inverter. It is challenging to compare the efficiency of these topologies, as extensive measurements are required to make any individual statements [8]. When retrofitting HSSs to existing PV systems, AC-coupled systems are advantageous since they can be easily connected on the AC side, avoiding interference with already installed PV components [8]. DC-coupled systems are attractive for a simultaneous installation of a PV system and an HSS as only the hybrid inverter is needed compared to both a PV and an HSS inverter. More information on PV systems can be found in [13] and [14], and system characteristics are evaluated in [15].

2.2 Lithium-ion batteries

Battery storage systems represent one of the most crucial technologies for short-term electrical energy storage [16]. These systems comprise multiple cells that store electrochemical energy, which can be converted back into electrical energy through chemical reactions [17]. In this thesis, the term "battery" refers to secondary battery cells that can store and release electrical energy for later use [18]. Among various battery technologies like lead-acid, nickel-cadmium, and nickel-metal-hydride, lithium-ion batteries (LIB) have gained significant importance for BSS applications [19]. Their popularity is primarily attributed to their low price, high energy density, and high coulomb efficiency [20]. Lithium-ion technologies lead the German HSS market, with nearly 100 % of newly installed systems in 2022 using them (see Chapter 3.3.1). In addition, the analyzed HSSs in this thesis use lithium-ion batteries.

2.2.1 Principle

Structure and Operation. This chapter uses the term lithium-ion battery to encompass various cell chemistries that share the same basic functionality [17]. Figure 2-1 illustrates the schematic structure of a lithium-ion cell comprising two electrodes with their current collectors, separated by an electrolyte and a separator [21]. The cathode and anode are the positive and negative electrodes, respectively, defined based on the discharging process [22].

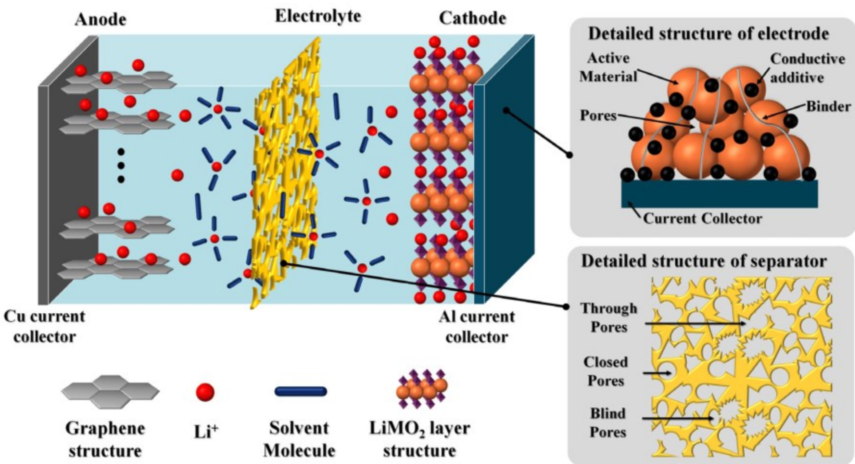

Figure 2-1: Structure of a lithium-ion battery by Ghani et al. [21], licensed under CC BY 4.0 [23]. The components are not drawn to scale and serve only for schematic visualization.

The electrodes comprise active materials to store lithium-ions and current collectors to facilitate the flow of electrons from and into the active material [18]. These current collectors consist of thin metal foils. While aluminum is employed for the cathode current collector, copper is used for the anode due to its better electrochemical stability at low potentials [17]. An ion-conductive electrolyte separates the transport of lithium ions and electrons, directing the electrons through the external circuit [17]. An ion-permeable separator acts as an electrical isolator to prevent a short circuit, maintaining a safe distance between the electrodes [21].

Cell design. Various form factors of lithium-ion cells are possible, such as pouch bag cells, prismatic cells, and cylindrical cells, all composed of multiple layers of electrodes and separators [22]. Pouch bag cells use stacked layers, while cylindrical cells are wound up, and prismatic cells can be realized using either approach [22].

Operation. LIB operation involves a reversible “rocking-chair” [24] process called intercalation, where lithium ions are inserted and extracted from the active materials in the electrodes through electrochemical redox reactions [17,25,26]. During discharging, the anode's active material releases lithium ions into the electrolyte and electrons into the external electrical circuit [17,27]. Both travel toward the cathode, where they get absorbed by its active material [17,27]. These processes are reversed upon charging, with lithium ions and electrons returning to the anode's active material [17,27]. The redox reactions at the two electrodes are represented by Equation (2-1) and (2-2), considering a cell with a metal oxide cathode (Li_xMeO_2) and a graphite anode (C_6) [17].

$$Li_x^I\, Me^{III} O_2 \underset{Discharging}{\overset{Charging}{\rightleftharpoons}} xLi^+ + xe^- + Me^{IV} O_2 \tag{2-1}$$

$$xLi^+ + xe^- + C_6 \underset{Discharging}{\overset{Charging}{\rightleftharpoons}} Li_x^I\, C_6^{-I} \tag{2-2}$$

Active materials. LIBs can use various active materials, leading to different characteristics [17]. Both electrodes' active materials have highly porous structures with fine-grained particle structures, resulting in a large surface area, which enables rapid reaction rates [22]. Mixed metal oxides are commonly employed for the cathode's active material, while graphite is the typical choice for the anode's active material [18].

Cathode materials. Cathode materials, in particular, define the various lithium-ion chemistries and their distinct characteristics [22]. Lithium cobalt dioxide ($LiCoO_2$ or LCO) was introduced as the first successful cathode material for commercial secondary LIBs [28]. While it offers high conductivity and structural stability, using cobalt raises concerns due to its high cost and ethical issues related to mining conditions [29,30] of small shares of the cobalt. Alternative cobalt-free cathode materials include lithium nickel dioxide ($LiNiO_2$ or LNO) and lithium manganese dioxide ($LiMnO_2$ or LMO). However, LNO suffers from thermal instability compared to LCO, and LMO faces the challenge of dissolving in the electrolyte at room temperatures [22,31]. To enhance the thermal stability of LNO, a small amount of aluminum can be introduced, leading to lithium nickel cobalt aluminum oxide ($LiNi_xCo_yAl_zO_2$ or NCA) [31]. Additionally, efforts to combine positive characteristics from different materials resulted in lithium nickel manganese cobalt oxides ($LiNi_xCo_yMn_zO_2$ or NMC), containing lesser quantities of cobalt while retaining the capacity of LCO, stability of LMO, and capacity and power of LNO [22,31] to a certain extend. Another cathode material, lithium iron phosphate ($LiFePO_4$ or LFP), offers higher thermal stability and power capability due to a different crystal structure but shows lower energy density [22,31]. In addition, different materials such as NMC, LMO, and NCA can be combined in so-called blends [32]. Each material exhibits specific attributes regarding energy and power density, safety, lifetime, cost, and environmental impact. Achieving the optimal battery cell design for a particular application requires carefully balancing these characteristics [22].

Anode materials. Anodes in lithium-ion batteries are commonly composed of carbon materials. They offer low cost, abundance, good energy and power density, and cycle life [31]. These carbon materials can be categorized as graphitic carbons and hard carbons. Despite having a reduced cycle life compared to hard carbons, Graphite is preferred due to its greater efficiency [31]. Lithium titanium oxide ($Li_4Ti_5O_{12}$ or LTO) is a suitable anode material, boasting thermal stability, power capability, and cycle life. However, it comes with a higher cost, lower energy density, and reduced cell voltage [31]. Promising alternatives are silicon-based anode materials, which offer a higher theoretical capacity than graphite [33,34]. Research is still required, as the high capacity leads to substantial volume changes, sometimes reaching several times the original volume [31,33]. Consequently, this increases mechanical stress, leading to the loss of electrical contact, continuous side reactions with the electrolyte, and rapid cell failure [33].

2.2.2 Definitions

This chapter defines several critical terminologies used in subsequent chapters.

Battery pack / battery. A battery pack comprises multiple modules, each with several battery cells [35]. The overall capacity of the pack is determined by the number of cells connected in parallel. At the same time, the battery voltage is the sum of the voltages of cells connected in series [35]. For cells connected in series, the cell with the lowest capacity determines the overall string capacity, which is important when the battery ages (see Chapter 2.2.4).

Battery management system (BMS). The Battery Management System (BMS) ensures a safe and reliable operation of the entire battery pack [35,36]. Its functions include controlling temperature, current, and voltage limits, monitoring the battery's state, and ensuring cell balancing when several cells show different voltages [36].

Nominal capacity in Ah. The nominal capacity C_N, measured in ampere-hours (Ah), is specified under nominal operating conditions, including defined temperatures and currents [37]. If the capacity C_T is measured at a temperature T different from the nominal temperature, it can be adjusted between 10°C and 30°C to the nominal capacity using Equation (2-3) with z being the capacity's temperature coefficient, which is dependent on the material [37].

$$C_N = \frac{C_T}{1 + z \cdot (T - 20°\mathrm{C})} \; with \; z \cong 0.006 \; K^{-1} \tag{2-3}$$

Nominal energy in Wh. The nominal energy E_N in Wh is given by the vendor and is subject to nominal operating conditions, such as temperature and current [37]. Between 10 °C and 30 °C an energy measurement at a temperature T different from the nominal temperature can be transformed to the nominal energy using the nominal capacity and the voltage V_T according to Equation (2-4), with z being the voltage's temperature coefficient, which depends on the material [37].

$$E_N = C_N \cdot \frac{V_T}{1 + z \cdot (T - 20°\mathrm{C})} \cdot \; with \; z \cong 0.002 \; K^{-1} \tag{2-4}$$

End of charge (EOC) voltage in V. The EOC voltage is the maximum voltage limit set by the BMS.

End of discharge (EOD) voltage in V. The EOD voltage is the minimum voltage limit set by the BMS.

Usable capacity in Ah. The usable capacity (C_{usable}) is the available capacity while cycling between EOD and EOC voltage. For example, this voltage range can be adjusted over time to offset capacity degradation. This study focuses on analyzing the usable capacity rather than the nominal capacity. The usable capacity depends on temperature and current rates.

Usable energy in Wh. The usable capacity (E_{usable}) is the energy between EOD and EOC voltage. This study focuses on analyzing the usable energy rather than the nominal energy. The usable energy depends on temperature and current rates.

C-rate in 1/h: The C-rate, expressed in units of 1/h (per hour), indicates the charging and discharging current relative to the battery's nominal capacity [38]. The reciprocal of the C-rate provides the time required for the battery with a capacity of C_N to be fully charged or discharged at the specified current [38]. The maximum C-rate is either limited by the maximum current of the battery or, for most HSSs, by the maximum battery converter current in relation to the battery capacity. Equation (2-5) presents the C-rate where C_N represents the nominal capacity of the battery in ampere-hours (Ah), and I_{Bat} is the battery current [38].

$$C\text{-}rate\ (t) = \frac{I_{bat}(t)}{C_N} \tag{2-5}$$

E-rate in 1/h. The E-rate, expressed in units of 1/h (per hour), indicates the charging and discharging power relative to the battery's nominal energy. The reciprocal of the C-rate provides the time required for the battery with an energy of E_N to be fully charged or discharged at the specified power. The maximum E-rate is either limited by the maximum power of the battery or, for most HSSs, by the maximal battery converter power in relation to the battery energy. Equation (2-5) presents the E-rate where E_N represents the nominal energy of the battery in watt-hours (Wh), and P_{bat} is the battery power.

$$\text{E-}rate\ (t) = \frac{P_{bat(t)}}{E_N} \tag{2-6}$$

State of charge (SOC) in %. SOC is a percentage-based indicator representing the remaining charge level of a battery in relation to its usable capacity [39]. The SOC is calculated by comparing the difference in charge concerning the remaining usable capacity [39]. This difference in SOC is also known as the depth of discharge (DOD) [37]. To calculate the SOC at a specific point in time, the difference in SOC, the initial SOC value, and the current flowing into the side reactions (I_{loss}) must be considered [39]. The side reactions are almost completely assigned to aging processes and are, therefore, very low, with little impact on short-term SOC determination. The formula to determine the current SOC is outlined in Equation (2-7) [39]. When the battery is fully charged under nominal conditions, the SOC is 100 %, reaching 0 % when empty [37]. If the nominal capacity is used for normalization instead of the usable capacity, this thesis refers to $SOC_{Nominal}$.

Capacity DOD in %. The capacity-related DOD_C is the difference in SOC as defined in Equation (2-7).

$$SOC(t) = SOC(t_0) + \underbrace{\frac{\int_{t_0}^{t_0+t} (I_{bat}(t) - I_{loss}(t))\, dt}{C_{usable}}}_{DOD_C} \tag{2-7}$$

State of energy (SOE) in %. Analogous to the SOC, the SOE is defined in Equation (2-8). If the nominal energy is used for normalization instead of the usable energy, this thesis refers to $SOE_{Nominal}$.

Energy DOD in %. The energy-related DOD_E is the difference in SOC as defined in Equation (2-7).

$$SOE(t) = SOE(t_0) + \underbrace{\frac{\int_{t_0}^{t_0+t} (P_{bat}(t) - P_{loss}(t))\, dt}{E_{usable}}}_{DOD_E} \tag{2-8}$$

Nominal capacity state of health (SOH_{NC}) in %. SOH_{NC} serves as an indicator of a battery's aging conditions and is derived from the ratio between the remaining maximum capacity (C_{max}) and the nominal capacity C_N, as represented in Equation (2-9) [37,39].

$$SOH_{NC}(t) = \frac{C_{max}(t)}{C_N} \tag{2-9}$$

Nominal energy state of health (SOH_{NE}) in %. The SOH can also be defined in terms of energy, as outlined in Equation (2-10).

$$SOH_{NE}(t) = \frac{E_{max}(t)}{E_N} \tag{2-10}$$

Usable capacity state of health (SOH_{UC}) in %. The SOH_{UC} serves as an indicator of a battery's aging conditions and limitations set by the BMS. It is derived from the ratio between the remaining usable capacity C_{usable} and its initial usable capacity $C_{usable,initial}$, as represented in Equation (2-9) [37,39]. The initial usable capacity value can equal the nominal value but does not have to. As this thesis has no initial capacity measurements, nominal capacity values are assumed to be the initial usable capacity values.

$$SOH_{UC}(t) = \frac{C_{usable}(t)}{C_{usable,initial}} \tag{2-11}$$

Usable energy state of health (SOH_{UE}) in %. The SOH can also be defined in terms of energy, as outlined in Equation (2-10). As this thesis has no initial energy measurements, the SOH_{UE} equals the SOH_{NE}.

$$SOH_{UE}(t) = \frac{E_{usable}(t)}{E_{usable,inital}} \tag{2-12}$$

Internal resistance in Ω. There are many definitions of the internal resistance, which can be described as a complex impedance curve [40,41]. For this thesis, the direct current resistance (DCR) is of special importance. It is derived from the battery's voltage response to a current pulse [40,41] and is extensively discussed in Chapter 6.

Internal resistance-related SOH$_R$ in %. The SOH can also be defined based on the internal resistance (SOH_R) [42] normalizing the actual value $R(t)$ by the initial resistance $R_{initial}$ according to Equation (2-13) [42].

$$SOH_R(t) = \frac{R_{initial}}{R(t)} \tag{2-13}$$

Begin of life (BOL). If a battery comes right out of production and still has its initial capacity and initial internal resistance, this is called BOL.

End of life (EOL). The EOL is reached if the capacity-related SOH or the energy-related SOH is less than 80 % or if the SOH$_R$ reaches 50 % (doubling of internal resistance) of its initial value. However, these are mathematical definitions and do not mean that the battery cannot be operated anymore (see Chapter 2.2.4).

Coulomb efficiency in %. The coulomb efficiency is defined by the ratio of discharged capacity $C_{discharge}$ to charged capacity C_{charge} computed through the integral of the battery current I_{bat} and outlined in Equation (2-14) [43].

The SOC range for the cycle must be identical with a start SOC (SOC, A) and an end SOC (SOC, B). The coulomb efficiency is typically close to 100 % for LIBs [42].

$$\eta_{coulomb} = \frac{C_{discharge}}{C_{charge}} = \frac{\left| \int_{t_{SOC,B}}^{t_{SOC,A}} I_{bat_{discharge}}(t)\, dt \right|}{\int_{t_{SOC,A}}^{t_{SOC,B}} I_{bat_{charge}}(t)\, dt} \tag{2-14}$$

Ohmic energy loss in Wh. The ohmic losses can be calculated according to Equation (2-15) and occur due to the ohmic resistance of a battery [44].

$$E_{loss_\Omega} = \int_{t_0}^{t_0+t} R(t) \cdot I(t)^2\, dt \tag{2-15}$$

Energetic efficiency in %. The energetic efficiency is determined by dividing the discharged by the charged energy, while integrating the battery power P_{bat} as depicted in Equation (2-16) [18]. The SOC range for the cycle must be identical with a start SOC (SOC, A) and an end SOC (SOC, B). The disparity between the two energies results from losses occurring within the battery, such as ohmic losses caused by the internal resistance [18]. In addition to the dominant ohmic losses over the internal resistance, there are also losses over the charge transfer and diffusion resistance [18,45]. The battery's efficiency is influenced by its cell chemistry [9]. Generally, the energetic efficiency of LIB is around 95 % for room temperatures and moderate C-rates [18,46,47].

$$\eta_{energy} = \frac{E_{discharge}}{E_{charge}} = \frac{|\int_{t_{SOC,B}}^{t_{SOC,A}} P_{bat_{discharge}}(t)\,dt\,|}{\int_{t_{SOC,A}}^{t_{SOC,B}} P_{bat_{charge}}(t)\,dt} \tag{2-16}$$

2.2.3 Cell voltage

The cell voltage provides essential information on the battery. Therefore, the open circuit voltage and the relaxation effects are described in more detail.

2.2.3.1 Open circuit voltage

Overview. The open circuit voltage (OCV) is the potential difference between the cathode and anode in equilibrium without any current flow [48,49]. These potentials are determined by the electrochemical properties of the electrode materials and represent the degree of lithiation of electrode materials, which changes during charging and discharging [50]. OCV measurement occurs after all balancing and diffusion processes have stabilized and minor to no voltage changes occur [37,39]. Another method is the measurement of quasi-OCV (qOCV) curves at low C-rates [51–56]. The OCV is a function of the SOC [38].

Electrode potential. Figure 2-2, left, shows the individual electrodes' open circuit potentials (OCP) and the resulting OCV curve of an LCO/NCO cell.

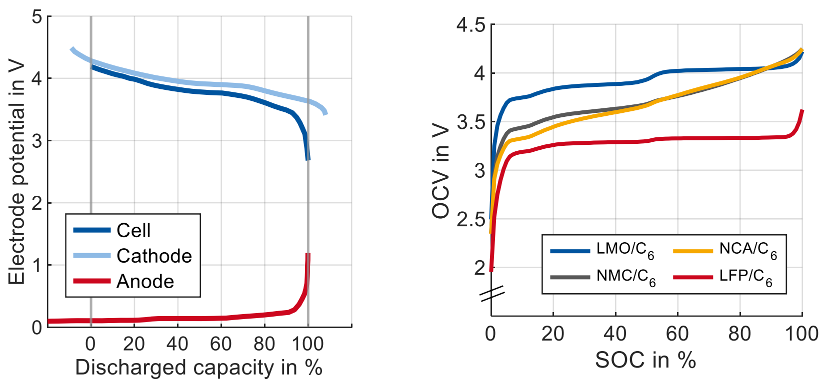

Figure 2-2: **Left:** OCV curve of an exemplary LCO/NCO vs. graphite cell with individual potentials for the cathode and the anode. Adapted from Birkl et al. [48], used under CC BY 4.0 [23]. **Right:** OCV curves of different lithium-ion chemistries. Data kindly provided by Matthias Kuipers based on [57].

The OCV curve's usable range is limited by the EOC and EOD voltages, represented as vertical lines in grey. When the cell is fully charged, the OCV is at its highest point, driven by the cathode potential toward the EOC voltage.

The cathode voltage decreases during discharge, while the anode potential increases. As a result, the cell voltage decreases until the sharp rise in anode potential (or a steep decline in cathode potential) leads to the reach of its EOD voltage. An accurate OCV curve is crucial for the BMS as it enables precise estimation of SOC and SOH, ensuring safe battery operation [58]. Since the OCV curve changes over time due to battery component aging, it needs continuous re-evaluation [59]. Moreover, the OCV curve contains valuable insights into the battery state and its individual components [59].

Cell chemistry. Figure 2-2, right, depicts the mean cell voltage of common active materials [17]. The voltage range for most LIBs is between 3 V and 4.2 V. Notably, the OCV curve of the LFP chemistry shows lower voltage (2.5 V to 3.4 V) and exhibits a smaller dependency on the SOC than the other chemistries. This flat OCV curve makes any voltage-based analytics challenging for LFP.

OCV measurement. The measurement of the open circuit voltage (OCV) of a battery can be challenging, especially while it is in use. This is because the voltage at the battery terminals includes additional voltage generated by electrical and chemical processes that occur inside the battery [60]. These overvoltage components change their sign during charging and discharging, creating a hysteresis in the battery terminal voltage [61]. The overvoltage consists of three components: the voltage drops due to internal ohmic resistance (V_{ohm}), the double layer voltage (V_{dl}), and the diffusion voltage (V_{df}). This leads to the relationship between terminal voltage (V_{bat}) and OCV (V_{OCV}), as shown in Equation (2-17) [61]. Chapters 5.2.2 and 6 discuss these in more detail.

$$V_{bat} = V_{OCV} + V_{ohm} + V_{dl} + V_{df} \tag{2-17}$$

Aging. As the battery ages, several processes cause shifts in the electrode potential, leading to a continuous change in the OCV curve. Chapter 7 discusses these processes in detail, and their utilization in estimating degradation modes is explored.

2.2.3.2 Relaxation effects

Charge and discharge lead to an uneven distribution of ions and electrons in the electrodes, leading to concentration gradients of charged particles or a state of disequilibrium [62]. This imbalance results in an overpotential, which is a potential difference compared to the OCV (equilibrium potential) caused by polarization [62–64]. The specific potential difference related to concentration is referred to as concentration overvoltage [65]. A charge redistribution occurs once battery charging or discharging stops, leading to a relaxation effect [62]. This relaxation effect is now referred to as the relaxation phase. Figure 2-3 illustrates relaxation phases after charging and discharging [66].

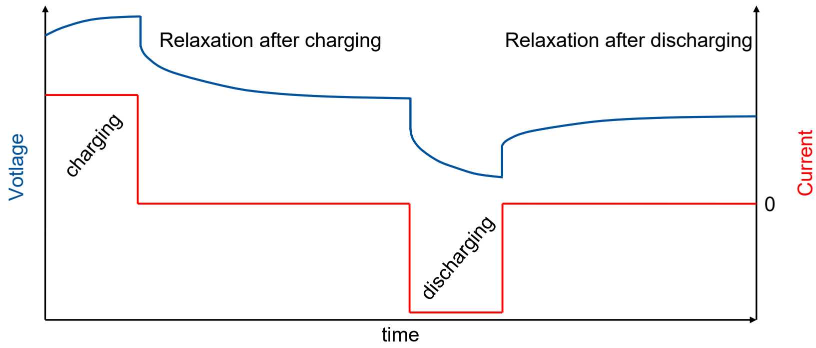

Figure 2-3: Schematic relaxation phases after charging and discharging, adapted from Kim et al. [66], used under CC BY-NC 4.0 [67].

An instantaneous voltage change occurs when the battery's current reaches zero [63,66]. The charge transfer overvoltage and diffusion overvoltage decay with distinct time constants representing the activation polarization and concentration polarization processes [62,63]. The charge transfer process is faster than the diffusion process [63]. Chemical reactions occur at the interface between the electrolyte and the electrode during the charge transfer process [63]. In contrast, there is actual mass transport, moving the products of the charge transfer process from the electrode surface to the interior during the slow diffusion process [63].

2.2.4 Aging

Researchers focus on understanding degradation mechanisms in lithium-ion batteries (LIB) to maximize their lifespan and optimize performance [22]. These degradation mechanisms target specific components of the battery cell [49] and generally lead to reduced capacity or increased resistance, resulting in capacity and power fade [68,69]. Figure 2-4 provides an overview of these degradation mechanisms, their underlying causes, the resulting degradation modes, and the directly observable effect [48]. These degradation mechanisms are diverse and influenced by numerous factors. Their causes can be broadly categorized into calendar aging and cycle aging [68]. Calendar aging encompasses all processes that occur inside the cell regardless of its operation [70]. In contrast, cycle aging is caused by operational stress on the cell's materials and components during charge and discharge cycles [68]. The following sections describe the various degradation mechanisms, their causes, and their impact on the battery's open circuit voltage (OCV). Chapter 7 discusses the degradation modes in more detail.

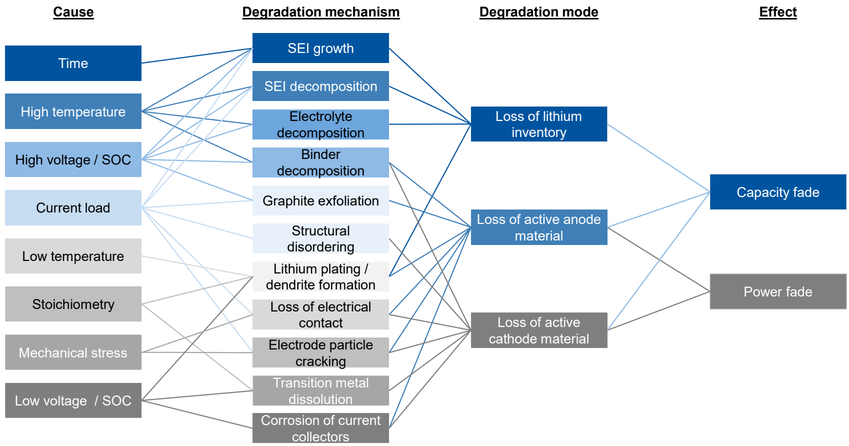

Figure 2-4: Overview of degradation causes, mechanisms, modes, and their effects. Adapted from Birkl et al. [48], used under CC BY 4.0 [23].

2.2.4.1 Calendar aging

Calendar aging involves degradation mechanisms that occur independently of charge-discharge cycles [70]. The primary contributors to calendar aging are chemical reactions at the electrode-electrolyte interfaces, forming passivation layers [70,71].

Anode. One of the major anode aging mechanisms is the growth of the solid electrolyte interphase (SEI) [70]. SEI is formed during the initial cycles of graphite-based LIB due to a chemical reaction between the anode and electrolyte [22,72]. This leads to an irreversible loss of lithium. Once formed, the SEI acts as a protective barrier, allowing only lithium ions to pass through and preventing further contact between the anode and the electrolyte [22,71]. However, continuous SEI growth leads to the further loss of active lithium, causing capacity fade, especially at high SOC and elevated temperature [70]. The reduced lithium content alters the electrode balancing, leading to an overall shift of the anode potential toward higher SOC. This results in an earlier increase in anode potential and a subsequent voltage drop in the cell's OCV during discharging [48]. In addition, the SEI growth leads to an increase in internal resistance, causing power fade [73,74]. Overall, the growth of the SEI is considered one of the main aging mechanisms in graphite-based lithium-ion batteries [68,74–76].

Cathode. The oxidation of the cathode against the electrolyte affects the cell impedance, increasing polarization and causing power fade [68]. High temperature and high SOC amplify the process [68]. In summary, both at the cathode and anode, high SOC and elevated temperatures drive calendar aging in LIB, making it crucial to avoid such conditions during operation. From the Arrhenius-Law, it can be deduced that a temperature increase of 10 K reduces the battery's lifetime roughly by half [22].

2.2.4.2 Cycle aging

In LIBs, every component undergoes a variety of degradation mechanisms during cycling. These mechanisms interact with each other and are difficult to distinguish. [77]. The following sections will explain the most critical cycle aging processes affecting different components. Generally, cycle aging is accelerated by high DODs and high C-rates [78].

Anode. Graphite is the most commonly used anode active material in LIBs [31]. It undergoes several main degradation mechanisms, including surface film formation, active material degradation, and lithium metal deposition on its surface, known as lithium plating [77]. Surface film formation involves the creation of the SEI. During cycling, the intercalation and deintercalation of lithium ions into the graphite result in repeated volume changes in the anode, causing mechanical stress [77]. This can lead to cracks in the crystals and particles of the anode's active material, where the cracked SEI exposes fresh graphite to the electrolyte, leading to additional SEI formation. Consequently, the loss of lithium leads to a capacity fade [51]. Moreover, the increased surface layer thickness leads to higher impedance, causing power fade [77]. The reduced amount of active material compresses the course of the anode OCP curve. This impacts the OCV curve, shifting the anode features toward lower SOCs [48]. Lithium plating occurs when lithium ion diffusion at the anode surface is insufficient to accommodate all arriving lithium ions. The local potential in this situation leads to the forming of a metal layer on the anode surface [79]. This phenomenon is particularly prevalent at high charging currents and low temperatures [79]. It causes capacity fade due to lithium loss, increased impedance, and power fade [68]. Additionally, it poses a safety risk, as repeated lithium plating results in small metallic lithium spikes called dendrites. These dendrites can lead to a short circuit within the battery cell [79].

Cathode. The cathode in LIB typically contains layered metal oxides as active materials, which are subject to degradation mechanisms. However, their impact on capacity loss is relatively minor compared to the capacity loss occurring through anode aging [77]. The aging mechanisms at the cathode involve the loss of active material due to mechanical stress and surface film formation. To prevent surface film formation, the cathode is prevented from reaching the required high potentials set by the EOC [77]. Consequently, the cathode's OCP curve is compressed, shifting its characteristic features toward higher SOCs. These changes in the cathode's behavior can be directly observed by examining the OCV curve [48].

2.2.4.3 Cell-to-cell variation

The environmental conditions and the individual operation of the storage systems already significantly influence battery aging. In addition to the differences, there is also variance between the individual cells from the production side and during cycling. Baumhöfer et al. [80] cycled 48 batteries of the same type under identical conditions in the laboratory. The underlying dataset from Sauer [81], published alongside the paper of Li et al. [82], is used to depict their capacity fade in Figure 2-5.

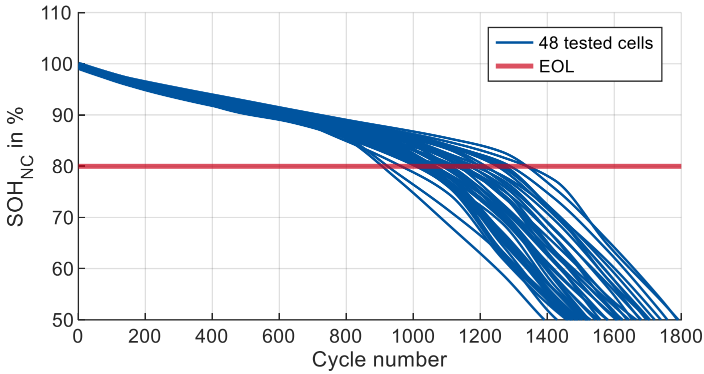

Figure 2-5: Test results showing the cell-to-cell variation during cycling. The 48 cells were cycled under the same environmental conditions, as described in Baumhöfer et al. [80]. Therefore, the spread in real-world operation is expected to be larger. The figure is created with data from Sauer [81], used under CC BY 4.0 [23]. The data was published in relation to Li et al. [82]. Design inspired by Baumhöfer et al. [80] and Li et al. [82].

At the beginning of the test, the batteries are in a narrow range close to 100 % of their nominal capacity. When the cycling starts, quasi-linear aging [80] can be observed, where the cells still show a similar SOH_{NC}. This is generally in line with other observations [83].

However, as the number of cycles increases, the cells drift apart. When reaching the EOL, a difference in capacity of about eight percentage points can be observed between the worst and the best cell. This corresponds to more than 400 additional cycles, which is about 30 % of the overall cycle life. HSS batteries typically comprise about 15 to 200 cells connected in series. Unfortunately, the worst cell in this interconnection determines the capacity of the series string as the current throughout it is identical. In aging analysis, predicting the so-called knee-point is considered a particular challenge [84]. After this point, the aging accelerates sharply, leading to a strong capacity fade.

2.2.5 State of health estimation

Accurate information about a battery's current state is crucial to ensure a safe and reliable operation [85]. However, once a battery is in use, obtaining data about its internal condition and tracking its characteristics becomes challenging due to the complex interactions of various aging mechanisms [86,87]. Precise monitoring of the battery SOH is essential for safety and enables predictive maintenance decisions regarding battery replacement [88,89]. Since the SOH cannot be directly measured, several methods have been developed to determine its value based on different definitions [88]. These methods can be categorized into offline and online approaches. Offline methods, often called experimental methods, involve capacity and resistance measurements [85]. On the other hand, online methods estimate battery SOH using operational data [86]. The literature review on specific state-of-the-art diagnostic methods is discussed in the corresponding sections of Chapter 5 to 7.

3 The development of stationary battery storage systems in Germany

This chapter discusses the market development of battery storage systems in Germany. After discussing recent literature, home, industrial, and large-scale battery storage systems markets are presented. It evaluates and combines several public and non-public databases and the current regulatory framework. The content of this chapter is based on peer-reviewed publications [4,90,91] and public reports [6,8,9,92–95] under the lead and collaboration of the author. Parts of it are identical to these references.

3.1 Overview

Energy storage systems play a significant role in a successful energy transition, enabling a de-fossilized, renewable, and reliable energy system [96–100]. Various energy storage technologies are currently active in the market, from the classic pumped hydro storage, heat storage, and power-to-X solutions to battery storage. Worldwide, battery storage systems have been showing rapid growth over the last few years, which is expected to continue [96,97,101].

Current forecasts on the development of the global battery market expect strong growth (see Figure 3-1). Nevertheless, estimates differ significantly and change over time due to different scenarios for the energy system, changing regulatory framework, geopolitical circumstances, and a lack of transparently accessible information, as a study on the European storage market points out [102].

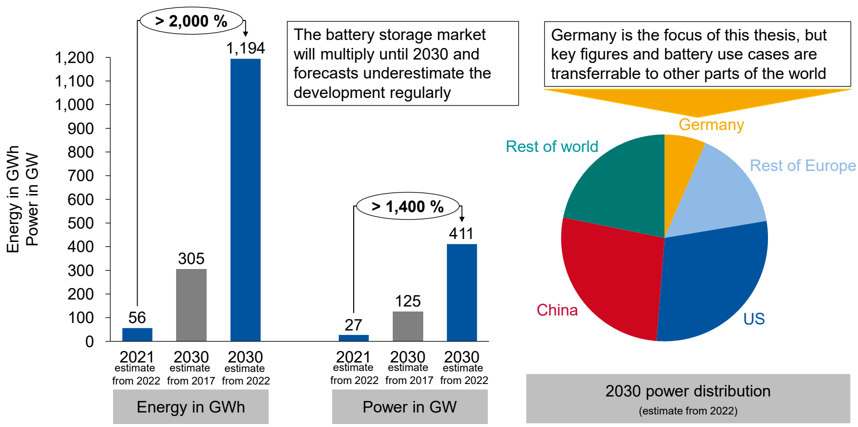

Figure 3-1: **Left:** Cumulative global battery storage deployments. Historic data for 2021 and estimates for 2030 made in 2017 and 2022. **Right:** Estimated power distribution of battery storage systems in 2030. The figure is created with data from [101,103].

To understand the market dynamics, previous forecasts can be analyzed. A 2017 study predicted the cumulative stationary battery installations for 2030 to range between around 100 GWh and 420 GWh worldwide, depending on the scenario [104]. Another 2017 study estimated cumulative installations of 305 GWh for 2030 [101]. Only a few years later, in 2022, the authors updated their estimate by a factor of four to 1,194 GWh as the storage world constantly evolves [103]. According to their assessment, the countries with the most battery storage installations in terms of power will be the United States, China, and Germany [103]. To contribute to market transparency, this thesis evaluates the current developments in Germany. However, many critical analyses like prices, use cases, and system design are also valid for more extensive parts of the world.

Literature review. Literature already presents many publications on the market development of battery storage. According to the classification in [4], these can be divided into the three fields of: (1) institutional publications, (2) peer-reviewed publications, and (3) consultant publications. Appendix, Table 9-1, gives an aggregated overview of the literature.

(1) The institutional publications are often from renowned organizations such as IRENA [104], the European Commission [102], or the IEA [105]. The reports, however, cover larger geographical areas such as the world or Europe and have either no or only isolated meta-information on individual countries. For the stationary BSS sector, there are two reports specifically for Germany from BVES and BSW-Solar, the two major associations in the storage sector. The BVES report [106] is freely available and provides an overview using parts of this analysis for the storage market update. The report offers high-level information but does not provide detailed information on technology development, such as battery chemistry. The BSW-Solar publishes isolated key details, such as installation numbers, in factsheets [107]. For the EV sector, in addition to the global analyses of the IEA [105], there are also reports from German institutions like the Federal Motor Transport Authority (FMTA) [108] or the NOW GmbH [109], which evaluate new registrations of EV in Germany but do not give information on data such as battery energy and charging power.

(2) The peer-reviewed publications are primarily based on the DOE database [110]. This is a recommended database with mostly large BSS projects from all over the world, but it needs to be completed for individual countries due to its global focus. In the publications, database analyses are sometimes supplemented by further information such as manual research or interviews [111–114]. In addition to a worldwide focus, there are analyses for individual countries [115,116], but the author is unaware of any detailed studies for Germany other than the publications related to this work [4,90,91,117]. Another database for BSS around the world is provided by in [118] but is not supplemented by any publication.

(3) Many consultant publications are fee-based and, therefore, not publicly available [119–122]. In some cases, there are also free reports or excerpts [101,123–126], but the methodology is usually not disclosed and is, therefore, non-transparent from a scientific point of view.

Conclusion. Motivated by these developments and the adoption of previous analyses under the collaboration of the author [4,90,91,117] in scientific literature, public reports [102,104], and the press [127,128], this chapter provides an update on the market development of BSS in Germany.

To keep selected figures on the stationary storage market up to date, the website “Battery Charts” (www.battery-charts.de) [129] was developed, which refers to [6] and accompanies it as supplementary material. Selected EV figures are available analogous on the website “Mobility Charts” (www.mobility-charts.de) [130] as presented in [117].

This analysis serves as a transparent primary source for the market development of battery storage systems in Germany. Researchers can use the results to parameterize simulation models and identify research areas. In addition, it provides policymakers and industry with information that supports decision-making in a dynamic market environment.

3.2 Methodology

This chapter describes the methodology used to analyze the stationary battery storage markets. After describing the storage system classification and its different databases, it explains the market estimations.

3.2.1 Battery storage classification

Looking closer at the applications and voltage levels presented in [131] and [132], the BSS market can be split into three submarkets. These markets differ in voltage level connection, rated power, storage capacity, and applications. Figure 3-2 gives an overview of the market classification. A detailed overview of all applications and grid connection possibilities is given in [131].

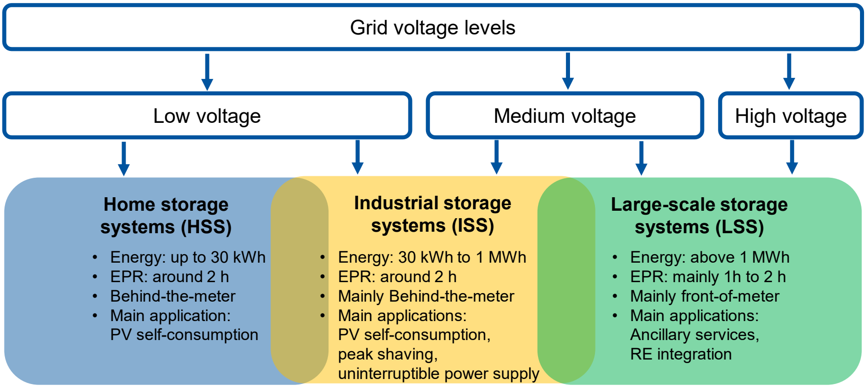

Figure 3-2: Overview of the different BSS markets and their grid connection in Germany. Note that there are no strict energy thresholds between HSSs, ISSs, and LSSs. Nevertheless, these are needed for a systematic evaluation, and the energy ranges cover the markets well. Own design with clustering according to [131] and [132].

The smallest BSSs are PV HSSs connected to the low voltage (LV, 0.4 kV AC) grid level. In this thesis, all BSSs with a battery energy below 30 kWh are classified as HSSs, although most of the systems have an energy below 10 kWh (see Chapter 3.3.1). Their main application is the increase in PV self-consumption to reduce electricity costs as a behind-the-meter use case. Moreover, decentralized HSSs are a promising technology for dealing with grid problems that can arise due to the high local penetration of PV power generation [133,134]. The ISSs are classified as systems with a battery energy between 30 kWh and 1 MWh. They are either connected to the low voltage level or to the medium voltage level (MV, 1 kV-36 kV), depending on their size and application. Their main applications are behind-the-meter use cases like increased PV self-consumption, peak shaving, or uninterruptible power supply (see Chapter 3.3.2). The front-of-meter LSSs are classified as BSSs with a battery energy above 1 MWh. They are either connected to the MV level or the high voltage level (HV, 36 kV-150 kV AC). Their main applications are ancillary services and renewable energy integration (see Chapter 3.3.3).

3.2.2 Dataset description

The analyses are based on the linkage of several public and private databases. An overview of used databases and their detailed description is given in Figure 3-3 and Table 3-1, respectively.

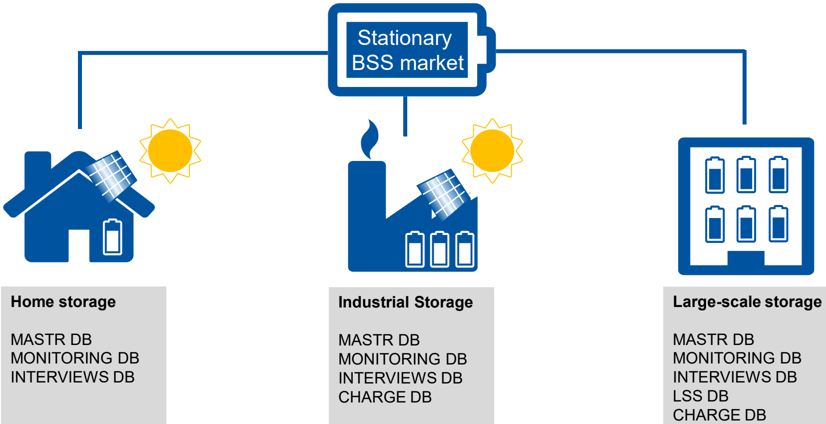

Figure 3-3: Overview of the databases used for the analyzed markets. See database descriptions and links in Table 3-1.

Table 3-1: Description of the databases used.

Database	Market	Description
MASTR DB [135] (public)	HSS, ISS, LSS	The MASTR DB [135] is the public database of the German Federal Network Agency (FNA, German: “Bundesnetzagentur”), where all stationary BSSs must be reported since January 2019. After some initial difficulties, the reported BSSs are almost complete, and the database offers a good overview of the market development, especially for newly registered BSSs (see Chapter 3.3.1). The data is based on manual entries by private persons, which results in regular confusion about technical quantities and incorrect information. To account for these irregularities, consistency checks are performed by the FNA and distribution system operators. In addition, the filters mentioned in Table 3-2 are applied for a consistent dataset. The collected data captures information about the location, operator, inverter power, and energy of the batteries. The dataset is licensed under dl-de/by-2-0 [136].

MONITORING DB [4,90,91] (private)	HSS, ISS	Until the beginning of MASTR DB, ISEA had the most comprehensive databases with around 30,000 HSSs and ISSs through the monitoring [4,90,91] of the national subsidy program of the German government (2013-2018) and the monitoring [93] of the local subsidy program of the federal state of Baden-Württemberg (2018-2022). The databases were collected via online questionnaires on subsidized HSSs and ISSs. They are used for detailed evaluations of the BSSs, such as technical characteristics or prices.
LSS DB [137] (public)	LSS	The "Forschungszentrum Jülich" compiled the LSS DB by manual research before the introduction of MASTR DB. This data was compared, extended, and aligned with the MASTR DB for this thesis. The data by Stenzel et al. [137] is licensed under CC BY-NC 3.0 [138].
CHARGE DB [139] (public)	ISS, LSS	The FNA maintains a register of all public charging stations reported in Germany, including installed charging power and location. These can be matched with ISS and LSS data. The data is provided by bundesnetzagentur.de, licensed under CC BY 4.0 [23].
INTERVIEWS DB (private)	HSS, ISS, LSS	Over the years, extensive connections have been established with associations, manufacturers, market research institutes, installers, wholesalers, and order brokers. The bilateral exchanges gather information about the storage market and current developments.

3.2.3 Market estimation

The Federal Network Agency (FNA) launched its MASTR DB in 2019, where all BSSs need to be registered. After its launch, it took a while for storage operators to be aware of the obligatory requirement of BSS registration, which led to many BSS that were not registered [4,90]. Due to the increasing completeness of the MASTR DB registrations, the stationary battery storage market analyses are based primarily on its evaluation [135]. The calculations are validated and supplemented using the private MONITORING DB, LSS DB [137], and data from bilateral exchanges with industry partners. Table 3-2 summarizes the filters applied to the database and the previous BSS classification from Chapter 3.2.1. Further information can be found in earlier works [4,90,91].

Table 3-2: Storage classification and filters applied to MASTR DB.

Market	Filter
HSS	battery energy ≤ 30 kWh
ISS	30 kWh < battery energy < 1,000 kWh
LSS	battery energy ≥ 1,000 kWh; operated by legal entities; voltage level “low voltage (230 V P-N)” only allowed if the grid operator has approved entry
HSS, ISS, LSS	BSS must be in operation, both energy and power must be registered, 0.1 h ≤ energy-to-power ratio (EPR) ≤ 15 h

3.3 Results and discussion

This chapter presents the market development of stationary storage in Germany. It includes home, industrial, and large-scale storage systems.

3.3.1 Home storage

This chapter discusses the market and technology development of home storage systems in Germany.

3.3.1.1 Market development

Overview. The HSS market is Germany's largest stationary storage market and has seen rapid growth in recent years. Figure 3-4 shows the estimate of annual HSS installations by battery technologies. According to the analysis, about 220,000 HSSs were installed in 2022, representing a market growth of 52 % in comparison to the previous year. This leads to an estimated stock of 650,000 installed HSSs in Germany by the end of 2022.

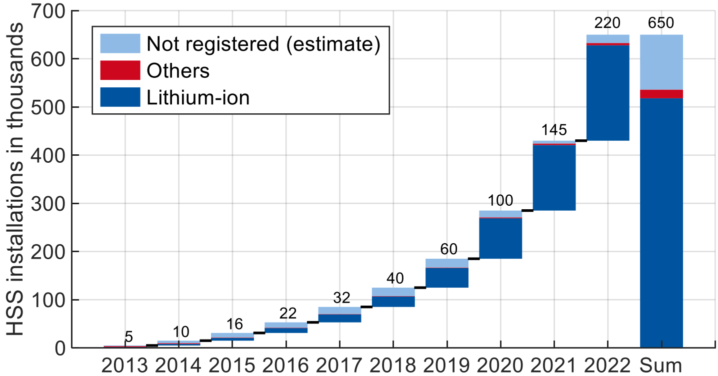

Figure 3-4: Estimated number of HSS installations in Germany based on own analyses of MASTR DB [135], used under dl-de/by-2-0 [136], and bilateral exchange with installers, retailers, and manufacturers. Based on the analysis, not all HSSs have been registered to the MASTR DB, but it is considered a reliable source.

Estimation. This estimate is based on analyzing the MASTR DB, where both PV systems and BSS are registered as separate datasets. However, the PV registrations also provide information on whether they were installed with an HSS, and they are considered more accurate than the HSS registrations themselves. This is because the feed-in tariff is only paid if the PV system is registered, meaning that all PV systems are included. In the MASTR DB, around 285,000 PV systems with a power between 2 kW and 30 kW were installed in 2022 (status February 2023). Of the new residential PV registrations, nearly 75 % state to be installed with an HSS, leading to 210,000 HSS installations with new PV systems. When matching the PV with the HSS registrations of 2022, 95 % of the HSS dataset is installed together with a new PV system of 2022, and 5 % are retrofitted to older PV systems. Considering these retrofits, the total HSS estimation reaches about 220,000 HSSs for 2022.

Non-reporting quota. The non-reporting quota of HSSs is estimated to be around 9 %, as 202,000 HSSs have been registered at the FNA for 2022 by February 2023. However, further analysis shows that this is about the same share of HSSs, which is typically registered belated after the end of a year. Thus, the MASTR DB is estimated to be the most reliable source to track the market development of stationary battery storage in Germany and can be used from now on without further analyses. This estimate is validated through bilaterally exchanged data from the DAA [140], which annually places tens of thousands of PV and HSS contracts. In 2022, 66 % of the orders included a PV system plus storage, 10 % included a PV system explicitly without storage, and 24 % of the inquiries had not yet been decided. The retrofits analyzed by DAA also account for 5 % to 7 %, and half of the undecided people likely opt for an HSS, which supports the analysis of 75 % of PV systems being installed together with an HSS. These estimates are in line with other analyses ranging from 197,000 HSSs (HTW Berlin [141]) to 214,000 HSSs (BSW [142]) to 220,000 HSSs (EUPD [143]).

Battery technology. The installed HSSs are almost completely (98 %) equipped with lithium-ion batteries, continuing the trend of previous years. While there were high shares of lead-acid batteries at the market's beginning, they have nearly disappeared. Other technologies, such as redox-flow and salt-water, also exist but are a niche. All non-lithium-ion technologies combined achieve a market share of only 2 % in 2022. As manual checks reveal, many lithium-ion HSSs were falsely classified as “Others” within this share. Within the lithium-ion batteries, LFP batteries are leading, followed by NCA and NMC [141].

Energy and power. In 2022, the newly installed battery energy was around 1,944 MWh, and the battery inverter power was about 1,164 MW (see Figure 3-5), representing a growth of 52 % (energy) and 60 % (power), respectively, relative to the previous year. Thus, by the end of 2022, a total HSS battery energy of 5,495 MWh and an inverter power of 3,098 MW was installed in Germany.

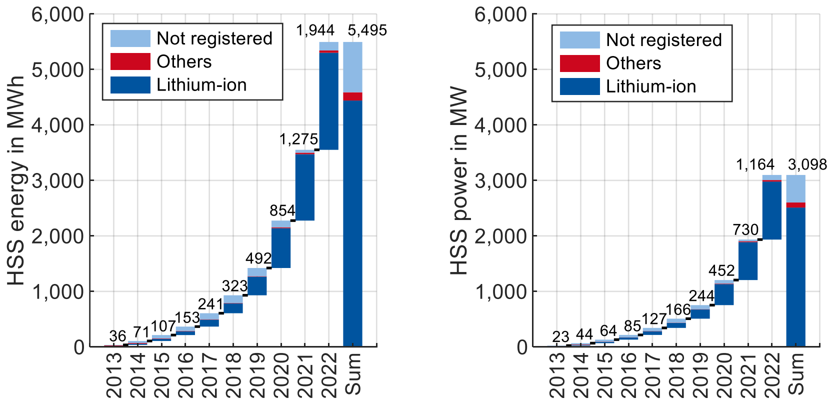

Figure 3-5: Estimated HSS battery energy (left) and inverter power (right) in Germany based on own analyses of MASTR DB [135], used under dl-de/by-2-0 [136], and bilateral exchange with installers, retailers, and manufacturers.

System design. The average energy per system stayed nearly constant at 8.8 kWh about the previous year, while the average power increased further from 5 kW to 5.3 kW (see Figure 3-6). Especially the segment of HSSs above 10 kWh accounts for an increasing share of HSS installations, with around 37 % of systems, while the majority of HSSs is still between 5 kWh and 10 kWh, with around 56 % of systems. Power ratings grew quicker than energy ratings, following customers' preferences to supply EVs and heat pumps with the HSS. The energy-to-power ratio (EPR) for most systems is around 2 h (see Appendix, Figure 9-2).

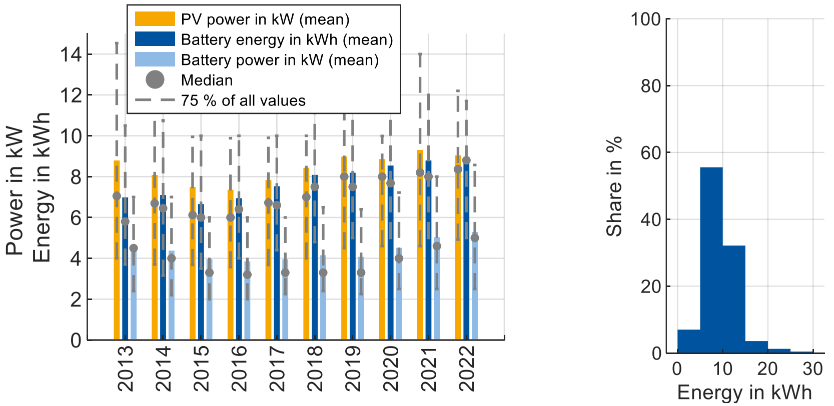

Figure 3-6: **Left:** Mean PV power (2 kW to 30 kW) and HSS battery energy and inverter power in Germany. **Right:** Battery energy size distribution. Based on analyses of MASTR DB [135], used under dl-de/by-2-0 [136].

Sector coupling and motivation. The sector coupling, which describes the energy exchange between the three sectors of electricity, heat, and mobility [144], is also a driver toward larger energy. While the share of new HSS installations combined with heat pumps increased from 30 % (2018) to 37 % (2021), the share of new HSSs combined with EVs grew from 8 % to 35 % in the same period (see Figure 3-7). In addition, the main purchase motivations are still participation in the energy transition (> 80 %) and rising electricity prices (> 75 %).

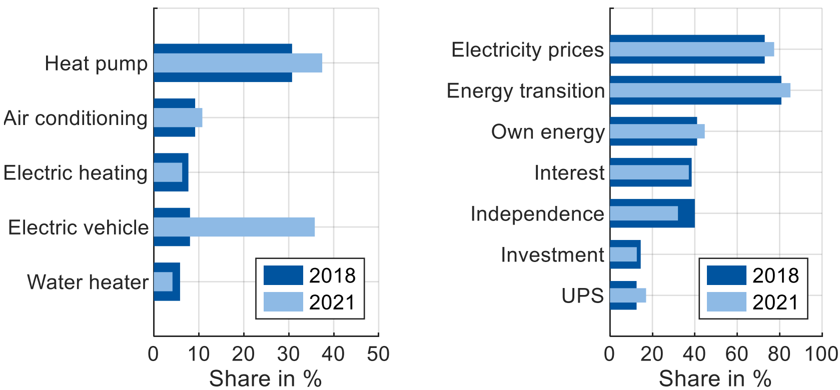

Figure 3-7: Large electrical consumers operated together with HSSs (left) and purchase motivation (right). More than one option can be chosen. Data from MONITORING DB.

3.3.1.2 Market outlook

The Federal Network Agency approved the grid development plan of the transmission system operators that currently plan with 97.7 GW to 113.4 GW for 2045, probably also including ISSs [145].

The PV market will most likely continue to grow due to the ambitious plans of the new government to reach yearly PV installations of 20 GW/a in comparison to 7.5 GW/a in 2022 [146]. In addition to the joint installations with new PV systems, more old PV systems that run out of the feed-in tariff will become available in the coming years. Further, higher energy prices and residential sector coupling drive the installations as more and more HSSs are operated with an EV or a heat pump [93]. While EVs and HSSs push each other right now, it remains unclear what effect EVs' vehicle-to-home application will have on the market. For some people, the EV will not be at home when the sun shines, and HSSs will be needed. For others (home office, second car), EVs could serve similarly to HSSs, reducing their sales.

3.3.2 Industrial storage

The industrial storage system (ISS) market is the smallest stationary storage market in Germany but is growing. In the following, the installation numbers and use cases are described.

3.3.2.1 Market development

Overview. The year 2022 showed the highest additions recorded until now (see Figure 3-8). The approximately 1,175 newly registered ISSs (see Appendix, Figure 9-3) have an energy of about 84 MWh and a power of 43 MW. In terms of energy, this is a growth of about 24 % over 2021. By the end of 2022, around 3,900 ISSs had a cumulative battery energy of 269 MWh and an inverter power of 144 MW.

Use case and sector. The analysis could assign 74 % of the ISS energy to a use case. About half of the ISS energy is used for renewable energy (RE) integration (match of MASTR DB for ISSs and PVs), 10 % for a combination of RE integration and EV charging, and 1 % solely for EV charging without a PV system (match of MASTR DB for ISSs, PVs, and CHARGE DB). Further, 12 % state in the MASTR DB to serve as an uninterruptible power supply.

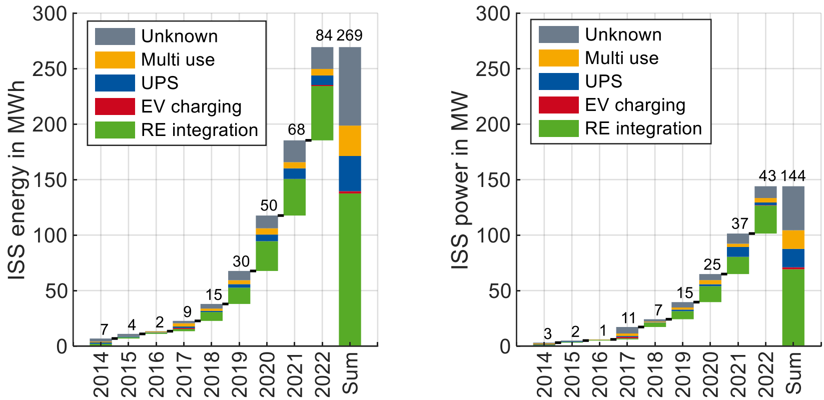

Figure 3-8: Development of ISS battery energy (left) and inverter power (right) in Germany by use case. Based on own analyses of MASTR DB [135] (used under dl-de/by-2-0 [136]), CHARGE DB [139] (used under CC BY 4.0 [23]), and further research.

Uncertainty. Due to the lack of information about the previous years of the ISS market described in [90] and multiple use cases, this analysis sticks solely to the MASTR DB registrations, even though there could also be ISSs that have not been registered as the BVES suspects [147]. However, the market is still quite small if a similar quote of non-reported ISSs is assumed according to the HSS or LSS markets (below 10 % each). Systems for uninterruptible power supply (UPS) are partly not included in the dataset as they only have to be registered if they are not exclusively used for uninterruptible power supply [148].

Battery technology. Regarding battery technology, lithium-ion systems continue to lead with 95 % of the ISS energy, and lead-acid systems account for about 3 % (see Appendix, Figure 9-4). The ISSs designated as "Others" in the MASTR DB are also predominantly lithium-ion systems according to manual triage, and redox-flow systems accounted for less than 1 % of the installed energy in 2022. Lead-acid batteries are often used for UPS, as the high mean SOC does not lead to accelerated aging [149]. Thus, their share could be higher (see paragraph above).

System design. Most ISSs are within the 30 kWh to 100 kWh class (see Appendix, Figure 9-1). This segment accounts for about 86 % of the systems. The share of ISSs between 100 kWh and 200 kWh accounts for nearly 8 % of the systems. ISSs above 200 kWh, however, remain the exception among large industrial operations, accounting for about 6 % of installed systems. While the median EPR is around 3 h, the energy-weighted mean is below 2 h (see Appendix, Figure 9-2). Thus, especially larger ISSs tend to have lower EPR.

Sectors. A share of 68 % of the ISSs could be assigned to a sector (see Appendix, Figure 9-5). The sector services and public administration is leading with 18 % of the ISS energy, followed by 10 % installed in manufacturing and 8 % in the energy supply sector. Trade and agriculture, and forestry and fishing, account for 5 % and 4 %, respectively. The sectors were chosen according to the NACE classification of the economic activities in the European Community [150].

3.3.2.2 Market outlook

Much stronger growth is expected in the coming years. The German Climate Protection Act stipulates a reduction in annual emissions volumes in the industry of around 35 % from 2020 to 2030 [151], and electricity prices for the industry are higher than ever [152]. However, this is also accompanied by a much higher fluctuation of the exchange electricity price during the day. If ISSs are managed wisely, this currently results in much higher margins, contributing significantly to the profitability of storage operations. ISSs play a critical role in CO_2-free industrial sites by decoupling generation and consumption over time. The versatile applications include, for example, increasing solar self-consumption, peak shaving for grid fee reduction, uninterruptible power supply, or the integration of renewable energies and electric vehicles. In particular, some of the planned fast charging stations will also have to be operated with buffer storage, which will lead to market growth. In such a scenario, the ISSs enable charging stations to provide higher power at short notice than the grid connection would allow. The recharge of the ISSs occurs when there are not many EVs at the charging station.

3.3.3 Large-scale storage

The large-scale storage market (LSS) is Germany's second-largest stationary BSS market.

3.3.3.1 Market development

Overview. After some years of decline, 2022 showed a record of 47 new LSS installations (see Appendix, Figure 9-6) with 467 MWh and 434 MW, which corresponds to a growth of 910 % in terms of energy additions (see Figure 3-9). In December 2022 alone, 250 MWh were registered. One reason for this end-of-year rally could be the last chance to register the LSSs to avoid grid tariffs according to § 18 StromNEV [153,154]. At the end of 2022, there were a total of 149 LSSs with an energy of 1,204 MWh and a power of 1,072 MW installed. The public announcements exceed the cumulative LSS installations until the end of 2022 for the next two to three years with 1,414 MWh / 1,123 MW.

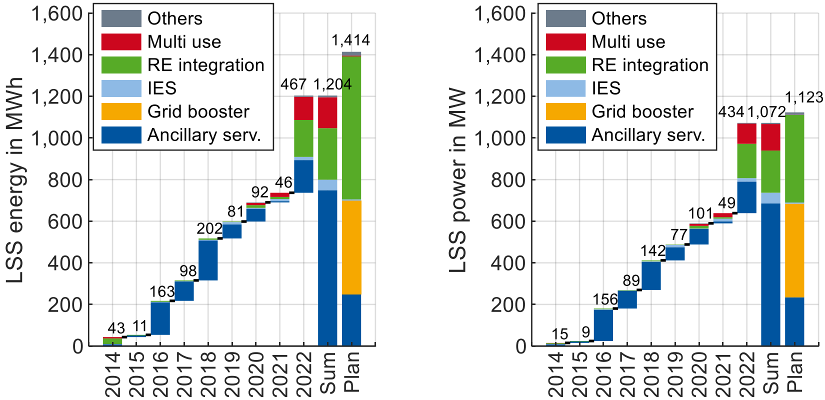

Figure 3-9: Development of LSS battery energy (left) and inverter power (right) in Germany by use case. Based on own analyses of MASTR DB [135] (used under dl-de/by-2-0 [136]), LSS DB [137] (used under CC BY-NC 3.0 [138]), and further research. “Plan”: announced projects for next 2-3 years.

Non-reporting quota. The analysis estimates that 9 % of LSSs have not been registered until the end of 2022 when comparing the MASTR DB data with LSS DB and further literature research of press releases and newspapers. The missing registrations for LSSs in operation are exclusively LSSs commissioned before the start of MASTR DB in 2019. Regarding planned LSS projects, only six additional projects could be found, although these are quite large (see Appendix, Figure 9-7). As for the HSS market, the MASTR DB is a reliable source for LSS deployments in Germany, especially for systems in operation. However, in terms of announcements, one either must wait for registration or collect press releases.

System design. Most LSSs are below 10 MWh (77 %), 18 % are between 10 MWh and 20 MWh, and single projects reach up to 80 MWh, while projects over 200 MWh are announced for the future. After some technologically versatile installations from 2016 to 2019, lithium-ion LSSs have been installed almost exclusively for the third year. With lithium-ion batteries manifesting their dominance in the LSS sector, the technology serves all stationary and mobile battery markets. Although some planned projects still state to have “Others” as battery technology or have not yet specified the technology, it is most likely that these projects will be realized as lithium-ion batteries.

Use cases. While the technology does not show any shift, the use cases do, as manual research indicates. Besides (1) ancillary services, (2) RE integration, (3) industrial energy supply, (4) multi-use operation including arbitrage trading, (5) grid booster projects, and (6) others gain traction. Figure 3-9 only shows the use case considered dominating, although some are also in multi-use operation. The EPR depends strongly on the use case, with about 1 h for ancillary services, 1 h to 2 h for RE integration, 1 h for grid booster, and a broad range from 0.5 h to 3 h for industrial energy supply (see Appendix, Figure 9-2).

(1) Ancillary services (in operation: 750 MWh / 685 MW) are still leading. Until 2019, LSSs have been built almost exclusively for the provision of frequency containment reserve (FCR) [4,90,155–157], which is evaluated in [158–164]. During this time, however, the prices for FCR initially dropped significantly, primarily due to the increasing saturation of the market volume by battery storage, which is why economic operation became more difficult, and the market declined until 2021 [4,90], but increased in 2022 again [165]. As of January 2023, the German FCR market is 570 MW [166], while already 630 MW of LSSs are officially prequalified to provide FCR [166], and national LSSs thus need to make use of the option to export 30 % of the FCR power to other countries. Although FCR prices are still attractive in early 2023 [167], analogous to all other energy markets, this price level will probably not be sustained in the long term due to high competition and further large projects announced for this market. This is why LSSs now also evaluate other possibilities like automatic frequency restoration reserve (aFRR), where the market is three to four times as large as the FCR market, and until now, only 60 MW of LSSs have been prequalified [166]. The ancillary service aFRR can be offered either as positive or negative power. LSSs can market both directions simultaneously, as negative and positive power are never activated simultaneously. Instead of the FCR market having a single power price, the aFRR market has a power and an energy price, making bidding strategies more complex. The maximum power must be provided for at least one hour, so the LSSs must have larger energy-to-power ratios than for FCR provision. The aFRR prices have increased over the last years, possibly leading to an attractive alternative [167].

(2) RE integration (in operation: 250 MWh / 200 MW) gained traction in the LSS market, and 700 MWh is already announced for the next years. Most projects are PV and LSS projects, and there is only one wind plus LSS project until now within the innovation auction. The Federal Network Agency (FNA) conducted the first five rounds of the so-called “innovation auctions” from 2020 to 2022 for the RE integration of large solar and wind parks that can bid in combination with a BSS [168]. The basis for the auctions is regulated in the Renewable Energy Sources Act [169] (Section 39j, EEG 2014, with amendments of 21.12.2020 and Section 39n, EEG 2021, respectively) and in the ordinance on innovation auctions [170]. The innovation auction BSS are mostly above 1 MWh (Figure 9-8), which is why they are listed in the LSS section, although there are also some BSS that would be classified as ISSs according to Table 3-2. As of February 2023, 21 BSS are already in operation, while 84 BSS are in construction, according to MASTR DB [90].

(3) Industrial energy supply (in operation: 50 MWh / 50 MW) is on the rise as the first large industrial sites operate LSS. For example, an engine manufacturer operates an LSS with an EPR of 4 h, presumably for self-consumption. At the same time, another uses a high-power LSS with an EPR of only 30 min, most likely for peak shaving. Further, some LSSs are installed next to power plants to optimize operation.

(4) In multi-use operation (in operation: 150 MWh / 130 MW), LSSs switch from one market to another and can combine front-of-meter use cases like ancillary services with behind-the-meter use cases such as self-consumption or peak shaving. The operating company of a couple of LSSs advertises on its website multi-use operation of energy arbitrage, load management, peak shaving, voltage stability, and FCR. Especially arbitrage trading is finally happening. While some years ago, this was economically not promising, the high price spreads on the spot market led to LSSs shifting energy from low to high prices. However, trading strategies must keep battery degradation costs in mind [171]. The energy throughput can be quite high for intensive arbitrage trading, and it is possible to exceed the cycle life of a battery. Typically, one to two cycles per day are realistic, not to exceed most warranty conditions. As a high cycle depth leads to accelerated aging [158], trading strategies should try to do many small cycles instead of a few large ones.

(5) Grid boosters (planned: 450 MWh / 450 MW) to temporarily relieve grid bottlenecks and save preventive redispatch have been increasingly discussed recently. These grid boosters will be among the largest storage projects in the world to date, with several hundred megawatts and megawatt-hours when completed. The planned pilot projects for concept validation by the transmission system operator TenneT, each with coordinated 100 MWh and 100 MW at the Audorf/Süd and Ottenhofen sites, and by the transmission system operator TransnetBW with 250 MWh and 250 MW at the Kupferzell site, were designed by the transmission system operators in the 2030 grid development plan and confirmed by the FNA in 2019 [172]. According to the 2035 network development plan, the two projects, P365 and P430, are each in preparing the planning and approval process. The expected commissioning of TenneT's project (P365) is planned for 2023, and that of TransnetBW's project (P430) for 2025. In contrast to the LSSs for providing FCR and the LSSs within the scope of the innovation auctions, grid boosters are used exclusively for grid operation management [172].

(6) Others (8 MWh / 6 MW) include two EV charging, one black start, and five LSSs not specified yet.

3.3.3.2 Market outlook

For the next two to three years, there are with 1.41 GWh more LSSs projects announced than the current stock by the end of 2022. LSS power with a focus on FCR already exceeds the national FCR market. Still, new use cases such as RE integration, industrial energy supply, arbitrage trading, automatic frequency restoration reserve, grid boosters, and multi-use operation emerge.

As an increasing number of conventional power plants with rotating masses disappear from the market, there will be a high demand for synthetic inertia [173]. Batteries can do this in principle [173], but the power electronics must ensure an extremely fast response [174]. The inverters must operate in a grid-forming and voltage-imprinting manner in the interconnected grid, emulating the characteristics of synchronous generators in the event of faults. In addition, EVs could also provide relevant shares of ancillary services [165,175,176], making the markets more competitive.

The Federal Network Agency approved the grid development plan of the transmission system operators that are currently planning with an LSS power of 43.3 GW to 54.5 GW for 2045 [145].

3.3.4 Prices

For many years, lithium-ion prices have been falling worldwide. However, in 2022, the world market battery prices increased by 7 % to 151 $/kWh (144 €/kWh), according to Bloomberg New Energy Finance (BNEF) [177].

Transparency problem. In general, prices are not transparently available for several reasons. Among these are: (1) prices vary largely depending on the region [177]. (2) It is not always clear what is included, and values can reach from pure prices for the hardware up to turnkey prices inclusive of ground and value-added taxes (VAT) covering large price ranges [90]. In this regard, some sources speak of prices while others of costs, both meaning probably the same [97]. (3) Information provided by manufacturers has to be seen as indicative, as the projects might have completely different circumstances [90]. The incentive for manufacturers to state low prices is questionable as this would set expectations for customers. (4) Further, demand and supply are quite dynamic, which leads to fluctuating prices to balance this situation. In addition, large customers such as EV manufacturers pay significantly less than relatively small manufacturers of stationary BSSs due to the high contract volumes.

HSS prices. For HSSs, end-customer prices (see Figure 3-10) from around 30,000 HSSs have been gathered until 2021 in a German-wide subsidy program and a subsidy program in Baden-Württemberg (BW) (see Table 3-1).

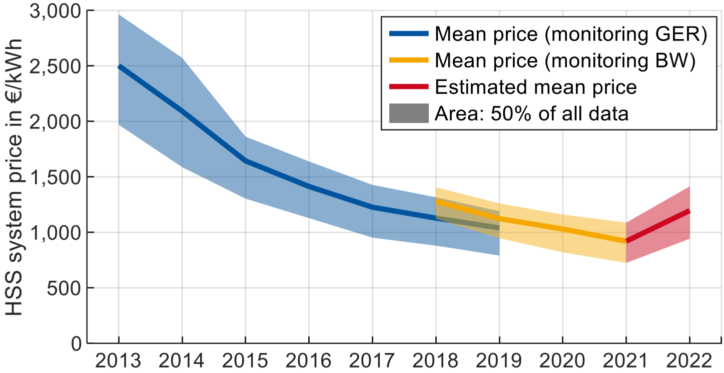

Figure 3-10: Price development of 30,000 HSSs per usable energy according to data in MONITORING DB and an estimated 30 % increase from 2021 to 2022 based on industry interviews. Values adjusted for inflation (base year: 2022) and without VAT.

The prices in BW for average-sized HSSs from 5 kWh to 15 kWh were slightly higher than in the German-wide monitoring, probably due to a generally higher price level in southern parts of Germany or higher subsidies [93]. From 2013 to 2021, HSS prices fell by 63 % from 2,500 €/kWh to 920 €/kWh. However, in 2022, a price increase of around 30 % is estimated after discussions with industry partners, leading to an estimated mean price of around 1,200 €/kWh. The price increase is due to the extremely high demand, which has continued to grow due to high energy prices and the war in Ukraine. Installers are at the limits of their installation capacities, and many people must wait more than half a year for a PV and HSS installation date. However, the prices vary largely, and prices ranged from 700 €/kWh up to 2,300 €/kWh in single offers analyzed in 2022.

ISS prices. For ISSs, the data from the subsidy program in BW until 2021 is used (mostly below 100 kWh), where average prices were 820 €/kWh (see Figure 3-11). The “pv magazine” (PVM) collects indicative prices from manufacturers for ISSs and LSSs in a database [178] at the very beginning of the year, which is why the prices are assigned rather to the previous year. This analysis deviates slightly from the reported values by PVM in [179–181] as the mean prices for 2022 and not the median prices are shown. In 2021, the mean prices range from 215 €/kWh to 990 €/kWh depending on the ISS energy and manufacturer.

From 2021 to 2022, mean values for ISSs up to 100 kWh increased by 23 % from 575 €/kWh to 710 €/kWh, for ISSs from 100 kWh to 500 kWh by 50 % from 390 €/kWh to 580 €/kWh, and for ISSs from 500 kWh to 1,000 kWh by 92 % from 310 €/kWh to 595 €/kWh. However, it should be noted that not exactly the same manufacturers provided prices for 2021 and 2022.

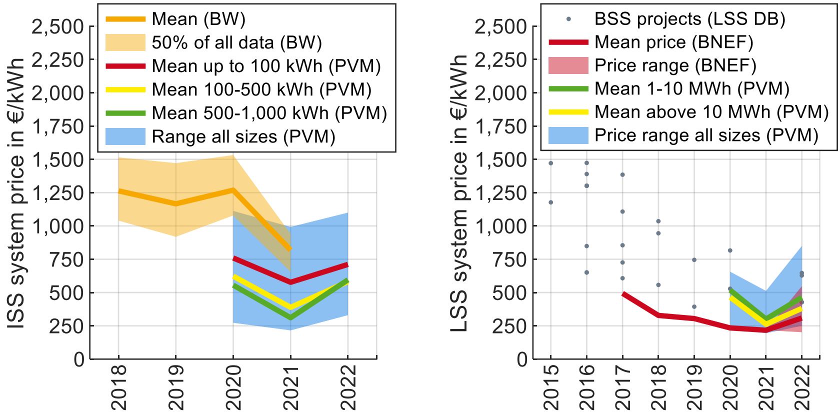

Figure 3-11: Price development of ISS (left) and LSS (right) according to data in MONITORING DB, extended LSS DB [137] (used under CC BY-NC 3.0 [138]), own analyses of pv magazine (PVM) database [178], and Bloomberg New Energy Finance (BNEF) [182]. Monitoring DB and PVM adjusted for inflation (base year: 2022), BNEF values (already adjusted for inflation by BNEF) converted from USD to EUR. Prices per usable energy and exclusive VAT except for unknown price components from LSS DB [137].

LSS prices. Single LSS project prices are included in the LSS DB for the years 2015 until 2020, and further press releases for 2021 and 2022 were scanned, but it is not always clear what exactly the prices include. They depict a price decrease from the average of 2017 (1,080 €/kWh) of around 50 % until 2022 (532 €/kWh). From 2021 to 2022, the prices from pv magazine show a price increase of 54 % for LSSs between 1 MWh and 10 MWh from 300 €/kWh to 464 €/MWh. LSSs above 10 MWh showed a price increase of 45 % from around 250 €/kWh to 380 €/kWh for the same period. For 2022, all values range from 250 €/kWh to 850 €/kWh depending on the energy and manufacturer. The 2022 mean prices from pv magazine are supported by the mean price of 310 €/kWh reported by BNEF for a four-hour turnkey LSS [182]. The authors point out that prices depend largely on region, energy, and system design, ranging from 202 €/kWh to 548 €/kWh [182]. The identified price increase of 27 % from 2021 to 2022 in USD [182] corresponds to an increase of 42 % when converted to EUR.

3.4 Conclusion

Figure 3-12 summarizes the key information of this chapter while focusing on the installed battery energy and inverter power. All in all, the stationary BSS markets are growing strongly. In 2022, additional battery energy of 2.5 GWh was installed, and all markets had a cumulative battery energy of about 7 GWh.

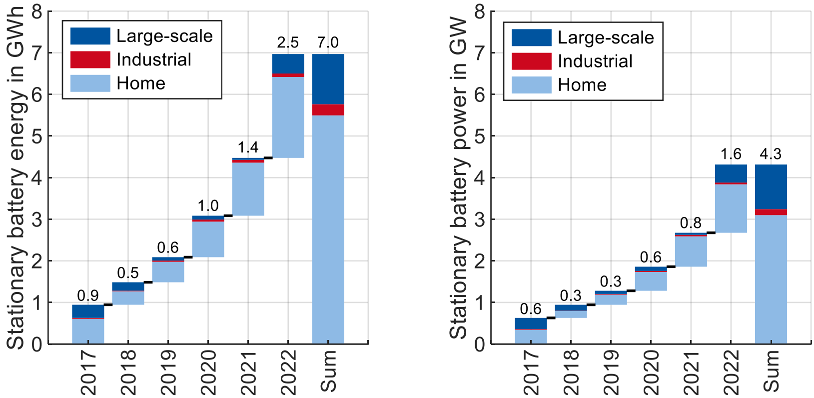

Figure 3-12: Development of the stationary battery storage market in Germany. Based on own analyses of MASTR DB [135] (used under dl-de/by-2-0 [136]), LSS DB [137] (used under CC BY-NC 3.0 [138]), and further research. Battery energy (left) and inverter power (right).

Markets. HSSs are leading with 78 % of the newly installed battery energy in 2022 and 79 % (5.49 GWh) of the stock, while ISSs account for 4 % (0.27 GWh) and LSSs for 17 % (1.2 GWh) of the stock. By the end of 2022, battery storage had nearly 20 % of the energy of the national pumped hydro storage power plants of 39 GWh [183]. This shows the enormous flexibility potential of battery storage in the energy system.

Future market tracking. To provide the readers with the latest registration figures, the website www.battery-charts.de [129] presents the stationary battery storage registrations in MASTR DB as supplementary material to the publication that was the base for this chapter [6]. Further, the reliable EV registrations at the German Federal Motor Transport Authority are depicted on www.mobility-charts.de [130], as presented in [117].

Motivation for thesis. HSSs, in particular, are widespread in Germany, and other countries record increasing sales figures. Due to the growing importance of battery storage, future regulation requires reliable and scalable methods for SOH estimation of battery storage [7]. On the one hand, these methods enable demand-oriented maintenance and, thus, a long use of important resources. On the other hand, warranty cases of the systems can be detected to support end users. The development of such methods is the core of the following chapters.

4 Dataset and field operation

This chapter describes the field measurements and the dataset used for all following analyses. Furthermore, it provides insights into the operation and characteristics of home storage systems. The chapter is based on and contains identical parts of [184] and its supplementary information under the lead of the author. In addition, parts of it are based on [8,9] under the lead of the author.

4.1 High-resolution field measurements

In the following, the field measurements and the gathered dataset [185] are presented and discussed.

4.1.1 Dataset and measurement

Overview. The ISEA measured 21 private HSSs in Germany over up to eight years from 2015 to 2022. All these HSSs are combined with residential PV systems to increase self-consumption. The measured quantities relevant to this thesis are system-level battery current, voltage, battery pack housing temperature, and room temperature, while the sample rate is one second. Single HSS manufacturers already have more than 100,000 HSSs in the field. Nevertheless, from a scientific perspective, the dataset is unique until the time of writing (year 2024). The author is unaware of any comparable scientific datasets for lithium-ion HSSs. About 106 system years represented by 14 billion data points totaling 146 GB were analyzed. Table 4-1 contains an overview of the measured HSS batteries and their main parameters.

Nomenclature. The operational behavior of the systems is determined by two main parameters, which are the system design and the used cell chemistry. While some metrics like the C-rate or the number of EFCs depend on the system design and the ratio of battery energy to inverter power, the cell chemistries have different OCV curves (see Figure 2-2) and specific aging characteristics. To account for this, the system nomenclature gives information on both parameters to interpret the results. Therefore, this thesis refers to “$\text{Small}_{\text{LMO}}$” (or “$\text{S}_{\text{LMO}}$”), “$\text{Medium}_{\text{NMC}}$” (or “$\text{M}_{\text{NMC}}$”), and ”$\text{Medium}_{\text{LFP}}$” (or “$\text{M}_{\text{LFP}}$”) HSSs. As there are already HSSs in the energy range above 15 kWh on the market, none of the systems are classified as large. $\text{Small}_{\text{LMO}}$ and $\text{Medium}_{\text{NMC}}$ systems share similar battery chemistries, but their system design is not comparable. While the $\text{Medium}_{\text{LFP}}$ and the $\text{Medium}_{\text{NMC}}$ systems show a similar system design, their battery chemistries are not comparable. These relationships must be considered for the interpretation of the results.

System design. The assumed nominal energy reaches from 2.2 kWh to 13.8 kWh with capacity values between 15 Ah and 300 Ah. These values were either seen on the modules, found in publicly available datasheets, or acquired through interviews. The inverter power ranges from 2 kW to 3.5 kW, leading to energy-to-power (EPR) ratios of around 1 h to 4 h, corresponding to maximum system E-rates of 1 E to 0.25 E. Most systems are low-voltage systems with a nominal voltage in the range of 46 V to 52 V. However, the Small$_{LMO}$ systems are considered high-voltage systems and have a nominal voltage of 146.7 V. In addition, these systems have an EPR of around 1 h and a relatively low battery energy, leading to different operational behavior. Nevertheless, they are operated with smaller PV systems, and the houses have smaller energy consumption.

Table 4-1: Aggregated overview of the measured HSSs.

Nomenclature & chemistry	Nominal energy in kWh	Inverter power in kW	Nominal voltage in V	Number of systems of one product	Aggregated number of systems
"Small$_{LMO}$" or "S$_{LMO}$" with LMO/NMC blend battery ("LMO")	2.2	2	146.7	6	6
"Medium$_{NMC}$" or "M$_{NMC}$" with NMC battery	8.6	2.5	50.4	1	7
	8.7	3	48.1	2	
	8.8	3	46.8	2	
	9.8	5	51.8	1	
	11.5	2.5	50.4	1	
"Medium$_{LFP}$", or "M$_{LFP}$" with LFP batteries	8.1	3	51.2	4	8
	9.2	3.3	46	2	
	10.0	3	51.2	1	
	13.8	3.5	46	1	

Cell chemistry. The different cathode materials are lithium nickel manganese cobalt (NMC), a blend of lithium manganese oxide (LMO) and NMC (simply referred to as "LMO" in this thesis), and lithium iron phosphate (LFP). Within the Medium$_{NMC}$ systems, there are differences in cell chemistry. Two of the NMC systems are sometimes classified as NCA, and the manufacturer appears to have changed the chemistry of the cells in several product generations. In any case, these batteries have a high nickel share, but their OCV curves examined in Chapter 7 are close to the ones of the other NMC systems.

Lack of metadata transparency. For most HSSs, only the usable energy is stated on the datasheets. However, this statement often includes an aging reserve and does not correspond to reality as larger energy ranges can be observed in operation. Thus, the batteries' metadata had to be gathered through further research. The obtained values are not guaranteed to be correct as the manufacturers did not always provide the information, and some packs have no labels. In addition, the interconnection scheme is not accessible either. Obtaining the provided metadata was a very time-intensive task that should not be underestimated if there is no direct access to a manufacturer's metadatabase. The conducted research ranged from simple manufacturer contact to the dissembling of the battery pack in the laboratory to identify cell types and interconnection schemes of the cells. The used cells are typically subject to non-disclosure agreements and cannot be shared. Table 9-2 in the appendix presents the gathered single-system metadata.

Measurement hardware. Table 4-2 depicts the measurement hardware used and the measured quantity. This thesis focuses on battery voltage, current, and temperature (room and pack housing), although PV generation, electrical household consumption, and grid exchange were also recorded. The first generation of measurement systems had a Gantner A127 measurement device with a Gantner Q.pac logger. In contrast, the second one used an Electrex Femto / Atto D4 and a Gantner Q.reader logger to enable online resets and configuration. The measurement sensors were installed between the DC side of the converter and the system-level battery. Thus, the provision of power to the BMS inside the storage system is included in the measurements.

Table 4-2: Aggregated overview of the measurement systems.

	Measured quantity	Hardware version 1 (+ accuracy)	Hardware version 2 (+ accuracy)
Measured quantity	Voltage	Gantner A127 (0.05 %)	Electrex Femto / Atto D4 (0.25 %)
	Current	Gantner A127 (0.05 %) + Shunt (0.5 %)	Electrex Femto / Atto D4 (0.25 %) + Shunt (0.5 %)
	Temperature (battery pack housing and room)	PT 100 ± (0,30 °C + 0,005 · T)	PT 100 ± (0,30 °C + 0,005 · T)
Logger		Gantner Q.pac	Gantner Q.pac / Gantner Q.reader
ID		14, 18, 21	1 – 13, 15 – 17, 19 -20

Measurement period. The measurement systems were installed in 2015 and 2016 in the first project, and in 2019 in the second one (see Figure 4-1, left).

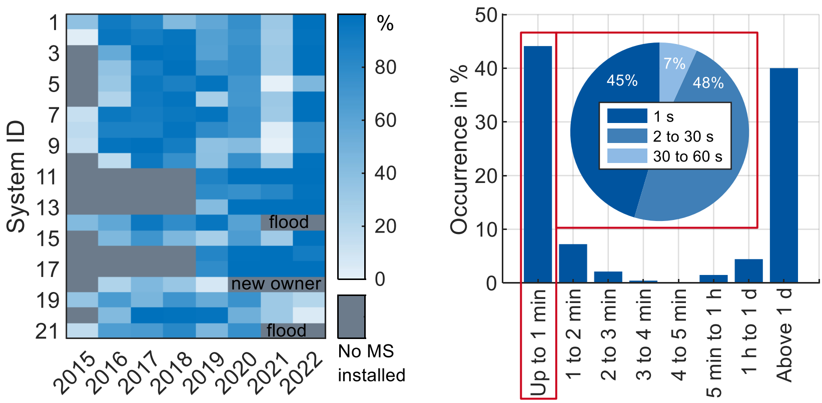

Figure 4-1: **Left:** Data availability overview. Note that measurement systems were installed in 2015, 2016, and 2019. Some measurement systems were decommissioned in 2020 (ID 18, new house owner) and 2021 (ID 14 and ID 21, flood catastrophe in Germany). **Right:** Occurrences of data gap lengths for all systems (except for system ID 7, which has nearly the same number of 1 s gaps on its own as all the others combined).

Three measurement systems had to be decommissioned. In 2020, a homeowner changed (ID 18), and the measurements were not continued. In 2021, two houses were affected by the flood catastrophe in western Germany, leading to defective HSSs (ID 14 and ID 21).

Data availability. In general, the database is well suited for any field diagnostics as the measurement systems have both a high accuracy [186] and a high sample rate of one second. The biggest data quality problem in the measurement of decentralized households is the failure of data transmission due to technical problems of the measurement system or the internet connection of the households. It was quite challenging to detect and correct the errors, given that appointments had to be scheduled with private persons, and the work related to the measurements was not funded over several years. Therefore, gaps occurred in the data.

Data cleaning. The cleaning of the data consists of the following steps:

1. Filters: Sometimes, the measurement system records invalid values outside the regular operational limits, such as a battery voltage of 0 V. These values are filtered. The filters are set according to the datasheet specifications and a manual observation of the measured values. For instance, the HSSs occasionally provide higher power than the specified nominal power, or such, which was validated through exchange with the manufacturers. The filtered outliers are changed to “not a number” (NaN).
2. Measurement gaps: The measurement systems do not always record a measured value every second exactly. A linear interpolation was used for gaps of up to 5 min, as over 50 % of measurement gaps are below 5 min, and nearly 45 % even below 1 min (see Figure 4-1, right).

From system to cell data. The HSSs show different voltage levels and capacities. The cells range from about 2.5 Ah round cells to over 60 Ah pouch bag cells, leading to various series and parallel connections. To make the analyses comparable, the system-level data is scaled to cell-level quantities using the obtained connection schemes of the battery packs. This way, only the average cell voltage and current can be calculated. If the BMS balances all cell voltages well, the mean value corresponds to single-cell data. If the balancing does not work reliably (see Chapter 2.2.4), values like the capacity can be overestimated as the weakest cell (and not the average cell) in a series connection limits the capacity of the whole string. This is also a problem if the cells age differently, which can be assumed according to Chapter 2.2.4.

Open data. The HSS dataset [185] is published with the journal article [184] to make it available for further research. It provides scientists worldwide with a database for versatile analyses of lithium-ion batteries and HSS operation.

4.1.2 Dataset representativeness

Overview. The measurements started in 2015, and at that time, some systems had already been in operation for about one year. In particular, the analyzed HSSs with measurement starting in 2015 can, therefore, be seen as first-generation systems. Even the HSSs with measurement start in 2019 are already outdated products. By 2022, the market has evolved significantly (see Chapter 3), and none of the products are still available on the market in the measured form. To mitigate these developments to a certain extent, technologically diverse storage systems have been selected for the measurement. In the following, some core parameters are discussed to show which system features are still relevant today and which have changed.

Table 4-3: Comparison of this dataset and the German HSS market.

	German market		This dataset		
	2015	2022	Small$_{LMO}$	Medium$_{NMC}$	Medium$_{LFP}$
Energy in kWh (mean)	6.7	8.8	2.2	9.3	9.3
Power in kW (mean)	4.0	5.3	2	3.1	3.3
E-rate in 1/h (mean)	0.60	0.60	0.91	0.33	0.35
Topology in % [141]	AC: 60 DC: 40	AC: 25 DC: 75	DC	AC & DC	AC
Battery chemistry in % [141]	LFP: 35 NMC: 53 NCA: 12	LFP: 68 NMC: 12 NCA: 20	LMO/NMC blend	NMC	LFP
Voltage level in V (nominal) [15]	Mostly ~ 50	~ 50 - 500	~ 150	~ 50	~ 50

Energy and power. Over the last few years, energy and power ratings have been growing in the home storage market (see Chapter 3.3.1). According to Table 4-3, the average battery energy has increased from 6.7 kWh (2015) to 8.8 kWh (2022). The average inverter power has grown from 4.0 kW to 5.3 kW. The dataset thus continues to cover a representative range of today's systems with the Medium$_{NMC}$ and Medium$_{LFP}$ HSS. Today's average E-rates correspond to about 0.6 E, which is higher than the average E-rates of the Medium$_{NMC}$ and Medium$_{LFP}$ datasets. Nevertheless, there are now also storage systems that offer around 1 E and are thus in the E-rate range of the Small$_{LMO}$ systems. These smaller HSSs are no longer common today. Nevertheless, they are operated primarily with smaller PV systems and in households with lower energy consumption. Although the operation is not the same (more EFCs, higher DODs), they still show comparable operational behavior, as shown in Chapter 4.2.

Topology. Analogous to the dataset, both AC- and DC-coupled storage systems exist on the market. While in 2015, more AC-coupled storage systems were sold (around 60 %), DC-coupled storage systems led the market in 2022 (around 75 %) [141].

Battery chemistry. In 2015, more than 50 % of the HSSs had an NMC battery [141]. In the meantime, LFP has become the leading battery chemistry with two-thirds of new installations [141]. In addition, the share of NCA batteries grew from 12 % to 20 % [141]. The battery chemistries of the dataset cover the LFP and NMC share well with 8 LFP, 7 NMC, and 6 LMO/NMC blend batteries. NCA batteries are not covered, although two NMC system batteries are sometimes classified as NCA (see Chapter 4.1.1). Nevertheless, the OCV curve shows similarities to the NMC and LMO batteries (see Chapter 2.2.3), which is why the developed methods should be transferrable.

Voltage levels. The measured $\mathrm{Medium_{NMC}}$ and $\mathrm{Medium_{LFP}}$ are all low-voltage systems with nominal voltages around 50 V. At around 150 V, the $\mathrm{Small_{LMO}}$ systems are more in the high-voltage range. Although low-voltage systems still exist today, there is a trend toward high-voltage systems. These reach nominal voltages of 200 V to about 500 V [15]. To achieve these voltages, more cells are connected in series and fewer in parallel in comparison to low-voltage HSSs with the same battery energy. The evaluations in Chapter 7 suggest that this improves the diagnostic capability since fewer parallel voltages overlap. Nevertheless, a series connection could lead to a faster capacity fade of the system. The reason for this is that cells age differently (see Chapter 2.2.4.3), and the cell with the lowest capacity determines the total capacity of a serial string.

Conclusion. Although the measured HSSs are no longer on the market, the systems continue to provide a representative dataset, and the methods developed are applicable to today's systems. While the $\mathrm{Medium_{NMC}}$ and $\mathrm{Medium_{LFP}}$ batteries cover today’s energy ratings and technology choices (except for NCA batteries), the $\mathrm{Small_{LMO}}$ systems cover typical E-rates, and their analysis can possibly be transferred to high-voltage systems to a certain extent.

4.2 Field operation of home storage systems

This chapter gives a condensed overview of the operational behavior of HSSs. Thus, it provides knowledge to interpret and understand the results of the methods developed in this thesis.

4.2.1 General operation

Regulatory background. Technical requirements influenced PV operation to ensure grid stability by limiting the feed-in power. The Renewable Energy Sources Act (EEG) imposed a fixed limitation on the feed-in of PV systems, amounting to 70 % of their nominal power [169]. This could be realized through a fixed limit within the PV inverter or a grid operator's remote feed-in control.

The government removed this limit for new PV systems up to 25 kW installed after 14.09.2022 and for existing PV systems up to 7 kW since 01.01.2023 with the EEG novel from 2023 [187]. PV systems between 7 kW and 25 kW can also remove the feed-in limit if they have smart meters. All measurements were conducted while the 70 % feed-in limit was valid.

Operational strategies. However, the HSSs were installed within a subsidy program implemented by the Federal Ministry for Economic Affairs and Climate Action (BMWK) in collaboration with the subsidy bank "Kreditanstalt für Wiederaufbau" (KfW). This subsidy program set more stringent regulations for PV systems operated with a subsidized HSS to incentivize grid-relieving operation. Depending on the installation period, the PV systems installed between 2013 and 2015 are subject to a maximum feed-in of 60 % of their nominal power, while those installed since 2016 are restricted to 50 %. Consequently, diverse operating strategies have been developed for HSSs to comply with these limitations and optimize self-consumption patterns and battery longevity [188]. Figure 4-2 depicts a typical day for two common strategies: excess-charging and forecast-based operation.

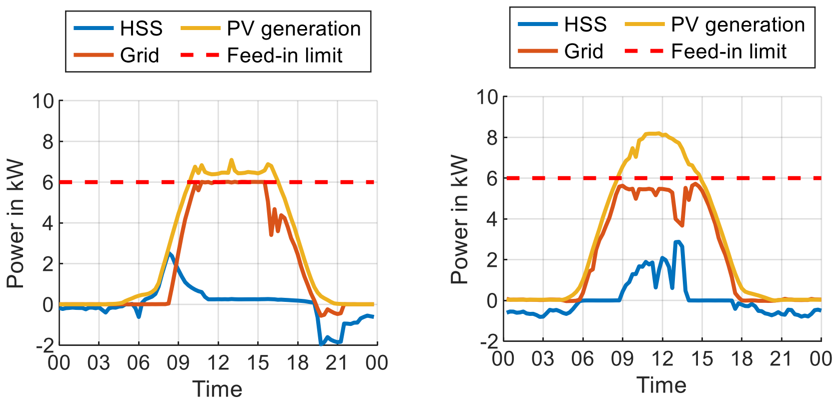

Figure 4-2: Exemplary power flows for different operational strategies for the same day and region. Positive HSS power represents charging. Positive grid power represents feed-in. **Left:** Excess-charging HSS that charges in the morning and is full at noon. The PV power must be curtailed to fulfill the 60 % feed-in limit, leading to losses. **Right:** Forecast-based HSS that charges during noon to limit the feed-in power. No PV curtailment losses occur. Both PV systems have a nominal power of 10 kW.

Excess-charging strategy. The excess-charging strategy initiates battery charging (positive power) when the solar power generation surpasses the household's electricity consumption. While this approach is relatively simple to implement, it may result in the battery reaching full capacity early in the day. Thus, PV production must be curtailed during noon to fulfill the feed-in limit, leading to energy losses. Furthermore, the battery remains at high SOCs for extended periods due to the early charging, accelerating its aging process [78].

Forecast-based strategy. The forecast-based strategy employs location-specific generation and load forecasts to minimize losses due to feed-in limitations. Utilizing forecast data, the battery's charging is postponed to times of peak PV production during midday, effectively avoiding curtailment losses. The PV power is fed into the grid during morning and evening hours if a PV surplus exists [189]. While this strategy requires a more complex energy management system (EMS), it reduces both PV curtailment losses and the time the battery remains at high SOC, consequently enhancing its overall lifespan. However, if the forecasts are inaccurate, this approach might prevent the battery from reaching its full charge potential, resulting in less stored energy than utilizing all excess PV power. In addition, a detailed analysis of the impact of HSSs on the grid is presented in [190], which uses the same dataset as this thesis.

4.2.2 Key metrics

This chapter provides key operational metrics of the HSSs, such as the operational parameter distributions of voltage, C-rate, and temperature. In addition, it depicts cycle characteristics such as the number of EFCs and occurring DODs.

4.2.2.1 Operational parameter distributions

Figure 4-3 depicts the distributions of voltage, current, battery pack housing temperature, and room temperature aggregated for all similar systems.

Voltage. The HSSs are either fully charged or fully discharged most of the time. While this can be seen by the wider parts of the violin plots at the top and the bottom of the voltage distribution of the $\mathrm{Small_{LMO}}$ and $\mathrm{Medium_{NMC}}$ systems, the $\mathrm{Medium_{LFP}}$ systems do not show this pattern due to their flat OCV curve (see Figure 2-2). Depending on the system design and the battery chemistry, there are differences in the voltage range. While LMO and NMC batteries show a similar range, the LFP voltage distribution is narrower due to the flat OCV curve. This can be attributed to the chemistry. The $\mathrm{Small_{LMO}}$ systems have a clear EOC voltage of around 4.15 V. Their EOD voltage shows two peaks, as the BMS decreases it over the lifetime to compensate for aging (see Chapter 4.2.4). The distribution of the $\mathrm{Medium_{NMC}}$ systems does not follow one of the LMO batteries, as the lower and the upper parts show three peaks each, representing the different EOD and EOC voltages of specific systems. The different EOC voltages are 4 V, 4.1 V, and 4.15 V, which are probably based on different BMS settings and not limited by the chemistry itself. Two of the EOD peaks occur, most likely, due to the use of different NMC cells. One system probably uses an NMC 111 cell that begins to decline at around 3.6 V EOD voltage. Another system uses a higher nickel share within the NMC, which declines around 3.4 V EOD voltage. A third system type most likely uses a similar NMC cell with higher nickel share, but applies an EOD voltage of around 3.6 V, showing a large aging reserve. The LFP distribution matches the OCV curve quite well, with most values around 3.3 V and some higher and lower voltage occurrences at SOC edges. It does not show the characteristic EOD and EOD peaks, as the currents are often still relatively high toward the EOD and EOC voltages. This leads to a comparably strong overvoltage and, consequently, to voltage relaxations toward medium voltages.

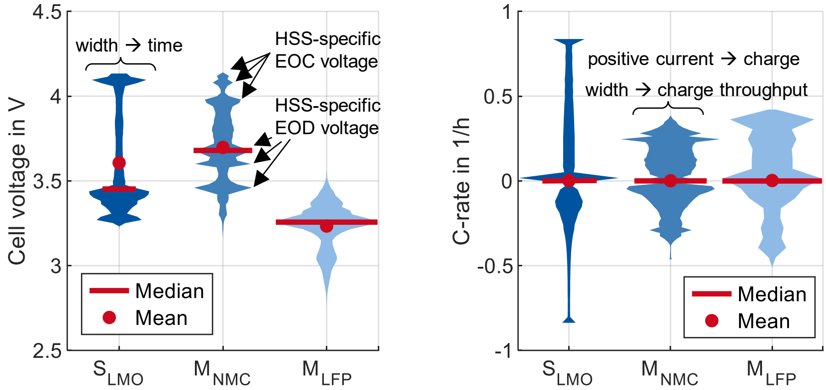

Figure 4-3: Operational data of **Small**$_{\mathbf{LMO}}$, **Medium**$_{\mathbf{NMC}}$, and **Medium**$_{\mathbf{LFP}}$ systems scaled down from system to cell level. **Left**: Voltage distribution. The width of the violin shows the cumulative time at a specific voltage level. The Medium$_{\mathrm{NMC}}$ systems show system-specific EOD voltages due to different electrochemical voltage limits of NMC compositions and BMS settings. LFP cells have a lower voltage. **Right**: Current distribution. The width of the violin shows the cumulative charge throughput at a specific C-rate. The maximum C-rates depend solely on the energy-to-power ratio of battery energy and inverter power and are not influenced by the chemistry for the shown ranges.

It is important to note that the parameter distributions of identical systems vary between households as the HSS operation is highly dependent on the PV generation and the electrical house consumption. If the system design of PV, house consumption, and battery energy is not ideally designed, the systems rarely get discharged during summer or rarely charged during winter.

C-rate. The C-rate distributions indicate that systems are charged at higher C-rates (positive values) than discharged (negative values). Charging often occurs at higher C-rates due to the relatively high PV power compared to the battery inverter. In contrast, discharge occurs largely during the night, in which household standby consumption is also met with a few hundred watts, resulting in low discharge rates. However, for more power-intense activities such as cooking or EV charging, the household load can exceed the inverter power, leading to a discharge at full power. The maximum C-rate of an HSS is limited by the minimum of the battery cell's nominal C-rate or by the system design. For the analyzed HSSs, the system design of the EPR of battery energy and inverter power is the limiting factor, as the battery cells could provide larger currents. The EPR sets the maximum E-rate in approximately the same order as the maximum C-rate (see Chapter 2.2.2). While the Medium$_{\mathrm{NMC}}$ and Medium$_{\mathrm{LFP}}$ have EPRs above 2 h, resulting in C-rates of up to 0.5 C, the Small$_{\mathrm{LMO}}$ systems have an EPR of 1.1 h and a maximum C-rate of approximately 0.85 C. As shown earlier, the

HSS classification into the three groups, $Small_{LMO}$, $Medium_{NMC}$, and $Medium_{LFP}$, is based on the measured HSS sample. Being a "small" system is not a general feature of the LMO chemistry. At the beginning of the measurements, there was simply one manufacturer who offered these small battery systems and used LMO batteries by chance. The difference in the operational behavior between S_{LMO} and M_{NMC} is therefore not correlated with the chemistry but depends solely on the system design.

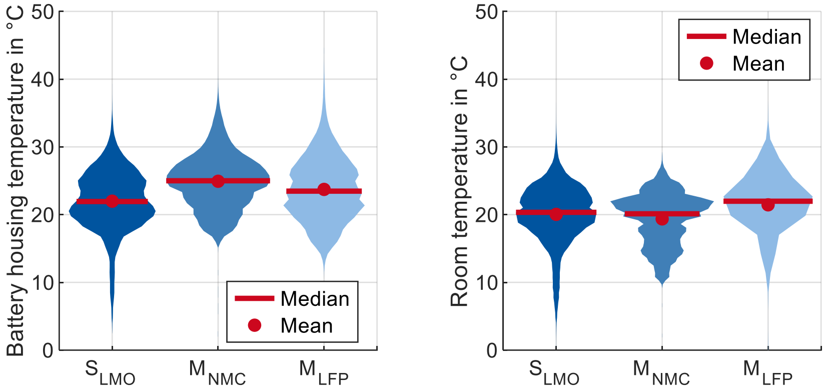

Figure 4-4: Distribution of battery housing temperature (left) and room temperature (right) of **S**mall$_{LMO}$, **M**edium$_{NMC}$, and **M**edium$_{LFP}$ systems. All systems except for one $Small_{LMO}$ HSS are installed in the basement, showing little temperature variation. The battery temperature is not the cell but the pack housing temperature.

Temperature. If possible, the battery temperature sensors are attached to the outside of the battery pack or in the HSS housing. Thus, it does not reflect the real battery temperature but indicates it. The distribution is dependent both on HSS operation and room temperature. The values of the battery temperature range mostly from 15 °C to 35 °C while the majority of recorded room temperature values are between 10 °C and 30 °C. The operational temperature is relatively high, as most HSSs are installed in the houses' basements. One $Small_{LMO}$ system is installed in a garage, showing low temperatures below 10 °C in rare cases. Comparing battery temperature and room temperature, the $Medium_{NMC}$ systems show the strongest increase caused by the operation. The primary reason for this is assumed to be the temperature sensor placement, which could be attached well to the metal housing of a module or even in between two modules for the $Medium_{NMC}$ systems. This was not possible for the $Small_{LMO}$ systems in the same way. Thus, the heat transfer of the cells to the housing area of sensor placement is expected to be lower, although the $Small_{LMO}$ cells experience the highest C-rates. There could also be other overlaid effects like heat generation from the power electronics or such. Thus, the measured battery temperatures should be used with care and cannot be directly compared between systems.

Nevertheless, the temperature measurement enables a more detailed analysis, as shown in the case of the internal resistance in Chapter 6.

4.2.2.2 Equivalent full cycles

Cycle number. Depending on the system design and the ratio of PV power to house consumption, HSSs reach 150 EFC to 300 EFC per year (see Figure 4-5). For the calculation of the cycles, the rainflow algorithm described in literature was applied [191–194]. The $\text{Small}_{\text{LMO}}$ HSSs run the most cycles per year as the PV generation is often large enough to fully charge them, and the overnight household electricity consumption is large enough to fully discharge them. The measurement gaps would lower the EFCs as no data is recorded (see Figure 4-1). To account for this, the monthly mean EFCs are linearly scaled in case data gaps occur within a specific month.

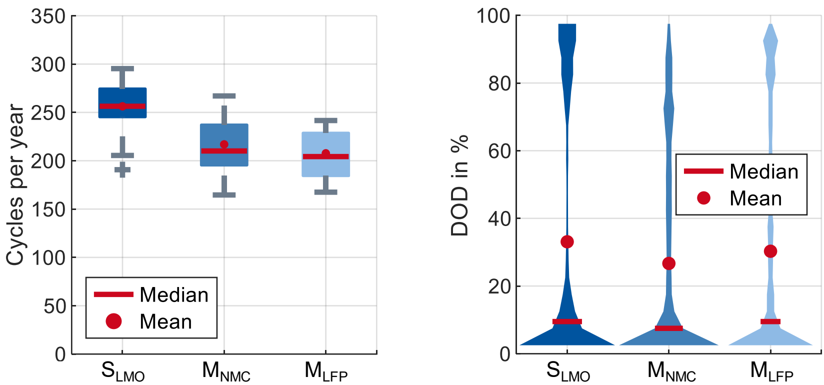

Figure 4-5: Distribution of the equivalent full cycles (left) and DODs (right) of $\textbf{S}\text{mall}_{\text{LMO}}$, $\textbf{M}\text{edium}_{\text{NMC}}$, and $\textbf{M}\text{edium}_{\text{LFP}}$ systems. The DOD distribution has a bin width of 5 pp and is depicted at the mid-point DOD, so DODs close to 0 % and 100 % are not shown, although they occur.

Cycle depth. Most cycles obtained via the rainflow method are relatively small, with DODs below 20 %. This corresponds primarily to operations in which there is only a small solar surplus in winter, and the storage system is discharged again. In addition, several partial cycles may occur even on sunny days when, for example, the storage system supplies the household during a temporarily cloudy sky and is possibly subsequently recharged. In addition to the small DODs, there are increased values at the upper end of the distribution, with DODs near 100 %. This kind of cycle corresponds to a full cycle. Such might occur on two consecutive sunny days with a high house consumption during the night in between. While sunny days can lead to a full charge, high night consumption can lead to a full discharge, completing the full cycle. The $\text{Small}_{\text{LMO}}$ HSSs show a more frequent occurrence of full cycles, as they are both quickly charged and discharged due to the low battery energy. In contrast, the medium-sized systems show slightly more half cycles. This is because there is less time during the year when PV generation is sufficient for a full charge or household consumption at night is not high enough to fully discharge a relatively larger battery by sunrise.

4.2.3 Seasonal effects

HSS operation relies on PV irradiance and shows clear seasonality in Germany. Figure 4-6 shows the current, voltage, and temperature distributions of an exemplary $Small_{LMO}$ system over a whole year.

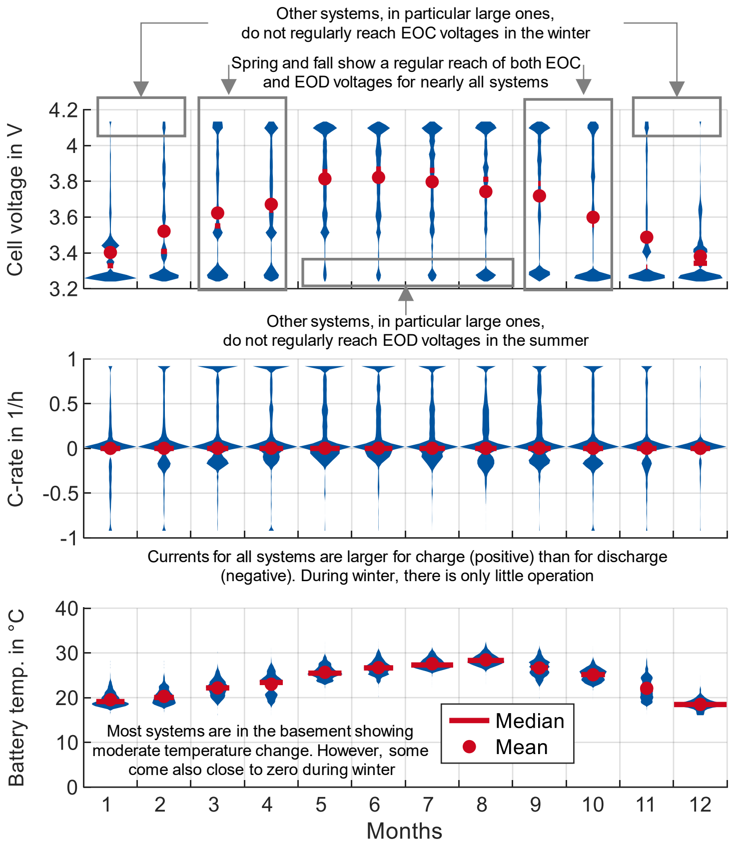

Figure 4-6: Seasonal analysis of one exemplary excess-charging $Small_{LMO}$ system. **Top:** Voltage distribution. **Middle:** Current distribution. **Bottom:** temperature distribution.

Monthly distributions. About 70 % of PV generation in Germany occurs in the summer, and the low generation rates in winter allow almost no storage operation. During spring and fall, the HSSs reach the EOC and EOD voltage regularly and are thus regularly fully charged and discharged. The regular full charge occurs because installed PV power is often much larger than the battery inverter power. Even after subtracting the household load, plenty of PV power is available for battery charging, leading to higher charging currents. Discharging usually occurs as the sun sets and predominantly occurs at low currents. Depending on household consumption and weather conditions, the HSSs also reach a discharged state every one or two days. During summer, the HSSs are fully charged for many hours of the day. While smaller systems reach EOD voltages regularly, larger systems reach only medium SOC values in some cases before sunrise. In the winter, HSSs are predominantly discharged, and only very sunny days or a planned maintenance charge from the grid lead to higher SOCs. Thus, larger systems than the one shown in Figure 4-6 can lack the regular reach of EOC voltage.

Daily operation. To analyze the seasonal operational behavior in more detail, Figure 4-7 shows the daily average of the same system's C-rate, voltage, and battery temperature. While positive currents correspond to charging, negative currents represent the discharge of the storage systems. The values shown correspond in each case to the arithmetic mean of all recorded measured data of a month within the respective hour of the day. Each value is assigned a color code based on the adjacent color scale.

C-rate. The excess-charging storage system is charged at the onset of the first PV surplus in the summer months, starting around 7 h to 8 h at average C-rates around 0.1 C to 0.3 C. Around 11 h to 12 h, the storage system is typically fully charged, and the house consumption can be covered directly by the PV system on average until around 18 h to 19 h. Therefore, the storage system barely shows operation between 12 h and 19 h during summer. Afterward, it discharges on average with C-rates around 0.1 C until the early morning hours.

Voltage. The voltage course shows clear seasonality following the charge and discharge behavior. As this excess-charging HSS starts charging with the first PV surplus, a fully charged state above 4 V is reached early in the day between 11 h and 13 h during summer, spring, and fall. The voltage decreases with the discharge. While the HSS gets fully discharged most of the time during winter, higher mean voltages in the early morning indicate that there are also nights during summer when the HSS remains at medium SOCs.

Temperature. The battery temperature follows the seasonal patterns of the outside temperature in Germany. However, the mean temperatures are quite high, up to 30 °C during the summer, when a warm room temperature combined with high charging power increases the temperature.

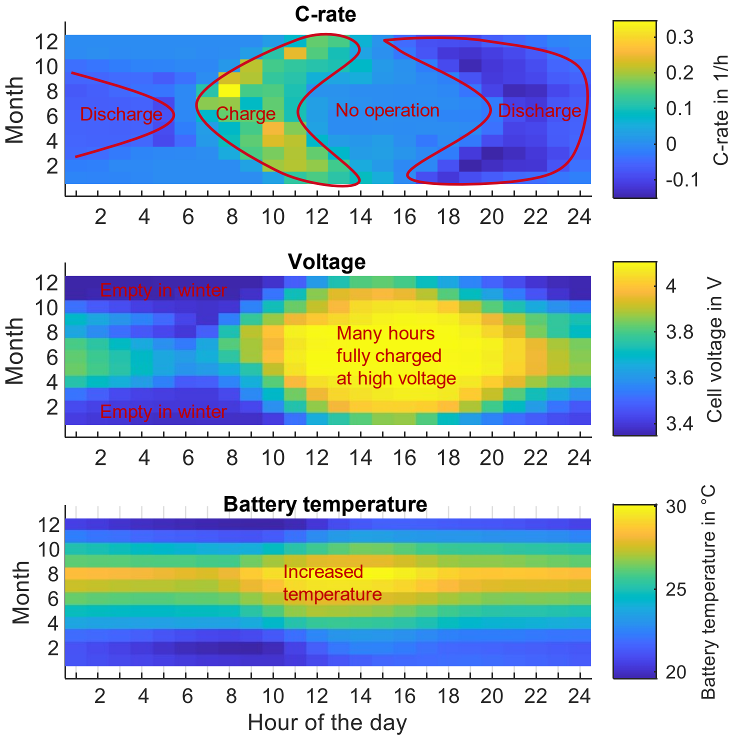

Figure 4-7: Seasonal arithmetic means of an exemplary Small$_{LMO}$ system over one year. **Top**: C-rate. **Middle:** voltage. **Bottom:** temperature.

In contrast to the discussed operational pattern, the charge of a forecast-based HSS is delayed until noon. It reaches comparably high battery voltages later at about 14 h to 16 h due to charging at midday. Since there are no fundamental differences in the discharge of the two types of storage systems, the later charging of the forecast-based storage leads to an overall reduction in idle times at high voltages. For lithium-ion batteries, this has a positive effect on the calendar aging of the cells [48-51]. It can, therefore, be expected that prognosis-based operating strategies will tend to achieve longer lifetimes. This is consistent with simulative studies of HSS aging [52, 53].

4.2.4 System characteristics

System analysis in the field has several challenges compared to laboratory measurements, as both the environmental conditions and the internal control strategies of the HSSs cannot be influenced. Software updates lead to continuously changing system behavior, which must be considered while analyzing the data. Figure 4-8 exemplarily presents two important characteristics relevant to the developed methods in Chapter 5 to Chapter 7.

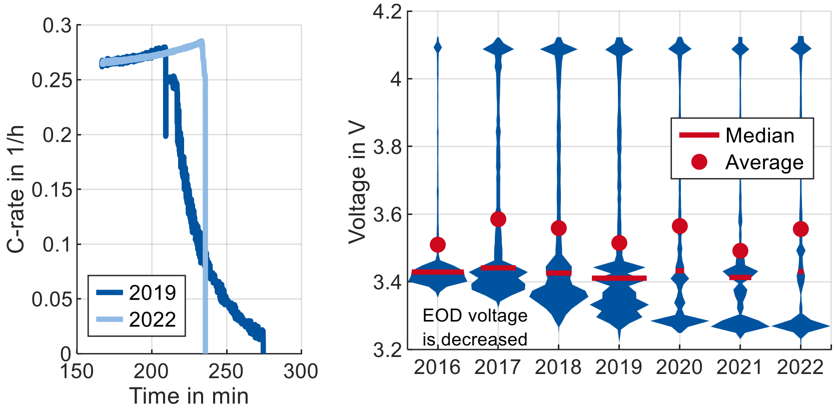

Figure 4-8: **Left:** Adjustment of the derating behavior of a Medium$_{NMC}$ system over time. **Right:** Adjustment of EOD voltage to compensate for capacity fade and control the usable capacity of an exemplary Small$_{LMO}$. These software updates can be done online.

Note that each system shows its operational characteristics. As the thesis does not focus on operational strategies in detail, not all of these are discussed here.

Adjustment of control strategies. The storage systems can usually receive new software via online updates. Control strategies can change with these updates, influencing the values of the capacity tests or other evaluations. Figure 4-8 (left) shows such a control logic change of the power during a high-power discharge. While the system had a continuous power derating in 2019, two years later, it abruptly set the power to zero in 2022. Such a change in control logic makes it impossible to compare the discharged capacity directly.

Adjustment of EOD or EOC voltage. To counteract capacity fade, some manufacturers decide to implement a capacity reserve. This reserve can be unlocked if the operating voltage window is widened by adjusting the EOD or EOC voltage. Figure 4-8 (right) shows the voltage window of a Small$_{LMO}$ system that continuously decreases the EOD voltage. In addition to the general extensions of the voltage window, some systems experience temporary or seasonal changes in the limits that are either set to influence aging or optimize key performance indicators like self-consumption or self-sufficiency. Therefore, without deeper analyses like those in Chapter 7, it is difficult to make statements about the actual battery aging, as customers or operators can only see the resulting usable capacity and energy (see Chapter 5).

The effects of widening the voltage range on the capacity and energy of an HSS are highlighted in Figure 4-9. This example shows the decrease in the EOD voltage, as discussed above. The Figure shows the discharging curve of both a new and an aged battery cell.

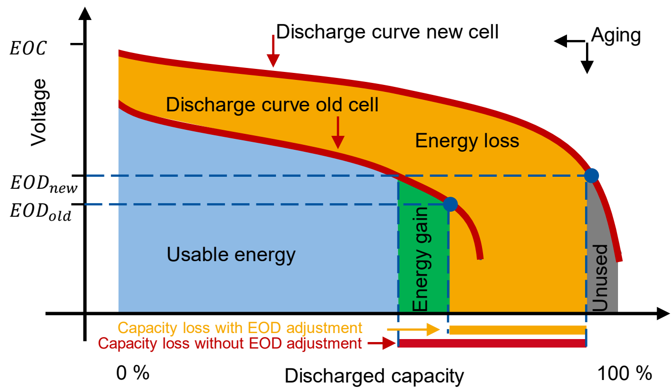

Figure 4-9: Schematic explanation of the EOD voltage adjustment to compensate for capacity fade.

While the discharged capacity is depicted on the x-axis, the energy corresponds to the integral of the discharge curve. When the battery ages, the discharge curve shifts to the left side as the capacity decreases. Furthermore, the discharge curve is shifted to lower voltage values as the internal resistance rises, leading to higher overvoltage. Consequently, the energy is reduced by the capacity fade and the increase of internal resistance. The widening of the voltage range (in this case, the decrease of the EOD voltage) can counteract the occurring degradation of the battery. However, the effect is limited if the voltage is already declining steeply.

4.3 Conclusion

Chapter 4 presents the field measurements and relevant operational patterns of HSSs as background knowledge central to the methods developed in Chapters 5 through 7.

Dataset. The analyses of this thesis are based on the measurements of 21 HSSs over a period of up to eight years. The HSSs are operated in private households and thus represent real-world operational behavior.

Measured quantities. The measured quantities are the battery voltage, current, power, housing temperature, and room temperature. All quantities are measured with a sample rate of one second and a high accuracy. From a scientific point of view, the dataset is valuable for lithium-ion HSSs to date (year 2024). It corresponds to about 106 system years, 146 gigabytes, and 14 billion data points, as presented in [184,185].

Nomenclature. The dataset comprises many different HSS products. The main differences are the system design in terms of energy and power ratings, and the battery chemistry used. To account for both, the nomenclature is a combination of system size and chemistry. The smallest HSSs have a battery energy of around 2 kWh and use an NMC/LMO blend battery. These systems are referred to as "$\text{Small}_{\text{LMO}}$" HSSs. There are different systems in the range of around 9 kWh, which is about the average system energy in Germany today. These systems are divided into HSSs with different NMC and different LFP batteries, referred to as "$\text{Medium}_{\text{NMC}}$" and "$\text{Medium}_{\text{LFP}}$" HSSs, respectively. Although the HSSs are from the first product generation, many relevant parameters of today's products are still covered by the dataset.

Operation. It is important to understand that HSSs regularly reach their EOC and EOD voltage, symbolizing that they are fully charged and discharged. They frequently show complete full cycles from spring to fall. Furthermore, the systems show changing control behavior due to software updates. This can lead, for example, to a different derating behavior or adjusted voltage ranges set by the BMS. These changes make it more complex to compare operational data of the same system over time. SOC and SOH algorithms need to consider all changes.

5 Capacity and energy estimation

This chapter depicts the development of innovative methods to estimate the usable battery capacity and energy based on operational data. The methods enable demand-oriented maintenance and can identify warranty claims. The chapter is based on and contains identical parts of [184] and its supplementary information under the lead of the author. In addition, parts of it are based on [8] under the lead of the author.

5.1 Overview

Introduction. Customers pay approximately 10,000 € for an average HSS [4,90,95]. To make this investment more appealing, manufacturers usually give a warranty period of ten years on the usable battery capacity or energy. However, it is questionable whether the HSS manufacturers can keep their promises for the majority of the HSSs, as only a few systems have been in operation that long (see Chapter 3). Being able to correctly track the usable capacity and energy of an HSS is, therefore, essential for maintenance and warranty management. Precise estimates of a system's SOH enable efficient use of resources and contribute to sustainable usage in a circular economy. However, manually conducted capacity tests are expensive and lead to system downtimes. Therefore, it is important to develop validated data-driven methods to extract information on the usable capacity and energy from existing operational data.

SOC estimation. Capacity analysis generally includes SOC estimation. The SOC gives information about the remaining usable capacity of the battery during a full charge-discharge cycle (see Chapter 2.2.2). This is important for further investigations of the battery's SOH [86]. Online methods can estimate the SOC during operation, while offline methods include tests and complex computations [86]. Commonly used online SOC estimation methods are ampere-hour counting, model-based, and data-driven methods [86]. Ampere-hour counting uses an initial SOC to estimate subsequent values by battery current integration [195]. Model-based methods use a battery model and voltage and current measurements to form a closed-loop SOC estimation [196]. Machine learning methods use large amounts of data to train neural networks and complex algorithms, which can estimate the SOC by processing input features like current, voltage, and temperature [86,197]. This comes with the advantage of not needing a detailed battery model [197]. Conversely, machine learning methods require large amounts of data, and their training can be time-consuming [86]. If the OCV is estimated with high accuracy or if the battery voltage is relaxed, the OCV can be mapped to an SOC curve [198]. The relationship between SOC and voltage changes over time and needs to be updated (see Chapter 7).

Types of aging analysis. The main effects of battery aging are capacity decrease and internal resistance increase [199]. Researchers worldwide work on identifying the electrochemical mechanisms inside the battery cells to investigate the causes of their aging. The methods used are either non-invasive by laboratory measurements and field data diagnostics [200] or invasive by post-mortem analyses. In these, cells are opened to allow in-depth investigation of the individual battery components [201].

Laboratory tests. Laboratory measurements are usually based on monitoring individual cells in a controlled environment, which are purposely aged by either cycling [80,199,202–209] or storing them [199,203,210,211] under specific conditions. The aging within these tests is tracked via regular capacity measurements, and results vary depending on the investigated chemistry and testing conditions [212]. Laboratory capacity tests typically consist of both a charge and a discharge phase. The charge phase often consists of a constant current phase, followed by a constant voltage phase. The discharge phase follows, during which the capacity is determined [78,80,199,202,211,213]. Current and voltage specifications are specific for each cell and can be extracted from the respective battery cell datasheet. Researchers sometimes apply lower C-rates [203,205,208] or higher C-rates [206,209]. However, these tests are time-consuming, as shown by an exemplary study lasting 8,000 EFC and around 800 days [214]. Further, real-world operation is always subject to unpredictable changes [215], which is why simulations of field operation are applied in the laboratory [47,216,217]. Besides the capacity measurements, the internal resistance is tracked. Chapter 6.1 provides more information on internal resistance.

Field tests. Field capacity tests available in literature vary in the deployed battery technology and application, such as grid storage [218–220], PV integration [215,221,222], telecommunication [223], and EVs [224,225]. While most of these use on-site capacity tests to monitor battery aging [215,218–221,223], others remove the battery for laboratory measurements [222,224]. Unfortunately, such capacity tests always require a certain system downtime, leading to increasing work time and decreasing revenue. Appendix, Table 9-4, presents a literature overview of field capacity tests.

Operational data analysis. Operational data analysis is a promising way to overcome the shortcomings of manually conducted capacity tests [225–233]. The capacity-based SOH estimation is widely used to track the decreasing capacity [234]. Ampere-hour counting is an established approach for this but comes with several challenges, like the required knowledge of an initial SOC and its sensitivity to error accumulation [235]. Therefore, different methods have been developed to estimate the SOH, which can be categorized into model-based and data-driven approaches [236]. Model-based methods [86] use either equivalent circuit models [235,237–240] or electrochemical models describing the internal electrochemical processes of the battery [241–244]. Model-based SOH estimators are mainly limited by their high computational costs, and their accuracy highly depends on the parameterization [234]. Machine learning methods do not model the internal working principles of the battery [85]. Instead, they map aging-related input features of the battery to its SOH [85,86], using algorithms like Gaussian process regression [245,246], support vector machines [247,248], and different types of neural network approaches [234,249–251].

Datasets. Many studies face the problem of insufficient publicly available field measurement datasets [252]. If such large datasets exist in rare cases, there are usually no reference measurements to validate the algorithms. Several battery datasets are accessible to the public, originating from laboratory measurements or synthetic cell simulations (see Appendix, Table 9-5). Constant cycling data for varying battery chemistries and conditions can be found in [206–209,253–257]. Specific discharging conditions are used in [258–262], where driving cycles are used to simulate the usage of the tested batteries in EV applications, while [263] uses randomized discharge profiles. Synthetic datasets simulating many degradation paths and corresponding battery data can be found in [264,265]. Real-world operational datasets of electric vehicles with lithium-ion batteries can be found in [262] and [266], as presented in [267] and [268]. A detailed overview of public datasets is given in [252].

This thesis. To the best of the author's knowledge, no comparable public dataset for various lithium-ion batteries of HSSs has been used to date (year 2024) for scientific capacity estimation.

5.2 Methodology

This chapter presents two methods for SOH estimation (see Figure 5-1).

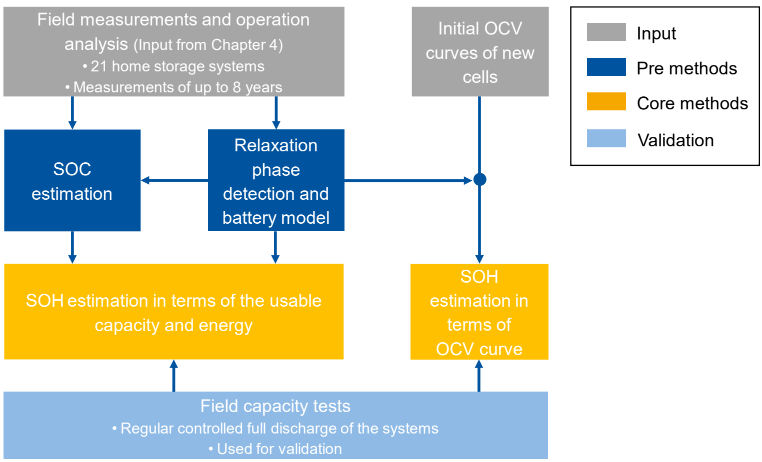

Figure 5-1: Structure of Chapter 5. Two kinds of SOH definitions are estimated by using detecting relaxation phases, parametrizing a battery model, and estimating the SOC. The results are validated by field capacity tests.

The first method is based on identifying full cycles. It uses an exact SOC estimation via detecting EOC and EOD relaxation phases and the parametrization of a battery model. The second method uses the same battery model, and the initial OCV curve of the batteries for SOH estimation. Both methods are validated through field capacity tests performed in parallel, providing reliable reference values. Due to the relatively low computational cost, these methods can also be applied to many HSSs.

5.2.1 Field capacity tests and warranty

The field tests were developed to track the battery aging and to investigate if the warranty periods were reached.

Background. The subsidy program by the Federal Ministry of Economic Affairs and Climate Action for HSSs introduced an obligatory seven-year warranty in its first period (2013-2015) and extended it to ten years in its second period (2016-2018) [91]. In this regard, document [269] specifies that a battery is considered defective if its capacity falls below 80 % of the nominal capacity. However, HSSs were a brand-new product in 2013. Therefore, neither standardized test routines nor a commonly agreed definition of the nominal capacity existed. Further, the datasheets predominantly state different energy quantities as the two values were not clearly separated. To change the lack of standards, a committee led by the two major storage associations in Germany (BVES and BSW) worked on transparent definitions and test routines, resulting in the Efficiency Guide [43]. The author was involved in the development of these test routines.

Capacity definition. Generally, two capacity types can be distinguished: the nominal and the usable battery capacity. The nominal battery capacity is specified by the module vendor in the module datasheet and is considered a warranty to the module purchaser. This information is neither available nor relevant for the end customer and cannot be measured during the operation of the storage system. The usable battery capacity remains after deducting safety margins and aging reserves from the installed battery. Thus, the storage system manufacturers decide which range of the installed battery capacity they release as usable for the everyday operation of the HSS.

Aging reserve. Aging reserves can be implemented in two ways (see Figure 5-2). The first option is that the datasheet information is stated as lower than the usable capacity in operation. In this case, the aging reserve is included in the usable capacity. The second option releases the capacity by continuously adjusting EOC or EOD voltage (see Chapter 4.2.4).

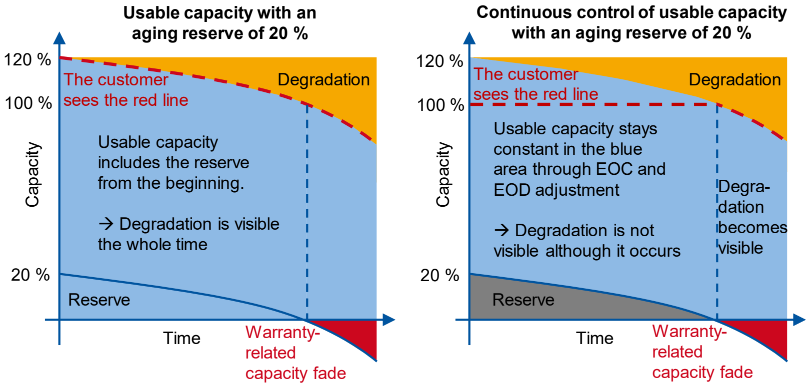

Figure 5-2: Schematic explanation of the usable capacity and aging reserve of a battery storage system. Adapted from Beck, Dechent et al. [270], used under CC BY 4.0 [23]. **Left**: The usable capacity includes an aging reserve, and more capacity can be used than stated as 100 % in the datasheet (most of the HSSs have this). **Right**: Continuous adjustment of the usable capacity according to Figure 4-9. **Difference**: Degradation (left) is immediately visible, degradation (right) only after reserve use. A warranty-related decline occurs when the datasheet value is reached in both cases.

The critical difference is the degradation visibility during operation. In the first case, the degradation is immediately visible. In the second case, the degradation becomes visible only when the reserve is fully used [270]. In both cases, degradation becomes warranty relevant if the usable capacity reaches its EOL. For the analyzed HSSs, most systems show the reserve-including option (left figure). Others, especially the $\text{Small}_{\text{LMO}}$ systems, combine both options (see Figure 4-9).

SOH normalization. It is important to distinguish between the nominal, the usable, and the value stated as “usable” on the datasheet (referred to as “warranty capacity” to avoid misunderstanding). From a technical perspective, the stated warranty capacity is not a suitable normalization quantity and should only be used for warranty management as it is no technical quantity.

The exact initial usable capacity is unknown for most HSSs as it is often not stated on the datasheets. Nevertheless, HSS manufacturers predominantly use voltage limits near the specified voltage ranges of the module suppliers for the HSS sample analyzed. The nominal values could be gathered from cell or module labels for the HSSs. Thus, this thesis assumes that the initial usable capacity is the nominal capacity as stated for the used module or cell and uses this value for SOH normalization. Consequently, reaching the physical EOL definition of 80 % does not correspond to a warranty case.

An extreme example is one $\text{Medium}_{\text{LFP}}$ HSS: it has a nominal energy of 13.8 kWh and states 9 kWh as usable. However, the BMS of the HSS makes its nominal energy directly usable without adjusting EOC or EOD voltages. Regarding normalization, measured energy of 9 kWh would lead to a warranty-related

$SOH_{Warranty}$ of 100 % if the datasheet information were used. However, the technical SOH_{UE} would be 9 kWh / 13.8 kWh = 65 %.

Test procedure. Reproducible test conditions are a basic prerequisite for meaningful capacity measurements. According to the Efficiency Guide, the usable battery capacity is recorded in a defined discharge test as a DC quantity at three power levels. The arithmetic mean of the measurements is then given on the datasheet of the storage system [43]. The usable battery energy is derived accordingly and widely used on the datasheets. Compared to the capacity, it includes the energetic losses occurring through the internal resistance of a battery.

However, the 21 HSSs investigated operate grid-connected in private households and could not be tested as specified in the Efficiency Guide [43]. The battery modules were not removed from the storage systems for several reasons:

- Potential malfunction of the EMS could occur if the batteries are removed and reconnected.
- A potential loss of warranty due to the battery removal is to be avoided.
- A measurement in the laboratory is perceived as a disproportionate burden for the operators since the HSS cannot be used during that time.

Therefore, a test procedure was developed to allow on-site measurement of the batteries (see Figure 5-3).

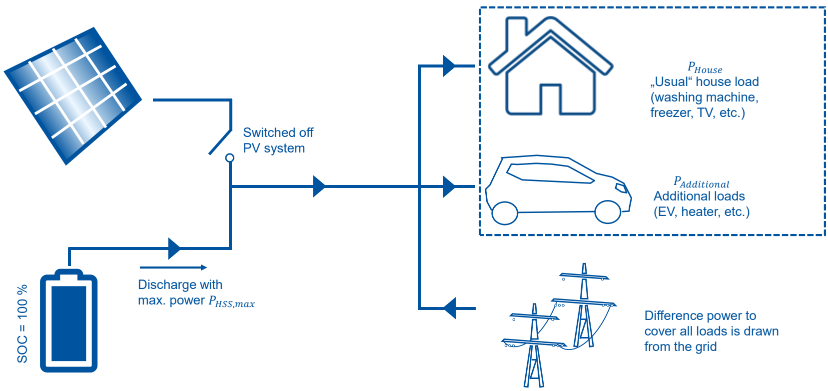

Figure 5-3: Scheme of the conducted filed capacity tests. After the HSS is fully charged, the PV system is switched off. The discharge is conducted under full load by applying consumers like an EV. The discharged energy and capacity values are the test results.

The in-house PV system is used for charging the HSS. Suitable weather conditions must be available for a capacity test to enable a reliable full charge. If the HSS offers the option of a manual full charge from the grid, this option was used as an alternative.

The HSS is considered fully charged when the EMS terminates charging automatically despite the continued presence of excess PV power and when the display or web portal indicates an SOC of 100 %. To make the test reproducible, the C-rate should be as constant as possible during discharge except for the system-specific derating behavior toward the EOD voltage. However, house consumption is always a superimposed element, even during the tests. Therefore, the only discharge power that can be reliably reproduced is the maximum discharge power of the HSS. For this purpose, an additional load, such as charging an electric car, is applied to permanently exceed the maximum discharge power of the HSS. This load is applied until the system stops discharging automatically and the display or web portal shows a state of charge of 0 %. Thus, the C-rates differ from system to system (0.25 C to 1 C) but are always identical for each single system. The capacity is determined by integrating the current, while the energy is calculated by integrating the power determined by the product of battery current and voltage. For reasons explained in Chapter 4.2.4, the obtained quantities are the usable capacity and energy as the real system behavior is measured.

Value of this dataset. The capacity tests performed have great value. In relation to the research, they validate developed methods such as these within this thesis. Such validation is not straightforwardly possible in other studies. In addition, the sheer amount of time required is worth emphasizing. The test preparation, conduction, and follow-up take about two days on average. The 60 successfully conducted capacity tests alone correspond to a working time of more than 120 days.

5.2.2 Battery model and relaxation phase detection

This chapter describes the parametrization of a battery model to analyze the relaxation phases. The model parameters are needed for the capacity estimation in this Chapter, the internal resistance estimation in Chapter 6, and the link of resistance parameters to the SOH in Chapter 6.2.3.

5.2.2.1 Relaxation phase detection

Various filters assess and identify relaxation phases to enable accurate parameter extraction.

Current filter. The current filter serves the purpose of defining a threshold for the current in each system under consideration. This threshold is crucial in distinguishing relaxation phases from other operational states. During a particular day, voltage values associated with the system are provisionally classified as relaxation points if the corresponding absolute values of the current remain below the defined C-rate threshold of around C/100 - C/10, depending on the HSS.

Peak filter. The peak filter is designed to identify instances of single current peaks occurring within relaxation phases. These peaks arise due to unknown control strategies of the BMS. If the duration of such peaks is sufficiently long to disrupt the voltage relaxation process (defined as 10 s), the corresponding relaxation candidates are excluded from further analysis.

Duration filter. Relaxation takes time, depending on the operation, up to some hours. The duration filter ensures that the relaxation phases meet a system-specific minimum duration requirement of a few minutes to achieve reliable fits (see Appendix, Figure 9-11). This criterion is crucial for parameter extraction in subsequent analyses. Relaxation phases failing to satisfy this minimum duration condition are not considered for further investigation.

Charge throughput filter. The charge throughput filter determines whether the relaxations occurred after a charge or discharge event. Furthermore, this filter verifies that a system-specific minimum capacity throughput of around 20 % SOC has occurred before the relaxation phase.

Conclusion. The systematic application of these filters enables a comprehensive assessment of relaxation phases (see Figure 5-4). The identified relaxation phases build the basis for accurate parameter extraction. The presented relaxation filters significantly impact the number of detections (see Appendix 9.3.1). Particularly, the current threshold influences the count of detected relaxation phases, where higher thresholds lead to more detections. Striking the right balance between the number of detections and the quality of identified relaxation phases is challenging.

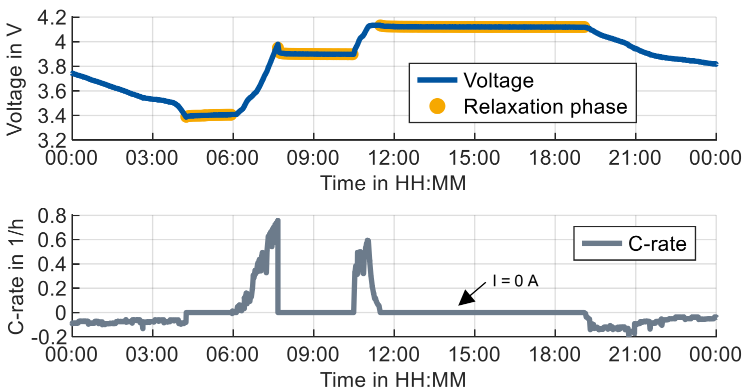

Figure 5-4: Exemplary relaxation detection for one day. The relaxations are detected by applying several filters, such as a current threshold and minimum duration.

5.2.2.2 Model parametrization

Lithium-ion batteries exhibit specific patterns in their relaxation behavior as they age. Researchers have translated these patterns into model parameters that concisely summarize the voltage relaxation curve's characteristics.

Equivalent circuit models. Studies by Li et al. [271] and Goldammer and Kowal [272] reveal various effects occurring at different time scales during battery operation. Jossen [273] suggests that time constants, resulting from charge transfer effects and double layer capacitance, range from milliseconds to seconds, while those arising from diffusion effects span seconds to minutes. However, precise time range definitions are difficult due to the dependency of time constants on battery chemistry, temperature, SOC, and SOH [273]. Researchers employ equivalent circuit models (ECMs) of different orders to model these processes effectively. A common choice is the second-order ECM, where the first RC element represents charge transfer and double layer capacitance processes with a fast time constant. In contrast, the second RC element models the diffusion process with a slow time constant, as presented by Stroe et al. [45], Qian et al. [62], and Pei et al. [63].

Time constants. Li et al. [271] use 4th and 5th order RC-models to investigate the time constants of an LFP cell relaxation behavior, observing time ranges of one hour and 24 hours, respectively. They identified time constants for the 4th order model as 1 s, 19 s, 110 s, and 1600 s. Goldammer and Kowal [272] employed the distribution of relaxation times to investigate polarization processes in LIBs, confirming the magnitude of time constants estimated by [271].

Chosen ECM. Due to the sample rate of one second (See Chapter 4), certain shorter physical processes like ohmic resistance, charge transfer, or double layer capacitance cannot be accurately modeled, as they are not fully measured. Despite this limitation, the presented literature review indicates that numerous effects overlap, leading to a range of reported time scales. Therefore, a second-order ECM with new parameter definitions is utilized, consisting of two RC elements, internal resistance, and voltage source (OCV) in series. However, the parameters of the RC elements are now redefined to represent separate slow and fast effects during relaxation, deviating from the single-effect representation presented in previous literature. Figure 5-5 shows the resulting ECM.

The ohmic resistance, represented by R_{ohm}, causes an immediate drop in voltage at the initiation of the relaxation phase. The time constants of the RC elements encompass two distinct processes – fast and slow. The first time constant ($\tau_{fast} = R_{fast} \cdot C_{fast}$) governs the rapid effects that predominate at the onset of the relaxation phase, including charge transfer, double layer capacitance, and diffusion effects. Conversely, the second time constant ($\tau_{slow} = R_{slow} \cdot C_{slow}$) models the medium to slow diffusion effects observed during the relaxation.

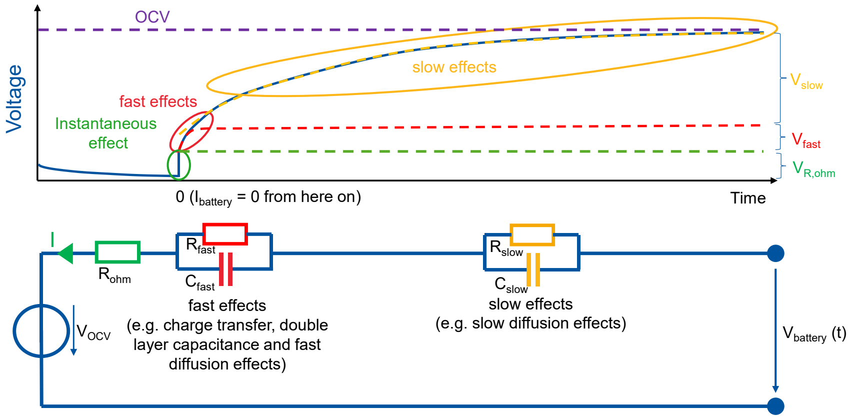

Figure 5-5: Second-order equivalent circuit model describing fast and slow relaxation effects. Inspired by descriptions in [45,62,63,65].

Upon examining the equation derived from the second-order ECM, two additional overvoltage parameters can be identified, referred to as V_{fast} and V_{slow}. These parameters are obtained from the voltage equation corresponding to the second RC element, as stated in Equation (5-1) based on [62].

$$I_{bat} = I_{R_{slow}} + I_{C_{slow}}$$

$$I_{bat} = \frac{V_{slow}}{R_{slow}} + C_{slow} \cdot \frac{dV_{slow}}{dt}$$

$$with\ I_{bat}(t > 0) = 0\ A \qquad (5\text{-}1)$$

$$\frac{dV_{slow}}{dt} = -\frac{V_{slow}}{R_{slow}C_{slow}}$$

$$V_{slow}(t) = V_{slow}(t = 0) \cdot e^{\frac{-t}{\tau_{slow}}}, with\ \tau_{slow} = R_{slow} \cdot C_{slow}$$

The derivation of the first RC element is similar, leading to comprehensive Equation (5-2) of the second-order ECM.

$$V_{bat}(t) = V_{OCV} + I(0^-) \cdot R_{ohm} \cdot \delta(t) + V_{fast}(t = 0) \cdot e^{\frac{-t}{\tau_{fast}}} + V_{slow} \cdot e^{\frac{-t}{\tau_{slow}}} \qquad (5\text{-}2)$$

$$\tau_{fast} = R_{fast} \cdot C_{fast}\ and\ \tau_{slow} = R_{slow} \cdot C_{slow}\ and\ \tau_{fast} < \tau_{slow}$$

The $\boldsymbol{\delta}$ symbolizes the dirac-delta-impulse and represents the instantaneous voltage drop at the beginning of the relaxation phase caused by the ohmic resistance. In the following, the parameter estimation and the fitting are explained.

Estimation of $\boldsymbol{R_{ohm}}$. The ohmic resistance for the ECM is not calculated as the sample rate of the measurement system is larger than the belonging voltage response following a current change. The ohmic overvoltage equilibration happens instantaneously, and the measurements of one second contain overvoltage effects of other resistant components, such as charge transfer resistance. Therefore, Chapter 6 introduces a new parameter called direct current resistance.

Non-transient effects. Non-transient effects are observed when analyzing voltage data from long-time relaxation phases, typically lasting more than four hours. These effects manifest as a linear decay in the voltage curve during the relaxation period. The primary factor contributing to this voltage decay is believed to be the BMS supply of the HSS and other peripheral electronics. To account for these non-transient effects, the system data is used in advance to create a comprehensive database based on various systems' available long-time relaxations. This database corrects the voltage based on a k-nearest-neighbor model with one neighbor (1-NN), as described in Appendix 9.3.1.

Estimation of $\boldsymbol{V_{OCV}}$. The estimation of the OCV is done at the end of a theoretical endless relaxation phase, wherein all electrochemical processes have reached equilibrium. The faster time constant can be disregarded at this stage, as its influence becomes negligible. Hence, the boundaries of the second time constant, which accounts for the slow effects, are utilized in the identification process, as defined by Equation (5-3).

$$V_{slow}(t) = V_{slow_{OCV\,fit}} \cdot e^{\frac{-t^{+}}{\tau_{slow_{OCV\,fit}}}} + V_{OCV}$$
$$with\ \tau_{slow_{min}} \leq \tau_{slow_{OCV\,fit}} \leq \tau_{slow_{max}} \tag{5-3}$$

Estimation of remaining ECM parameters. The OCV fitting is used for computing the residual against the actual voltage curve. Another exponential function is used to fit this residual (see Appendix, Figure 9-9) according to Equation (9-1). The sign of the overvoltage $V_{fast_{residual\,fit}}$ aligns with the OCV fit. The parameter t^{+} signifies the time after the equilibrium in ohmic overvoltage.

$$V_{bat}(t) - V_{slow}(t) = V_{fast_{residual\,fit}} \cdot e^{\frac{-t^{+}}{\tau_{fast_{residual\,fit}}}}$$
$$with\ \tau_{fast_{min}} \leq \tau_{fast_{residual\,fit}} \leq \tau_{fast_{max}} \tag{5-4}$$

The obtained time constants and overvoltages from the residual and OCV fits are designated as the initial parameters for a final fitting of both RC elements. This final fitting process computes the parameters of the second-order ECM with increased stability. The estimated OCV is used to account for the offset voltage. Equation (5-5) shows the final parameter identification.

$$V_{bat}(t) - V_{OCV} = V_{fast} \cdot e^{\frac{-t^+}{\tau_{fast}}} + V_{slow} \cdot e^{\frac{-t^+}{\tau_{slow}}}$$
$$with\ \tau_{fast_{min}} \leq \tau_{fast} \leq \tau_{fast_{max}}\ and\ \ \tau_{slow_{min}} \leq \tau_{slow} \leq \tau_{slow_{max}} \tag{5-5}$$

Final fit. An exemplary final fit of the second-order ECM is shown in Figure 5-6. The general voltage course and the relaxation phase is fitted well.

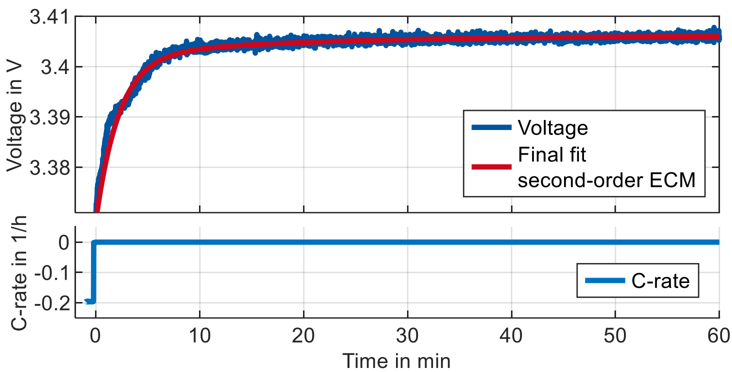

Figure 5-6. Final fit of a relaxation phase after discharge based on the second-order ECM.

For some systems, the overlap of several diffusion processes in different battery cells of the HSSs leads to small errors within the first minutes, as seen at the beginning of the relaxation phase. However, these characteristics play no significant role in further analyses. Appendix, Figure 9-10, evaluates the root mean squared error (RMSE) and shows that the chosen second-order ECM has a higher accuracy than a first-order ECM.

5.2.2.3 Relaxation phase filters

To determine the usable capacity by applying ampere-hour counting, relaxation phases close to the EOC and EOD voltage are necessary. Several filters are applied to get valid relaxation points for the capacity estimation algorithms. Depending on the technology, these filters must be set individually for each cell type due to the material-specific voltage curves. Figure 5-7 shows the relaxation phases and the chosen voltage limits based on conducted sensitivity analysis for an exemplary $Small_{LMO}$ HSS, which is subject to a decrease in EOD voltage over time as presented in Chapter 4.2.4 and a seasonal EOD voltage adjustment.

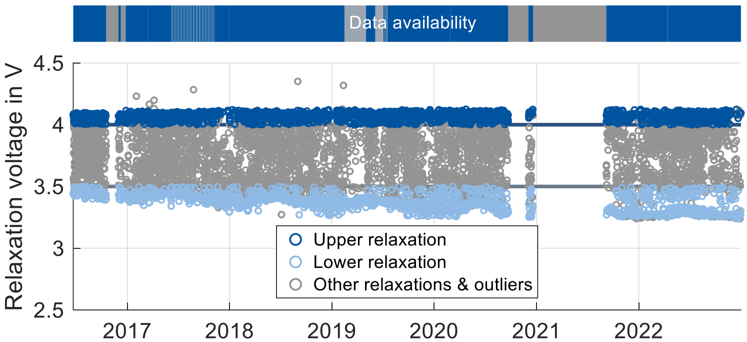

Figure 5-7: Relaxation phases and applied filters over time. To identify full cycles, EOC and EOD relaxation phases are selected by applying several filters, such as voltage thresholds.

Upper and lower thresholds for the relaxation voltage are set for each system to get relaxations near the EOC and EOD voltage, respectively. Some outliers occur due to fitting, shown exemplarily by OCV estimates beyond 4.2 V. These high values do not occur in the measurement data, as a BMS would not allow for such high voltage values for safety reasons.

5.2.3 Usable capacity and energy SOH estimation

After identification of the relaxation phases, full cycles can be identified and used to integrate the current and power while considering offset currents. This way, the SOH values, namely SOH_{UC} and SOH_{UE}, for the usable capacity (UC) and the usable energy (UE) can be obtained.

5.2.3.1 Identifying full cycles

Figure 5-8 shows the storage operation of two exemplary days. During this period, the HSS shows a full cycle: It is empty at the beginning of day one, gets fully charged until noon, stays at a high SOC during the day, and is fully discharged overnight. The next day, it gets fully charged again. Based on this storage operation, four integration possibilities exist to estimate the capacity:

1. Empty-to-empty (E2E) integration
2. Full-to-full (F2F) integration
3. Empty-to-full (E2F) integration
4. Full-to-empty (F2E) integration

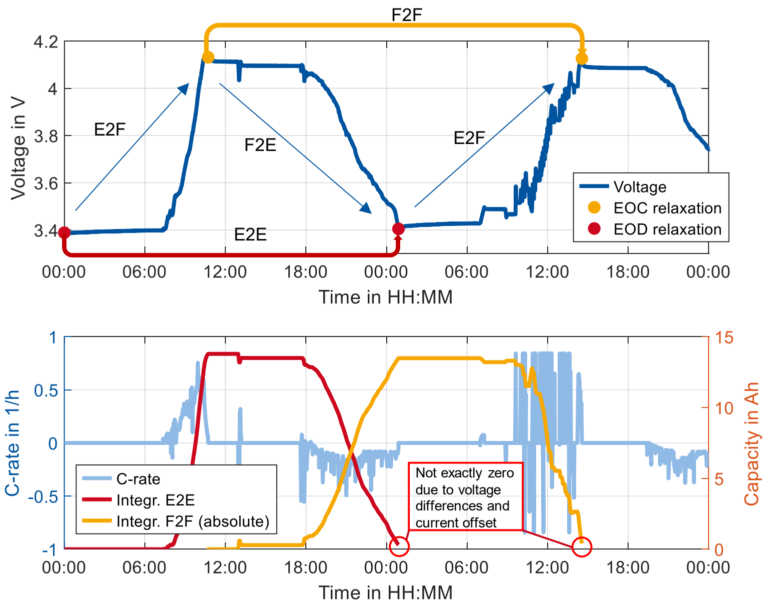

Figure 5-8: Methodology of the capacity estimation based on field measurements of an exemplary $Small_{LMO}$ HSS (15 Ah cell). **Top**: Voltage and relaxation points. To identify full cycles, EOC and EOD relaxations can be combined. Full cycles are represented between E2E and F2F. A full charge is represented by E2F, and a full discharge by F2E. **Bottom**: C-rate and capacity estimate. The current can be integrated between the identified relaxation points to compute the capacity.

When integrating the full cycles in the form of E2E and F2F operations, it becomes apparent that the integrated current is not exactly equal to zero. There are two reasons for this: firstly, the respective start and end points in the form of EOC and EOD voltage are not identical, as these vary during operation. Secondly, the BMS and other peripheral electronic components are also partly supplied by the HSS itself. Next to the BMS power supply, balancing different cell voltages requires energy as well. Both effects ensure that a capacity difference remains after a full cycle. The variation of EOC and EOD affects capacity and energy estimation but does not produce a systematic error. The reason for this is that the variation in voltage averages out over multiple estimations. In contrast, the offset current leads to a cumulative measurement error, especially for integration periods of more than one day, and must therefore be adjusted for. The current for side reactions mentioned in Equation (2-7) plays only a secondary role in the current offset as the coulomb efficiency of lithium-ion batteries is close to 100 % [274].

5.2.3.2 Offset current correction

The reasonably constant energy supply of the battery to the BMS and regular balancing activities lead to an error in capacity estimation (see Figure 5-8). The reason for this is that the measurement system is attached to the DC poles of the whole HSS's battery. Thus, the internal energy supply of the BMS and balancing activities are not measured directly. Nevertheless, a voltage decay can be observed even when no current is measured.

A linear correlation between charge throughput and the voltage difference of EOC and EOD voltage can be identified. This leads to the assumption that a relatively constant offset current must be present. This offset current is depicted over the EOC and EOD voltage difference, respectively (see Figure 5-9).

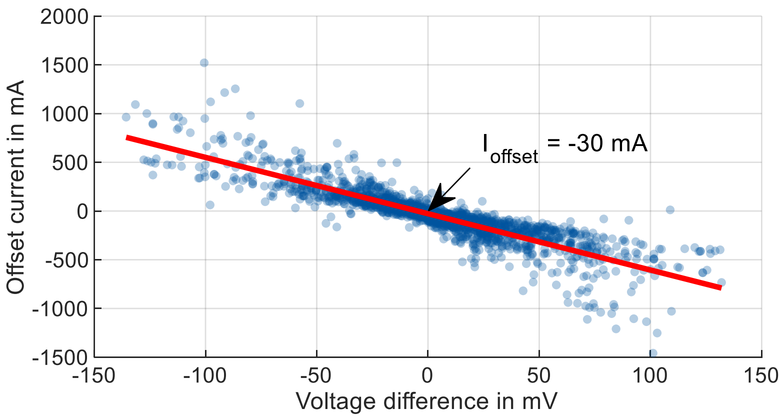

Figure 5-9: Identification of the offset current while analyzing voltage pairs from F2F and E2E full cycles.

The intersection of the trend line with the y-axis is defined as the offset current, which has a value of -30 mA for the shown system. This value includes the current, which flows into side reactions and causes aging. However, this current is within a neglectable range and not further considered (see Chapter 2.2). The system-specific mean offset value is subtracted to integrate two relaxation phases. It is also used to correct the energy estimates. The resulting power loss aligns with the values observed by Orth et al. [15].

5.2.3.3 SOC estimation

In addition to the estimation of the remaining usable capacity, a continuous SOC is needed for Chapter 6 and 7. To develop a computationally scalable method motivated by the regular relaxation recalibration possibilities, ampere-hour counting is used in this work to generate a continuous SOC time series (see Figure 5-10).

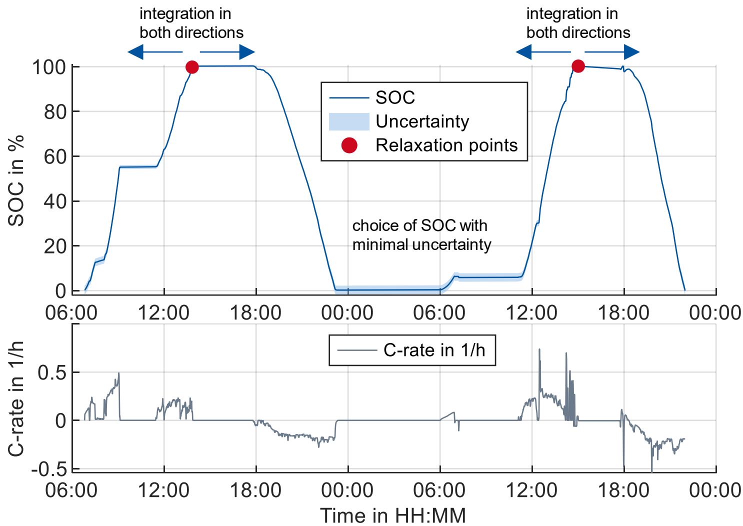

Figure 5-10. SOC course of an exemplary $\text{Small}_{\text{LMO}}$ system. The SOC is integrated between EOC relaxation points. Due to measurement inaccuracies, an uncertainty range is added. The uncertainty is not observable in steeper SOC slopes of the figure (although it exists), as the curves are close to each other. The SOC algorithm integrates forward and backward, reducing uncertainty toward the reset points.

The current measurement system of the investigated HSSs has a certain measurement accuracy, as presented in Chapter 4.1. Two additional current vectors are created to integrate this uncertainty into the SOC estimation by assuming maximum measurement errors toward charge and discharge currents. The current is integrated forward and backward concerning time. Therefore, the uncertainty is low near the reset relaxation points and high between the two reset points.

In the shown example, the EOC voltage is used for an SOC reset to 100 %. For some HSSs, the reset during winter is done via the EOD voltage, as especially larger HSSs barely reach a fully charged state during low solar irradiance. When the time series of the current integral is obtained, the SOC is normalized by the remaining usable capacity, as described in Equation (2-7). An example of SOC reset to 0 % at EOD relaxation points and the discounting of the offset current is presented in Appendix, Figure 9-15.

5.2.4 SOH estimation using OCV curve

The method developed in Chapter 5.2.3 is important for determining the usable capacity and energy. Its strength is that it considers all influencing factors, such as control strategies and aging. However, this means that only limited conclusions can exclusively be drawn regarding aging. Furthermore, the method requires that the HSSs are fully charged and discharged regularly. While this is the case for most HSSs in this work, the trend toward larger storage systems suggests that this is not true for all storage systems. For example, some HSSs do not get empty in the summer or full in the winter. In addition, applications such as electric vehicles or large-scale storage systems generally only use certain ranges of the SOC. Figure 5-7 shows that HSSs still have many relaxation points between the EOD and EOC voltage. These relaxation phases can continuously estimate the SOH even without full cycles. According to Figure 5-11, two successive relaxations are projected onto the OCV curve of a new cell and thus determine a reference value for the capacity and energy.

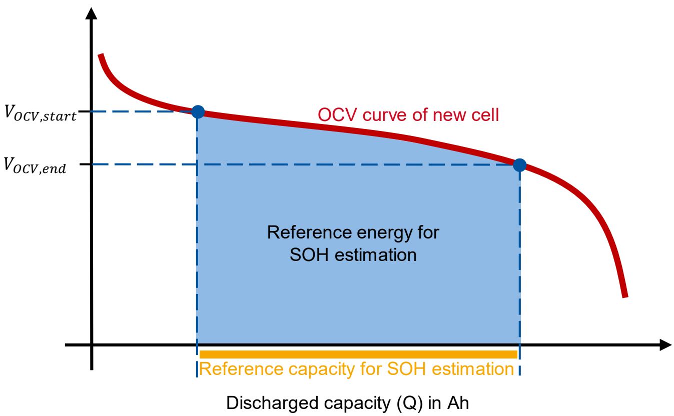

Figure 5-11: Schematic illustration of using the OCV curve of a new cell to continuously track the $SOH_{C,OCV}$ of an HSS. The capacity and energy of operational data between two relaxation points with the OCV voltages $V_{OCV,start}$ and $V_{OCV,end}$ is compared to those of a new cell through mapping the relaxation voltage on its OCV curve.

These reference values can be compared to the capacity and energy values out of the operational data according to Equations (5-6) and (5-7). They can be used to determine the $SOH_{C,OCV}$ and $SOH_{E,OCV}$ related to the initial OCV curve, with Q being the discharged capacity of a new cell. The battery current I_{Bat} is corrected with the offset current obtained from Chapter 5.2.3.

$$SOH_{C,OCV} = \frac{\int_{V_{OCV,start}}^{V_{OCV,end}} I_{Bat}(t)\, dt}{Q(V_{OCV,end}) - Q(V_{OCV,start})} \tag{5-6}$$

$$SOH_{E,OCV} = \frac{\int_{V_{OCV,start}}^{V_{OCV,end}} V_{Bat}(t) \cdot I_{Bat}(t)\, dt}{\int_{V_{OCV,start}}^{V_{OCV,end}} V_{OCV}(Q)\, dQ} \tag{5-7}$$

Influence of system-level data. This thesis has access to system-level field data. With this data, only the average cell voltage can be calculated. If the cells are not perfectly balanced, there are cells with a lower voltage. These cells limit the discharge capacity, leading to an overestimation of the reference capacity. Note that the capacity of the series connection is determined by the weakest cell, leading to lower capacity values in reality.

Availability of OCV curves. Using OCV curves has some challenges for third parties like a scientific institution. The cells used are often a manufacturer's trade secret, and the OCV curves are unavailable to customers or other third parties without cooperation (see Chapter 4.1). Some HSSs were even opened in the laboratory to obtain the necessary cell information. These HSSs were exclusively laboratory systems and not operated in households to ensure safety for private persons. The OCV curves were researched online and reconstructed from datasheets, scientific publications [275], and public tests [276]. Some assumed cells were confirmed by expert interviews and bilateral exchange with manufacturers, while others are still conjectures. Following non-disclosure agreements, no exact cell names are assigned to the analyzed systems in this thesis.

5.3 Results and discussion

This chapter describes and discusses the results of the field capacity tests, relaxation phases, usable capacity energy estimation, and SOH estimation.

5.3.1 Field capacity tests

Regular field capacity tests were conducted to track the usable capacity and energy of the HSSs. These tests were used to validate the developed methods.

Discharge behavior. Figure 5-12 shows the normalized current and voltage of different HSSs during conducted field capacity tests. While some systems use a constant current discharge, others reveal a constant power discharge with a rising current over time to compensate for the decreasing voltage. Toward the EOD, some systems apply a constant current phase or a controlled decline of the discharge current. Other systems abruptly abort the discharge process and reduce the current from maximum to zero in just a few seconds. Constant voltage phases are not observed in the shown systems. Especially the abrupt discharge termination at the EOD voltage significantly impacts the measured usable capacity and energy.

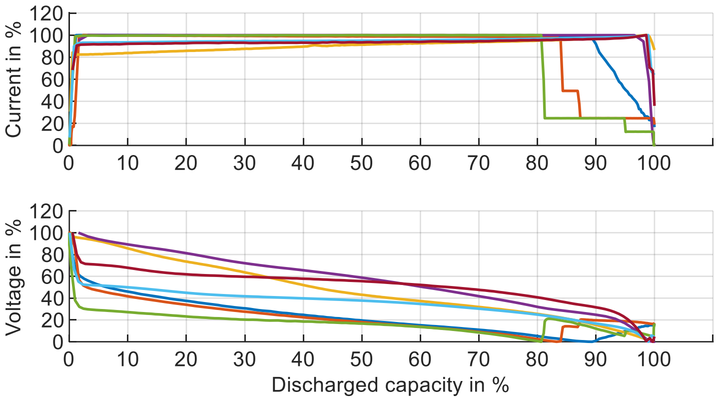

Figure 5-12: Current and voltage during field capacity tests of different HSSs. **Top:** Current values normalized to the maximum current of the HSSs. Discharged capacity is normalized to its sum. **Bottom:** Voltage values of each capacity test scaled to the range of 0 % to 100 %. The HSSs predominantly show constant current and constant power discharge behavior. Toward the EOL, different derating strategies are visible.

Due to the high overvoltage at high currents, the BMS measures the EOD voltage sooner than at lower powers and smaller overvoltage values allowing for less dischargeable capacity. Notably, the discharge durations differ more significantly from each other, as Figure 5-12 shows only the current over the discharged capacity. For example, the constant current phase of the green curve at

25 % of the maximum current would be about four times as long if the current were plotted against time.

Test results. Figure 5-13 shows the development of the SOH_{UC} based on the usable capacity over time. Each point corresponds to a manual capacity test.

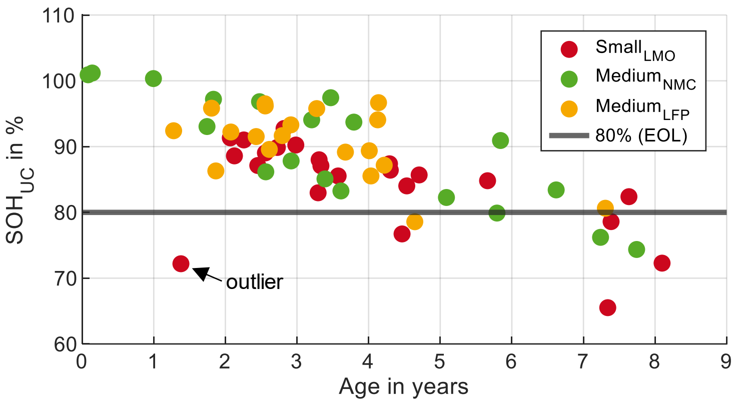

Figure 5-13: SOH_{UC} over system age based on field capacity tests. Normalized to nominal capacity. The EOL does not define a warranty case, as datasheets often contain an aging reserve in their stated value (see Figure 9-12).

Usable capacity. The usable capacity decreases over the years. While $Small_{LMO}$ HSSs show an average capacity decrease of 2.1 pp/a, $Medium_{NMC}$ systems show an average decrease of 3.2 pp/a, and $Medium_{LFP}$ systems of 2.2 pp/a. Note that these given linear trends simplify aging behavior explained in Chapter 2.2.4. After seven years, the first clear EOL cases can be identified following the test results, although some tests show slightly lower values than 80 % after already 4.5 a. The test result below 80 % of one $Small_{LMO}$ HSS between one and two years is considered an outlier, as not the whole voltage range was used.

Cycles. Figure 5-14 shows the test results over the EFCs. The average decrease is 0.9 pp/100 EFC for $Small_{LMO}$, 1.7 pp/100 EFC for $Medium_{NMC}$, and 0.9 pp/100 EFC for $Medium_{LFP}$ systems. Figure 5-15 analyzes the relationship between age, EFC, and SOH_{UC} in more detail.

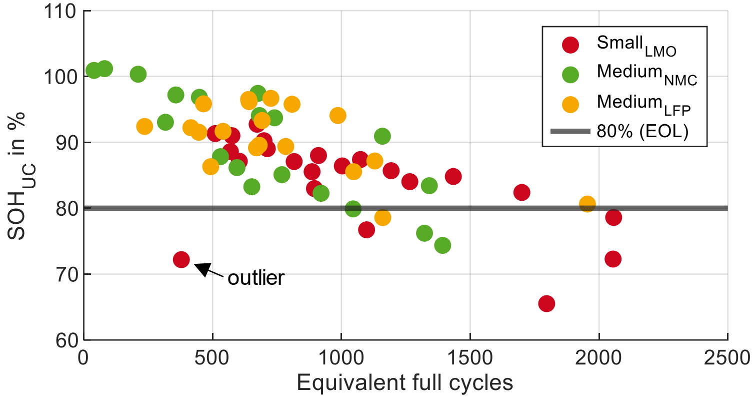

Figure 5-14: SOH$_{UC}$ over equivalent full cycles based on field capacity tests. Normalized to nominal capacity. The EOL does not define a warranty case, as datasheets often contain an aging reserve in their stated value (see Figure 9-12).

The EFCs increase approximately linearly for the different HSS classifications. The Small$_{LMO}$ systems show the most cycles followed by the medium systems. Nevertheless, one Medium$_{LFP}$ system reaches a similar number of EFCs as the Small$_{LMO}$ systems after more than seven years (see Figure 5-15).

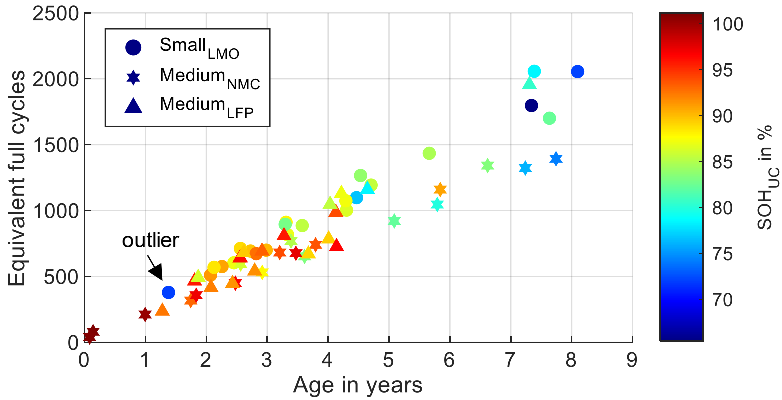

Figure 5-15: Field capacity test results of the SOH$_{UC}$ according to system age and equivalent full cycles. Each marker corresponds to a capacity test conducted. Normalized to nominal capacity. The EOL does not define a warranty case, as datasheets often contain an aging reserve in their stated value (see Figure 9-12).

Regarding aging, a capacity fade can be observed for all HSSs. The SOH_{UC} values depend on the specific HSS within a system type. Especially for the older $Small_{LMO}$ systems, varying SOH_{UC} results can be observed at similar age. In addition, the aging behavior differs among the system types. The $Small_{LMO}$ systems do not show lower SOH_{UC} values compared to the $Medium_{NMC}$ systems despite more EFCs at a comparable age. Note that the values are not corrected by temperature, as only the battery housing temperature is known, making a normalization to 20 °C according to Equation (2-3) challenging.

Usable energy. The results for the usable energy look similar to the capacity analysis (see Appendix, Figure 9-12), leading to the conclusion that the loss of capacity is the dominant aging effect. At the same time, a possible increase in internal resistance appears secondary. Otherwise, the SOH_{UE} values would be significantly lower than the SOH_{UC} values.

Warranty. To compensate for aging, many systems show an aging reserve (see Figure 5-2). Manufacturers often state a lower usable energy value in their datasheet to meet warranty conditions. According to Figure 9-12, the first warranty cases can be identified after seven years. These systems were installed in the first period of the subsidy program, which required a seven-year warranty. Thus, based on the field capacity tests, the manufacturers of the observed HSSs could hold their warranty statements for the systems that are still in operation. Considering these systems were predominantly from the first product generation, this can be considered a good result for the overall market.

5.3.2 Relaxation phases

Figure 5-16 shows the distribution of relaxation voltages for the analyzed systems and the relaxation phase duration distribution. The distribution of relaxation phases aligns with the voltage distribution previously discussed in Chapter 4.2.2, as most relaxations are observed at the voltage edges. Moreover, the distribution provides insights into the control strategies employed. A peak in the distribution (x-axis direction) suggests precise control of EOC or EOD voltage by the BMS, remaining constant over time. The $Small_{LMO}$ systems exhibit a distinct EOC voltage range above 4.1 V, while the EOD relaxations show a wider voltage range because the EOD voltage gradually decreases, as outlined in Chapter 4.2.4. In contrast, the $Medium_{NMC}$ systems show different behavior, characterized by specific EOD and EOC voltages. The $Medium_{LFP}$ systems do not share such distribution peaks toward EOD and EOC voltage due to their flat OCV curve.

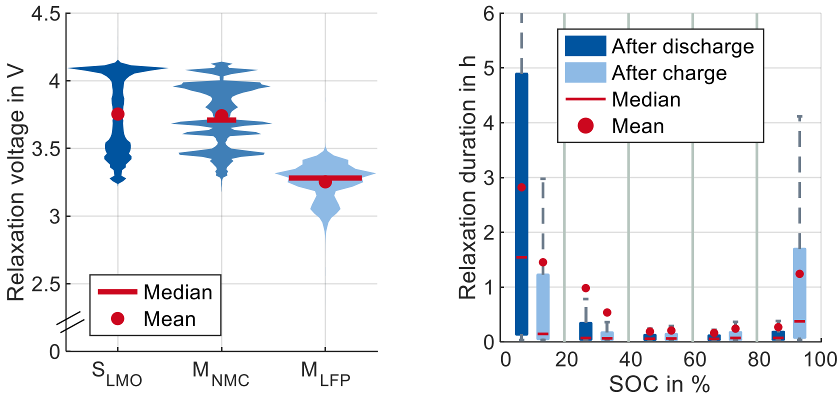

Figure 5-16. **Left**: Distribution of relaxation OCVs. The width corresponds to the number of occurrences. The peaks symbolize EOD and EOC voltages. The MediumNMC systems use different NMC composites, so EOD and EOC values vary between systems. **Right:** Duration of relaxation phases defined as the idle time of the HSSs with current close to zero. It is not the time constant of the relaxation processes. The duration gets longer toward the SOC edges.

Figure 5-16 (right) depicts the distribution of the relaxation durations after charge and discharge. These are defined as the idle times of the HSSs at a current nearly equal to zero and are not the time constant of the relaxation process. The analysis reveals that relaxation durations are longer at the SOC edges. Furthermore, a sensitivity analysis shows that an accurate relaxation fit requires a minimum relaxation duration (see Appendix, Figure 9-11). This is why this thesis primarily focuses on relaxations occurring at the SOC edges close to 0 % SOC and 100 % SOC, such as relaxations after charging at full states and relaxations after discharging at empty states. These longer relaxation phases can be explained through the operational characteristics. For example, fully charged systems remain unused, as PV generation often covers household consumption until the sun sets. Consequently, the HSSs begin to discharge hours after reaching their EOC voltage (see Figure 4-2). Similarly, fully discharged systems remain idle, often throughout the night, until they are charged with the rising sun the next day.

5.3.3 SOH according to usable capacity and energy

Figure 5-17 shows the results of the capacity estimate for one $\mathrm{Small_{LMO}}$ HSS. While the orange dots represent the manual field capacity tests, the dark blue dots show the algorithmic capacity estimates. The confidence interval in light blue (CI) contains 75 % of all estimates and is used as an accuracy variable.

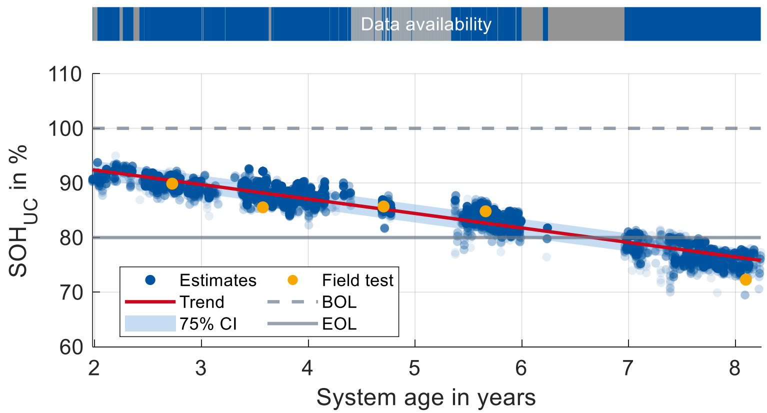

Figure 5-17: SOH_{UC} estimate (normalized to nominal capacity) of an exemplary $Small_{LMO}$ system validated by field capacity tests. The darker the blue points are, the more estimates exist. The trend is a linear fit of the estimates. The confidence interval (CI) of 75 % of all estimates is shown in light blue.

Capacity decrease. Full cycles are regularly identified throughout the year, mostly from spring to fall (see Figure 4-6). The range of the usable capacity estimates originates from different relaxation voltages near the EOC and EOD voltages (see Figure 5-9) and different C-rates. The fitting of the aging trends is a complex topic that is not the core of this thesis. Therefore, a linear fit is applied to the values of the algorithmic capacity estimate, and its gradient is defined as the aging rate. A SOH_{UC} of 2.7 pp/a is observed for the presented system. A linear fit is in line with some observations in literature [277], although both linear and non-linear aging behavior are possible [83]. However, the so-called knee point [84,278] cannot yet be observed for the systems.

Comparison of estimates and tests. The values of the manual capacity tests are not at the upper limit of estimated capacities, although systems are controlled discharged from 100 % to 0 % SOC. This has several reasons. First, during the manual capacity tests, the HSSs are discharged at higher C-rates, leading to a smaller capacity, as shown in [279]. Second, the higher overvoltage leads to an earlier reach of the EOD voltage. While some HSSs show a stepwise current derating toward the EOD voltage, others employ an abrupt shutdown (see Figure 5-12). In contrast, HSSs provide relatively low power during the night and thus have a lower overvoltage, leading to higher discharge capacities for the algorithm. This phenomenon becomes more obvious when analyzing the remaining usable energy, which is even more dependent on the C-rate due to the internal resistance (see Chapter 6).

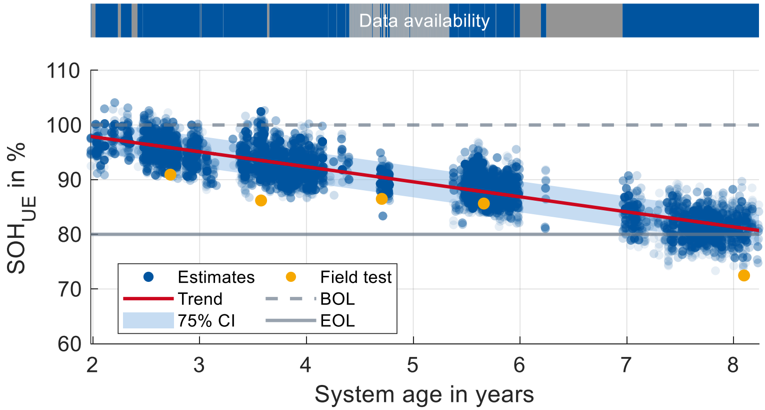

Figure 5-18: SOH_{UE} estimate (normalized to nominal energy) of an exemplary $Small_{LMO}$ system validated by field capacity tests. The darker the blue points are, the more estimates exist. The trend is a linear fit of the estimates. The confidence interval (CI) of 75 % of all estimates is shown in light blue.

Exemplary $Medium_{NMC}$ and $Medium_{LFP}$ HSSs are shown in Appendix, Figure 9-13. The algorithm shows different confidence intervals and, thus, varying accuracy for the analyzed HSSs. To illustrate this, Figure 5-19 depicts the distribution of the 75 % CIs for all classified systems.

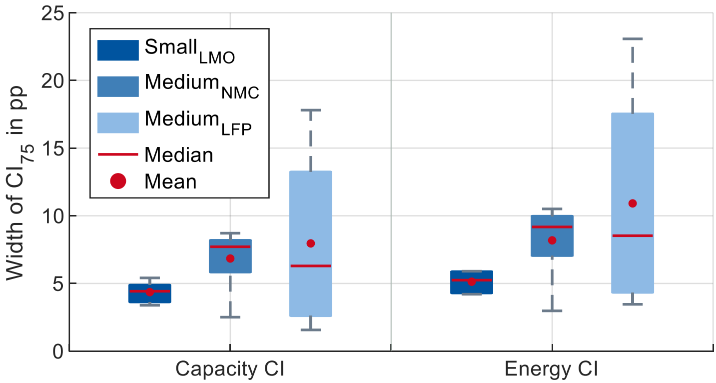

Figure 5-19: Width of the 75 % confidence interval (CI_{75}) for usable capacity and energy estimates. The CI_{75} is used as an accuracy measure. The method is quite accurate for $Small_{LMO}$, $Medium_{NMC}$, and some $Medium_{LFP}$ systems. Other $Medium_{LFP}$ systems show a larger CI width.

General accuracy findings. The $Small_{LMO}$ systems show the lowest mean capacity confidence width with a value of 4.4 pp, followed by the $Medium_{NMC}$ systems with 6.8 pp and the $Medium_{LFP}$ systems with 8.0 pp. The reason for the high accuracy of $Small_{LMO}$ systems can be explained by their high cycle number and an accurate identification of EOC and EOD voltage due to the LMO OCV curve. The $Medium_{NMC}$ systems with NMC cells share this voltage characteristic but show fewer full cycles, leading to fewer estimates and, consequently, wider confidence ranges. LFP has a significantly flatter OCV curve than LMO and NMC, leading to less accurate EOC and EOD detection. Combined with a medium number of full cycles, their average usable capacity and energy estimates are worse, although some systems reach comparably good values below 5 %.

Comparing capacity and energy. The energy estimates of all systems are less accurate than the capacity estimates, as they are more dependent on temperature and C-rate due to the internal resistance. Considering the algorithm is meant to determine whether an HSS is a warranty case, it should be significantly more accurate than 20 % of the usable battery capacity and energy. The reason for this is that the relevant warranty range is between 100 % and 80 %, with the latter being defined as the EOL. Therefore, the results are considered reasonable except for some LFP systems.

Influence of interconnection. Some of the systems have a high number of cells in parallel and series. The parallel cells lead to a greater variation of EOC and EOD voltage detections due to overlapping diffusion processes of different modules and cells. In contrast, the series connection limits the battery capacity as the weakest cell determines the capacity of one string. If the cells are not well balanced, this effect gets larger.

Aggregated analysis. Figure 5-20 provides all aging rates for the three system types identified by the linear fit for the HSSs both for capacity and energy on an annual basis and per 100 EFC.

The mean values for the decrease in SOH_{UC} are 3.1 pp/a for $Small_{LMO}$, 1.9 pp/a for $Medium_{NMC}$, and 2 pp/a for $Medium_{LFP}$. Concerning 100 EFC, the aging rates are 1.2 pp/a for $Small_{LMO}$, 0.9 pp/a for $Medium_{NMC}$, and 0.7 pp/a for $Medium_{LFP}$. However, a range of approximately 2 pp/a can be observed for the classified system types, showing differences in aging behavior between similar HSSs. Purely from the gradients, the physical EOL can be estimated after 5 a (for 4 pp/a) and after 20 years. While the shorter durations can already be confirmed for some HSSs, linear extrapolation is not reasonable for the HSSs with low aging ranges based on the non-linear aging toward the EOL (see Figure 2-5). Nevertheless, a lifetime of around 10 a seems reasonable, especially when considering the aging reserve (see Figure 9-12).

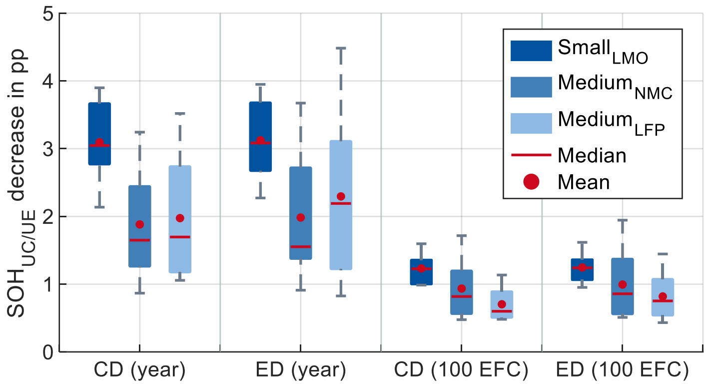

Figure 5-20: Decrease in SOH_{UC} (usable capacity decrease (CD)) and SOH_{UE} (usable energy decrease (ED)) per year and per 100 EFC. The boxplot contains the gradient of the linear aging fit from Figure 5-17 and Figure 5-18.

Based on the small sample size of 21 HSSs, drawing any statistically significant conclusions or computing meaningful correlations with the operating conditions is impossible. Nevertheless, some qualitative assumptions can be made.

Comparing small and medium HSSs. The higher aging rates for the $Small_{LMO}$ systems can possibly be related to the small battery energy and the resulting operating conditions. These HSS run more cycles and, on average, show larger DODs than the medium systems. In addition, the $Small_{LMO}$ HSSs stay longer at high SOCs. These operating conditions result in accelerated aging (see Chapter 2.2.4). While the gradient concerning 100 EFC is only slightly increased compared to the medium systems, the decrease in usable capacity per year is much higher due to the many cycles.

Comparing NMC and LFP HSSs. The $Medium_{NMC}$ and the $Medium_{LFP}$ systems show similar decreases in usable capacity. Nevertheless, the $Medium_{NMC}$ systems have a lower average decrease per year but a higher decrease per 100 EFC than the $Medium_{LFP}$ systems. This could indicate that calendar aging is more pronounced than cyclic aging in the LFP systems than in NMC systems. This assumption is supported by similar EFC numbers and DOD distributions shown in Chapter 4.2.2.

Comparing capacity and energy fade. For all systems, the average SOH_{UE} decrease is larger than the SOH_{UC}. This is because energy is also affected by the increasing internal resistance. The energy fade is only slightly higher, leading to the conclusion that the limiting factor of the usable energy is the capacity fade and not a possible increase in internal resistance (see Chapter 6).

5.3.4 SOH according to initial OCV curve

Figure 5-21 shows the SOH in terms of the initial OCV curve of a new cell ($SOH_{C,OCV}$) estimated according to 5.2.4 for the same $Small_{LMO}$ HSS as in the previous section. This method compares the capacity and energy to the reference values of a new cell using its initial OCV curve.

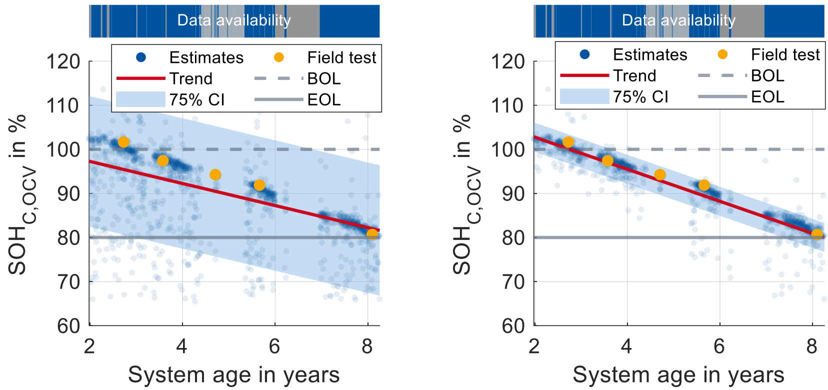

Figure 5-21: Exemplary $Small_{LMO}$ system with continuous $SOH_{C,OCV}$ estimate validated by field capacity tests. The darker the blue points are, the more estimates exist. **Left**: Use of any two consecutive relaxation points. **Right:** Use of relaxation points with a minimum voltage difference of 0.5 V. **Difference:** A small delta between relaxation voltages leads to outliers and a biased trend. Values normalized to initial OCV curve capacity.

The estimates have a larger confidence interval than the usable capacity estimates. Nevertheless, a clear trend represented by dark blue areas that predominantly contain full cycles can be observed. If only cycles with a minimum cell voltage data of 0.5 V are used, outliers can be filtered out (see Figure 5-21, right).

The wider range of $SOH_{C,OCV}$ estimates shows that the method is not as robust as the presented one for the SOH_{UC}. This has the following reasons:

1. The SOH_{UC} estimation does not rely on an absolute precise OCV estimate. If the EOC and EOD voltages and, thus, fully charged and discharged states are detected correctly, the capacity can be calculated by integrating the current between these states. Detecting a fully charged or discharged state is less complex than estimating the exact OCV needed for the $SOH_{C,OCV}$ estimation. Slightly inaccurate OCV estimates can already greatly impact the result if the OCV curve slope is flat (especially for LFP).

2. Small DODs have a small difference in OCV, leading to low capacity and energy values. These small values lead to outliers, especially when the denominator of Equation (5-6) and (5-7) gets small. Thus, filters such as a minimum voltage difference or a minimum capacity throughput should be applied.
3. This thesis used OCV curves of either unknown measurement technique or measured as qOCVs at low C-rates (~C/10). Therefore, operation at higher power has different capacity and energy values, leading to low estimates. In addition, it is not certain that the cell OCV curves of all HSSs used are correct.
4. The aging can affect different parts of the OCV shape. Therefore, the analysis of one part must not correspond to the analysis of another part.

These reasons result in worse estimates for the gradients shown in Appendix, Figure 9-14. Although comparable gradient results are obtained for $Small_{LMO}$ and $Medium_{NMC}$ systems as for the SOH_{UC}. The larger confidence interval range of 75 pp of all data underlines this with 40 pp ($Small_{LMO}$), 30 pp ($Medium_{NMC}$), and 220 pp ($Medium_{LFP}$). The large range of $Medium_{LFP}$ estimates predominantly occurs due to the flat voltage range of LFP and the poor quality of the gathered OCV curves from a datasheet, making OCV estimates challenging. When only the EOC and EOD relaxation voltages are considered, the results clearly improve (Figure 9-14).

Although the observed decrease rates are similar, the absolute $SOH_{C,OCV}$ values are higher than the SOH_{UC} values (see Figure 5-17). It can probably be attributed to the normalization of the estimated usable capacity, as the exact usable capacity is unknown.

5.4 Conclusion

This chapter presents data-driven capacity estimations that accurately estimate the usable capacity and the SOH from the daily operating data.

Field capacity tests. The field capacity tests show yearly average decreases in usable capacity from 2.2 pp/a to 3.2 pp/a. The gradient per 100 EFC ranges from 0.9 pp/100 EFC to 1.7 pp/100 EFC, depending on the HSS type. Since some manufacturers adjust the usable capacity by widening the voltage range, the trends do not necessarily correspond to the actual aging. Due to a field study, certain standards from the laboratory field could not be met. Nevertheless, the manual field capacity tests are as reproducible as possible for the individual system due to the discharge under full load. Thus, the C-rate is predetermined for each HSS by the dimensioning of battery energy and inverter power and differs between systems. In addition, the different derating characteristics and operating temperatures lead to differences between the systems.

Relaxation phases. To determine the exact SOC, a battery model is parametrized based on automatically detected relaxation phases of the HSSs. These happen when the current is small, and the voltage relaxes to its OCV (see Chapter 2.2.3). The identified relaxation phases are then used to parameterize a second-order equivalent circuit model. This allows for the estimation of the OCV. This voltage is used as start and end values of current and power integrations and as recalibration points for the SOC estimation.

SOH_{UC} and SOH_{UE}. The SOH_{UC} and SOH_{UE} of an HSS are estimated by identifying full cycles. Only the relaxation phases near the EOC and EOD voltage are used for identification. These full cycles estimate the usable capacity and energy, applying coulomb counting and considering offset current correction. Afterward, the SOH_{UC} and SOH_{UE} are calculated by dividing their values through their nominal values. The algorithm is validated through the conducted field capacity tests. LMO and NMC systems can be analyzed with good precision, but the flat OCV curve of LFP makes their analysis more challenging, though still possible. The mean values for SOH_{UC} decrease are 3.1 pp/a for $Small_{LMO}$, 1.9 pp/a for $Medium_{NMC}$, and 2 pp/a for $Medium_{LFP}$. Concerning 100 EFC, the aging rates are 1.2 pp/a for $Small_{LMO}$, 0.9 pp/a for $Medium_{NMC}$, and 0.7 pp/a for $Medium_{LFP}$. Thus, especially the many cycles of the $Small_{LMO}$ HSSs lead to accelerated aging. As the SOH_{UC} and SOH_{UE} are in a comparable range, the energy fade can mainly be attributed to the capacity fade. Thus, a possible increase in internal resistance seems to play a secondary role.

$SOH_{C,OCV}$ and $SOH_{E,OCV}$. The SOH_{UC} and SOH_{UE} estimates are not only influenced by battery aging but also by changing BMS characteristics. In addition, the method can only be applied if an application shows the regular reach of EOC and EOD voltages. Therefore, another method is applied to estimate the $SOH_{C,OCV}$ and $SOH_{E,OCV.}$ In this method, the SOH is tracked by mapping two consecutive relaxation phases on the OCV curve of a new battery cell and comparing the field data with its reference capacity and energy. This enables a continuous evaluation of the aging behavior even if no full cycles occur. The observed aging rates are in a similar range. However, the results tend to have a higher uncertainty, probably arising from inaccuracies in OCV estimation, varying operational power, and some uncertainty regarding the information on the cells used. Therefore, this method is considered less robust, although applied filters such as a minimum capacity throughput can improve the results.

6 Internal resistance estimation

This chapter analyzes the internal resistance based on the field measurements. Furthermore, the results are used for the degradation mode analysis in Chapter 7. This chapter is based on and contains identical parts of [280] under the lead of the author.

6.1 Overview

The internal resistance is the second important SOH criterion besides the capacity [234,281–283]. The main contributors to battery resistance are the ohmic, the charge transfer, and the diffusion resistance [284]. Chapter 5.1 contains a literature review on SOH estimation, which is extended by literature on internal resistance. In general, electrochemical impedance spectroscopy (EIS) and current pulses are used to characterize the internal resistance [40,41].

Electrochemical impedance spectroscopy. The EIS method is a comprehensive measurement of the voltage response to an AC current applied in frequency ranges from about 0.01 Hz (or lower) to more than 1,000 Hz, resulting in a complex impedance curve (see Figure 6-1, left) [285] that shifts with aging [41]. The shifting and stretching of different sections enable the identification of degradation modes during aging [41]. However, applying this method requires either a laboratory setup or an online EIS possibility on the BMS, which is no precondition to this dissertation.

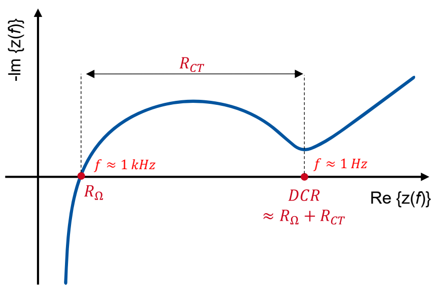

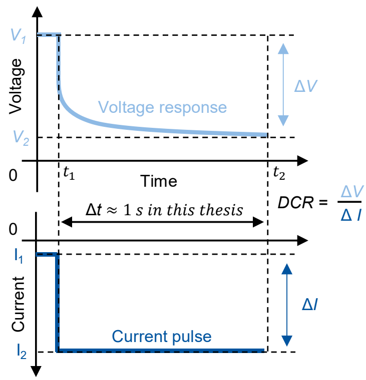

Figure 6-1: **Left**: Schematic illustration of a battery's complex impedance curve, adapted from Rastegarpanah et al. [285], used under CC BY 4.0 [23]. **Right**: Voltage response to a current pulse, adapted from Chung [286], used under CC BY 4.0 [23]. The DCR in this thesis corresponds to the pulse resistance calculated after one second.

Current pulses. Figure 6-1 (right) shows the voltage response to a current pulse, which can be used to analyze the internal resistance [286]. When the pulse begins, the instantaneous voltage change due to pure ohmic resistance

(R_{Ω}) is visible, followed within a few milliseconds to a few seconds by a further voltage change due to polarization, charge transfer (R_{CT}), and double-layer capacitance [41]. The superposition of these voltage changes is often used to calculate the so-called direct current resistance (DCR) [286]. The DCR can also be calculated during operation and used for performance predictions [41]. It is in the order of magnitude of the real part at the end of the first half cycle, as shown in Figure 6-1, and has similar electrochemical behavior as discussed below [41].

Slow diffusion voltage. The further voltage drop after a few seconds is mainly due to the diffusion processes in the active materials (see Chapter 5.2.2) [41]. In the following, this voltage is called slow diffusion voltage (SDV) and is represented by the parameter V_{slow} of the ECM presented in Figure 5-5. The SDV is dependent on both short-term and long-term influencing factors.

Short-term influence SDV. In their study, Baghdadi et al. [287] investigate the short-term impact of operational parameters on the SDV under various conditions for three distinct cell chemistries, namely NMC, LFP, and LMO. The research analyzes the voltage reached during the relaxation period after 30 minutes. The results unveil a subtle correlation between the voltage relaxation profile and the three factors: (1) initial SOC in combination with the charge throughput until relaxation, (2) C-rate, and (3) temperature [287]. Bernardi et al. [65] confirm the effect of the C-rate on overvoltage during both the charging and discharging relaxation phases, where a higher C-rate leads to increased overvoltage. The SOC at which the relaxation occurs also influences the relaxation duration. Relaxation phases taking place at an SOC of 35 % exhibit longer duration compared to those at 65 % [65].

Long-term influence SDV. The calendar aging exhibits a correlation with the relaxation phase. Distinct variations in the relaxation profile follow the charging process across all observed cell chemistries [287]. Specifically, for the NMC and LMO chemistries, this leads to an amplified magnitude of the voltage change during the relaxation phase. In contrast, the LFP profile shows a slight decrease in this magnitude of voltage change [287]. It is crucial to consider this pronounced dependency on battery technology when analyzing relaxation profiles [287]. Qian et al. [62] have made similar observations regarding the impact of cyclic aging on NMC cells. As the cycle count increases, higher magnitudes of the overvoltage can be identified during the relaxation phase both for charging and discharging [62]. Furthermore, a linear relationship between the 30-minute relaxation voltage and the remaining capacity becomes evident [287].

For the aging analysis, the dependencies of DCR and SDV on the temperature, SOC, and current are explained below:

- **Dependency on temperature.** The DCR and the SDV have an almost exponential dependency on temperature. They are low at high temperatures and high at low temperatures. With aging, this dependency remains without major changes. [41]

- **Dependency on SOC.** The DCR and the SDV are lowest at medium SOCs and significantly increased at the edges. There is a tendency for values to be larger at low SOCs than at high SOCs. With aging, this effect increases. [41]
- **Dependency on current.** At room temperature and for a new battery, the dependency of DCR on the C-rate is almost negligible. However, aging reveals a small change as a function of the C-rate. [41]

Field data analysis. In the recent past, publications on field data measurements and internal resistance estimation have emerged. In [288], a data-driven approach is applied to real-world operational data from lead-acid solar off-grid systems to determine the resistance and predict the EOL. Online impedance modeling can further diagnose battery degradation on the electrode level, as conducted in [289]. Similar DCR analyses for the operational data of an electric vehicle are presented in [267], showing temperature and SOC dependencies.

6.2 Methodology

This chapter describes the methodology to estimate the direct current resistance. Furthermore, it investigates other relevant quantities for the internal resistance, such as the slow diffusion voltage and other relaxation parameters derived from the second-order equivalent circuit model from Chapter 5.2.2. In addition, it links these relaxation parameters to the capacity fade (see Figure 6-2).

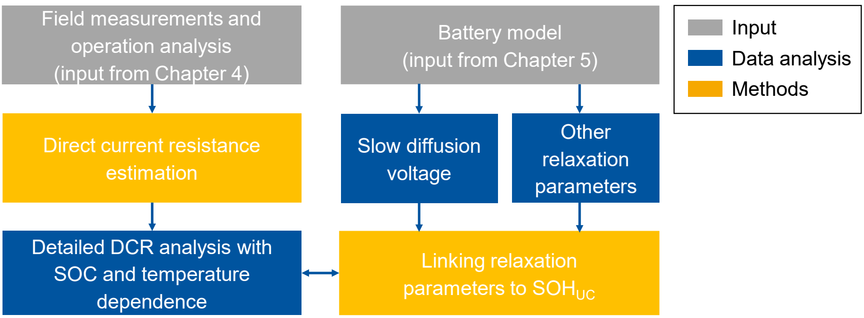

Figure 6-2: Structure of Chapter 6. This chapter develops a method to estimate the DCR and a method to link the internal resistance components to the SOH$_{UC}$.

6.2.1 Direct current resistance estimation

Current pulse identification. The battery resistance estimation uses the response of the battery voltage to current changes at specific temperatures and SOC during operation. Therefore, it can be seen as an online version of the current pulse method. The main difference is that field operation does not allow for a specified pulse intensity or duration. Still, it shows generation and load-induced current changes that can be used for DCR estimation. Furthermore, it is an extension to the parameter estimation in Chapter 5 that excluded the DCR estimation during model parametrization. Once the dynamic current changes are identified by differentiation, the resistance is calculated using Equation (6-1), adapted from [267,286].

$$\mathrm{DCR}(t_1, t_2) = \frac{V(t_2) - V(t_1)}{I(t_2) - I(t_1)} \qquad if\ \Delta I > 10\ \% \cdot I_{max} \tag{6-1}$$

In some cases, measurement inaccuracies occur, or the signals of voltage and current are not perfectly aligned. Therefore, a period of five seconds before and after the current pulse is considered to identify maximum and minimum values of current and voltage to calculate the DCR.

DCR estimation. The DCR is determined by considering both SOC and temperature, utilizing data from detected operating points. Since the current dependency is relatively small and the specific C-rates fall within a relatively narrow range, the current influence is disregarded to ensure a larger sample size for specific temperature-SOC combinations. Given the nonlinear relationship between DCR, SOC, and temperature, a lookup table is constructed to average the estimated resistance values within discrete SOC and temperature bands using the median, thus disregarding statistical outliers that may arise during field data analyses. A two-dimensional linear interpolation creates a resistance function dependent on SOC and temperature. This is done to maintain smoothness and prevent abrupt DCR changes from one combination of SOC and temperature to another. Figure 6-3 presents the resulting resistance estimation for an exemplary system.

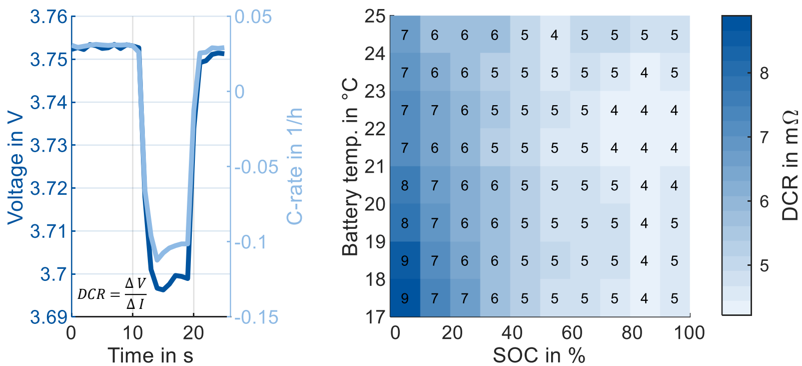

Figure 6-3: **Left:** Identified current pulse and voltage response to calculate the DCR by dividing the voltage delta by the current delta. **Right:** Estimated DCR values for an exemplary Small$_{LMO}$ system (cell level) according to SOC and temperature (right).

It showcases how internal resistance tends to increase at low SOC and low temperatures, which aligns with findings in the literature [41]. Throughout most operating conditions, the DCR values of the shown system remain around 5 mΩ, but they can reach up to 9 mΩ at low temperatures and SOC levels.

6.2.2 Slow diffusion voltage estimation

The slow diffusion voltage was introduced in Chapter 5.2.2 as V_{slow}. The parameter is extracted from the fitted second-order equivalent circuit model to analyze the relaxation phases. Based on literature research, the development of both high and low SOC ranges are analyzed as these change the most during battery aging [41].

6.2.3 Linking relaxation parameters to capacity fade

Literature describes a correlation between capacity fade and relaxation phases [62,287,290–292]. Therefore, this chapter describes how to link these to the capacity estimates from Chapter 5. To explore the potential information contained in the relaxation parameters regarding the SOH_{UC}, a principal component analysis is conducted (PCA). Subsequently, two machine learning models (linear regression and the neural regression network) are trained to estimate the SOH based on relaxation parameters.

Dataset and limitations. Regression models and neural networks typically require data from many systems. This is impossible with this thesis's small sample size of 21 HSSs, especially as the largest number of similar systems is six for the $Small_{LMO}$ HSSs. Therefore, the $Small_{LMO}$ systems are used for further analysis to demonstrate the methodology. When analyzing the results, limited expressiveness should be considered. It is important to note that this thesis does not focus on the machine learning methods used. Thus, the described methodology is condensed, and the proposed methods must be seen as proof of concept.

Model inputs. Ten parameters of the ECM are used as input data for the machine learning models (see Chapter 5.2.2). These parameters include the four relaxation parameters ($\boldsymbol{V_{fast}}, \boldsymbol{\tau_{fast}}, \boldsymbol{V_{slow}}, \boldsymbol{\tau_{slow}}$), operating conditions during the relaxation (current before, charge throughput before, temperature, OCV), relaxation duration of the fit, and the RMSE of the fit.

Principal component analysis. A dimensionality reduction using PCA is performed to validate the adequacy of these parameters for predicting the capacity-based SOH of a system. The PCA represents one of the widely employed techniques in dimensionality reduction [293]. It is a linear and unsupervised method for subspace and manifold learning [294]. The obtained reduced subspace aims to preserve the majority of the variance present in the original, higher dimensional data [293]. The principal components can be envisioned as a new coordinate system defined by orthogonal vectors within the lower dimensional subspace (see Figure 6-4 (left)) [293,295]. The first principal component acts as the axis capturing the highest variance of the original, higher dimensional dataset [293,295]. The following principal components each capture less variance according to their number. Employing all principal components leads to a new dataset obtained through the rotation of the original dataset [294]. Before PCA, the data must be centered and normalized [294].

Linear regression. Regression analysis investigates and models the relationship between variables as a statistical technique [296]. It predicts numerical outputs by analyzing multiple input variables [297]. The commonly used linear regression computes the output through a weighted sum of the inputs with an offset value [297]. In the corresponding Equation (6-2), $\boldsymbol{x}$ symbolizes the input vector, $\boldsymbol{w}$ denotes the parameters (also referred to as weights), and $\hat{\boldsymbol{y}}$ represents the estimated output [297].

$$\hat{y} = w^T x, with\ x, w \in \mathbb{R}^n\ and\ y \in \mathbb{R} \tag{6-2}$$

The performance evaluation of the regression model typically involves error minimizing, such as the mean squared error, between the training output $\boldsymbol{y}$ and the estimated output $\hat{\boldsymbol{y}}$ [297].

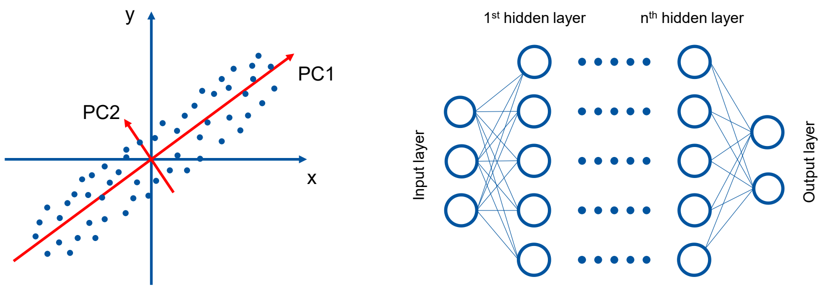

Figure 6-4: **Left:** PCA adapted from Werner et al. [295], used under CC BY 4.0 [23]. The first principal component (PC1) explains most of the variance present, as the range of the second one (PC2) is narrow. Consequently, the dimension could be reduced to 1D. **Right:** Neural network consisting of an input layer, several hidden layers, and an output layer, adapted from Hassan et al. [298], used under CC BY 4.0 [23].

Neural regression network. Figure 6-4 (right) shows an exemplary neuronal network. In this thesis, a shallow neural regression network is built, comprising two hidden layers, each accommodating ten neurons. Within these hidden layers, the commonly used activation function “ReLU” captures patterns and non-linear relationships in the data [297]. Notably, the output layer is linearly activated, facilitating a seamless transition to a linear regression-like computation. Specifically, the connection from the final hidden layer to the output can be perceived as linear regression.

According to Equation (6-3), the output of a neuron in a layer can be calculated where the parameter h is the neuron's output, W is the weights of the connections from the input neurons x, c is the bias, and g the activation function [297].

$$h = g(W^T x + c) \tag{6-3}$$

The two hidden layers in the neural regression network convert the 10-dimensional input dataset's features into more representative linear combinations. These refined features are then utilized in the subsequent regression task, spanning from the second hidden layer to the output layer.

Model training. To avoid overfitting, both models are trained with systems different from those used to test the model performance. In addition, the input values are normalized after removing outliers.

6.3 Results and discussion

This chapter presents the results of the direct current resistance, the slow diffusion voltage, and the relationship between internal resistance components and the capacity fade.

6.3.1 Direct current resistance

Single system. Figure 6-5 depicts the internal resistance estimation for one exemplary $\mathrm{Medium}_{\mathrm{NMC}}$ system over seven years. The influence of temperature dominates that of the SOC for the system under consideration. The seasonality is visible due to the lower DCR values in summer (around 20 mΩ to 25 mΩ) and higher DCR values in winter (around 30 mΩ to 40 mΩ). Thus, the winter's DCR values are twice as high as in the summer. In addition to the influence of the temperature, the SOC amplifies the mean DCR since the HSS are predominantly empty in winter (high DCR at low SOC) and regularly full in summer (low DCR at high SOC).

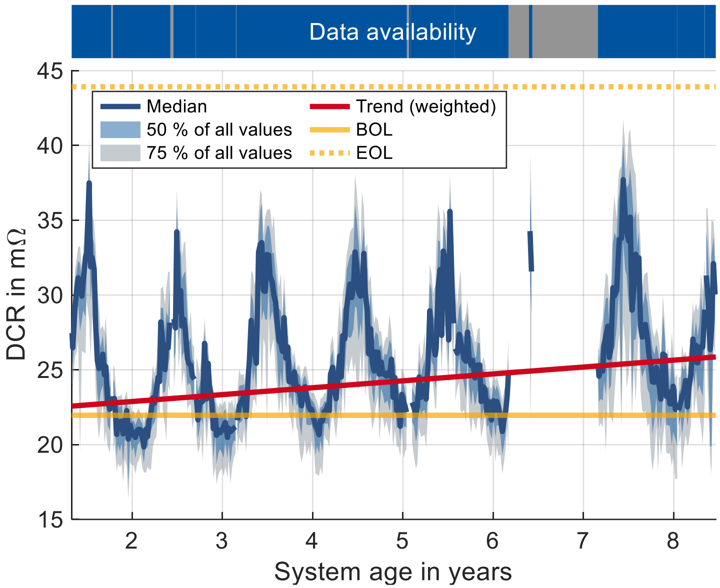

Figure 6-5: Development of the DCR of an exemplary Medium$_{NMC}$ (system level). The effect of different SOC and temperature values is visible. In the summer, high temperatures and elevated SOCs lead to a low DCR. In the winter, low temperatures and small SOCs lead to an increased DCR. The fit accounts for all estimates and is mainly influenced by estimates during summer due to the higher operational hours.

Over the years, an increasing trend can be observed, which is attributable to battery aging, according to the literature presented above. Therefore, the trend is based on all values and is closer to the summer values since more estimates are possible here due to the higher operational hours. The colored confidence intervals show that the estimates have a higher certainty in summer than in winter. Since the initial value of the DCR is unknown, estimates are made using the trend to extrapolate the DCR at the time of installation. Overall, the trend increases by less than 1 mΩ/a in the case shown, which corresponds to a relative increase of around 2.5 pp/a. Thus, the HSS does not come close to its EOL within the analyzed period, as the EOL is defined as a doubling of the estimated initial DCR (see Chapter 2.2).

SOC dependence. Figure 6-6 shows the DCR values of a $Small_{LMO}$, $Medium_{NMC}$, and $Medium_{LFP}$ HSS. The chosen temperature range is 20 °C to 25 °C, and the SOC step size is 10 %. These adjustable ranges are a trade-off between the number of estimates and accuracy.

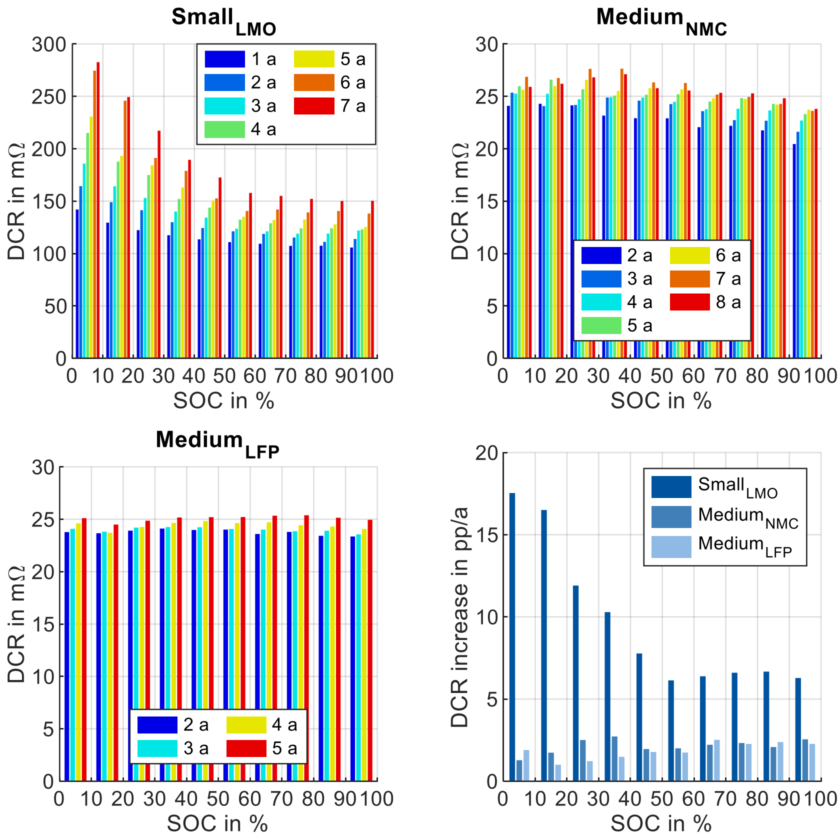

Figure 6-6: SOC-dependent DCR development for exemplary $Medium_{NMC}$, $Medium_{LFP}$, and $Small_{LMO}$ systems plus the average annual increase in percentage points. Temperature range is 20 °C to 25 °C. The DCR values are calculated on system level as the cell-level DCR values are different, too. The legend contains information about the system age.

While the $Medium_{LFP}$ system shows no clear SOC dependence, the $Medium_{NMC}$ and $Small_{LMO}$ systems show lower DCR values for higher SOCs. This effect is more pronounced for the $Small_{LMO}$ HSS. Regarding aging, the HSSs show an increase in DCR for all SOC ranges. The highest increases are seen for the $Small_{LMO}$ system, especially at low SOCs.

A simple linear trend is fitted for better comparability. The determined gradient is normalized by the initial value of the first year shown using the fit. The mean increase in the $Small_{LMO}$ system is over 15 pp/a for the lower SOCs of up to 20 %. It drops in the medium SOC range and is about 6.5 pp/a between 50 % and 100 % SOC. The $Medium_{NMC}$ and $Medium_{LFP}$ systems show only small DCR increases of up to 2.5 pp/a. Both systems show slightly increased values, especially at higher SOCs. The $Medium_{NMC}$ system has slightly increased values between 20 % and 30 % SOC, and the $Medium_{LFP}$ system below 10 % SOC. The reason for the strong DCR increase of the $Small_{LMO}$ system for a low SOC range can possibly be attributed to a deeper discharge of the anode. This is assumed to have two reasons. Firstly, the EOD voltage is lowered over the years by the BMS (see Figure 4-8), leading to lower lithiation states of the graphite. Secondly, the aging mode analysis in Chapter 7 indicates that the loss of lithium inventory amplifies this effect.

Temperature dependence. Figure 6-7 depicts the temperature-dependent DCR development for exemplary HSSs. The values are shown for an SOC range of 40 % to 60 %, as there are only minor overlayed SOC dependencies compared to the edge SOC ranges. The chosen temperature ranges are 18 °C to 20 °C (low), 23 °C to 25 °C (medium), and 28 °C to 30 °C (high). A clear trend of lower DCRs at higher temperatures can be identified for the $Small_{LMO}$ and $Medium_{NMC}$ systems. This difference equals a DCR decrease of around 25 % from low to high temperatures for the first year of the shown $Small_{LMO}$ and the $Medium_{NMC}$ systems. The $Medium_{LFP}$ system does not show a clear temperature dependence and has no data for high temperatures. In terms of aging, no clear trends can be identified in temperature dependence, which the DCR gradients visualize in Figure 6-7 (bottom right).

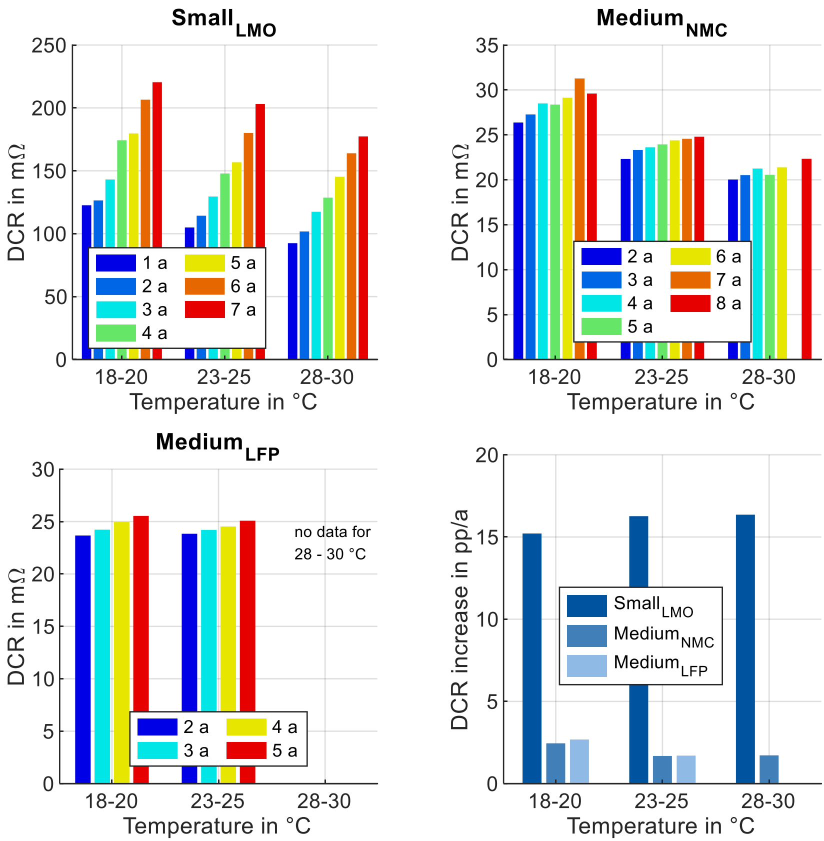

Figure 6-7: Temperature-dependent DCR development for exemplary and $Small_{LMO}$, $Medium_{NMC}$, and $Medium_{LFP}$ systems, plus the average annual DCR increase in percentage points. SOC range is 40 % to 60 %. The DCR values are calculated on system level as the cell-level DCR values are different, too. The legend contains information about the system age. Note that the $Small_{LMO}$ system is not the same as in Figure 6-6 because the temperature range was too narrow.

All systems – SOC dependence. In the following, only the SOC dependence is further investigated, as no difference in aging based on the temperature could be identified. Applying the presented methodology to all systems, Figure 6-8 depicts the gradients of the linear DCR trends for low, medium, and high SOC ranges. It shows the increase in percentage points per year (left) and per 100 EFC (right).

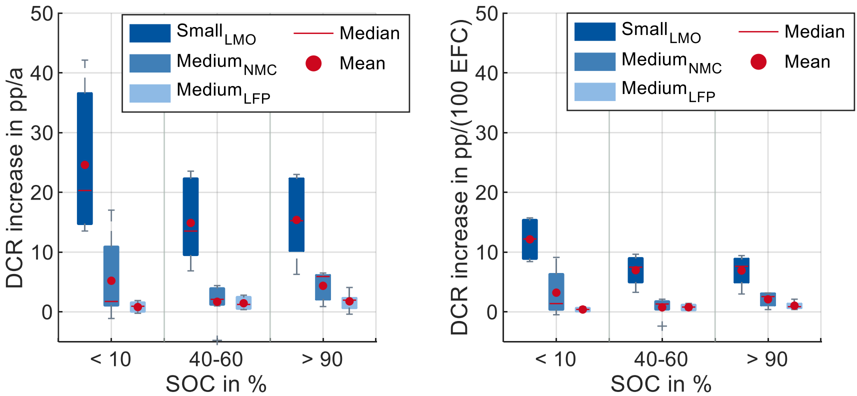

Figure 6-8: Gradients of DCR increase. The Small$_{LMO}$ systems show significantly larger DCR increases than the medium systems. Although a mean increase of about 20 pp/a would lead to an EOL after five years, the increase in DCR results only in a minor increase in energy fade (see Figure 5-20).

The systems show different DCR developments. The Small$_{LMO}$ systems have the same DCR development as the exemplary system discussed above, with higher DCR increases for lower SOCs. While the mean gradient is 24.6 pp/a for an SOC below 10 %, the mean values are around 15 pp/a for the SOC ranges of 40 % to 60 % and above 90 %. The Medium$_{NMC}$ HSSs show increased aging both for low (mean 5.2 pp/a) and high SOCs (mean 4.4 pp/a), while the aging is less for medium SOCs (1.7 pp/a). The Medium$_{LFP}$ HSSs show only small mean DCR increases from 0.8 pp/a to 1.8 pp/a with higher gradients for higher SOCs. Single negative values for the Medium$_{LFP}$ and Medium$_{NMC}$ systems can be attributed to poor data availability for the combinations of different SOC and temperature ranges for some systems, as the temperature varies between systems.

The DCR development per 100 EFC shows the same qualitative course as discussed for the annual gradients. The mean increases reach from 6.9 pp/(100 EFC) to 12.1 pp/(100 EFC) for Small$_{LMO}$ systems, from 0.8 pp/(100 EFC) to 2.1 pp/(100 EFC) for Medium$_{NMC}$ systems, and from 0.4 pp/(100 EFC) to 1.0 pp/(100 EFC) for Medium$_{LFP}$.

Influence on energy fade. If the EOL criterion of the SOH related to the internal resistance is applied, HSSs would be considered warranty cases after a doubling in internal resistance (see Chapter 2.2.2). Single Small$_{LMO}$ systems would reach their EOL according to this definition after two to three years when the HSSs with the highest increases are considered. However, the observed decrease in usable energy is only slightly higher than the value for the decrease in usable capacity (see Figure 5-20). This indicates that the strong decrease in usable energy from Chapter 5 is mainly driven by capacity fade. In general, an increased DCR leads to two types of energy decrease. These types are the efficiency losses during operation with current flow and the unusable energy due to an earlier reach of the EOD voltage (during discharge) or the EOC voltage (during charge). Figure 6-9 illustrates the DCR influence on the energy and capacity fade for a discharge scenario showing two discharge curves with a high and a low DCR, respectively.

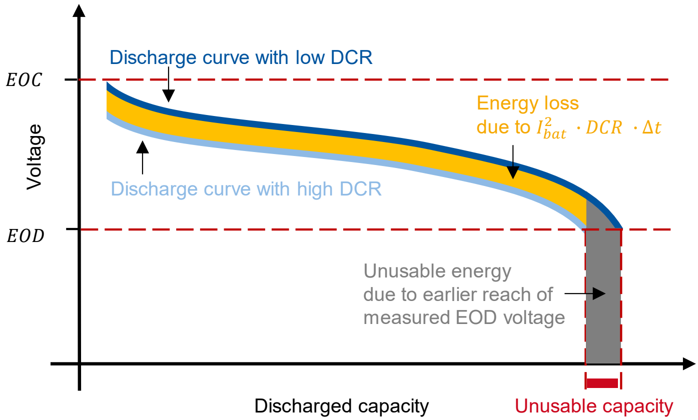

Figure 6-9: Energy and capacity losses due to an increase in DCR. The orange energy losses occur during current flow. The grey energy losses and the red capacity losses occur due to an earlier reach of the EOD voltage.

Efficiency losses. Assume the initial DCR of the Small$_{LMO}$ system to be 120 mΩ. An increase of 20 pp/a would lead to a DCR of 288 mΩ after seven years. The maximum system current $I_{bat,max}$ of this HSS is around 12 A, representing a C-rate of nearly 1 C and a discharge duration Δt of around 1 h. Equation (6-4) presents the calculation of losses for field capacity tests according to Chapter 5 with the initial DCR ($DCR_{initial}$) and the one after seven years (DCR_{7a}).

$$E_{loss,initial} = {I_{bat,max}}^2 \cdot DCR_{initial} \cdot \Delta t = (12\ A)^2 \cdot 120\ \text{m}\Omega \cdot 1\ \text{h} \approx 17\ \text{Wh}$$

$$Share_{E,loss,initial} = \frac{E_{loss,initial}}{E_{bat}} = \frac{17\ \text{Wh}}{2200\ Wh} \approx 0.8\ \%$$

(6-4)

$$E_{loss,7a} = {I_{bat,max}}^2 \cdot DCR_{7a} \cdot \Delta t = (12\ A)^2 \cdot 288\ \text{m}\Omega \cdot 1\ \text{h} \approx 41\ \text{Wh}$$

$$Share_{E,loss,7a} = \frac{E_{loss,7a}}{E_{bat}} = \frac{41\ \text{Wh}}{2200\ Wh} \approx 1.9\ \%$$

More than a doubling in losses ($E_{loss,7a}$) is still less than two percent of the battery energy E_{bat} in the chosen extreme scenario. The average C-rate in operation is only a fraction of its maximum value (see Figure 4-3). Compared to a capacity decrease of up to 20 % during the same period, the DCR-based operational losses do not have a major impact on the energy fade.

Unusable energy due to EOD voltage. The higher overvoltage due to an increased DCR leads to an earlier reach of the EOD voltage. Thus, the BMS terminates the discharge earlier and the discharged energy and capacity are lower compared to a battery with a lower DCR. This effect is stronger if the current toward the EOD voltage is higher. While some HSSs reduce their currents at lower SOCs, other end the discharge abrupt (see Chapter 5.3.1). However, even in case of a field capacity test with the maximum current $I_{bat,max}$, the difference between the initial overvoltage ($V_{over,initial}$) and the overvoltage after seven years ($V_{over,7a}$) is 2 V for the whole system (see Equation (6-5)). This corresponds to a cell overvoltage $V_{over,diff,cell}$ of around 50 mV. Toward the EOD voltage, the OCV curve is already in steeper decline, see Figure 2-2, and shows a gradient of around 20 mV/(% SOC), see Figure 7-9, leading to a maximum unusable SOC range ($C_{unused,DCR}$) of maximum 2.5 %. Nevertheless, the Small$_{LMO}$ systems show a current derating toward the EOD voltage and the average C-rates in operation are low. Thus, the effect is below the calculated maximum value.

$$V_{over,initial} = I_{bat,max} \cdot DCR_{\,initial} = 12\,A \cdot 120\ \mathrm{m\Omega} \approx 1.44\ \mathrm{V}$$

$$V_{over,7a} = I_{bat,max} \cdot DCR_{\,7a} = 12\,A \cdot 288\ \mathrm{m\Omega} \approx 3.46\ \mathrm{V}$$

$$V_{over,diff,cell} = \frac{V_{over,7a} - V_{over,initial}}{N_{cells\ in\ series}} = \frac{2.02\ \mathrm{V}}{40} \approx 50\ mV \tag{6-5}$$

$$C_{unused,DCR} = \frac{V_{over,diff,cell}}{DV_{EOD}} = \frac{50\ mV}{20\,\frac{mV}{\%\,SOC}} \approx 2.5\ \%\ SOC$$

To draw a conclusion, the resulting capacity and energy losses due to an increase in DCR seem neglectable even in extreme cases compared to the observed capacity fade of around 20 %.

6.3.2 Slow diffusion voltage

This chapter presents the characteristics of the slow diffusion voltage (SDV) divided into short-term and long-term influence factors.

6.3.2.1 Short-term influence factors

The analyzed short-term influence factors include the current and charge throughput before the relaxation, relaxation OCV, and temperature, as identified in the literature (see Chapter 6.1). To analyze these factors, only relaxations within one year are taken into account to minimize the effect of aging. Each influencing factor was analyzed while holding the others in comparable ranges. The HSSs behave differently for some of the analyzed short-term influencing factors. Therefore, this chapter presents only findings observed for most of the systems.

Figure 6-10 presents the short-term effects on the SDV after discharge observed for an exemplary $Small_{HSS}$. The visualization depicts the data downsized to a one-minute resolution and smoothed using a moving average technique to reduce measurement noise. The analysis shows the relaxation voltage over time, with the color indicating different short-term influencing factors.

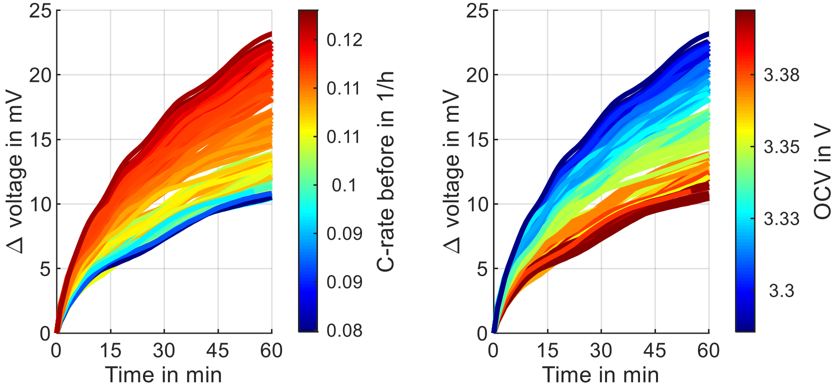

Figure 6-10: Short-term influence factors on relaxation voltage after discharge of an exemplary $Small_{LMO}$ system. **Left**: Relaxation voltage as a function of the C-rate (year 2018, values before relaxation: temperature between 20 °C and 22 °C, charge throughput > 80 % battery capacity). **Right**: Relaxation voltage as a function of the relaxation OCV (year 2018, values before relaxation: temperature between 20 °C and 22 °C, charge throughput > 80 % of usable capacity, C-rate < 1/6 C).

C-rate. A clear positive correlation exists between the C-rate on the SDV after discharging with a higher current, leading to higher overvoltage. A similar, albeit less pronounced, effect can also be observed for relaxations after charging. This suggests that as the current before relaxation increases, the voltage change during the relaxation phase also increases for nearly all systems. This result aligns with findings in literature [65].

OCV. Considering the relaxation OCV, a negative correlation is evident between the SDV and increasing voltage for relaxations after discharging with a lower OCV, leading to a higher overvoltage. This effect is probably attributable to the steep OCV curve of LMO and NMC in these OCV ranges, where the battery cell is at its electrochemical edges (see Figure 2-2). After charging, this effect cannot be confirmed for relaxations at high OCV values.

Charge throughput before relaxation. The charge throughput appears to exert a minor influence on the relaxation course, particularly concerning the time constants and the magnitude of the voltage change.

Temperature. The HSSs experience comparatively constant operational temperatures as they are mainly installed in houses, and the C-rates are not very high (see Chapter 4.2.2). Within the range of 20 °C and 30 °C, the temperature seems to have only a minor influence on the SDV, as further analysis reveals.

6.3.2.2 Long-term influence factors

Single system. Figure 6-11 shows the development of an exemplary Small$_{LMO}$ system's overvoltage relaxation after charge to EOC voltage and discharge to EOD voltage.

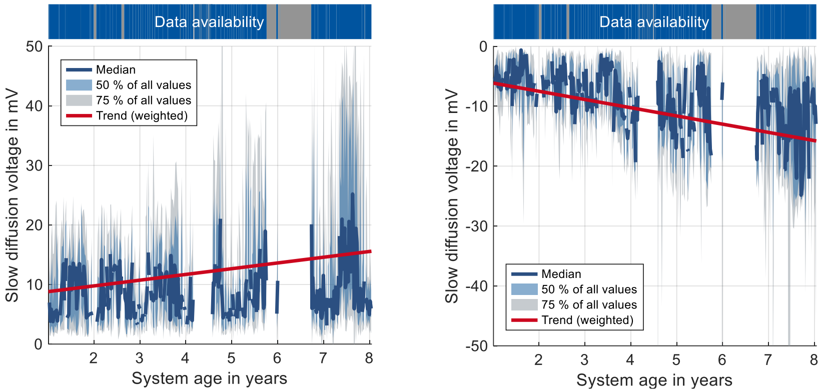

Figure 6-11: Increasing SDV (V_{slow}) over different years for EOC relaxations (left) and EOD relaxations (right) for an exemplary Small$_{LMO}$ HSS (cell level). The SDV increases after charge and decreases after discharge, meaning that overvoltage increases for both events.

The magnitude of the SDV increases for both EOC and EOD relaxations. For EOC relaxations, this corresponds to a positive increase. For EOD relaxations, this corresponds to a negative increase due to the decay behavior of the exponential functions (see Chapter 5.2.2). The values partly cover a large range because of the short-term influencing factors. However, target-oriented filtering of these factors is difficult due to the high sensitivity of some short-term factors that would reduce the data basis strongly. Therefore, the entire period is used to calculate a linear trend. The gradient of the SDV after charging corresponds to about 1 mV/a and that after discharging to about -1.4 mV/a, which means that more change is detected during EOD relaxation. It must be considered that the EOD voltage of the system shown was continuously lowered between year one and year five. Thus, the adjustment of control strategies can influence such analysis. However, even with the constant EOD voltage, there is a further decrease from year five onward. The EOC voltage was constant over the entire period, and its change can possibly be attributed to aging.

All systems. Figure 6-12 depicts the results obtained after applying the methodology to all systems. In addition, it depicts the time constants of the second RC element of the battery model (see Figure 5-5). Except for the EOC relaxation of Medium$_{LFP}$ systems, the results for SDV are close for each single system type but show differences between them.

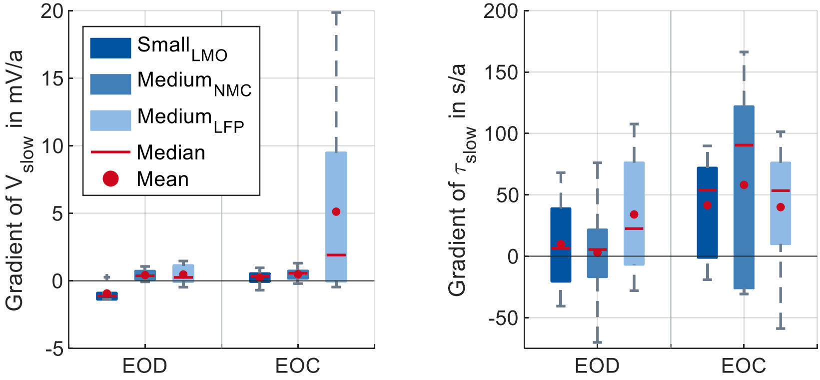

Figure 6-12: Annual gradients of the SDV (left, parameter V_{slow}) and the time constant (right, parameter τ_{slow}) with increasing system age.

While the Small$_{LMO}$ systems show increased overvoltage over time in the EOD relaxation except for one system (symbolized by a mean negative gradient of -0.9 mV/a, see Figure 6-11), the Medium$_{NMC}$ and the Medium$_{LFP}$ systems are rather at low positive mean values of 0.42 mV/a (Medium$_{NMC}$) and 0.47 mV/a (Medium$_{LFP}$). All system types show positive mean gradients for EOC relaxation, although individual HSSs show negative gradients. For EOC voltage, the positive gradients correspond to an increase in overvoltage and may, therefore, indicate aging processes. While the gradients for the Small$_{LMO}$ systems with 0.24 mV/a and the Medium$_{NMC}$ systems with 0.48 mV/a symbolize a moderate increase, the Medium$_{LFP}$ systems with a mean gradient of 5.1 mV/a show significantly higher increases. This may be due to some systems exhibiting slightly increased EOC relaxation voltages with time and the voltage curve in this region being relatively steep and electrochemically close to full charge.

Regarding time constants, the system types consistently show positive mean gradients for both EOD and EOC relaxation. The mean increases of the EOC time constant of 42 s/a (Small$_{LMO}$), 58 s/a (Medium$_{NMC}$), and 40 s/a (Medium$_{LFP}$) are above the values for the EOD relaxation. Here, the values for Small$_{LMO}$ with 10 s/a are only a quarter, and for Medium$_{NMC}$ with 3 s/a, they are almost 20 times less than their EOC values. In contrast, the Medium$_{LFP}$ values with 34 s/a correspond to a similar order of magnitude. The results of increasing overvoltage and increasing time constants, especially at high states of charge, are consistent with the literature [41] and can be used to indicate aging.

6.3.3 Linking relaxation parameters to capacity fade

Principal component analysis. The PCA is conducted to investigate if the relaxation parameters obtained from the battery model in 5.2.2 contain information about the capacity-related SOH_{UC}. Figure 6-13 depicts the PCA results of the EOD relaxations for an exemplary $Small_{LMO}$ system.

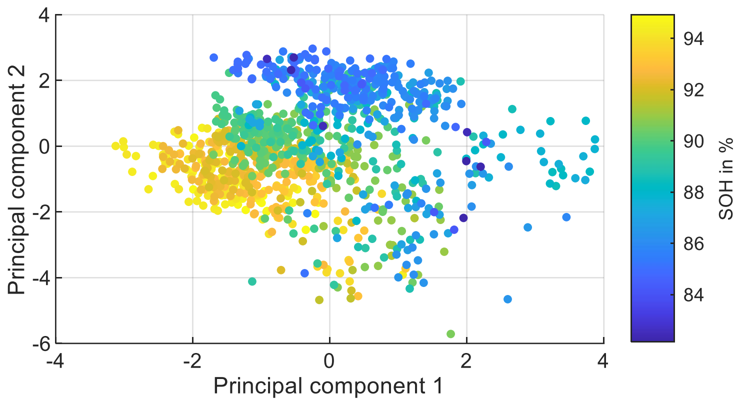

Figure 6-13: SOH_{UC} dependence on the principal components for EOD relaxations of an exemplary $Small_{LMO}$ HSS. The clustering of similar SOH_{UC} values shows that the relaxation components contain significant information on the capacity-related SOH_{UC}. There are single points outside of the shown axis range that are considered outliers.

The reduction analysis utilizes the initial two principal components to portray the 10-dimensional data in a 2-D representation. The resulting PCA plot reveals a notable clustering of similar SOH_{UC} values in proximity, affirming that the first two principal components contain essential information regarding the SOH_{UC} of the systems. The clustered SOH_{UC} values show an increasing trend for lower values of principal components one and two.

Figure 6-14 (left) depicts a scree plot of the conducted PCA. It quantifies how much of the data variance can be explained by using different numbers of principal components. Two principal components can explain around 50 % of the variance in this case. This suggests that the SOH_{UC} information in the complete dataset is likely even more significant. Figure 6-14 (right) shows the biplot of the conducted PCA. It illustrates the relationship of the analyzed parameters in the two-dimensional space obtained through the PCA. The larger the parameter vectors, the higher their influences on the PCA are. The smaller the angle between the vectors, the higher their correlation is.

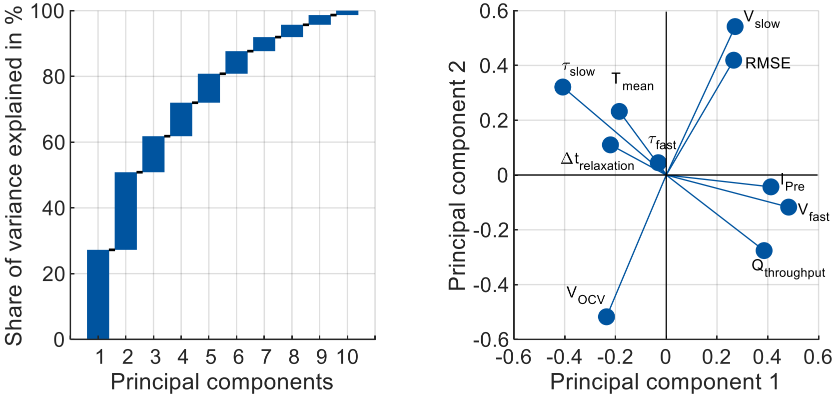

Figure 6-14: **Left:** Scree plot of PCA for relaxation dataset, explaining the variance through the number of principal components. **Right:** Biplot of PCA for relaxation dataset, explaining the importance (length) and correlation (angle) of the input parameters. The biplot function normalizes the principal components.

Capacity-related SOH_{UC} estimation. Figure 6-15 depicts the results of the machine learning models. The red and blue lines show the results of the linear regression and neural regression network, respectively.

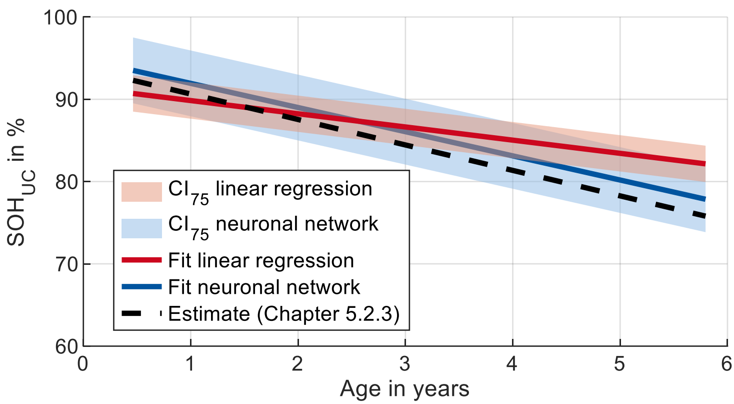

Figure 6-15: SOH estimation using EOD relaxation data for one exemplary $Small_{LMO}$ HSS. The predicted SOH_{UC} values correlate with the observed capacity fade. The neural network has a higher accuracy than the linear regression model, estimating similar SOH values as obtained in Chapter 5.

Both machine learning models exhibit fluctuations in their SOH_{UC} estimations, which are symbolized by the 75 % confidence interval (CI_{75}). The linear regression model has a confidence interval width of approximately 4.5 pp, while the neural regression network shows around 8 pp. Despite these higher fluctuations, the neural regression network yields estimations that closely align with the linear fit derived from the usable capacity estimation from Chapter 5.2.3, surpassing the precision of the linear regression results. This enhancement can be attributed to the neural regression network's superior expressive capacity compared to linear regression. Thus, the neural network demonstrates a better ability to represent and generalize the SOH_{UC} information of the relaxation dataset. Nevertheless, the linear regression boasts smaller fluctuations, rendering it suitable even when limited relaxation data is available. Although the small sample size does not allow for valid general conclusions, it seems like the presented approach could have the potential for a larger number of systems, and simple machine learning models may hold potential for estimating the capacity-based SOH_{UC} of similar systems solely based on relaxation data.

6.4 Conclusion

This chapter analyzed the second criterion to determine the SOH of a battery, the internal resistance.

Direct current resistance. The measurements allow for the calculation of the DCR using the voltage response to a current pulse. This DCR is sensitive to both temperature and SOC. The results vary significantly between the systems. $Small_{LMO}$ systems show high mean DCR increases of 24.6 pp/a for SOCs below 10 % and 15.4 pp/a for high SOCs above 90 %. $Medium_{NMC}$ and $Medium_{LFP}$ systems show smaller DCR increases. While $Medium_{NMC}$ HSSs have a mean DCR increase of 5.2 pp/a for low SOC values, the mean DCR increase for high SOCs is 4.4 pp/a. The gradients for $Medium_{LFP}$ systems are the lowest, with 0.8 pp/a for low SOC values and 1.8 pp/a for high SOC values. Despite the strong increase in DCRs for $Small_{LMO}$ systems, the energy fade can still mainly be attributed to the capacity fade. The DCRs are still relatively low, leading to little losses, especially due to the low C-rates during operation. The method is robust as many values can be computed during operation.

Slow diffusion voltage. The SDV shows higher overvoltage with increasing age for most of the systems. Especially for EOC relaxations, higher overvoltage indicates battery aging, according to literature. In line with this development, the time constants of the relaxation phases increase. When analyzing short periods of relaxation behavior, the short-term influence factors must be considered carefully, as especially the C-rate and the edge SOC ranges show highly increased sensitivity to changing values.

SOH_{UC} estimation. As the relaxation parameters change with system age, machine learning models can link information about the relaxation components to the capacity-related SOH_{UC}. A case study on the $Small_{LMO}$ HSSs demonstrates that the SOH_{UC} can be estimated by a neural regression network. Yet, many systems are needed to confirm the observations for the small sample size.

7 Degradation mode estimation

This chapter investigates the underlying degradation modes responsible for the capacity fade (Chapter 5) and the increase in internal resistance (Chapter 6). It presents an innovative method to recreate the qOCV curves from field operation. In addition, it transfers the methods of incremental capacity analysis and differential voltage analysis to system-level field data. The chapter is based on and contains identical parts of [280] under the lead of the author.

7.1 Overview

A battery's OCV curve describes the relation between SOC and cell voltage at an open circuit (see Chapter 2.2.3). It enables deducing the SOC from the OCV and vice versa and is therefore often used as a simple method to estimate the SOC [86,299,300]. The OCV curve is a characteristic of the active material in both anode and cathode, the cell balancing, and the temperature [198,301]. As active material and balancing degrade over the battery lifetime, the OCV curve changes. Tracking the OCV curve is a widespread approach to gaining insights into aging modes [48,302].

OCV types. Measuring the OCV requires the battery to be in a relaxed state, excluding all influence of kinetic overvoltage on the measured battery voltage. Hence, it cannot be measured directly during operation. Two standard techniques to determine OCV curves are low current and incremental OCV measurements [303]. With the focus on investigating the changes in the OCV curves, most researchers use the low current OCV tests, where the cell voltages are measured at low C-rates down to C/20 [51–56]. Both approaches require high measuring precision and controlled temperature conditions and, thus, are usually conducted under laboratory conditions. The curves approximated in that way are called quasi-OCV (qOCV) curves. Other publications use higher C-rates, some of which intend to mimic real-life scenarios, at C-rates between C/3 and 1C [89,206,304–309]. The impact of the C-rate on these measurements is investigated in [303] and [310]. Instead of monitoring aging cells repeatedly by these measurements, the development of OCV curves for artificial scenarios can be simulated using models based on initial open circuit potentials (OCP) measurements of the electrodes, as shown in [48] and [311].

OCV analysis. Leveraging the power of OCV-curve tracking to analyze field data would improve SOH estimation and prediction of battery systems by transferring the detailed knowledge gained in laboratory tests. Only a few publications exist to this date discussing the creation of OCV curves directly from monitoring field operation. In [312], EV driving voltage data is transformed into an OCV curve by selecting voltage measurements at low current rates (< C/20) and mapping them to an SOC. The resulting curve, however, does not show the level of detail required for in-depth aging analysis and is exclusively used for battery modelling. EV charging data can also be used to create incremental capacity (IC) curves directly, representing the derivative of OCV curves concerning voltage [227]. The authors create one curve per charging phase and then use it to estimate the battery's capacity development and SOH. Other publications present concepts to create OCV curves from field data without applying actual field data. They use partial charging data at varying C-rates representing a realistic charging process to reconstruct the OCV curve using a battery model [58,313] or neural network [59]. In [314,315], the OCV curve is reconstructed by determining the length of individual voltage plateaus in the curve from normal charging or discharging processes. One of the main challenges to overcome when recreating OCV curves from field data is the high noise level in these measurements, which is often filtered using Gaussian filtering [55]. The impact of noise and different approaches to reduce its influence on these measurements are presented in [316].

Once the battery OCV curves are available over the lifetime of an aging battery, their development can be analyzed directly or by applying the incremental capacity analysis (ICA) or the differential voltage analysis (DVA).

Incremental capacity analysis. The ICA is a method to investigate the derivation of the OCV curve, which contains information about the electrochemical properties of the materials and can be analyzed during aging to obtain information about their changes [275,304]. By differentiating the capacity toward the voltage, voltage plateaus of the OCV curve are translated into clearly identifiable peaks in the IC curve [275,304]. The development of the intensity and position of these peaks contain information regarding the battery's aging and the underlying degradation modes [87,275,305]. The IC curve is determined as the deviation of the charge concerning the voltage [55,275]. Since the OCV curve is often only available as discrete values, the IC curve is usually computed as the gradient using Equation (7-1) [281].

$$\frac{\mathrm{dQ}}{\mathrm{dV}} \approx \frac{\Delta \mathrm{Q}}{\Delta \mathrm{V}} \tag{7-1}$$

Differential voltage analysis. The DVA can be used to investigate the utilization and balancing between the electrodes [70]. Here, the OCV curve is differentiated concerning SOC using the gradient function in Equation (7-2) [281]. Peaks in the differential voltage (DV) curve represent transitions between voltage plateaus in the OCV, and their positions can be used to investigate cathode and anode degradation separately, as well as shifts in the electrode balancing [70,317].

$$\frac{\mathrm{dV}}{\mathrm{dQ}} \approx \frac{\Delta \mathrm{V}}{\Delta \mathrm{Q}} \tag{7-2}$$

Degradation modes. The three commonly investigated degradation modes (DMs) across the presented literature are loss of lithium inventory (LLI) and loss of active material of both the anode and cathode (LAM_{NE} and LAM_{PE}, respectively) [275]. In the case of blended cathodes, the losses of the different active materials must be investigated individually [275]. In [48] (laboratory data) and [314]

(EV charging data), battery models based on initial half-cell measurements are fitted to the measured OCV curves, quantifying the number of different DMs inside the battery. Many publications use ICA for aging analyses, with [89,227,310,316,318–322] focusing on SOH estimation and [54,56,87,219,304–307,311,323–326] using it as a method to identify DMs in varying scenarios. Publications using DVA generally investigate electrode degradation and changes in electrode balancing [51,53,317,327–330]. Since ICA and DVA allow varying insights into battery aging, they can also be combined to gather additional information about DMs, as done in [52,55,206,309,331,332].

Features of interest. A recent addition to these methods is investigating varying features of interest (FOIs) within the characteristic IC and DV curves and their correlations with individual DMs. In the case of ICA, FOIs usually are the location or intensity of specific features like minima or maxima [275]. In the case of DVA, the distances between different characteristic peaks are usually used as FOIs. Their choice depends on the technology of the investigated battery, which strongly influences the shape of IC and DV curves [331]. Exemplary studies examining such correlations of several FOIs in both the IC and DV curves of different battery chemistries can be found in [275,331]. Appendix, Table 9-6, contains selected literature on ICA and DVA topics.

Scientific contribution. While many publications focus on ICA, DVA, and the way DMs can be quantified using them, these findings have not yet been applied to actual field data to the best of the author's knowledge. Two comparable and recent publications at the time of writing are presented by Dubarry et al. in [333] and their extended analysis [334]. In their studies, they apply ICA to synthetic data of HSS, identify clear sky conditions as suitable for the analysis of charging curves, and state that there is a lack of field data [333]. With up to eight years of operational data of HSS in private homes at a high resolution of one second, this work contributes to recreating the OCV curve from real-world field data [184,185]. The method developed helps to gain insights into the battery aging of HSSs in field operation by applying laboratory-proven knowledge to field data analytics. It can be used by BSS operators, battery analytic companies, and researchers to analyze problems of battery aging in real-world applications using existing field data.

Future prediction possibilities. Battery aging is non-linear and complex (see Chapter 2.2.4). The identified aging modes could serve as a basis for knee-point prediction, one of the most crucial challenges in battery diagnostics [84]. In addition, the aging modes can possibly be used to calculate how close a cell is to lithium plating. This is another major challenge in safety and lifetime predictions.

7.2 Methodology

The methodology of this work is displayed in Figure 7-1. Based on the SOC estimation from Chapter 5 and the internal resistance estimation in Chapter 6, the OCV curves are reconstructed from the field data using several filters and voltage correction. The obtained qOCV curves are analyzed and used for both ICA and DVA to determine the occurring degradation modes. This is validated by literature and the field capacity tests.

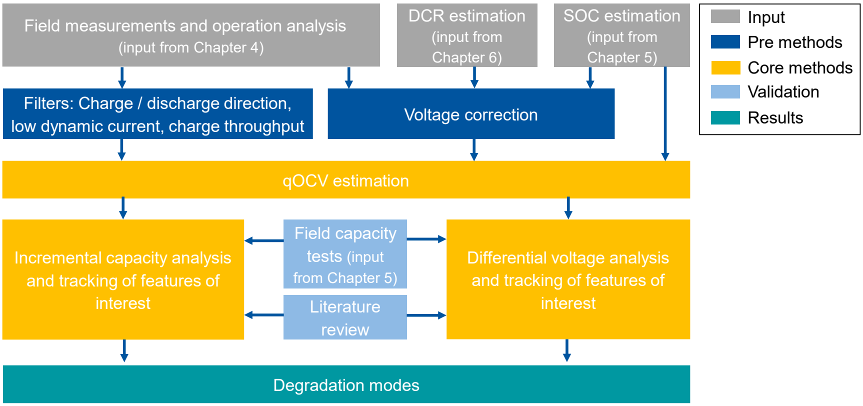

Figure 7-1: Structure of Chapter 7 to estimate the qOCV curve and identify the degradation modes through the incremental capacity analysis and the differential voltage analysis.

7.2.1 Derivation of the qOCV curves

The algorithm used in this work to derive qOCV curves from field data is based on detecting low dynamic dis-/charging phases. The voltage and SOC course can be combined during these phases, resulting in a partial qOCV curve. These single phases can then be combined to form a complete qOCV curve. In the following, the individual steps of the algorithm will be presented in detail.

Charge / discharge filter. The qOCV curves are created both for charge and discharge direction. Following the definition in Chapter 4, a charge phase is identified by finding periods during which the current sign is strictly positive. In contrast, the discharge phase current needs to be strictly negative.

Charge throughput filter. The charge throughput filter reduces the charge and discharge phases to those containing voltage information over a predefined minimum SOC range. The SOC range covered by an individual phase is determined by the absolute difference in SOC from the beginning of the phase to the end of the phase. The limit is set to a percentage value of 5 % of the battery capacity, resulting in an individual absolute limit for each battery depending on its size.

Overvoltage correction. For the overvoltage correction, the internal resistance from Chapter 6 is used. Figure 7-2, left, shows an exemplary voltage correction according to Equation (7-3). The voltage correction is not perfect, but it leads to smoother voltage courses. Many overlaying discharging phases and a subsequent Gaussian filter further smooth the obtained OCV curve.

$$V_{\text{corrected}}(\text{SOC},\text{T}) = V_{bat}(t) - \text{I}_{bat}(\text{t}) \cdot \text{DCR}(\text{SOC},\text{T}) \tag{7-3}$$

Dynamics filter. The overvoltage correction does not work perfectly for all possible operational behavior. A dynamics filter is implemented to avoid ripples in the qOCV curve caused by high-dynamic operation (see Figure 7-2, right). The dynamic is the absolute short-term change in current, which can be directly determined from the measurement data. By setting an upper limit of 10 % of the C-rate to this dynamic, the data can be reduced to periods consisting of low-dynamic data only. These periods can then be separated into charge and discharging phases.

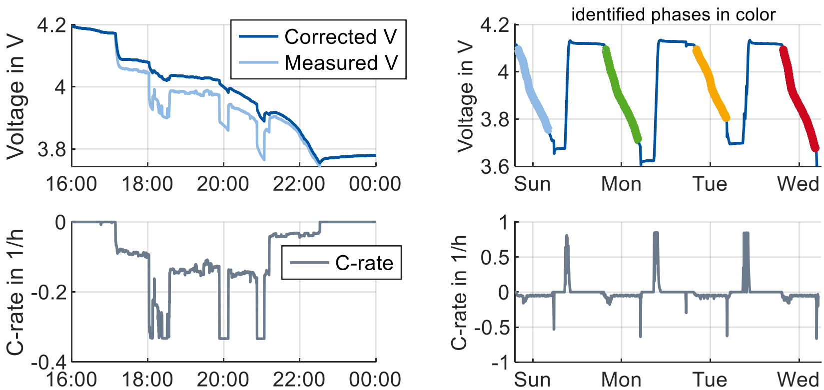

Figure 7-2: **Left:** Exemplary overvoltage correction (top) for the shown current profile (bottom). The corrected voltage is quite smooth, especially for low-dynamic phases. **Right:** Identified low-dynamic current phases represent partial qOCV curves.

7.2.1.1 Creating partial qOCV curves

A detected low-dynamic phase represents a partial qOCV curve on its own if the corrected voltage is plotted against the SOC. Combining many of these partial qOCV curves leads to an overall qOCV curve for the whole cell, which can be updated continuously. Figure 7-3 (left) visualizes this process for a limited number of exemplary discharge phases. Sometimes, SOC errors occur, leading to a horizontal deferral of single identified phases. In this case, the SOC values are shifted horizontally to the mean value of all partial qOCV curves. This way, the voltage course is maintained as only the SOC values are adjusted.

The resulting qOCV curves from individual operational phases cover different SOC and voltage ranges. The overall qOCV curve is computed by taking the mean SOC of all available phases at small voltage steps, resulting in a high-resolution qOCV curve (see Figure 7-3 (right)). The qOCV curves are created separately from the discharging or charging phases to account for overvoltage and hysteresis effects. The actual OCV curve of the battery lies between the charge and discharge qOCV curves.

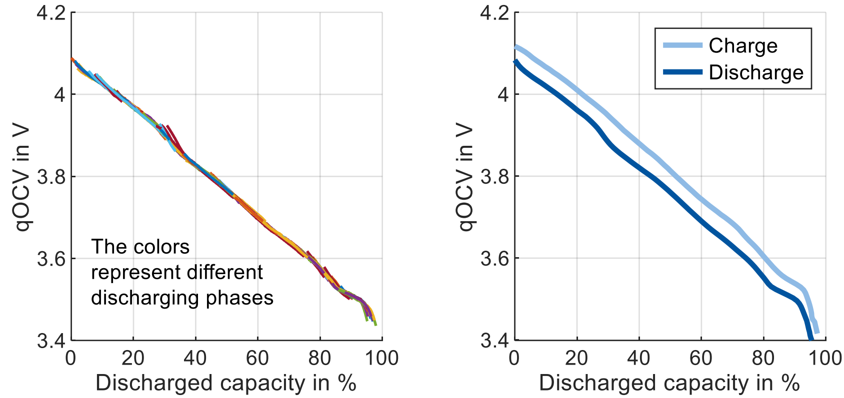

Figure 7-3: **Left:** Combination of partial qOCV curves from low-dynamic discharge current phases. Their mean is taken as the estimated qOCV curve of a specific period. **Right**: Resulting qOCV curves for charge and discharge.

The discharge phases show lower dynamics and lower C-rates (see Figure 4-3 and Figure 7-2) than the charge phases, which lead to higher-quality qOCV curves. Thus, only the discharging qOCV curves are used from here on. However, acceptable results can be obtained from the charge phases as well.

The investigations performed on the qOCV curves are focused on analyzing aging behavior. For this reason, the data is split into periods so that independent continuous qOCV curves are created for each of them. Depending on the data quality and operation of the system, a different minimum period is required to acquire enough phases to create a qOCV curve. To illustrate the methodology, the continuous qOCV curves in this work are created yearly. Note that this interval could be shorter, and sometimes, a month is enough to recreate a qOCV curve using this methodology if the analyzed HSS is cycled regularly.

7.2.2 Application of ICA and DVA

To analyze the qOCV curves' characteristics, both the incremental capacity analysis (ICA) and differential voltage analysis (DVA) are applied. The IC and DV curves are obtained by numerically differentiating the continuous qOCV curve concerning the voltage and SOC using Equation (7-1) and (7-2). Before determining the derivative, the curve is slightly smoothed using a Gaussian filter, which has been proven to be a good method according to literature [55,275]. This smoothing is required since the investigated features, such as voltage plateaus in the qOCV curve, are quite sensitive to noise and trembling [55,275]. The analyses performed on the IC and DV curves are based on various studies available in literature, depending on the battery chemistry.

7.2.3 Selection of features of interest

To determine the contribution of different DMs to battery aging, features of interest (FOIs) are selected from literature, for which a correlation between their development and specific DMs could be determined. These are then tracked by identifying the corresponding extrema in specified voltage ranges. Since different chemistries show different characteristic features in their IC and DV curves, FOIs are chosen individually for each technology. While selected ICA FOIs are mainly based on [275], DVA FOIs are selected from various sources.

LMO/NMC. The FOIs for Small$_{LMO}$ systems are marked in Figure 7-4 and based on [53,275,317,330,331,335,336].

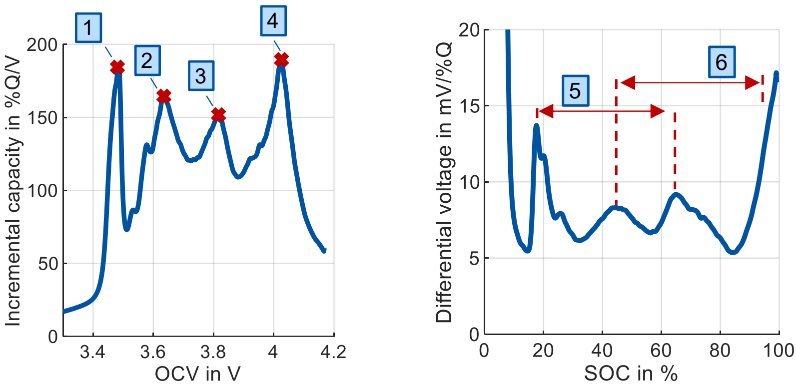

Figure 7-4: Individual FOIs for ICA (left) and DVA (right) for LMO/NMC. Figure created with data from Dubarry and Anseán [337] (used under CC BY 4.0 [23]) and inspired by Dubarry and Anseán [275]. Data smoothed with Gaussian filter. FOIs selected from literature as presented in the text.

FOI 1 tracks the first peak and shows correlations with LLI and LAM$_{PE}$ through a decrease in intensity and a shift to higher voltages [275]. FOI 2 mainly correlates with LLI but can also indicate LAM$_{NE}$ and LAM$_{PE}$ [275].

FOI 3 correlates with LLI and tends to shift to higher voltage with increasing aging [275]. FOI 4 correlates with LLI, LAM_{NE}, and LAM_{PE} and typically decreases in intensity [275]. FOI 5 and 6 mark the distances of the characteristic peaks in the DVA, where FOI 5 measures the distance of the graphite peaks [330,335,336], and FOI 6 measures the distance of a cathode feature toward the fully charged state [335,336]. A loss of anode capacity due to LAM_{NE} causes a decreasing distance in FOI 5, while LAM_{PE} reduces the distance measured by FOI 6.

NMC. Figure 7-5 shows the FOIs chosen for NMC systems based on [53,275,306,307,330].

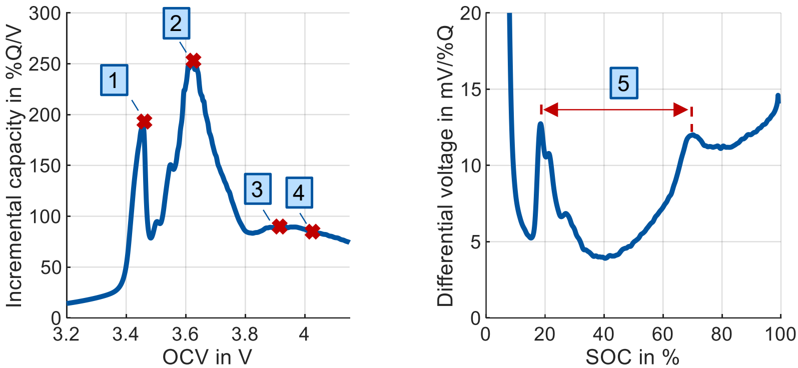

Figure 7-5: Individual FOIs ICA (left) and DVA (right) for NMC. Figure created with data from Dubarry and Anseán [337] (used under CC BY 4.0 [23]) and inspired by Dubarry and Anseán [275]. Data smoothed with Gaussian filter. FOIs selected from literature as presented in the text.

FOI 1 is the first peak in the IC, and its increase correlates with LLI [275,307]. FOI 2 tracks the main peak whose intensity decrease correlates with LLI, and LAM_{PE} [275,307]. FOI 3 can be attributed to LLI [275,306]. FOI 4 is the beginning of the falling edge and can be attributed to LLI and LAM_{PE} when decreasing [275]. The DVA is used for LAM_{NE} quantification. FOI 5 measures the distance between the two peaks at approximately 10 % and 70 % SOC [330]. Since LAM_{NE} causes a shift of the higher graphite peak toward lower voltages, it correlates negatively with FOI 5 [330].

LFP. The choice of FOIs and their correlations with DMs for LFP systems are based on [275,330,331]. Figure 7-6 shows the course of IC and DV. Typically, the area underneath LFP IC is used to analyze the degradation modes [275]. However, as the qOCV curves are not comparable to laboratory measurements, noise in the curve has a major impact on the areas obtained and did not lead to usable results.

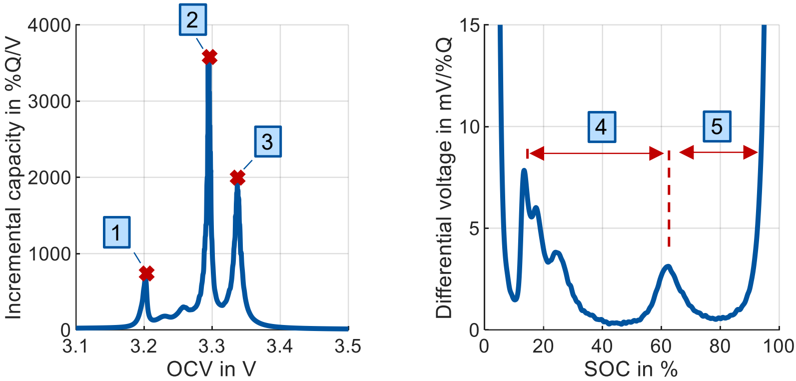

Figure 7-6: Individual FOIs (ICA and DVA) for LFP. Figure created with data from Dubarry and Anseán [337] (used under CC BY 4.0 [23]) and inspired by Dubarry and Anseán [275]. Data smoothed with Gaussian filter. FOIs selected from literature as presented in the text.

This is why the tracking of peaks is chosen instead, which is also applied in literature. FOI 1 tracks the first peak, which is sensitive to LLI and LAM_{PE} [275]. The decrease of the highest peak (FOI 2) correlates with LLI, LAM_{PE} and LAM_{NE}. [275]. FOI 3 indicates LLI by decreasing [275]. FOI 4 and FOI 5 are anode features indicating LAM_{NE} and LLI, respectively [330,331].

Correlation of FOI and SOH. The tracked change in FOI intensity, position, and distance is correlated with the SOH_{UC} values from Chapter 5 to investigate a possible relationship between capacity fade and FOI shift. In this context, the so-called “p-values” are calculated. In correlation analysis, the p-value is a statistical metric that helps assess the significance of the observed correlation coefficient between two variables [338]. It quantifies the probability of obtaining a similar correlation as the one observed in the data, assuming no true correlation exists. A low p-value of typically less than 0.05 indicates that the correlation is statistically significant, suggesting that the relationship between the variables is not due to random chance [338]. In contrast, a high p-value indicates that the observed correlation could have occurred by chance alone and is not statistically significant [338]. Thus, the p-values are used to make informed decisions about the strength and validity of correlations.

Validation through capacity tests. Appendix, Figure 9-16, shows that the conducted field capacity tests can be used to validate the obtained qOCV, IC, and DV curves. However, ICA and DVA are quite sensitive to small noise in measurement data and the qOCV curve obtained through the presented method in this chapter is considered more reliable than the field capacity tests.

7.3 Results and discussion

This chapter analyzes the degradation modes responsible for the capacity fade (Chapter 5) and the increase in internal resistance (Chapter 6). It discusses the development of the reconstructed qOCV discharge curves using ICA and DVA. After a single-system discussion, the tracked FOIs for all systems are presented. For simplification, this chapter uses qOCV discharge curves and OCV curves as synonyms.

7.3.1 Single system analysis

This chapter discusses the OCV, DVA, and ICA results of exemplary $\mathrm{Small}_{\mathrm{LMO}}$, $\mathrm{Medium}_{\mathrm{NMC}}$, and $\mathrm{Medium}_{\mathrm{LFP}}$ systems.

7.3.1.1 LMO/NMC blend

OCV. Figure 7-7 shows the OCV curves of an exemplary $\mathrm{Small}_{\mathrm{LMO}}$ system over seven years. The LMO/NMC OCV curve shows the characteristic of an approximately linear voltage increase with a steeper beginning. To illustrate the capacity fade, this chapter normalizes the charge by the nominal capacity, which is why OCV values of aged systems do not reach 100 % $\mathrm{SOC}_{\mathrm{Nominal}}$.

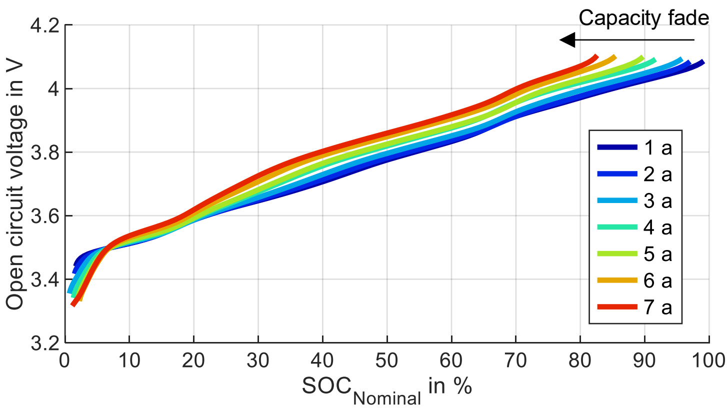

Figure 7-7: LMO/NMC OCV of an exemplary $\mathrm{Small}_{\mathrm{LMO}}$ system. Values normalized by nominal capacity. Note that the $\mathrm{Small}_{\mathrm{LMO}}$ systems lower their EOD voltage, leading to different voltage values for the same SOC.

With ongoing aging, the curves show a horizontal shift to lower SOC values as the remaining capacity decreases. The capacity fade is quantified by the difference of the SOC from year one to year seven at the EOC charge voltage of 4.15 V. This capacity decrease amounts to 17 % over the measurement period, which aligns with the results from Chapter 5.

The voltage at low SOC values decreases from about 3.4 V to 3.3 V. This effect is not due to aging and can be attributed to the decrease of EOD voltage controlled by the BMS (see Chapter 4.2.4). It leads to a slight shift of the OCV curves, showing the gain in capacity due to EOD voltage reduction.

ICA. Figure 7-8 shows the determined IC curves of the same $Small_{LMO}$ system over the monitored period.

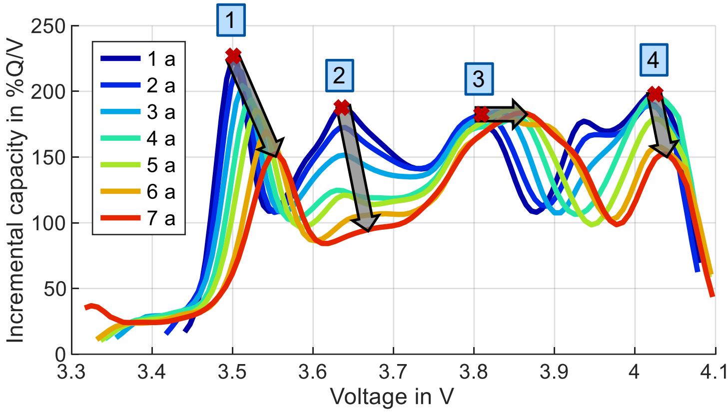

Figure 7-8: LMO/NMC ICA of an exemplary $Small_{LMO}$ system. All peaks presented in literature are observable.

FOI 1 is identifiable and shows a shift toward higher voltages from 3.5 V to 3.55 V and a decrease in intensity from 225 %Q/V to 150 %Q/V. The shift corresponds to capacity loss, indicating LLI, a rise in internal resistance, and possibly LAM_{PE} [275,323,336]. These results are in line with the analysis done in Chapter 5 and 6. The intensity of FOI 2 is declining over time, which can be attributed mainly to LLI [275,336]. FOI 3 shifts to higher voltages, confirming the occurrence of LLI and possibly indicating LAM_{NE} [275,336]. In addition, the intensity decrease of FOI 4 could support the presence of LAM_{PE} [275,336]. Overall, LLI seems to be the dominant DM based on the ICA conducted.

DVA. Figure 7-9 depicts the determined DV curves of the same $Small_{LMO}$ system. The steep rise at both ends of the DV represents the fully charged and discharged state. The LMO/NMC DV curve shows characteristic peaks resulting from the underlying electrode DVs [335,336]. The peak starting at around 65 % to 70 % SOC represents the transition from the medium to the low voltage plateau of the anode potential [335,336]. The peak at middle SOCs results from the cathode potential and allows conclusions about the cathode state [335,336].

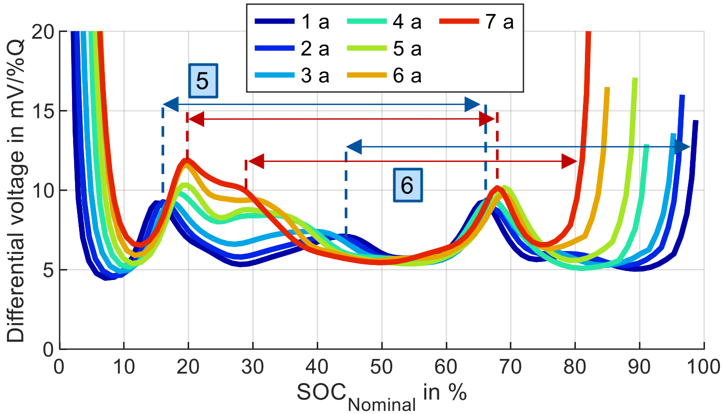

Figure 7-9: LMO/NMC DVA of an exemplary $Small_{LMO}$ system. Values normalized by nominal capacity. All peaks presented in literature are observable.

FOI 5 is the distance from the graphite peak at around 65 % to the first peak at 10 % to 20 % SOC. It is slightly reduced, indicating a decreasing storage capability of the anode in the form of LAM_{NE} [335,336]. In absolute SOC, this distance is reduced by 3.5 % SOC within the monitored period. The cathode feature, represented by FOI 6, would indicate LAM_{PE} if the distance decreased between the peak around 45 % SOC and the steep DV at the fully charged state [335,336]. However, the 45 % SOC peak changes in shape and becomes difficult to track. The assumed distance stays approximately constant and does not lead to clear findings. The capacity loss of the individual electrodes does not correspond to the loss of battery capacity since the electrodes usually have excess active material, especially on the anode side [48]. Rather, the loss of capacity can be attributed to the loss of cyclable lithium (LLI) which can be observed as a shift of the anode and cathode related DVA peaks toward each other. Overall, the DVA supports the assumption originating from the ICA that LLI is the dominant DM.

For easier FOI tracking, Figure 7-10 summarizes the results discussed above. The shown trends are computed for every HSS and discussed in Chapter 7.3.2. It shows the average change of each FOI per year relative to its initial value.

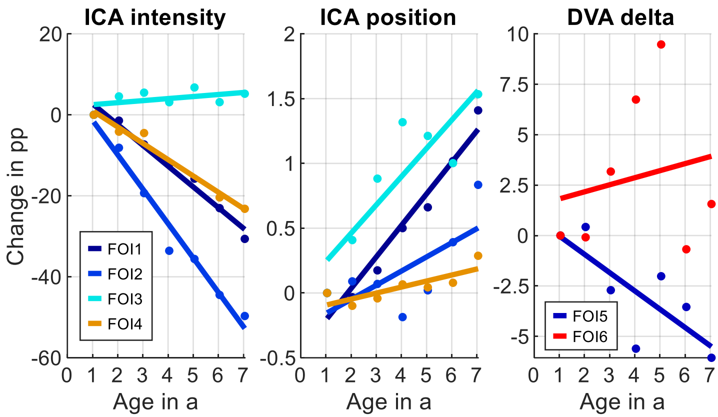

Figure 7-10: LMO/NMC FOI development of an exemplary Small$_{LMO}$ system for intensity and position of ICA and delta of DVA.

7.3.1.2 NMC

OCV. Figure 7-11 shows the OCV of an exemplary Medium$_{NMC}$ system over seven years. The NMC OCV curve has a voltage increase over its SOC range that can generally be divided into three parts. These parts have different voltage gradients (below 20 % SOC, between 20 % and 50 % SOC, and above 50 % SOC).

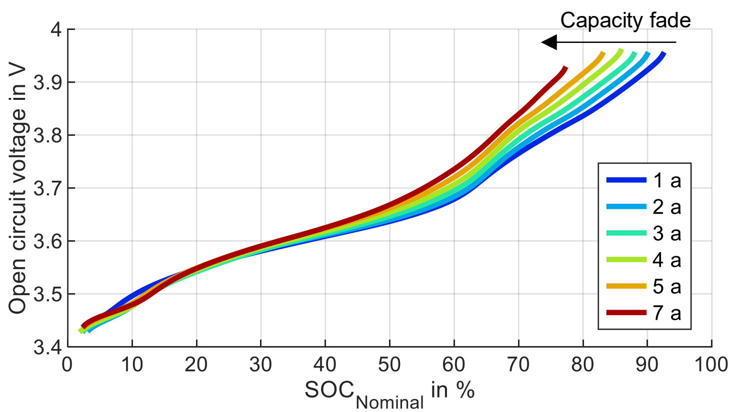

Figure 7-11: NMC OCV of an exemplary Medium$_{NMC}$ system. Year six is missing due to measurement problems. Values normalized by nominal capacity.

During aging, the capacity fade is observed by a horizontal shift of the curves toward lower SOC values. This capacity fade amounts to approximately 15 % and matches the results presented in Chapter 5. Consequently, the initial voltage slope becomes steeper, shifting the transition between parts two and three to lower SOC values. Additionally, this transition shows a change in curvature.

ICA. Figure 7-12 shows the ICA results for the same Medium$_{NMC}$ system. The NMC IC curves show the three peaks observed in literature (see Chapter 7.2.3). FOI 1 is at around 3.45 V, near the EOD voltage. The second one has a wide and high course, around 3.6 V, representing the flat area of its OCV curve at lower SOCs. The third peak can be seen at higher voltages, at more than 3.8 V.

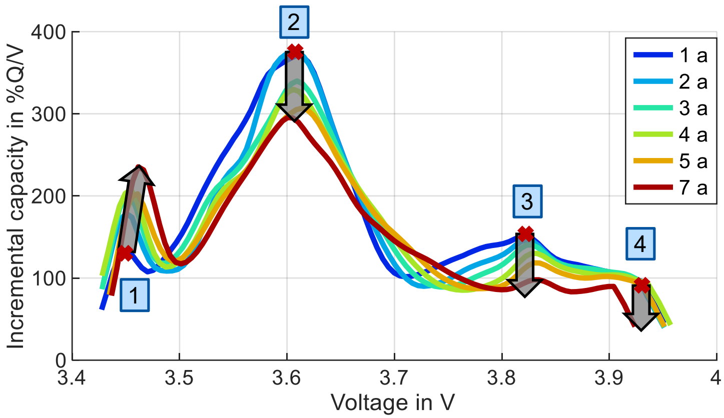

Figure 7-12: NMC ICA of an exemplary Medium$_{NMC}$ system. Year six is missing as no data is available due to measurement problems. All peaks presented in literature are observable.

FOI 1 shifts toward higher voltages (position) and higher ICs (intensity), indicating LLI [275,306]. FOI 2, the main peak, decreases in intensity from 380 %Q/V to 300 %Q/V, which supports occurring LLI [275,306,307] and could also indicate LAM$_{PE}$ [275]. The intensity decrease of FOI 3 at higher voltages supports the occurrence of LLI [275,306,307]. FOI 4 is decreasing due to occurring LLI and possibly LAM$_{PE}$ [275]. Based on the ICA, LLI is considered the dominant DM for the system.

DVA. Figure 7-13 shows the DV curves of the same NMC system. The SOC edges are represented by sharply inclining DV curves. The NMC DV consists of a large valley over a wide SOC range, with two characteristic peaks at its sides. These characteristics mainly originate from the graphite anode since the phase transition of the NMC cathode is not reached within the voltage range [70,199]. Therefore, the distance between the two characteristic peaks indicates the storage capability of the anode [70] and is defined as FOI 5. With increasing age, this distance gets smaller, indicating LAM$_{NE}$.

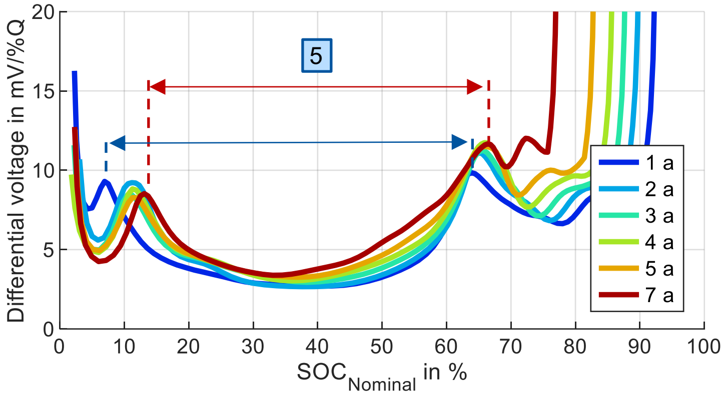

Figure 7-13: NMC DVA of an exemplary Medium$_{NMC}$ system. Year six is missing as no data is available due to measurement problems. Values normalized by assumed nominal capacity. All peaks presented in literature are observable.

Additionally, the distance of the steep rise in DV at the fully charged state of the battery to the peak at low SOCs indicates LLI [330]. As a result, the capacity decreases by 15 % absolute SOH, equal to an average capacity loss of 2.5 pp/a. Furthermore, the decreasing distance between the high edge of the DV curve and the high SOC peak reveals a shift in the electrode balancing [70].

FOIs. Figure 7-14 summarizes the development of the discussed FOIs. It shows the average change of each FOI per year relative to its initial value. The shown trends are computed for every HSS and discussed in Chapter 7.3.2.

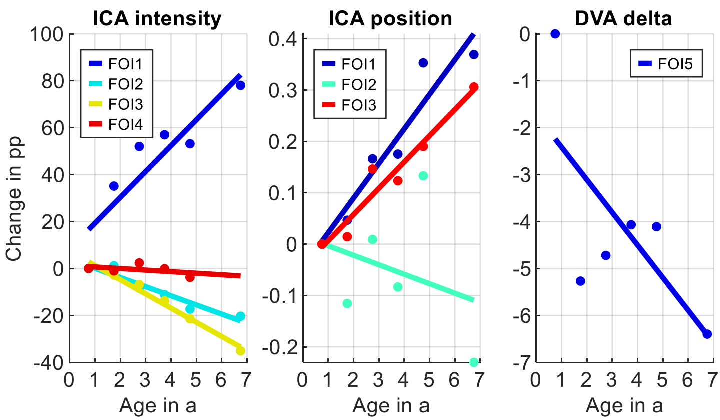

Figure 7-14: NMC FOI development of an exemplary NMC system for intensity and position of ICA and delta of DVA. The position of FOI 4 is not tracked as it is set constant according to literature.

7.3.1.3 LFP

OCV. The LFP OCV shows a flat course over most of the SOC range, with steeper voltage gradients toward the start and end.

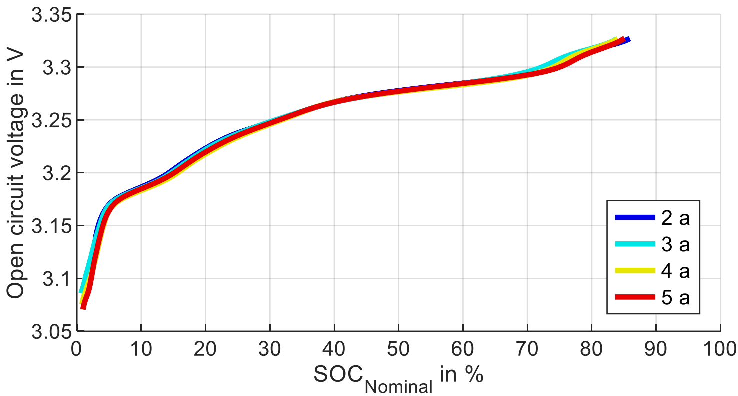

Figure 7-15: LFP OCV of an exemplary $Medium_{LFP}$ system. The measurements started one year after HSS installation and ended after four years in 2022. Values normalized by nominal capacity.

Overall, the LFP curve shows subtle changes over time. With ongoing aging, the curves slightly drop in voltage, following each other closely. Additionally, a small change in curvature can be identified at the beginning and end of the OCV.

ICA. Figure 7-16 shows the resulting ICA for the same $Medium_{LFP}$ system. The curve shows three peaks, one below 3.2 V, a large one below 3.3 V, and one above 3.3 V. FOI 1 does not show clear changes, and no conclusion can be drawn. The main peak (FOI 2) results from the large flat voltage plateau, which can be seen in the OCV curve. It possibly shows a slight decrease in intensity, which could indicate LLI, LAM_{NE}, or LAM_{PE} [331] but its change in the figure is not considered clear. FOI 3 shows a decline in intensity, which symbolizes LLI [275].

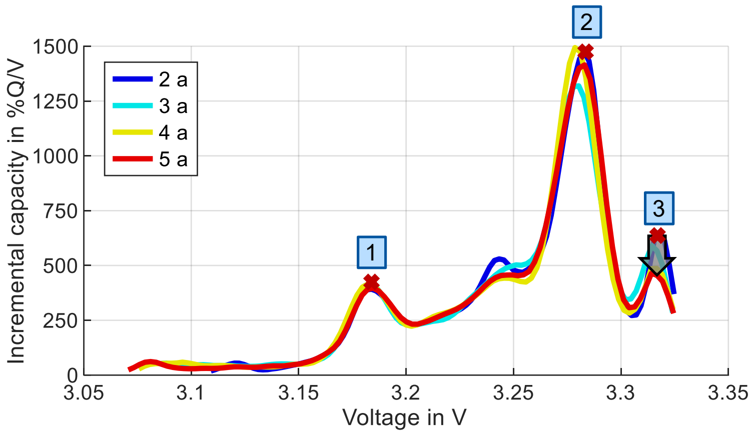

Figure 7-16: LFP ICA of an exemplary Medium$_{LFP}$ system. The measurements started one year after HSS installation and ended after four years in 2022. All peaks presented in literature are observable.

DVA. Figure 7-17 presents the DV curves obtained from the same Medium$_{LFP}$ system. It consists of two main peaks, one at lower SOC and the other at higher SOC.

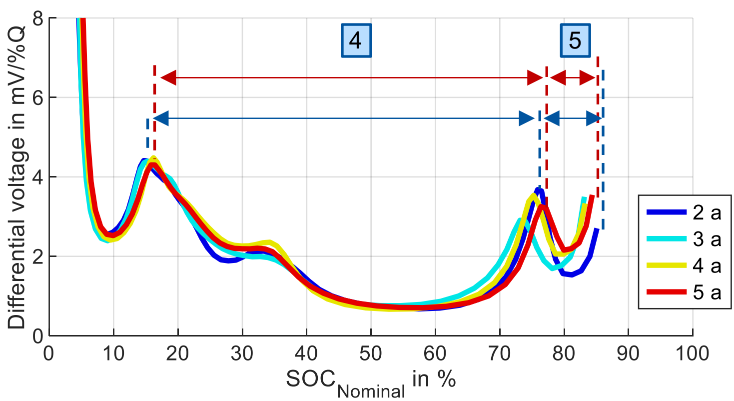

Figure 7-17: LFP DVA of an exemplary Medium$_{LFP}$ system. The measurements started one year after HSS installation and ended after four years in 2022. Values normalized by nominal capacity. All peaks presented in literature are observable.

The LFP cathode itself does not have clear features in the DV curve due to its flat open circuit potential (OCP) curve [330]. Therefore, the shape and characteristics seen in the DVA originate mainly from the graphite anode, and the distance between its characteristic peaks allows direct conclusions about its capacity content [339]. The distance of the two peaks represented by FOI 4 stays approximately constant. As reported in literature [339,340], this is a sign of little to no LAM_{NE} occurring. FOI 5 possibly indicates LLI as the peak's distance to the steep rise at the EOC voltage slightly decreases.

FOIs. Figure 7-18 summarizes the results discussed. It shows the average change of each FOI per year relative to its initial value. The shown trends are computed for every HSS and discussed in Chapter 7.3.2.

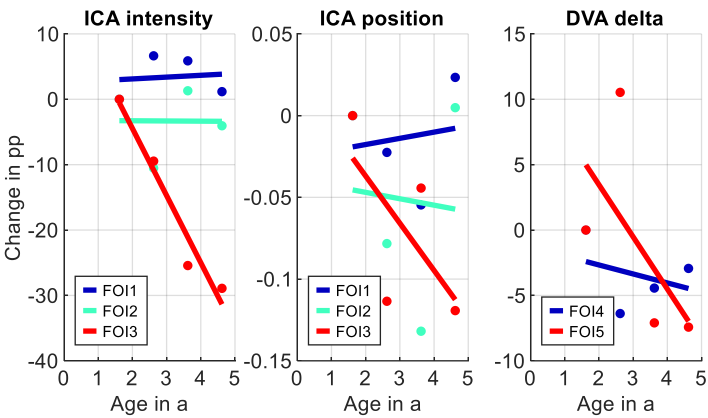

Figure 7-18: LFP FOI development of an exemplary $Medium_{LFP}$ system for intensity and position of ICA and distance of DVA.

7.3.2 Aggregated analysis

In this chapter, the FOIs of the single systems are aggregated to identify aging trends and degradation modes that occur across systems. The normalization of the position is done through the voltage range of the whole cell and the intensity through the maximum intensity of the overall IC. The normalization of the distance between peaks or edges of the DV is done through the SOC range of 100 %.

LMO/NMC. Figure 7-19 depicts the aggregated results of the $Small_{LMO}$ FOI tracking. It shows the average change of each FOI per year to its initial value. In general, the trends across the systems are comparable.

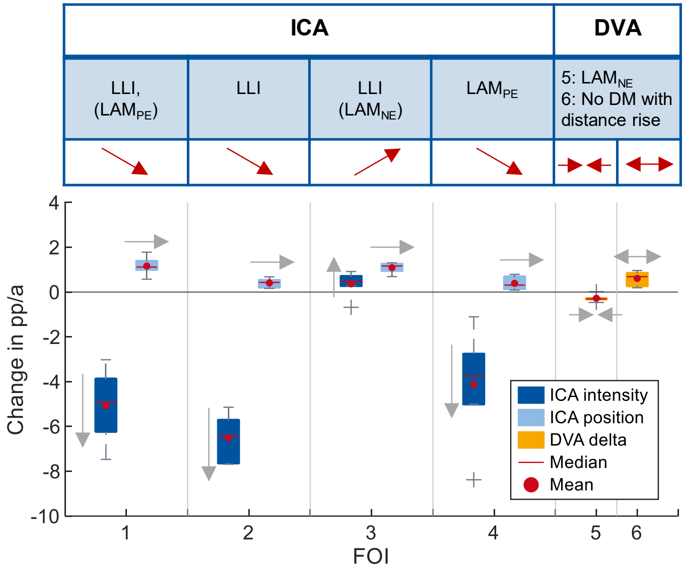

Figure 7-19: FOI tracking results of LMO/NMC systems. The observed main degradation modes are written on top of the table. The arrows symbolize the shift of the corresponding FOI. The boxes contain the FOI gradients of the HSSs.

The $Small_{LMO}$ systems show predominately LLI, while LAM_{NE} and LAM_{PE} could also occur in notably lower quantity. The detection of LLI is supported through three FOIs: the shift from FOI 1 and FOI 2 to lower intensities and higher voltages, and the shift of FOI 3 to higher voltages. Concerning the anode, small amounts of LAM_{NE} may be detected through FOI 3 and the distance shrink of FOI 5. Regarding the cathode, the development of FOI 1 and FOI 4 to a lower intensity could indicate LAM_{PE}. However, FOI 6 leads to the assumption that LAM_{PE} is likely not prominent, but the FOI becomes challenging to track.

In the following, the individual FOI shifts of all $Small_{LMO}$ systems are correlated with their respective SOH_{UC} (Table 7-1). In addition to the correlation coefficient, the corresponding p-values are shown, representing the probability of the estimated correlation being random. In the case of $Small_{LMO}$ systems, all p-values except for FOI 3's intensity are smaller than 0.05, showing high confidence in the correlation coefficients. Using these, the highest correlation with SOH development can be seen for FOI 1 (intensity: 0.91, position: -0.95). FOI 2 strongly correlates with SOH, especially its intensity (0.91).

Table 7-1: Correlations of LMO FOIs with SOH development.

FOI	1		2		3		4		5	6
Tracking	**Int**	**Pos**	**Int**	**Pos**	**Int**	**Pos**	**Int**	**Pos**	**Dist**	**Dist**
Correlation SOH_{UC}	0.91	-0.95	0.91	-0.78	-0.03	-0.89	0.85	-0.74	0.34	-0.42
p-value	< 0.05	< 0.05	< 0.05	< 0.05	0.85	< 0.05	< 0.05	< 0.05	< 0.05	< 0.05

Overall, FOI 1 to FOI 3 depict a significant correlation of LLI with SOH. FOI 4 also suggests a correlation between LAM_{PE} and SOH. FOI 5 and FOI 6 do not show a high correlation with SOH.

NMC. Figure 7-20 shows the accumulated trends of the FOIs across the $Medium_{NMC}$ systems. Overall, LLI is considered dominant, while LAM_{NE} and LAM_{PE} could slightly be present for some systems.

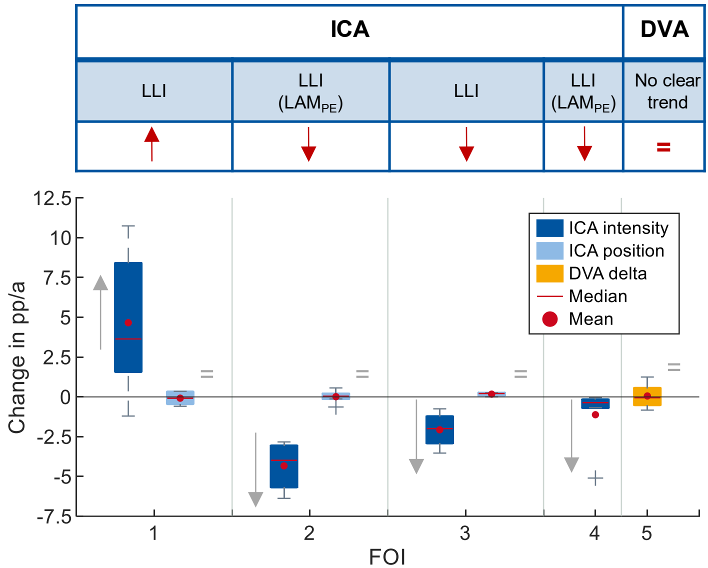

Figure 7-20: FOI tracking results of NMC systems. The observed main degradation modes are written on top of the table. The arrows symbolize the shift of the corresponding FOI. The boxes contain the FOI gradients of the HSSs.

The increase in intensity of FOI 1 and the decrease of FOI 2, FOI 3, and FOI 4 are associated with LLI and observable for most systems. LAM_{NE} is assumed for some systems through a shrinking distance tracked by FOI 5. However, FOI 5 is not uniform for all systems because positive and negative values exist. Furthermore, FOI 2 and FOI 4 are also sensitive to LAM_{PE}. However, this DM is not supported by other FOIs.

Table 7-2 presents the correlations and p-values. FOI 1, 2, and 3 show high confidence in their correlation coefficient with p-values below 0.05. From these, FOI 3 shows the highest correlation of 0.75 with SOH development, suggesting LLI is the driving factor for capacity loss in the Medium$_{NMC}$ systems.

Table 7-2: Correlations of NMC FOIs with SOH development.

FOI	**1**		**2**		**3**		**4**	**5**
Tracking	**Int**	**Pos**	**Int**	**Pos**	**Int**	**Pos**	**Int**	**Dist**
Correlation SOH$_{UC}$	-0.12	-0.61	0.60	0.29	0.75	-0.72	0.25	0.35
p-value	0.58	< 0.05	< 0.05	0.10	< 0.05	< 0.05	0.20	0.09

LFP. Figure 7-21 illustrates the aggregated FOI trends of LFP systems. The only FOIs that show clear trends are FOI 3 (decreasing intensity) and FOI 5 (decreasing distance), both indicating LLI as the dominant DM across systems.

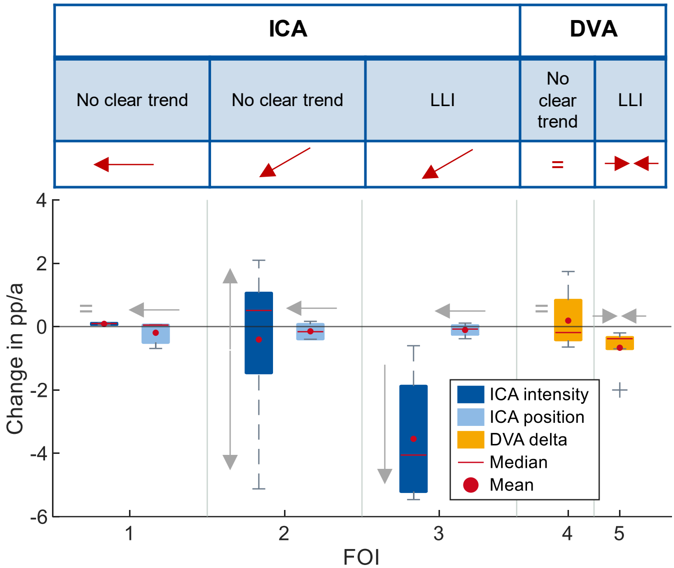

Figure 7-21: FOI tracking results of LFP systems. The observed main degradation modes are written on top of the table. The arrows symbolize the shift of the corresponding FOI. The boxes contain the FOI gradients of the HSSs.

FOI 1 does not show clear trends. Depending on the systems, FOI 2 shows both increases and decreases in intensity and does not lead to general conclusions. Some systems possibly show LAM$_{NE}$ through a shrinking distance of FOI 4, although no general trends are observable for this FOI.

Table 7-3 shows the correlations and p-values that could be detected across the LFP systems. Only the correlation between FOI 5 and SOH has a p-value which is less than 0.05, supporting the occurrence of LLI. Nevertheless, the correlation between FOI 5 and SOH is only moderate with a correlation coefficient of 0.64. The p-value of FOI 3 is close to 0.05, making it a possible indicator for LLI.

Table 7-3: Correlations of LFP FOIs with SOH development.

FOI	**1**		**2**		**3**		**4**	**5**
Tracking	Int	Pos	Int	Pos	Int	Pos	Dist	Dist
Correlation SOH_{UC}	-0.48	-0.43	-0.22	0.28	0.44	0.06	-0.29	0.64
p-value	0.10	0.14	0.29	0.18	0.06	0.82	0.12	< 0.05

7.4 Conclusion

Creating qOCV curves. This chapter has identified the degradation modes responsible for the capacity loss and the increase in internal resistance. The developed innovative method first reconstructs the qOCV curves. For this purpose, partial low-dynamic operational phases such as clear sky conditions during charging or steady overnight supply of household are combined. Both operational modes show reasonable results, although the resulting curves from the discharging phases show higher accuracy than those from the charging phases. The low-power discharge phases can predominantly explain this.

Applying ICA and DVA. After reconstructing the annual qOCV curves, the evolution of the curves over time is analyzed. Purely from the qOCV curves, it can already be seen that the capacity is decreasing. The methods of incremental capacity analysis and differential voltage analysis are applied for detailed investigation. Here, features of interest derived from literature enable to identify peaks and distances in the derived curves. The shift of these FOIs can be used to identify the degradation modes. For all technologies studied (LMO/NMC, NMC, LFP), the same FOIs can be obtained from the field data as described in literature.

Evaluating degradation modes. For the $Small_{LMO}$ systems, the degradation mode LLI is dominant, while LAM_{NE} and LAM_{PE} could also be present in lower quantity for some systems. In addition, the evaluations confirm an increase in internal resistance. For the $Medium_{NMC}$ systems, LLI shows the strongest correlation with SOH development, and the analyses still indicate possible correlations between SOH and both LAM_{NE} and LAM_{PE}. For the $Medium_{LFP}$ systems, the method does not reach high certainty across systems, even though the results indicate that the occurrence of LLI is most likely. The less accurate LFP analysis is probably due to slightly inaccurate SOC and OCV estimates due to its flat voltage curve. Although the FOIs presented in literature are obtained, the accuracy combined with the curves' smoothing makes it challenging to use the minimal shifts in FOIs for statistically meaningful identification of correlations between DMs and SOH development. All in all, the analysis of degradation modes confirms the capacity and energy loss quantified in Chapter 5 and the increase in internal resistance observed in Chapter 6.

8 Summary and outlook

This chapter summarizes the key findings of the dissertation and gives an outlook on possibilities to extend the presented work.

8.1 Summary

Battery storage systems are an important element of the energy transition. They enable the integration of volatile renewable energy generation and stabilize the energy system. Today, home storage systems (HSSs) represent the largest amount of grid-connected stationary battery capacity in Germany, a pioneering storage market. In the context of sustainable raw material use, it is important to ensure a long operational life. Current warranty periods are about ten years, but whether these lifetimes can be achieved is questionable and unknown to customers. No validated analyses exist to date (year 2024) since most HSSs are only a few years old. Therefore, the future digital battery passport of the European Union [7] requires reliable state of health (SOH) estimation based on field data.

This dissertation contributes to battery research by developing novel data-driven diagnostic methods using field data. For this purpose, it analyzes field measurements of 21 HSSs over a measurement period of up to eight years. The dataset is, to date, unique for a scientific dataset in terms of measurement duration and sample rate. It consists of about 106 system years represented by 14 billion data points. Its 146 gigabytes cover three important lithium-ion battery technologies: lithium iron phosphate (LFP), lithium nickel manganese cobalt oxide (NMC), and a blend of lithium manganese oxide (LMO) and NMC. The different chemistries and HSS products present a challenge for method development, which this thesis overcomes. The elaborated methods include the SOH estimation in terms of capacity and energy, the determination of the internal resistance, and the identification of degradation modes. In addition, important operational parameters are extracted from the field measurements, and the market development of stationary battery storage systems in Germany is reviewed as part of the dissertation. Most of the current literature focuses either on single-cell laboratory measurements or simulations, while this thesis analyzes system-level field data.

Capacity and energy SOH estimation. The developed SOH estimation automatically detects the electrochemical processes of overvoltage relaxation at low currents and uses their characteristics for the parameter estimation of a second-order equivalent circuit battery model. With these parameters, the exact state of charge at both full charge and full discharge is calculated. These values compute the remaining capacity, energy, and SOH while analyzing current, voltage, and temperature. The analyzed storage systems show average decreases in usable capacity of around two to three percentage points per year. From a technical perspective, single systems with a higher capacity fade reach their EOL after five to seven years, defined as 80 % of their nominal capacity. Others still show reasonable SOH values after the same operational period, indicating a longer lifetime. Nevertheless, the given warranty periods can be reached in most cases by including aging reserves. Considering that the measured HSSs were from the first product generation, this is a positive sign for the industry.

Internal resistance estimation. The internal resistance of a battery consists of different components like ohmic and diffusion resistances. It increases over time and is the second fundamental criterion for determining battery aging besides capacity fade. The developed method to estimate the direct current resistance adopts the system dynamics and automatically identifies characteristic operating points. The increase of the direct current resistance varies between systems, with mean values of around one to 25 percentage points per year, depending on the temperature and SOC range analyzed. Nevertheless, the energy fade is mainly influenced by the capacity fade, and the internal resistance is only a secondary aging parameter in HSSs. One of the reasons for this is probably the low mean C-rate during operation. Furthermore, the relaxation parameters, such as the slow diffusion voltage, contain information on the capacity fade, shown using machine learning methods.

Degradation mode analysis. A battery's open circuit voltage (OCV) curve can be seen as its electrochemical signature. Its shape and age-related shift provide information on electrochemical aging processes and material composition on both electrodes. The developed method reconstructs the OCV curve continuously over the lifetime of a battery. It innovatively transfers the incremental capacity analysis and differential voltage analysis, known predominantly from single-cell analysis in the laboratory environment, to system-level field data. It corrects the measured voltage during low-dynamic operational phases by the overvoltage due to the internal resistance. The obtained partial voltage curves during suitable operational phases, such as the overnight household supply with electricity, are combined to estimate the overall OCV curve. The change of the obtained OCV curves over the lifetime allows for determining the occurring degradation modes. The dominant degradation mode observed is the loss of lithium inventory across many systems. Additionally, the loss of active material on both anode and cathode can be identified in some case.

Operational metrics. The long measurement period enables the quantification of key operational metrics, such as the yearly equivalent full cycles (around 200 EFC to 250 EFC) and current distributions (charge with high and discharge with low C-rates). These parameters are important for product development and model parametrization and were previously mainly based on simulations.

Market development. The market for grid-connected battery storage is relatively young and growing rapidly. This leads to a lack of transparent market information. Accompanying the market ramp-up, extensive data analyses of self-gathered and publicly accessible databases are carried out to transparently draw a picture of the market development in Germany. In total, around seven gigawatt-hours of stationary battery storage were in operation by the end of 2022, which corresponds to almost 20 % of the cumulative energy of the national pumped-hydro storage power plants, symbolizing the important role of battery storage for the energy system. The latest numbers for the German market can be seen on the website www.battery-charts.de and are updated automatically.

8.2 Outlook

This dissertation presents comprehensive knowledge of various aspects of home storage systems, which can be used for future studies. The industry can use these methods for demand-oriented maintenance, ensuring a long-lasting operation of HSSs. Researchers can improve these methods further and use the results for model parameterization. The extensive dataset was published to help address the lack of freely available datasets [184,185]. Policymakers can refer to the comprehensive market analysis to align their objectives with the current state of battery deployments and use it as a solid planning foundation. The following topics show promising starting points for research extension.

Scaling to storage population. The methods are designed for a short computational time. However, analyzing 21 HSSs represents only a fraction of the more than 100,000 systems operated by single vendors today, and it was already a challenge to make the methods work for all systems. Therefore, applying the methods to a whole HSS population would be necessary to recognize which additional problems can arise. The data resolution for the measured component (cell, module, system), sample rate, and measurement accuracy also play a decisive role. Analyzing a large HSS population would also enable statistically significant correlation with the operating conditions such as C-rate, SOC, and temperature distributions, which the small HSS number in this thesis did not allow. In addition, a large dataset would enable lifetime predictions, extending the SOH analysis done in this thesis.

Use of single-cell data. This dissertation had access to system-level field data and could already identify relevant parameters such as the remaining usable capacity, the internal resistance, and the degradation modes. Using module-level or cell-level data could allow even more detailed analyses of the variation in aging between the cells of a storage system. Investigation of the cell-to-cell variation should lead to more precise estimations of lifetimes, degradation modes, and refurbishment measures.

Lifetime and safety. This thesis used linear fits to quantify the aging rates of capacity, energy, direct current resistance, slow-diffusion voltage, and degradation modes. Although the general trend is covered well, more advanced fitting methods could be applied to account for more details. This will become especially important when the HSSs reach their knee-point, where the linear assumption is not valid anymore. The shown estimation of degradation modes can be used to predict non-linear aging mechanisms and can possibly be used for knee-point prediction. In addition, safety diagnostics could extend the analyses done.

Laboratory validation. The field capacity tests already serve as validation of the capacity estimates and of the degradation mode identification. Nevertheless, the estimations could be confirmed in future laboratory tests and the degradation mechanisms in post-mortem analyses.

Extended research topics. The large dataset [185] enables a variety of further research topics, such as operational strategy optimization, energy market participation modeling, or product improvement and analysis of any kind. Besides new topics, different methods can also be developed for the same objectives as the ones of this dissertation.

Standards and norms. Standards are the base for efficient and transparent battery use. This is why the European battery passport requires SOH estimates from field data. The presented challenges and solutions could contribute to discussions about standards and norms.

Transfer to other applications. The method for determining the internal resistance can presumably be applied to all storage types since it uses the operating data of all SOC ranges. However, the usable capacity estimation method requires the regular occurrence of EOC and EOD voltage to calculate the capacity between these voltage limits. While some storage systems in use cases, such as intraday trading and renewable energy integration, might have a suitable profile, other storage applications do not show regular full cycles. An EV is usually not driven until it is empty but regularly fully charged. Storage systems for frequency containment reserve have an average SOC of around 50 % most of the time, rarely reaching the voltage limits. Thus, partial voltage ranges would have to be evaluated in more detail. In addition, a different method for SOC calculation would probably be necessary, which does not require a recalibration based on relaxation phases. Nevertheless, the proposed SOH method, which compares the operational data to the OCV curve of a new cell, holds potential for these applications. It can be used even if the application does not reach EOC or EOD voltage. Furthermore, the partial open circuit voltage curves could be used to analyze the degradation modes if the operating range contains the relevant peaks to track degradation.

Future battery technologies. At the time of writing, three relevant lithium-ion technologies are covered: LMO, NMC, and LFP. All of which can be analyzed using the methods presented. LFP, in particular, is gaining market share due to its low costs. Nevertheless, new promising candidates for the mid-term future are emerging. Sodium-ion batteries promise possible cost reduction potential at lower energy density using cheaper raw materials. However, this potential must be unlocked through successful scaling of the production and proven quality in field operation. Other technologies, such as solid-state, sodium-sulfur, redox-flow, and zinc-ion batteries, are also discussed at the moment. New technologies require new diagnostic algorithms. If this dissertation could inspire future researchers to develop these, I would be grateful.

9 Appendix

The appendix holds additional information for different main chapters. A short introduction in each chapter gives orientation on where the parts belong.

9.1 Market analysis

This chapter provides further analyses for Chapter 3. First, the storage markets are compared with energy size distributions and energy-to-power ratios. In addition, extended analyses on industrial and large-scale storage systems are depicted, as the main part of Chapter 3 focuses on home storage systems in line with the other parts of the thesis. In addition, a compact literature overview is presented.

9.1.1 Comparing storage markets

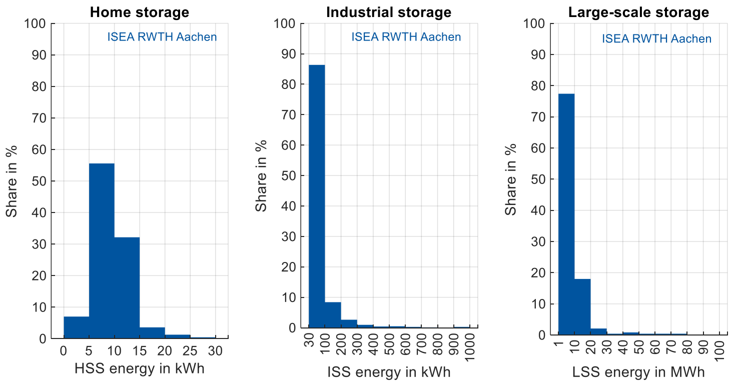

Figure 9-1: Share of BSS number in energy classes of HSS (left), ISS (middle), and LSS (right) in Germany based on own analyses of BSS in operation and registered in MASTR DB [135], used under dl-de/by-2-0 [136].

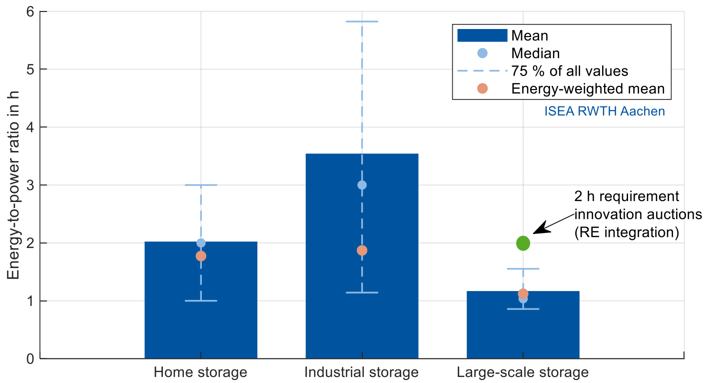

Figure 9-2: Energy-to-power ratio (EPR) distribution of stationary battery storage systems in Germany based on own analyses of BSSs in operation and registered in MASTR DB [135], used under dl-de/by-2-0 [136]. Only some LSSs of the innovation auctions were commissioned at the end of 2022, which is why their higher EPR values do not influence the energy-weighted mean to a larger extent.

9.1.2 Industrial storage

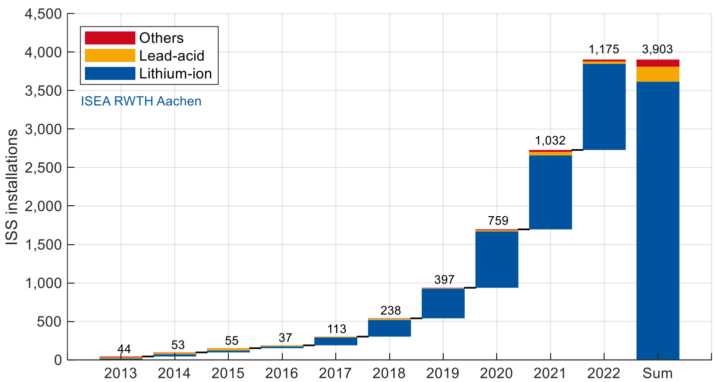

Figure 9-3: Estimated number of ISS installations in Germany based on own analyses of MASTR DB [135], used under dl-de/by-2-0 [136].

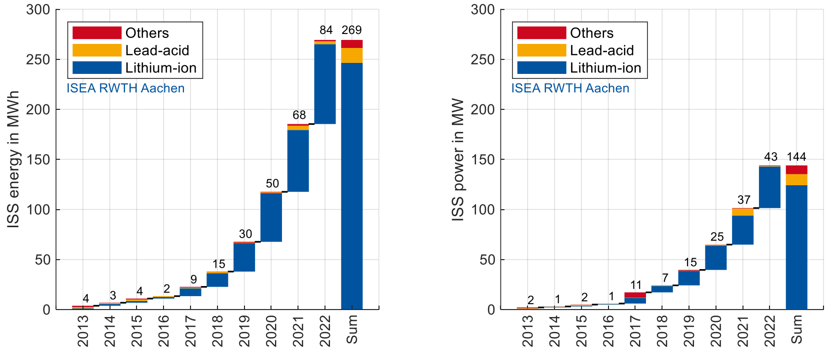

Figure 9-4: Development of ISS battery energy (left) and inverter power (right) by battery technology in Germany based on own analyses of MASTR DB [135], used under dl-de/by-2-0 [136], and further research.

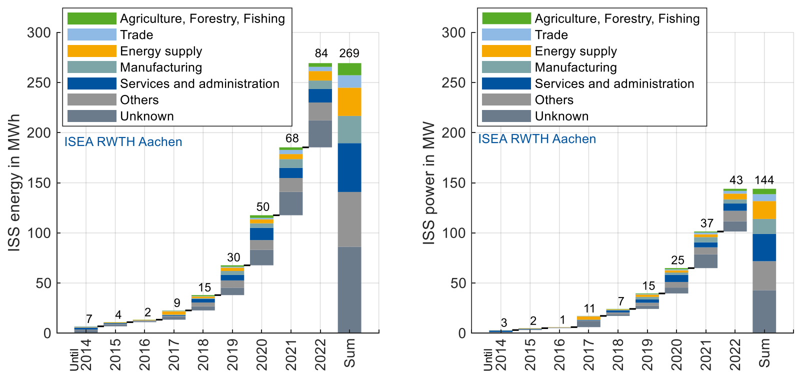

Figure 9-5: Development of ISS battery energy (left) and inverter power (right) by economic sector in Germany based on own analyses of MASTR DB [135], used under dl-de/by-2-0 [136], and further research.

9.1.3 Large-scale storage

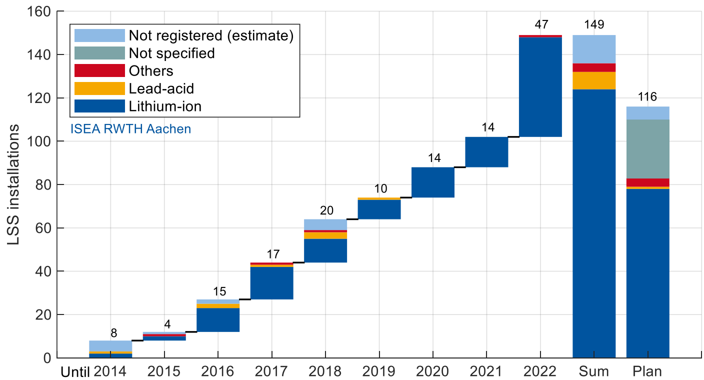

Figure 9-6: Estimated number of LSS installations in Germany based on own analyses of MASTR DB [135] (used under dl-de/by-2-0 [136]), LSS DB [137] (used under CC BY-NC 3.0 [138]), and further literature research. “Plan” includes all announced LSS. “Not registered” refers to LSS not yet registered in MASTR DB.

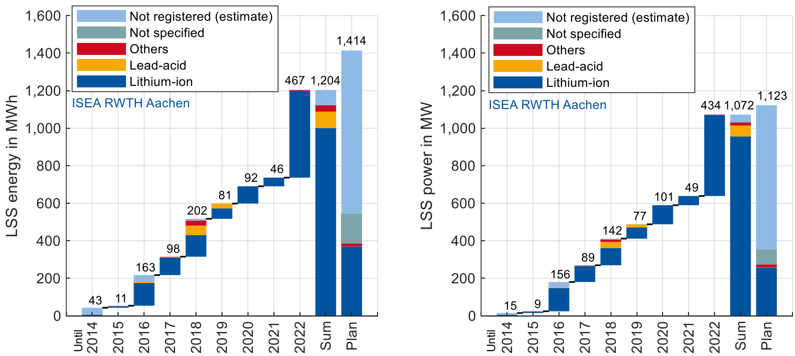

Figure 9-7: Estimated LSS battery energy (left) and inverter power (right) in Germany based on own analyses of MASTR DB [135] (used under dl-de/by-2-0 [136]), LSS DB [137] (used under CC BY-NC 3.0 [138]), and further literature research. “Plan” includes all announced LSSs for the next 2-3 years. “Not registered” refers to LSSs not yet registered in MASTR DB [135].

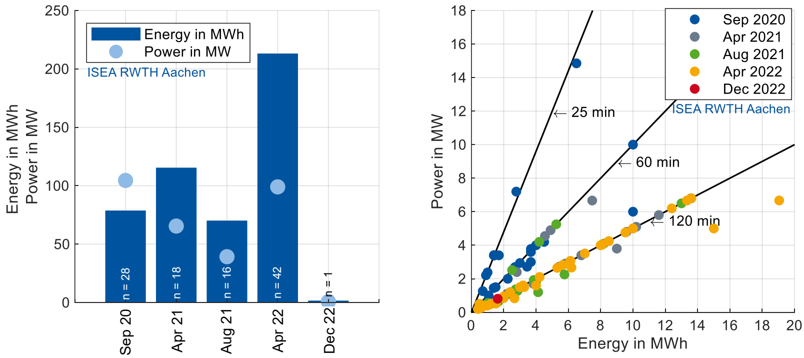

Figure 9-8: BSS energy and inverter power (left) of the first five innovation auction rounds [168] and the system design (right) of the single BSSs based on MASTR DB [135], used under dl-de/by-2-0 [136]. As of February 2023, 21 BSSs are already in operation, while 84 BSSs are under construction. All BSSs are either lithium-ion batteries or not specified.

Innovation auctions (see Figure 9-8). The BSS power must be at least one-third of the RE power. However, the single innovation rounds have differences in the EPR, ranging from an average of 0.75 h in September 2020 to an average of 2.15 h in April 2021. The reason for this is the changed regulations after the first round in September 2020. In this first round, it was still debatable whether the BSSs should have been designed for one hour or 25 min. The one-hour design is based on the requirements of the transmission system operators for limited energy storage [341]. However, as the BSSs do not have to reach the minimum size to participate in the aFRR market as specified in the innovation auctions regulation, some projects are also designed only to meet the test protocol for aFRR. The protocol is used to verify two test calls of ten min of full power each, which requires about 25 min of full power, including buffers [341]. These two options are clearly shown in the project-specific allocation of BSS in Figure 9-7 (right). Here, most of the registered BSS are distributed along these two options. A larger EPR of at least two hours was required for the following rounds. However, there are still projects following an EPR of one hour, which will probably change their EPR design to meet the requirements. After high award volumes in April 2022, there was a sharp drop in the December round in which only one operator submitted a bid. Again, this was due to a change in regulation. Whereas a fixed market premium was tendered until April 2022, a flexible market premium was introduced in December 2022, which reduced the rate of return and led to a drop in bid submissions.

9.1.4 Market literature

Table 9-1: Literature overview of BSS market development (written in 2019).

	Source	Related Topic	Focus Region	Covered period	Selected source information
Institutional reports	IRENA [96]	Installations, Costs, BSS	Worldwide, single information on Germany	Historic: until 2017 Forecast: until 2030	DOE, literature
	Ioannis et al. [97] (European Commission / European Union)	Installations, Costs, BSS, EV	Worldwide	Historic: until 2017 Forecast: until 2040	DOE, literature
	Energy Storage Council [342]	Installations HSS, LSS	Worldwide, short German part	Historic: until 2014 Forecast: until 2019	DOE, literature
	Stenzel et al. [343,344]	LSS	Germany	Until 2018	FZJ LSS database
	Kairies et al. [345,346]	HSS	Germany	2013-2015	ISEA HSS database
	Figgener et al. [8,9,347]	HSS	Germany	Until 2018	ISEA HSS database
	Figgener et al. [94]	HSS, ISS	Germany	Until 2018	ISEA HSS & ISS database
	Team Consult with BVES [348]	Installations HSS, ISS, LSS	Germany	Historic: until 2018 Forecast: until 2019	self-gathered data
	BSW-Solar [349]	Installations	Germany	Until 2018	MASTR
	BSW-Solar [350]	Fee-based			

Peer-reviewed publications	Schmidt et al. [113]	Costs, installations, BSS, EV, electronics	Worldwide	Historic: 2004-2016 Forecast until 2040	DOE, interviews, literature
	Malhotra et al. [112]	Installations BSS, application	Worldwide	Until 2015	DOE, self-added projects
	Battke et al. [111]	Lifecycle costs BSS, applications	Worldwide	Until 2012	DOE, interviews, literature
	Müller et al. [114]	Costs, installations, applications	Worldwide	Historic: until 2016 Forecast: until 2025	DOE, literature, self-gathered data
	Tan et al. [351]	Installations, applications	Worldwide, focus China	Until 2016	DOE (assumed)
	Rohit et al. [116]	Installations, applications	India	Until 2017	DOE, India Energy Storage Database
	Kairies et al. [91]	HSS	Germany	2013-2017	ISEA HSS database
Consultant reports	EuPD Research [119]	Fee-based (sometimes extracts available such as [101,123–125]; see also other free consultant news like McKinsey [352] or BCG [353])			
	Macrom [120]				
	IHS Markit [121]				
	BNEF [122]				
	AVICENNE Energy [354,355]				
	Navigant [356,357]				
	GTM Research/ESA [358]				
	Total Battery Consulting [359]				
	LAZARD [126]	Levelized Costs, HSS, ISS, LSS, applications	Worldwide, single information on Germany	Historic: until 2018 Forecast: until 2038	self-gathered data, literature

9.2 Dataset

This chapter supplements Chapter 4 and gives additional information on the HSSs' metadata.

Table 9-2: Meta information on the measured HSSs.

ID	Capacity in Ah (nominal)	Voltage in V (nominal)	Energy in kWh (nominal)	Warranty condition Energy in kWh (datasheet)	Inverter power in kW
1	15	146.7	2.2	2.0	2.0
2	15	146.7	2.2	2.0	2.0
3	15	146.7	2.2	2.0	2.0
4	15	146.7	2.2	2.0	2.0
5	15	146.7	2.2	2.0	2.0
6	15	146.7	2.2	2.0	2.0
7	180	48.1	8.7	8.5	3.0
8	188	46.8	8.8	8.5	3.0
9	180	48.1	8.7	8.5	3.0
10	188	46.8	8.8	8.5	3.0
11	172	50.4	8.6	7.5	2.5
12	229	50.4	11.5	10.0	2.5
13	189	51.8	9.8	8.8	5.0
14	158	51.2	8.1	8.0	3.3
15	195	51.2	10.0	10.0	3.3
16	158	51.2	8.1	8.0	3.3
17	158	51.2	8.1	8.0	3.3
18	158	51.2	8.1	8.0	3.3
19	200	46	9.2	7.0	3.0
20	200	46	9.2	7.0	3.0
21	300	46	13.8	10.5	3.5

9.3 Capacity estimation

This chapter provides additional information on the capacity, energy, and SOH estimation elaborated in Chapter 5.

9.3.1 Relaxation

The following information supplements the fitting of the battery model and relaxation parameters of Chapter 5.2.2.

Fitting boundaries. Using the time constants discussed in Chapter 5.2.2, the permissible interval for both time constants of the second-order ECM is stipulated to fall within a duration of less than sixty minutes (see Table 9-3). The range is wider than the established numerical figures found in literature. This choice is made to preempt any artificial imposition on the fitting process, ensuring its applicability across diverse battery technologies and operational scenarios, even as the battery ages. Nevertheless, the fitting algorithm maintains the condition that $\boldsymbol{\tau_{fast}}$ is invariably smaller than $\boldsymbol{\tau_{slow}}$, aligning with the fundamental definitions.

Table 9-3: Identification restrictions.

Variable		Relaxation after charging	Relaxation after discharging
$\boldsymbol{\tau_{fast}}$ in sec	min	0	
	max	3600	
$\boldsymbol{\tau_{slow}}$ in sec	min	0	
	max	3600	
$\boldsymbol{V_{fast}}$ in V	min	0	-inf
	max	inf	0
$\boldsymbol{V_{slow}}$ in V	min	0	-inf
	max	inf	0
$\boldsymbol{V_{OCV}}$ in V	min	-inf	$V_{relax}(end)$
	max	$V_{relax}(end)$	inf
Starting point: $[\boldsymbol{V_{fast}}, \boldsymbol{\tau_{fast}}, \boldsymbol{V_{slow}}, \boldsymbol{\tau_{slow}}]$		$[V_{fast_{residual\ fit}}, \tau_{fast_{residual\ fit}}, V_{slow_{OCV\ fit}}, \tau_{slow_{OCV\ fit}}]$	

Non-transient effects. The voltage constantly decreases over time as the battery supplies the BMS through small discharge currents. This discharge is considered approximately linear within a certain SOC range. The data from long relaxation phases is used to construct a database to account for this effect. The database operates as a k-nearest-neighbor model, consisting of one neighbor (1-NN). This approach involves anticipating an unclassified sample's category based on the established classifications of neighboring samples [360]. The 1-NN model is trained at a system level. Based on the operational data as the input, the output is the gradient of the non-transient fitting. This gradient is subtracted from the measured voltage to correct it. Further insights into the k-nearest-neighbor methodology are presented in [360] and [361].

Residual Fit. Figure 9-9 represents this fitting procedure, specifically for relaxation after discharging, showing the OCV fit (top) and the residual fit (bottom).

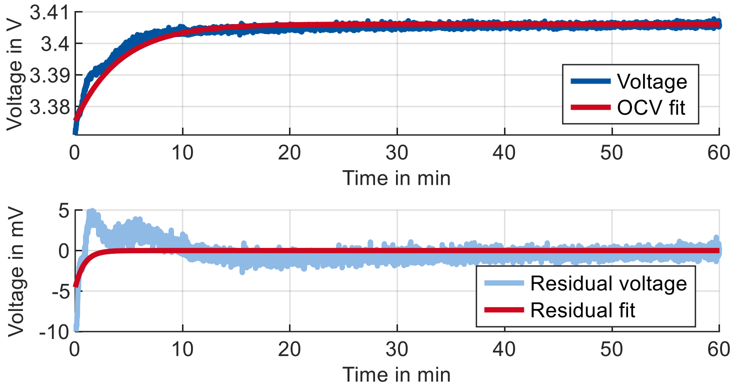

Figure 9-9. OCV fit (top) and residual fit (bottom) to estimate the starting points of the final second-order ECM fit. The residual voltage is the difference between the measured voltage and the OCV fit from the upper plot.

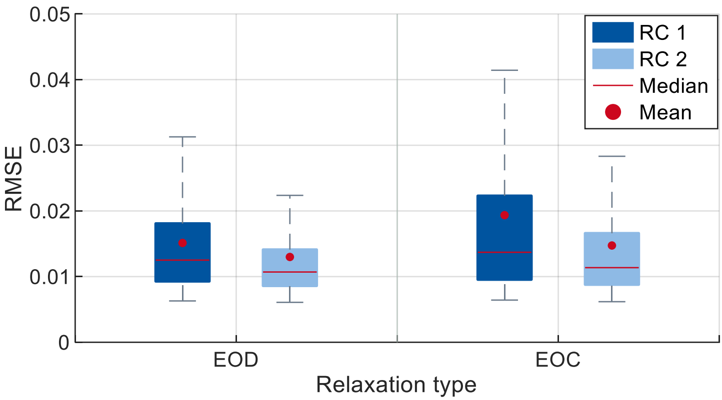

Figure 9-10: Fitting RMSE for first-order (RC 1) and second-order (RC 2) ECMs for EOD and EOC relaxations of all systems. The second-order ECM has a higher accuracy than the first-order ECM (also valid for each single system), which is why it was used in this thesis. Outliers are not displayed.

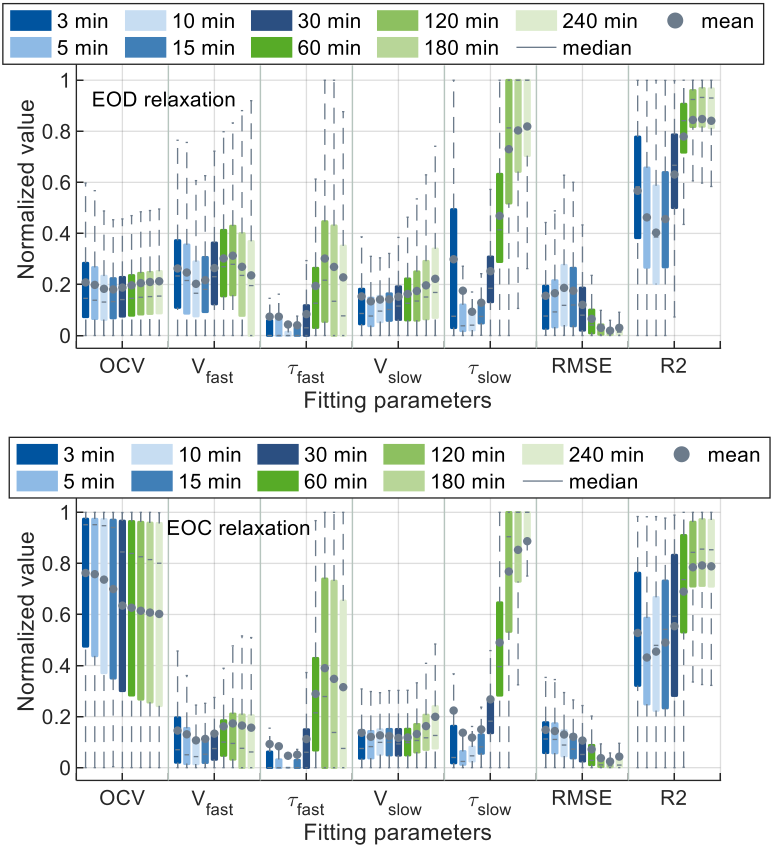

Figure 9-11: Impact of relaxation duration on relaxation parameters after discharge (top) and charge (bottom). The value ranges are scaled from 0 % to 100 %.

9.3.2 Field capacity tests

Figure 9-12 depicts the results of the field capacity tests. Each dot represents one test. The values are normalized to the energy taken from module information (left) and to values stated in the datasheet (right). The SOH_{UE} values are normalized to assumed usable energy values based on module labels, operational analysis, and further research. To show the influence of normalization, the $SOH_{Warranty}$ values are normalized to datasheet information, typically stated lower as they include an aging reserve and are subject to warranty conditions. However, the stated usable energy does typically not reflect the "real" usable energy for operation. This corresponds rather to the stated nominal energy (but not always).

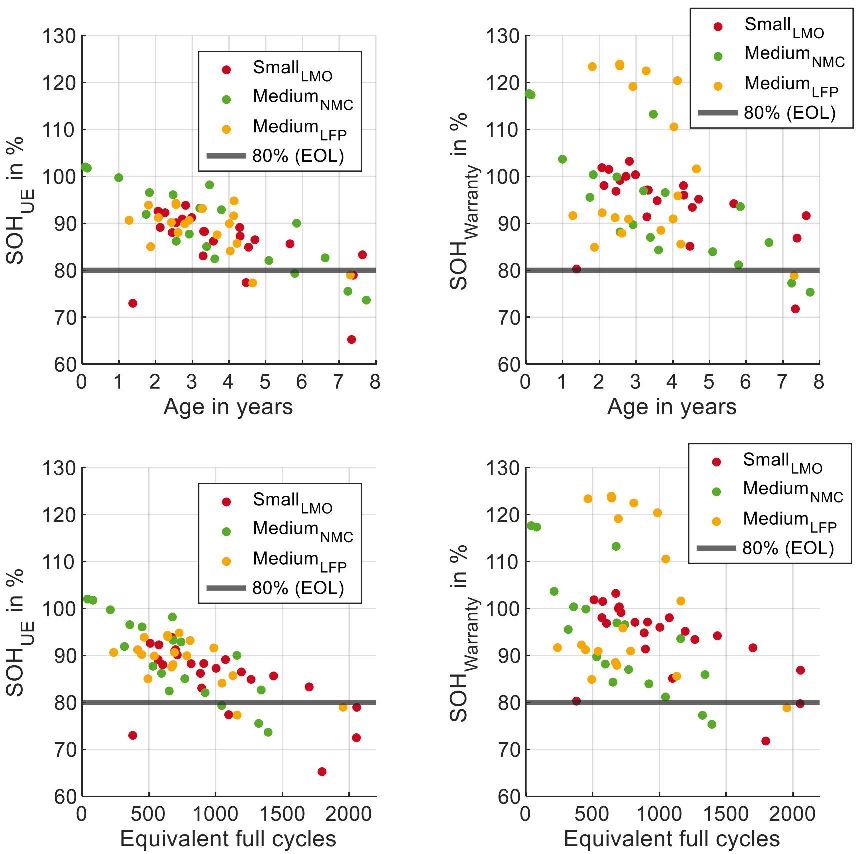

Figure 9-12: SOH_{UE} (left) and $SOH_{Warranty}$ (right) based on field capacity tests. Results are shown according to system age (top) and to equivalent full cycles (bottom).

9.3.3 State of health

Figure 9-13 shows additional results for the methods shown in Chapter 5.2.3. The Medium$_{NMC}$ system is an example that does not work very accurately (but other Medium$_{NMC}$ systems show higher confidence). The Medium$_{LFP}$ system is a good example of LFP diagnostics. Both systems were chosen as there were enough capacity tests for validation.

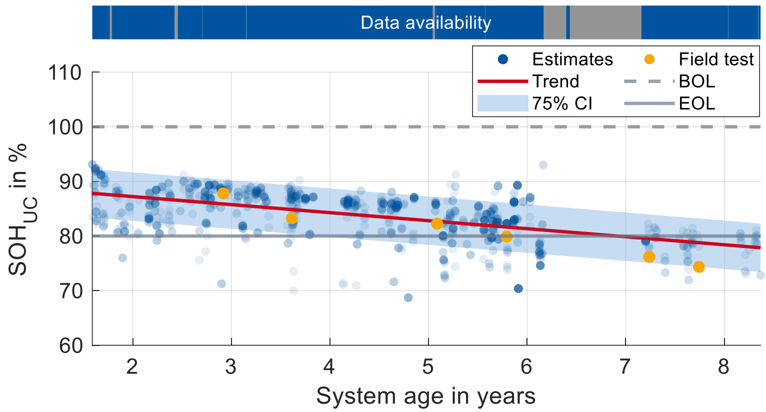

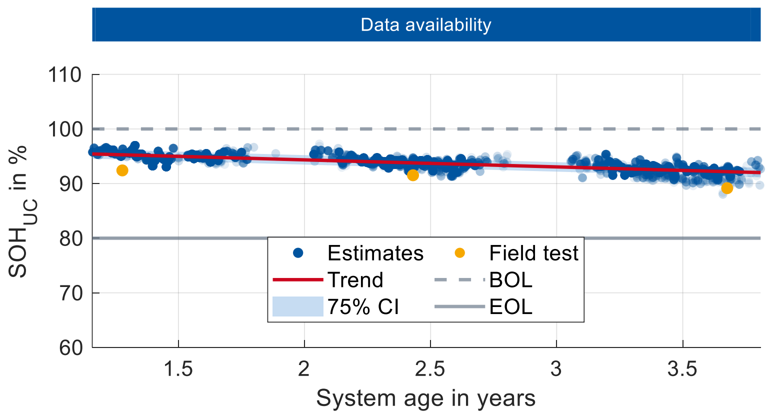

Figure 9-13: SOH$_{UC}$ results of an exemplary Medium$_{NMC}$ system (top) and a Medium$_{LFP}$ system (bottom).

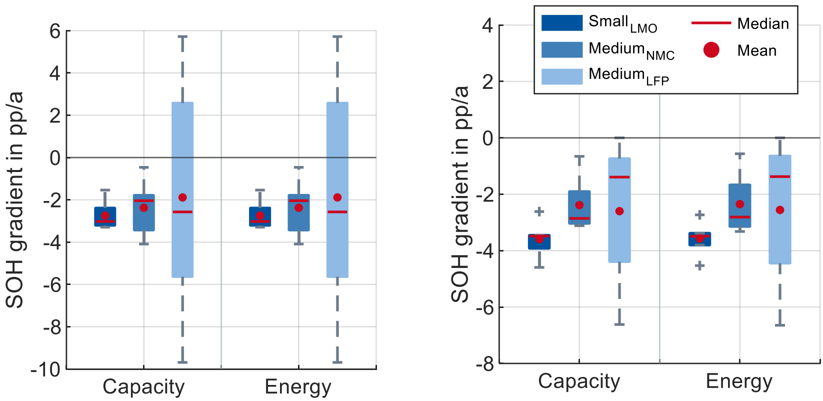

Figure 9-14: SOH gradients for capacity ($SOH_{C,OCV}$) and energy ($SOH_{E,OCV}$) per year. **Left:** Current and power integration between any two relaxation points. **Right:** Current and power integration only between EOC and EOD voltages. **Difference:** Small OCV differences lead to higher inaccuracy and explain the difference. The results for Small$_{LMO}$ and Medium$_{NMC}$ HSSs are comparable to the estimation of the SOH_{UC} and SOH_{UE} in Chapter 5.2.3. However, for Medium$_{LFP}$ systems, the estimations are worse due to the flat OCV curve and the quality of the gathered OCV curve.

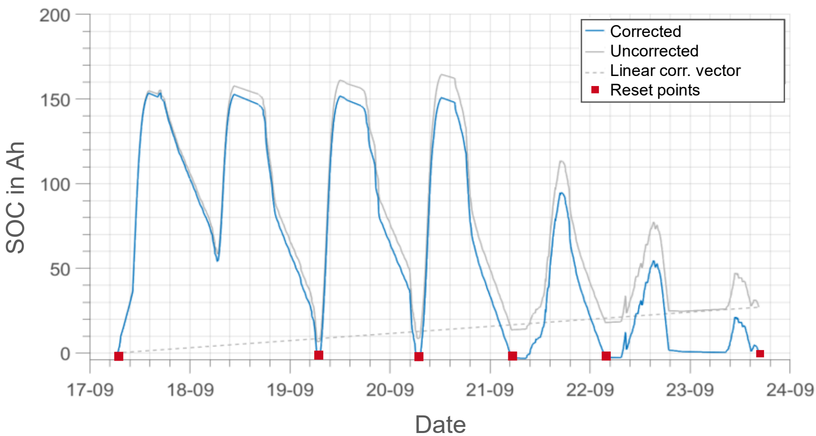

Figure 9-15: SOC estimation with EOD relaxation reset points and offset current correction.

9.3.4 Literature capacity estimation

Table 9-4: Literature overview on field capacity tests.

Source	Application	Type	Conditions	Results capacity loss
[215]	PV + BSS (LIB & vanadium redox flow)	Field	C/5 constant power discharge (monthly)	-3.7 %/year
[218]	Grid utility (LTO)	Field	Cell voltages at end of full cycle are compared to OCV curve	-2.5 %/year (-7 % after 1000 days & >5000 cycles)
[219]	Grid utility (LTO)	Field	Cell voltages at end of full cycle are compared to OCV curve and 50 kW slow charge and discharge (P/6.5)	Modules: 5-10 % (7yrs) BESS: 15 % (7yrs)
[222]	HSS (lead acid)	Laboratory	Fully charged and then 55 W dis-charge	55 % of initial capacity remaining
[221]	PV (lead acid)	Field	C/16-C/18	14 months: 89 % of C_N
[226]	Consumer load management (LIB & lead acid)	Field (algorithmic)	Calculated monthly from discharged energy in operation	80 % after 1766 cycles (LIB)
[220]	Grid storage, “minimal opera-tion” (LIB)	Field	50, 100, 150 kW (~10-~90 % SOC) (C/6-C/16)	7 % in 3 years
[223]	Standby BSS in telecom. (Ni-Cd)	Field & Lab	C/5 discharge	~1 % per year
[224]	EV (lead acid)	Lab	C/20 discharge	~42 % in 100 cycles
[227]	EV (LIB)	Field (algorithmic)	Algorithmic from driving data	~15 % per year, own estimation
[228]	BSS in building (LIB)	Field (algo-rithmic)	Algorithmic	Varying capacity loss

Table 9-5: Selected battery datasets.

Source	**Origin**	**Type**
[252]	Literature	Overview of datasets
[185]	Field	Large HSS field dataset (used in this dissertation)
[266]	Field	Large EV field dataset
[262]	Field	Large EV field dataset
[206,253]	Laboratory	Fast charging LFP cell data
[209]	Laboratory	LCO cycling data
[254]	Laboratory	LIB cycling data
[207]	Laboratory	Cycling data at varying conditions for NMC, LMO, and LFP
[263]	Laboratory	Cycling data with randomized current profiles & reference cycles
[255]	Laboratory	0.5C CC cycling data (LCO)
[264,265]	Simulation	Simulated degradation data (LFP)
[208]	Laboratory	Cycling data at 1.5C for NMC and LCO
[258]	Laboratory	LCO cycling data (drive cycle discharge profile)
[259]	Laboratory	Cycling data using a mix of different driving cycles
[260]	Laboratory	Simulated driving cycles (NMC)
[261]	Laboratory	LIB cycled using DST profile
[256]	Laboratory	Cycle tests at 0.5C in different voltage bands (LMO)
[257]	Laboratory	Galvanostatic discharge tests (LFP, NMC, LMO)
[224,362]	Field	Lead-acid field measurements compared to laboratory test
[226]	Field	Field study on performance and economics (LIB, lead-acid)
[363]	Laboratory	Measurement of cells from field-tested EVs
[215]	Laboratory	Laboratory measurements under field conditions
[222]	Field	Lead-acid field measurements
[221]	Laboratory	Field-used batteries tested in laboratory
[223]	Field	Laboratory measurements compared with field test
[217]	Laboratory	Long-term testing of commercial battery packs

9.4 Degradation modes

This chapter gives additional information on Chapter 7. It validates the obtained ICA and DVA curves through the field capacity tests and summarizes selected literature on ICA and DVA.

9.4.1 Validation through capacity tests

Figure 9-16 displays the IC and DV curves obtained from the developed algorithm for exemplary systems contrasted with curves from field capacity tests. The discharge-derived curves follow the general patterns observed in field capacity tests. However, the algorithm is considered more accurate, as the field capacity tests have high C-rates and show only one voltage course, which has a lot of noise. Often, it was not possible to obtain a suitable IC and DV curve from the field capacity tests.

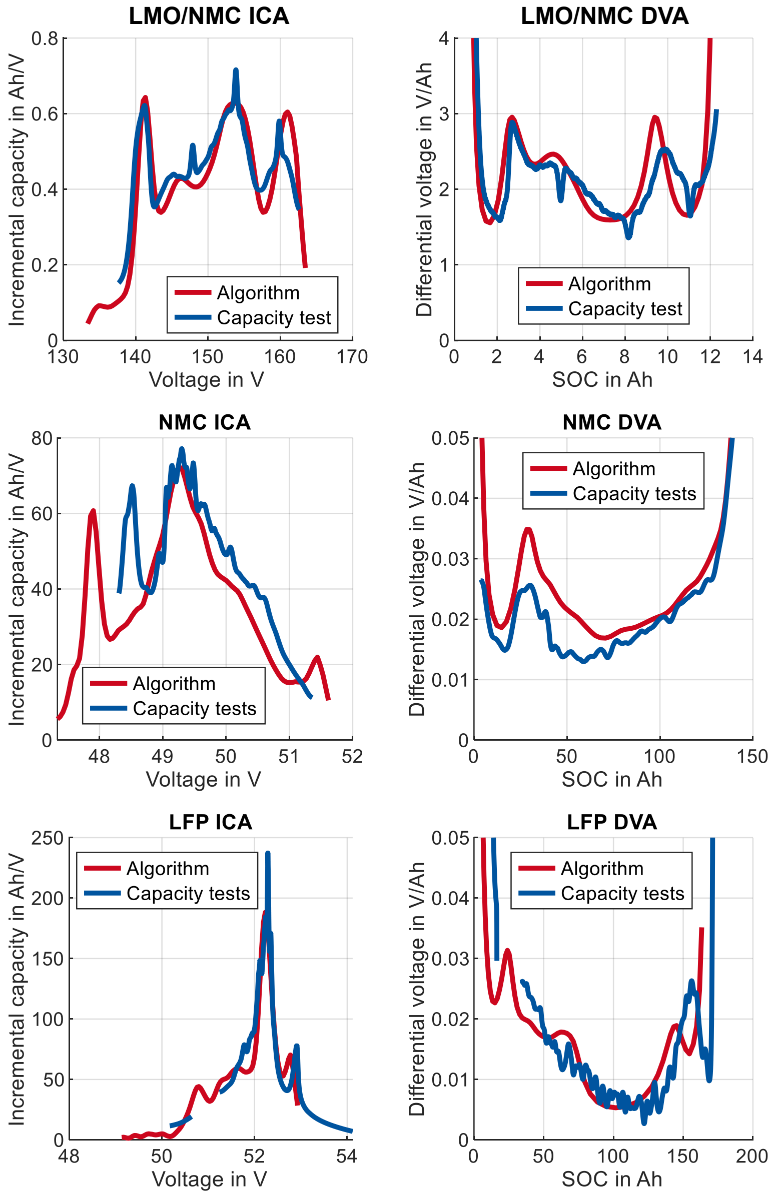

Figure 9-16: Algorithmic ICA and DVA validated by capacity test data.

9.4.2 Literature on ICA and DVA

Table 9-6: Selected literature overview on incremental capacity and differential voltage analysis.

Source	Investigation	Methods	DMs	OCV source	Results
Dubarry and Anseán [275]	Best practices for ICA	ICA	LLI, $LAM_{PE/NE}$	Laboratory	Shifts in FOIs are discussed and explained
Dubarry et al. [333]	HSS	ICA	LLI, $LAM_{PE/NE}$	Simulation based on measurements	ICA may be possible from field operation
Dubarry et al. [334]	HSS	ICA	LLI, $LAM_{PE/NE}$	Simulation based on measurements	Follow-up study on [333]
Dubarry et al. [311]	Presentation of simulation model	ICA	LLI, $LAM_{PE/NE}$	Simulation based on measurements	Impact of different DM scenarios on cell OCV
Dubarry and Beck [331]	Analysis of synthetic datasets	ICA / DVA using FOIs	LLI, $LAM_{PE/NE}$	Simulation based on measurements	Training datasets for deep learning prognosis and FOI-based statistical analysis of the impact of degradation paths on OCV
Li et al. [55]	SOH estimation, Gaussian smoothing	ICA / DVA using FOIs	LLI, LAM	Laboratory	SOH estimation from FOI analysis of IC/DV curves with maximum error of 2.5 %
Severson et al. [206]	Data-driven prediction of battery cycle life	ICA / DVA	LLI, $LAM_{PE/NE}$	Laboratory	Predict EOL using initial 100 cycles with a test error of 9.1 %
Dubarry et al. [87]	Identifying battery aging mechanisms in LFP cells	ICA	LLI, $LAM_{PE/NE}$	Laboratory	LLI and LAM_{PE} identified as origins of degradation
Keil et al. [330]	Calendar aging of lithium-ion batteries	DVA	LAM_{NE}, electrode balancing	Laboratory	Capacity fade is mainly due to changes in electrode balancing, strongly dependent on low anode potentials at high SOC

10 Nomenclature

Table 10-1: Abbreviations.

Abbreviation	**Meaning**
AC	Alternating current
aFRR	Automated frequency restoration reserve
BMBF	Bundesministerium für Bildung und Forschung (Federal Ministry of Education and Research)
BMS	Battery management system
BMWK	Bundesministerium für Wirtschaft und Klimaschutz (Federal Ministry of Economic Affairs and Climate Action)
BNEF	Bloomberg New Energy Finance
BOL	Begin of life
BSS	Battery storage system
BSW	Bundesverband Solarwirtschaft (BSW-Solar)
BVES	Bundesverband Energiespeicher Systeme (Energy Storage Systems Association)
BW	Baden-Württemberg
CD	Capacity decrease
CI	Confidence interval
C-rate	Current rate
DAA	Deutsche Auftragsagentur
DC	Direct current
DCR	Direct current resistance
DM	Degradation modes
DOD	Depth of discharge
DOE	Department of Energy
DV	Differential voltage
DVA	Differential voltage analysis
E2E	Empty-to-empty (full cycle)
E2F	Empty-to-full (half cycle)
ED	Energy decrease
EEG	Erneuerbare-Energien-Gesetz (Renewable Energy Sources Act)
EFC	Equivalent full cycles
EIS	Electrochemical impedance spectroscopy
EOC	End of charge
EOD	End of discharge
EV	Electric vehicle

EOL	End of life
EPR	Energy-to-power ratio
E-rate	Energy rate
F2E	Full-to-empty (half cycle)
F2F	Full-to-full (full cycle)
FCR	Frequency containment reserve
FMTA	Federal Motor Transport Authority
FNA	Federal Network Agency (German: Bundesnetzagentur)
FOI	Feature of interest
HSS	Home storage system
HV	High voltage
IC	Incremental capacity
ICA	Incremental capacity analysis
ID	Identification (number)
IEA	International Energy Agency
IRENA	International Renewable Energy Agency
ISEA	Institute for Power Electronics and Electrical Drives
ISS	Industrial storage system
LCO	Lithium cobalt oxide
LFP	Lithium iron phosphate
LIB	Lithium-ion battery
LAM	Loss of active material
LLI	Loss of lithium inventory
LMO	Lithium manganese oxide
LNO	Lithium nickel oxide
LSS	Large-scale storage system
LTO	Lithium titanate oxide
LV	Low voltage
MASTR	Marktstammdatenregister (battery storage registration database of the FNA)
$Medium_{LFP}$	Home storage systems with a medium battery energy and a lithium iron phosphate battery
$Medium_{NMC}$	Home storage systems with a medium battery energy and a lithium nickel manganese cobalt oxide battery
MV	Medium voltage
NCA	Lithium nickel cobalt aluminum oxide
NMC	Nickel manganese cobalt oxide
NOW	Nationale Organisation Wasserstoff- und Brennstoffzellentechnologie
OCP	Open circuit potential
OCV	Open circuit voltage
PCA	Principal component analysis
pp	Percentage points

PV	Photovoltaic
PVM	pv magazine
qOCV	Quasi OCV
RE	Renewable energy
RWTH	RWTH Aachen University
SDV	Slow diffusion voltage
SEI	Solid electrolyte interface
$Small_{LMO}$	Home storage systems with a small battery energy and a lithium manganese oxide / lithium nickel manganese oxide blend battery
SOC	State of charge normalized to actual capacity
SOH	State of health
$SOH_{C,OCV}$	State of health normalized to capacity of initial OCV curve
$SOH_{E,OCV}$	State of health normalized to energy of initial OCV curve
SOH_{NC}	State of health normalized to nominal capacity
SOH_{NE}	State of health normalized to nominal energy
SOH_{UC}	State of health normalized to initial usable capacity
SOH_{UE}	State of health normalized to initial usable energy
UC	Usable capacity
UE	Usable energy
UMBW	Ministerium für Umwelt, Klima und Energiewirtschaft Baden-Württemberg (Ministry of Environment, Climate Protection and the Energy Sector Baden-Wuerttemberg)
UPS	Uninterruptible power supply
VAT	Value-added taxes

Table 10-2: Parameters.

Parameter	Unit	Meaning
c	-	Bias
C_{charge}	Ampere-hour	Charged capacity
$C_{discharge}$	Ampere-hour	Discharged capacity
C_N	Ampere-hour	Nominal capacity
C_6	-	Graphite
DOD_C	Percent	Depth of discharge capacity
DOD_E	Percent	Depth of discharge energy
e^-	-	Electron
E_{charge}	Watt-hour	Charged energy
$E_{discharge}$	Watt-hour	Discharged energy
E_{loss}	Watt-hour	Energy losses
E_N	Watt-hour	Nominal energy
g	-	Activation function
h	-	Output neuron
I_{bat}	Ampere	Battery current
$I_{C_{fast}}$	Ampere	Current through the fast diffusion capacitance

$I_{C_{slow}}$	Ampere	Current through the slow diffusion capacitance
I_{max}	Ampere	Maximum current
$I_{R_{fast}}$	Ampere	Current through the fast diffusion resistance
$I_{R_{slow}}$	Ampere	Current through the slow diffusion resistance
Li	-	Lithium
Me	-	Metal
O_2	-	Oxygen
P_{bat}	Watt	Battery power
Q	Ampere-hour	Charge / capacity
R	Ohm	Internal resistance
R_{CT}	Ohm	Charge transfer resistance
R_{fast}	Ohm	Fast diffusion resistance
$R_{initial}$	Ohm	Initial internal resistance
R_{ohm}	Ohm	Ohmic resistance
R_{slow}	Ohm	Slow diffusion resistance
SOC	Percent	State of charge
SOE	Percent	State of energy
SOH	Percent	State of health
SOH_{NC}	Percent	State of health in terms of the nominal capacity
SOH_{NE}	Percent	State of health in terms of the nominal energy
SOH_R	Percent	State of health in terms of the internal resistance
SOH_{UC}	Percent	State of health in terms of the usable capacity
SOH_{UE}	Percent	State of health in terms of the usable energy
V_{bat}	Volt	Battery voltage
$V_{\mathrm{corrected}}$	Volt	Corrected battery voltage (overvoltage is corrected)
V_{fast}	Volt	Fast diffusion voltage
V_{OCV}	Volt	Open circuit voltage
V_{over}	Volt	Overvoltage
V_{slow}	Volt	Slow diffusion voltage
W	-	Connection weights
x	-	Input neurons / input vector
$\hat{y}$	-	Estimated output
z	1/Kelvin	Temperature coefficient
$\eta_{coulomb}$	Percent	Coulomb efficiency
η_{energy}	Percent	Energy efficiency
τ_{fast}	Seconds	Time constant of the fast diffusion processes
τ_{slow}	Seconds	Time constant of the slow diffusion processes

11 References

[1] IPCC. Climate Change 2023: Synthesis Report. Contribution of Working Groups I, II and III to the Sixth Assessment Report of the Intergovernmental Panel on Climate Change [Core Writing Team, H. Lee and J. Romero (eds.)]. IPCC, Geneva, Switzerland, 184 pp. 2023. https://doi.org/10.59327/IPCC/AR6-9789291691647.

[2] European Commission. Communication from the Commission to the European Parliament, the European Council, the Council, the European Economic and Social Committee and the Committee of the Regions: The European Green Deal. 2019. https://eur-lex.europa.eu/resource.html?uri=cellar:b828d165-1c22-11ea-8c1f-01aa75ed71a1.0002.02/DOC_1&format=PDF. [accessed August 13, 2023].

[3] Schmidt O, Melchior S, Hawkes A, Staffell I. Projecting the Future Levelized Cost of Electricity Storage Technologies. In: Joule 2019. 3(1):81–100. https://doi.org/10.1016/j.joule.2018.12.008.

[4] Figgener J, Stenzel P, Kairies K-P, Linßen J, Haberschusz D, Wessels O, Angenendt G, Robinius M, Stolten D, Sauer DU. The development of stationary battery storage systems in Germany – A market review. In: Journal of Energy Storage 2020. 29:101153. https://doi.org/10.1016/j.est.2019.101153.

[5] European Commission. Directorate General for Communication. Circular economy action plan: For a cleaner and more competitive Europe. https://data.europa.eu/doi/10.2779/05068. [accessed August 13, 2023].

[6] Figgener J, Hecht C, Haberschusz D, Bors J, Spreuer KG, Kairies K-P, Stenzel P, Sauer DU. The development of battery storage systems in Germany: A market review (status 2023). 2023. http://arxiv.org/pdf/2203.06762v3.

[7] European Commission. Regulation (EU) 2023/1542 of the European Parliament and of the Council of 12 July 2023 concerning batteries and waste batteries, amending Directive 2008/98/EC and Regulation (EU) 2019/1020 and repealing Directive 2006/66/EC. 2023. https://eur-lex.europa.eu/legal-content/EN/TXT/PDF/?uri=CELEX:32023R1542. [accessed July 21, 2024].

[8] Figgener J, Haberschusz D, Kairies K-P, Wessels O, Tepe B, Sauer DU. Wissenschaftliches Mess- und Evaluierungsprogramm Solarstromspeicher 2.0: Jahresbericht 2018. Institut für Stromrichtertechnik und Elektrische Antriebe, RWTH Aachen University. 2018. http://dx.doi.org/10.13140/RG.2.2.30057.19047.

[9] Figgener J, Haberschusz D, Kairies K-P, Wessels O, Tepe B, Ebbert M, Herzog R, Sauer DU. Wissenschaftliches Mess- und Evaluierungsprogramm Solarstromspeicher 2.0: Jahresbericht 2017. Institut für Stromrichtertechnik und Elektrische Antriebe, RWTH Aachen University. 2017. http://dx.doi.org/10.13140/RG.2.2.16917.42727.

[10] Haberschusz D, Kairies K-P, Wessels O, Magnor D, Sauer DU. Are PV Battery Systems Causing Ramping Problems in the German Power Grid? In: Energy Procedia 2017. 135:424–33. https://doi.org/10.1016/j.egypro.2017.09.512.

[11] Bayer B, Marian A, Matschoss P, Thomas H. Integration von Photovoltaikanlagen in die deutschen Niederspannungsnetze. 2017. https://doi.org/10.2312/iass.2017.008.

[12] Weniger J, Tjaden T, Quaschning V. Vergleich verschiedener Kennzahlen zur Bewertung der energetischen Performance von PV-Batteriesystemen. HTW Berlin. 2017. https://solar.htw-berlin.de/publikationen/kennzahlen-performance-pv-batteriesysteme/. [accessed August 07, 2023].

[13] Wesselak V, Schabbach T, Link T, Fischer J. Handbuch Regenerative Energietechnik. Berlin, Heidelberg: Springer Berlin Heidelberg. 2017.

[14] Sze SM, Ng KK. Physics of Semiconductor Devices. Hoboken, New Jersey: John Wiley & Sons, Inc. 2006.

[15] Orth N, Munzke N, Weniger J, Messner C, Schreier R, Mast M, Meissner L, Quaschning V. Efficiency characterization of 26 residential photovoltaic battery storage systems. In: Journal of Energy Storage 2023. 65:107299. https://doi.org/10.1016/j.est.2023.107299.

[16] Luo X, Wang J, Dooner M, Clarke J. Overview of current development in electrical energy storage technologies and the application potential in power system operation. In: Applied Energy 2015. 137:511–36. https://doi.org/10.1016/j.apenergy.2014.09.081.

[17] Sterner M, Stadler I. Energiespeicher - Bedarf, Technologien, Integration. Berlin, Heidelberg: Springer Berlin Heidelberg. 2014.

[18] Korthauer R (ed.). Handbuch Lithium-Ionen-Batterien. Berlin, Heidelberg: Springer Berlin Heidelberg. 2013.

[19] Rahimi M. Lithium-Ion Batteries: Latest Advances and Prospects. In: Batteries 2021. 7(1):8. https://doi.org/10.3390/batteries7010008.

[20] Manthiram A. A reflection on lithium-ion battery cathode chemistry. In: Nat Commun 2020. 11(1):1550. https://doi.org/10.1038/s41467-020-15355-0.

[21] Ghani F, An K, Lee D. A Review on Design Parameters for the Full-Cell Lithium-Ion Batteries. In: Batteries 2024. 10(10):340. https://doi.org/10.3390/batteries10100340.

[22] Ecker M, Sauer DU. 8. Batterietechnik Lithium-Ionen-Batterien. In: MTZ-Motortechnische Zeitschrift 2013. https://doi.org/10.1007/s35146-013-0014-9.

[23] Creative Commons. Attribution 4.0 International: CC BY 4.0. https://creativecommons.org/licenses/by/4.0/. [accessed August 03, 2024].

[24] Guyomard D, Tarascon J-M. Rocking-chair or lithium-ion rechargeable lithium batteries. In: Adv. Mater. 1994. 6(5):408–12. https://doi.org/10.1002/adma.19940060516.

[25] Maruyama S, Fukutsuka T, Miyazaki K, Abe Y, Yoshizawa N, Abe T. Lithium-ion intercalation and deintercalation behaviors of graphitized carbon nanospheres. In: J. Mater. Chem. A 2018. 6(3):1128–37. https://doi.org/10.1039/c7ta07902h.

[26] Garche J, Dyer CK (eds.). Encyclopedia of electrochemical power sources. Amsterdam, Boston: Imprint of Elsevier, Academic Press. 2009.

[27] Ozawa K (ed.). Lithium ion rechargeable batteries: [materials, technology, and new applications]. 1st ed. Weinheim: Wiley-VCH. 2011.

[28] Mizushima K, Jones P, Wiseman P, Goodenough J. Li_xCoO_2 ($0<x\leqslant 1$): A new cathode material for batteries of high energy density. In: Solid State Ionics 1981. 3-4:171–4. https://doi.org/10.1016/0167-2738%2881%2990077-1.

[29] Li M, Lu J. Cobalt in lithium-ion batteries. In: Science 2020. 367(6481):979–80. https://doi.org/10.1126/science.aba9168.

[30] Sovacool BK. The precarious political economy of cobalt: Balancing prosperity, poverty, and brutality in artisanal and industrial mining in the Democratic Republic of the Congo. In: The Extractive Industries and Society 2019. 6(3):915–39. https://doi.org/10.1016/j.exis.2019.05.018.

[31] Nitta N, Wu F, Lee JT, Yushin G. Li-ion battery materials: present and future. In: Materials Today 2015. 18(5):252–64. https://doi.org/10.1016/j.mattod.2014.10.040.

[32] Andre D, Kim S-J, Lamp P, Lux SF, Maglia F, Paschos O, Stiaszny B. Future generations of cathode materials: an automotive industry perspective. In: J. Mater. Chem. A 2015. 3(13):6709–32. https://doi.org/10.1039/C5TA00361J.

[33] Kwon HJ, Hwang J-Y, Shin H-J, Jeong M-G, Chung KY, Sun Y-K, Jung H-G. Nano/Microstructured Silicon-Carbon Hybrid Composite Particles Fabricated with Corn Starch Biowaste as Anode Materials for Li-Ion Batteries. In: Nano Lett 2020. 20(1):625–35. https://doi.org/10.1021/acs.nanolett.9b04395.

[34] Andre D, Hain H, Lamp P, Maglia F, Stiaszny B. Future high-energy density anode materials from an automotive application perspective. In: J. Mater. Chem. A 2017. 5(33):17174–98. https://doi.org/10.1039/C7TA03108D.

[35] Sen C, Kar NC. Battery pack modeling for the analysis of battery management system of a hybrid electric vehicle. In: IEEE Conference on Vehicle Power and Propulsion (VPPC):207–12. https://doi.org/10.1109/VPPC.2009.5289848.

[36] Xing Y, Ma EW, Tsui KL, Pecht M. Battery Management Systems in Electric and Hybrid Vehicles. In: Energies 2011. 4(11):1840–57. https://doi.org/10.3390/en4111840.

[37] Sauer DU, Bopp G, Jossen A, Garche J, Rothert M, Wollny M. State of charge - What do we really speak about ? 1999. https://www.researchgate.net/publication/287336237_State_of_charge_-_What_do_we_really_speak_about. [accessed July 24, 2023].

[38] Kurzweil P, Dietlmeier OK. Elektrochemische Speicher. Wiesbaden: Springer Fachmedien Wiesbaden. 2018.

[39] Sauer DU, Bohlen O, Sanders T, Waag W, Schmidt R, Gerschler J. Batteriezustanderkennung: Mögliche Verfahrens- und Algorithmenansätze, Grenzen der Batteriezustandserkennung. https://www.researchgate.net/publication/284222616_Batteriezustanderkennung_Mogliche_Verfahrens-_und_Algorithmenansatze_Grenzen_der_Batteriezustandserkennung. [accessed August 07, 2023].

[40] Piłatowicz G, Marongiu A, Drillkens J, Sinhuber P, Sauer DU. A critical overview of definitions and determination techniques of the internal resistance using lithium-ion, lead-acid, nickel metal-hydride batteries and electrochemical double-layer capacitors as examples. In: Journal of Power Sources 2015. 296:365–76. https://doi.org/10.1016/j.jpowsour.2015.07.073.

[41] Waag W, Käbitz S, Sauer DU. Experimental investigation of the lithium-ion battery impedance characteristic at various conditions and aging states and its influence on the application. In: Applied Energy 2013. 102:885–97. https://doi.org/10.1016/j.apenergy.2012.09.030.

[42] Waag W, Fleischer C, Sauer DU. Critical review of the methods for monitoring of lithium-ion batteries in electric and hybrid vehicles. In: Journal of Power Sources 2014. 258:321–39. https://doi.org/10.1016/j.jpowsour.2014.02.064.

[43] Bundesverband Energiespeicher e.V., Bundesverband Solarwirtschaft e. V. Effizienzleitfaden für PV-Speichersysteme 2.0. 2019. https://www.bves.de/publikation/effizienzleitfaden-fuer-pv-speichersysteme/. [accessed August 25, 2023].

[44] Prechtl A. Vorlesungen über die Grundlagen der Elektrotechnik. 2nd ed. Wien, New York: Springer Wien New York. 2017.

[45] Stroe A-I, Stroe D-I, Swierczynski M, Teodorescu R, Kaer SK. Lithium-ion battery dynamic model for wide range of operating conditions. In: 2017 International Conference on Optimization of Electrical and Electronic Equipment (OPTIM) & 2017 Intl Aegean Conference on Electrical Machines and Power Electronics (ACEMP). IEEE. 2017 - 2017, p. 660–666. https://doi.org/10.1109/OPTIM.2017.7975044.

[46] Baumann M, Peters JF, Weil M, Grunwald A. CO_2 Footprint and Life-Cycle Costs of Electrochemical Energy Storage for Stationary Grid Applications. In: Energy Technol. 2017. 5(7):1071–83. https://doi.org/10.1002/ente.201600622.

[47] Elliott M, Swan LG, Dubarry M, Baure G. Degradation of electric vehicle lithium-ion batteries in electricity grid services. In: Journal of Energy Storage 2020. 32:101873. https://doi.org/10.1016/j.est.2020.101873.

[48] Birkl CR, Roberts MR, McTurk E, Bruce PG, Howey DA. Degradation diagnostics for lithium ion cells. In: Journal of Power Sources 2017. 341:373–86. https://doi.org/10.1016/j.jpowsour.2016.12.011.

[49] Birkl C. Diagnosis and prognosis of degradation in lithium-ion batteries [PhD thesis]. University of Oxford. 2017.

[50] Karthikeyan DK, Sikha G, White RE. Thermodynamic model development for lithium intercalation electrodes. In: Journal of Power Sources 2008. 185(2):1398–407. https://doi.org/10.1016/j.jpowsour.2008.07.077.

[51] Gantenbein S, Schönleber M, Weiss M, Ivers-Tiffée E. Capacity Fade in Lithium-Ion Batteries and Cyclic Aging over Various State-of-Charge Ranges. In: Sustainability 2019. 11(23):6697. https://doi.org/10.3390/su11236697.

[52] Schindler S, Danzer MA. A novel mechanistic modeling framework for analysis of electrode balancing and degradation modes in commercial lithium-ion cells. In: Journal of Power Sources 2017. 343:226–36. https://doi.org/10.1016/j.jpowsour.2017.01.026.

[53] Zhu J, Dewi Darma MS, Knapp M, Sørensen DR, Heere M, Fang Q, Wang X, Dai H, Mereacre L, Senyshyn A, Wei X, Ehrenberg H. Investigation of lithium-ion battery degradation mechanisms by combining differential voltage analysis and alternating current impedance. In: Journal of Power Sources 2020. 448:227575. https://doi.org/10.1016/j.jpowsour.2019.227575.

[54] Gao Y, Jiang J, Zhang C, Zhang W, Ma Z, Jiang Y. Lithium-ion battery aging mechanisms and life model under different charging stresses. In: Journal of Power Sources 2017. 356:103–14. https://doi.org/10.1016/j.jpowsour.2017.04.084.

[55] Li Y, Abdel-Monem M, Gopalakrishnan R, Berecibar M, Nanini-Maury E, Omar N, van den Bossche P, van Mierlo J. A quick on-line state of health estimation method for Li-ion battery with incremental capacity curves processed by Gaussian filter. In: Journal of Power Sources 2018. 373:40–53. https://doi.org/10.1016/j.jpowsour.2017.10.092.

[56] Ouyang M, Ren D, Lu L, Li J, Feng X, Han X, Liu G. Overcharge-induced capacity fading analysis for large format lithium-ion batteries with $Li_yNi_{1/3}Co_{1/3}Mn_{1/3}O_2$+ $Li_yMn_2O_4$ composite cathode. In: Journal of Power Sources 2015. 279:626–35. https://doi.org/10.1016/j.jpowsour.2015.01.051.

[57] Kuipers ML. Development of a virtual cell design tool for objective comparisons between state-of-the-art battery cells and next generation technologies [Dissertation]. RWTH Aachen University. 2023. https://doi.org/10.18154/RWTH-2023-11897.

[58] Weng C, Sun J, Peng H. A unified open-circuit-voltage model of lithium-ion batteries for state-of-charge estimation and state-of-health monitoring. In: Journal of Power Sources 2014. 258:228–37. https://doi.org/10.1016/j.jpowsour.2014.02.026.

[59] Tian J, Xiong R, Shen W, Sun F. Electrode ageing estimation and open circuit voltage reconstruction for lithium ion batteries. In: Energy Storage Materials 2021. 37:283–95. https://doi.org/10.1016/j.ensm.2021.02.018.

[60] Ovejas VJ, Cuadras A. Effects of cycling on lithium-ion battery hysteresis and overvoltage. In: Sci Rep 2019. 9(1):14875. https://doi.org/10.1038/s41598-019-51474-5.

[61] Tang X, Mao X, Lin J, Koch B. Li-ion Parameter Estimation for State of Charge. In: American Control Conference 2011. https://doi.org/10.1109/ACC.2011.5990963.

[62] Qian K, Huang B, Ran A, He Y-B, Li B, Kang F. State-of-health (SOH) evaluation on lithium-ion battery by simulating the voltage relaxation curves. In: Electrochimica Acta 2019. 303:183–91. https://doi.org/10.1016/j.electacta.2019.02.055.

[63] Pei L, Wang T, Lu R, Zhu C. Development of a voltage relaxation model for rapid open-circuit voltage prediction in lithium-ion batteries. In: Journal of Power Sources 2014. 253:412–8. https://doi.org/10.1016/j.jpowsour.2013.12.083.

[64] Petzl M. Zerstörungsfreie Charakterisierung von Lithium-Plating in Lithium-Ionen-Batterien [Dissertation]. Universität Ulm. 2015. https://doi.org/10.18725/OPARU-3343.

[65] Bernardi DM, Go J-Y. Analysis of pulse and relaxation behavior in lithium-ion batteries. In: Journal of Power Sources 2011. 196(1):412–27. https://doi.org/10.1016/j.jpowsour.2010.06.107.

[66] Kim J, Park S, Hwang S, Yoon W-S. Principles and Applications of Galvanostatic Intermittent Titration Technique for Lithium-ion Batteries. In: J. Electrochem. Sci. Technol 2022. 13(1):19–31. https://doi.org/10.33961/jecst.2021.00836.

[67] Creative Commons. Attribution-NonCommercial 4.0 International: CC BY-NC 4.0. https://creativecommons.org/licenses/by-nc/4.0/. [accessed August 03, 2024].
[68] Broussely M, Biensan P, Bonhomme F, Blanchard P, Herreyre S, Nechev K, Staniewicz RJ. Main aging mechanisms in Li ion batteries. In: Journal of Power Sources 2005. 146(1-2):90–6. https://doi.org/10.1016/j.jpowsour.2005.03.172.
[69] Edge JS, O'Kane S, Prosser R, Kirkaldy ND, Patel AN, Hales A, Ghosh A, Ai W, Chen J, Yang J, Li S, Pang M-C, Bravo Diaz L, Tomaszewska A, Marzook MW, Radhakrishnan KN, Wang H, Patel Y, Wu B, Offer GJ. Lithium ion battery degradation: what you need to know. In: Phys Chem Chem Phys 2021. 23(14):8200–21. https://doi.org/10.1039/d1cp00359c.
[70] Keil P, Schuster SF, Wilhelm J, Travi J, Hauser A, Karl RC, Jossen A. Calendar Aging of Lithium-Ion Batteries. In: J. Electrochem. Soc. 2016. 163(9):A1872-A1880. https://doi.org/10.1149/2.0411609jes.
[71] Vetter J, Novák P, Wagner MR, Veit C, Möller K-C, Besenhard JO, Winter M, Wohlfahrt-Mehrens M, Vogler C, Hammouche A. Ageing mechanisms in lithium-ion batteries. In: Journal of Power Sources 2005. 147(1-2):269–81. https://doi.org/10.1016/j.jpowsour.2005.01.006.
[72] Verma P, Maire P, Novák P. A review of the features and analyses of the solid electrolyte interphase in Li-ion batteries. In: Electrochimica Acta 2010. 55(22):6332–41. https://doi.org/10.1016/j.electacta.2010.05.072.
[73] Colclasure AM, Smith KA, Kee RJ. Modeling detailed chemistry and transport for solid-electrolyte-interface (SEI) films in Li–ion batteries. In: Electrochimica Acta 2011. 58:33–43. https://doi.org/10.1016/j.electacta.2011.08.067.
[74] Ecker M, Gerschler JB, Vogel J, Käbitz S, Hust F, Dechent P, Sauer DU. Development of a lifetime prediction model for lithium-ion batteries based on extended accelerated aging test data. In: Journal of Power Sources 2012. 215:248–57. https://doi.org/10.1016/j.jpowsour.2012.05.012.
[75] Ploehn HJ, Ramadass P, White RE. Solvent Diffusion Model for Aging of Lithium-Ion Battery Cells. In: Journal of Power Sources 2004. 151(3):A456. https://doi.org/10.1149/1.1644601.
[76] Aurbach D. Review of selected electrode–solution interactions which determine the performance of Li and Li ion batteries. In: Journal of Power Sources 2000. 89(2):206–18. https://doi.org/10.1016/S0378-7753%2800%2900431-6.

[77] Timmermans J-M, Nikolian A, Hoog J de, Gopalakrishnan R, Goutam S, Omar N, Coosemans T, van Mierlo J, Warnecke A, Sauer DU, Swierczynski M, Stroe DI, Martinez-Laserna E, Sarasketa-Zabala E, Gastelurrutia J, Nerea N. Batteries 2020 — Lithium-ion battery first and second life ageing, validated battery models, lifetime modelling and ageing assessment of thermal parameters. In: 18th European Conference 2016, p. 1–23. https://doi.org/10.1109/EPE.2016.7695698.

[78] Schmalstieg J, Käbitz S, Ecker M, Sauer DU. A holistic aging model for Li(NiMnCo)O_2 based 18650 lithium-ion batteries. In: Journal of Power Sources 2014. 257:325–34. https://doi.org/10.1016/j.jpowsour.2014.02.012.

[79] Petzl M, Kasper M, Danzer MA. Lithium plating in a commercial lithium-ion battery – A low-temperature aging study. In: Journal of Power Sources 2015. 275:799–807. https://doi.org/10.1016/j.jpowsour.2014.11.065.

[80] Baumhöfer T, Brühl M, Rothgang S, Sauer DU. Production caused variation in capacity aging trend and correlation to initial cell performance. In: Journal of Power Sources 2014. 247:332–8. https://doi.org/10.1016/j.jpowsour.2013.08.108.

[81] Sauer DU. Time-series cyclic aging data on 48 commercial NMC/graphite Sanyo/Panasonic UR18650E cylindrical cells. 2021. https://doi.org/10.18154/RWTH-2021-04545.

[82] Li W, Sengupta N, Dechent P, Howey D, Annaswamy A, Sauer DU. One-shot battery degradation trajectory prediction with deep learning. In: Journal of Power Sources 2021. 506:230024. https://doi.org/10.1016/j.jpowsour.2021.230024.

[83] Keil J, Paul N, Baran V, Keil P, Gilles R, Jossen A. Linear and Nonlinear Aging of Lithium-Ion Cells Investigated by Electrochemical Analysis and In-Situ Neutron Diffraction. In: J. Electrochem. Soc. 2019. 166(16):A3908-A3917. https://doi.org/10.1149/2.1271915jes.

[84] Attia PM, Bills A, Brosa Planella F, Dechent P, dos Reis G, Dubarry M, Gasper P, Gilchrist R, Greenbank S, Howey D, Liu O, Khoo E, Preger Y, Soni A, Sripad S, Stefanopoulou AG, Sulzer V. Review—“Knees” in Lithium-Ion Battery Aging Trajectories. In: J. Electrochem. Soc. 2022. 169(6):60517. https://doi.org/10.1149/1945-7111/ac6d13.

[85] Xiong R, Li L, Tian J. Towards a smarter battery management system: A critical review on battery state of health monitoring methods. In: Journal of Power Sources 2018. 405:18–29. https://doi.org/10.1016/j.jpowsour.2018.10.019.

[86] Wang Z, Feng G, Zhen D, Gu F, Ball A. A review on online state of charge and state of health estimation for lithium-ion batteries in electric vehicles. In: Energy Reports 2021. 7:5141–61. https://doi.org/10.1016/j.egyr.2021.08.113.

[87] Dubarry M, Liaw BY, Chen M-S, Chyan S-S, Han K-C, Sie W-T, Wu S-H. Identifying battery aging mechanisms in large format Li ion cells. In: Journal of Power Sources 2011. 196(7):3420–5. https://doi.org/10.1016/j.jpowsour.2010.07.029.
[88] Berecibar M, Gandiaga I, Villarreal I, Omar N, van Mierlo J, van den Bossche P. Critical review of state of health estimation methods of Li-ion batteries for real applications. In: Renewable and Sustainable Energy Reviews 2016. 56:572–87. https://doi.org/10.1016/j.rser.2015.11.042.
[89] Wu Y, Xue Q, Shen J, Lei Z, Chen Z, Liu Y. State of Health Estimation for Lithium-Ion Batteries Based on Healthy Features and Long Short-Term Memory. In: IEEE Access 2020. 8:28533–47. https://doi.org/10.1109/ACCESS.2020.2972344.
[90] Figgener J, Stenzel P, Kairies K-P, Linßen J, Haberschusz D, Wessels O, Robinius M, Stolten D, Sauer DU. The development of stationary battery storage systems in Germany – status 2020. In: Journal of Energy Storage 2021. 33:101982. https://doi.org/10.1016/j.est.2020.101982.
[91] Kairies K-P, Figgener J, Haberschusz D, Wessels O, Tepe B, Sauer DU. Market and technology development of PV home storage systems in Germany. In: Journal of Energy Storage 2019. 23:416–24. https://doi.org/10.1016/j.est.2019.02.023.
[92] Figgener J, Haberschusz D, Hecht C, Zurmühlen S, Sauer DU. Speichermonitoring BW 2.0 Schlussbericht (inhaltlicher Teil). 2022. http://dx.doi.org/10.13140/RG.2.2.17036.59528.
[93] Figgener J, Haberschusz D, Zurmühlen S, Sauer DU. Speichermonitoring BW: Schlussbericht (inhaltlicher Teil). Institut für Stromrichtertechnik und Elektrische Antriebe, RWTH Aachen. 2021. http://dx.doi.org/10.13140/RG.2.2.30516.37768.
[94] Figgener J, Haberschusz D, Kairies K-P, Wessels O, Zurmühlen S, Sauer DU. Speichermonitoring BW: Jahresbericht 2019. 2019. http://dx.doi.org/10.13140/RG.2.2.16244.30088. [accessed October 03, 2019].
[95] Figgener J, Hecht C, Haberschusz D, Bors J, Spreuer KG, Kairies K-P, Stenzel P, Sauer DU. The development of battery storage systems in Germany: A market review (status 2022). 2022. https://arxiv.org/abs/2203.06762v2.
[96] International Renewable Energy Agency. Electricity storage and renewables: Costs and markets to 2030. 2017. https://www.irena.org/-/media/Files/IRENA/Agency/Publication/2017/Oct/IRENA_Electricity_Storage_Costs_2017.pdf. [accessed August 05, 2023].
[97] Ioannis T, Dalius T, Natalia L. Li-ion batteries for mobility and stationary storage applications - Scenarios for costs and market growth 2018. https://doi.org/10.2760/87175.

[98] Ulbig A. Operational Flexibility in Electric Power Systems [Dissertation]. ETH Zurich. 2014. https://doi.org/10.3929/ETHZ-A-010337152.
[99] Ulbig A, Andersson G. Analyzing operational flexibility of electric power systems. In: International Journal of Electrical Power & Energy Systems 2015. 72:155–64. https://doi.org/10.1016/j.ijepes.2015.02.028.
[100] Ulbig A, Andersson G. On operational flexibility in power systems. In: 2012 IEEE Power and Energy Society General Meeting: San Diego, California, USA, 22-26 July 2012. [Piscataway, N.J.]: IEEE. 2012, p. 1–8. https://doi.org/10.1109/PESGM.2012.6344676.
[101] Bloomberg New Energy Finance. Global Storage Market to Double Six Times by 2030. 2017. https://about.bnef.com/blog/global-storage-market-double-six-times-2030/. [accessed August 05, 2023].
[102] Andrey C, Barberi P, Lacombe L, van Nuffel L, Gérard F, Gorenstein Dedecca J, Rademaekers K, El Idrissi Y, Crenes M. Study on energy storage – Contribution to the security of the electricity supply in Europe. European Commission. 2020. https://op.europa.eu/de/publication-detail/-/publication/a6eba083-932e-11ea-aac4-01aa75ed71a1. [accessed August 06, 2023].
[103] Bloomberg New Energy Finance. Global Energy Storage Market to Grow 15-Fold by 2030. 2022. https://about.bnef.com/blog/global-energy-storage-market-to-grow-15-fold-by-2030/. [accessed August 05, 2023].
[104] International Renewable Energy Agency. Electricity storage and renewables: Costs and markets to 2030. 2017. https://www.irena.org/publications/2017/oct/electricity-storage-and-renewables-costs-and-markets. [accessed August 05, 2023].
[105] International Energy Agency. Global EV Outlook 2022. 2022. https://www.iea.org/reports/global-ev-outlook-2022. [accessed August 05, 2023].
[106] 3Energie-Consulting GmbH & Co. KG. BVES Sector analysis 2022: Development and Perspectives for the German Energy Storage Sector. 2022. https://www.bves.de/publikation/bves-sector-analysis-2022/. [accessed August 03, 2023].
[107] German Solar Association. Statistical data on the German Solar Battery Storage and E-mobility Market. 2022. https://www.solarwirtschaft.de/datawall/uploads/2020/08/bsw_factsheet_solar_battery_storage_emob_eng.pdf. [accessed August 03, 2023].
[108] German Federal Motor Transport Authority. Vehicle Registrations. 2022. https://www.kba.de/EN/Statistik_en/Fahrzeuge_Vehicles/vehicles_node.html. [accessed August 05, 2023].
[109] NOW GmbH. Auswertung KBA Zahlen: Juni 2022. 2022. https://www.now-gmbh.de/wp-content/uploads/2022/07/KBA_Report_06-2022.pdf.[accessed November 30, 2022].

[110] Department of Energy. DOE Global Energy Storage Database. https://gesdb.sandia.gov/. [accessed August 03, 2023].

[111] Battke B, Schmidt TS, Grosspietsch D, Hoffmann VH. A review and probabilistic model of lifecycle costs of stationary batteries in multiple applications. In: Renewable and Sustainable Energy Reviews 2013. 25:240–50. https://doi.org/10.1016/j.rser.2013.04.023.

[112] Malhotra A, Battke B, Beuse M, Stephan A, Schmidt T. Use cases for stationary battery technologies: A review of the literature and existing projects. In: Renewable and Sustainable Energy Reviews 2016. 56:705–21. https://doi.org/10.1016/j.rser.2015.11.085.

[113] Schmidt O, Hawkes A, Gambhir A, Staffell I. The future cost of electrical energy storage based on experience rates. In: Nat Energy 2017. 2(8):964. https://doi.org/10.1038/nenergy.2017.110.

[114] Müller M, Viernstein L, Truong CN, Eiting A, Hesse HC, Witzmann R, Jossen A. Evaluation of grid-level adaptability for stationary battery energy storage system applications in Europe. In: Journal of Energy Storage 2017. 9:1–11. https://doi.org/10.1016/j.est.2016.11.005.

[115] Tan Z, Tan Q, Wang Y. A critical-analysis on the development of Energy Storage industry in China. In: Journal of Energy Storage 2018. 18:538–48. https://doi.org/10.1016/j.est.2018.05.013.

[116] Rohit AK, Rangnekar S. An overview of energy storage and its importance in Indian renewable energy sector: Part II – energy storage applications, benefits and market potential. In: Journal of Energy Storage 2017. 13:447–56. https://doi.org/10.1016/j.est.2017.07.012.

[117] Hecht C, Spreuer KG, Figgener J, Sauer DU. Market Review and Technical Properties of Electric Vehicles in Germany. In: Vehicles 2022. 4(4):903–16. https://doi.org/10.3390/vehicles4040049.

[118] Gruber L. Battery Database. 2023. https://lorenz-g.github.io/tesla-megapack-tracker/all-big-batteries.html. [accessed August 05, 2023].

[119] EuPD Research Sustainable Management GmbH. EndCustomer Monitor 9.0: The German PV Market from an End Customer Perspective Focus: Digitalization and post EEG. 2019. https://www.eupd-research.com [accessed July 06, 2019].

[120] macrom Marketingresearch & Consult. Der deutsche Markt für PV-Batteriespeicher-Systeme 2016. 2016. http://www.macrom.de [accessed July 06, 2019].

[121] IHS Markit Ltd. Grid-Connected Energy Storage Market Tracker. https://connect.ihsmarkit.com/. [accessed July 06, 2019].

[122] BloombergNEF. Energy Storage Market Outlook. https://about.bnef.com/. [accessed July 06, 2019].

[123] Pillot C. The rechargeable battery market 2017-2025. https://www.avicenne.com/reports_energy.php. [accessed October 05, 2019].

[124] GTM Research/ESA. U.S. Energy Storage Monitor - Executive Summary. 2016. https://www.ourenergypolicy.org/wp-content/uploads/2016/10/US-Energy-Storage-Monitor-Q3-2016_Exec-Summary.pdf. [accessed October 05, 2019].

[125] Anderman M. Extract from the xEV Industry Report: April 2019 Edition. 2019. https://totalbatteryconsulting.com. [accessed September 24, 2019].

[126] Wilson, Mark. Lazard's Levelized Cost of Storage Analysis: Version 4.0. 2018. https://www.lazard.com. [accessed September 24, 2019].

[127] pv magazine. Growing German storage market buoyed by falling prices. 2020. https://www.pv-magazine.com/2020/12/04/growing-german-storage-market-buoyed-by-falling-prices/. [accessed August 03, 2023].

[128] energate GmbH. Stationäre Batteriespeicher gefragt wie nie. 2020. https://www.energate-messenger.de/news/201630/stationaere-batteriespeicher-gefragt-wie-nie. [accessed August 20, 2023].

[129] Figgener J, Hecht C, Sauer DU. Battery Charts: Stationary battery storage registrations in Germany. www.battery-charts.de. [accessed August 18, 2023].

[130] Hecht C, Figgener J, Sauer DU. Mobility Charts: Electric vehicle registrations in Germany. www.mobility-charts.de. [accessed August 18, 2023].

[131] Palizban O, Kauhaniemi K. Energy storage systems in modern grids—Matrix of technologies and applications. In: Journal of Energy Storage 2016. 6:248–59. https://doi.org/10.1016/j.est.2016.02.001.

[132] Hesse H, Schimpe M, Kucevic D, Jossen A. Lithium-Ion Battery Storage for the Grid—A Review of Stationary Battery Storage System Design Tailored for Applications in Modern Power Grids. In: Energies 2017. 10(12):2107. https://doi.org/10.3390/en10122107.

[133] Haberschusz D, Kairies K-P, Wessels O, Magnor D, Sauer DU. Are PV Battery Systems Causing Ramping Problems in the German Power Grid? In: Energy Procedia 2017(135):424–33. https://doi.org/10.1016/j.egypro.2017.09.512.

[134] Fortenbacher P, Ulbig A, Andersson G. Optimal Placement and Sizing of Distributed Battery Storage in Low Voltage Grids Using Receding Horizon Control Strategies. In: IEEE Trans. Power Syst. 2018. 33(3):2383–94. https://doi.org/10.1109/TPWRS.2017.2746261.

[135] Bundesnetzagentur für Elektrizität, Gas, Telekommunikation und Eisenbahnen. Marktstammdatenregister. https://www.marktstammdatenregister.de/MaStR. [accessed August 03, 2023].

[136] Föderale IT-Kooperation. Data licence Germany – attribution – version 2.0. https://www.govdata.de/dl-de/by-2-0. [accessed August 03, 2024].

[137] Stenzel P, Linssen J, Robinius M, Stolten D. Data for: The Development of Stationary Battery Storage Systems in Germany – status 2020. In: Mendeley Data 2020. v1. https://doi.org/10.17632/jzfknp7sjv.1.

[138] Creative Commons. Attribution-NonCommercial 3.0 Unported: CC BY-NC 3.0. https://creativecommons.org/licenses/by-nc/3.0/. [accessed August 03, 2024].

[139] Bundesnetzagentur für Elektrizität, Gas, Telekommunikation, Post und Eisenbahnen. Namensnennung für Nutzung der Daten unter CC BY 4.0 Lizenz: "bundesnetzagentur.de". Elektromobilität: Öffentliche Ladeinfrastruktur. https://www.bundesnetzagentur.de/DE/Fachthemen/ElektrizitaetundGas/E-Mobilitaet/start.html. [accessed August 03, 2023].

[140] DAA GmbH. Bilateral data exchange. 2022. https://www.solaranlagen-portal.com/. [accessed May 01, 2022].

[141] Weniger J, Orth N, Meissner L, Schlüter C, Meyne J, Schreier R, Schwarz B, Munzke N. Stromspeicher-Inspektion 2023. Hochschule für Technik und Wirtschaft (HTW) Berlin; Karlsruher Institut für Technologie (KIT). 2023. https://solar.htw-berlin.de/studien/stromspeicher-inspektion-2023/. [accessed August 10, 2024]

[142] BSW-Solar. Solarbatterien boomen exponentiell. 2023. https://www.solarwirtschaft.de/2023/03/02/solarbatterien-boomen-exponentiell/. [accessed August 03, 2023].

[143] EuPD Research Sustainable Management GmbH. Heimspeicherboom: 220.000 neue Installationen im Heimspeichersegment dieses Jahr erwartet. 2022. https://www.eupd-research.com/heimspeicherboom-220-000-neue-installationen-im-heimspeichersegment-dieses-jahr-erwartet/. [accessed August 03, 2023].

[144] Robinius M, Otto A, Heuser P, Welder L, Syranidis K, Ryberg D, Grube T, Markewitz P, Peters R, Stolten D. Linking the Power and Transport Sectors—Part 1: The Principle of Sector Coupling. In: Energies 2017. 10(7):956. https://doi.org/10.3390/en10070956.

[145] Bundesnetzagentur für Elektrizität, Gas, Telekommunikation und Eisenbahnen. Genehmigung des Szenariorahmens 2023-2037/2045. 2022. https://www.netzentwicklungsplan.de/sites/default/files/2023-01/Szenariorahmen_2037_Genehmigung.pdf. [accessed August 20, 2023].

[146] Bundesministerium für Wirtschaft und Klimaschutz. Eröffnungsbilanz Klimaschutz. 2022. https://www.bmwi.de/Redaktion/DE/Downloads/Energie/220111_eroeffnungsbilanz_klimaschutz.pdf?__blob=publicationFile&v=22. [accessed August 03, 2023].

[147] Lichner C. Jetzt wirklich ein Durchbruch? 2023. https://www.pv-magazine.de/archiv/jetzt-wirklich-ein-durchbruch/. [accessed August 03, 2023].

[148] German Federal Network Agency. Hinweise zur Registrierungspflicht im Marktstammdatenregister für Notstromaggregate und Unterbrechungsfreie Stromversorgungssysteme (USV) und Sicherheitsbeleuchtungsanlagen. 2021. https://www.marktstammdatenregister.de/MaStRHilfe/files/regHilfen/Hinweise_zur_Registrierungspflicht_bei_Notstromaggregaten_USVs_und_Sicherheitsbeleuchtung.pdf. [accessed March 01, 2022].

[149] Sauer DU. Optimierung des Einsatzes von Blei-Säure-Akkumulatoren in Photovoltaik-Hybrid-Systemen unter spezieller Berücksichtigung der Batteriealterung [Dissertation]. Universität Ulm. 2003. https://doi.org/10.18725/OPARU-1816.

[150] Eurostat. NACE Rev. 2: Statistical classification of economic activities in the European Community. https://ec.europa.eu/eurostat/documents/3859598/5902521/KS-RA-07-015-EN.PDF.pdf/dd5443f5-b886-40e4-920d-9df03590ff91?t=1414781457000. [accessed August 07, 2023].

[151] Bundesministerium der Justiz. Bundes-Klimaschutzgesetz (KSG). 2021.

[152] BDEW Bundesverband der Energie- und Wasserwirtschaft e.V. BDEW-Strompreisanalyse Januar 2022: Haushalte und Industrie. 2022. https://www.bdew.de. [accessed March 05, 2022].

[153] Bundesministeriums der Justiz sowie des Bundesamts für Justiz. Verordnung über die Entgelte für den Zugang zu Elektrizitätsversorgungsnetzen (Stromnetzentgeltverordnung - StromNEV). 2005.

[154] Schäfer C. Hohe Erlöschancen für Großbatteriespeicher. 2023. https://www.pv-magazine.de/archiv/hohe-erloeschancen-fuer-grossbatteriespeicher/. [accessed August 03, 2023].

[155] Fleer J, Zurmühlen S, Meyer J, Badeda J, Stenzel P, Hake J-F, Uwe Sauer D. Price development and bidding strategies for battery energy storage systems on the primary control reserve market. In: Energy Procedia 2017. 135:143–57. https://doi.org/10.1016/j.egypro.2017.09.497.

[156] Fleer J, Zurmühlen S, Badeda J, Stenzel P, Hake J-F, Sauer DU. Model-based economic assessment of stationary battery systems providing primary control reserve. In: Energy Procedia 99 2016:11-24. https://doi.org/10.1016/j.egypro.2016.10.093.

[157] Fleer J, Stenzel P. Impact analysis of different operation strategies for battery energy storage systems providing primary control reserve. In: Journal of Energy Storage 2016. 8:320–38. https://doi.org/10.1016/j.est.2016.02.003.

[158] Jacqué K, Koltermann L, Figgener J, Zurmühlen S, Sauer DU. The influence of frequency containment reserve on the cycles of a hybrid stationary large-scale storage system. In: Journal of Energy Storage 2022. 52:105040. https://doi.org/10.1016/j.est.2022.105040.

[159] Jacqué K, Koltermann L, Figgener J, Zurmühlen S, Sauer DU. The influence of frequency containment reserve on the efficiency of a hybrid stationary large-scale storage system. In: Journal of Energy Storage 2022. 52:104961. https://doi.org/10.1016/j.est.2022.104961.

[160] Jacqué K, Koltermann L, Figgener J, Zurmühlen S, Sauer DU. The Influence of Frequency Containment Reserve on the Operational Data and the State of Health of the Hybrid Stationary Large-Scale Storage System. In: Energies 2022. 15(4):1342. https://doi.org/10.3390/en15041342.

[161] Koltermann L, Jacqué K, Figgener J, Zurmühlen S, Sauer DU. Operational Validation of a Power Distribution Algorithm for a Modular Megawatt Battery Storage System. In: Batteries & Supercaps 2023. https://doi.org/10.1002/batt.202200414.

[162] Koltermann L, Jacqué K, Figgener J, Zurmühlen S, Sauer DU. Balancing group deviation & balancing energy costs due to the provision of frequency containment reserve with a battery storage system in Germany. In: International Journal of Electrical Power & Energy Systems 2022. 142:108327. https://doi.org/10.1016/j.ijepes.2022.108327.

[163] Xu B, Oudalov A, Poland J, Ulbig A, Andersson G. BESS Control Strategies for Participating in Grid Frequency Regulation. In: IFAC Proceedings Volumes 2014. 47(3):4024–9. https://doi.org/10.3182/20140824-6-ZA-1003.02148.

[164] Borsche TS, Ulbig A, Andersson G. Impact of Frequency Control Reserve Provision by Storage Systems on Power System Operation. In: IFAC Proceedings Volumes 2014. 47(3):4038–43. https://doi.org/10.3182/20140824-6-ZA-1003.02257.

[165] Figgener J, Tepe B, Rücker F, Schoeneberger I, Hecht C, Jossen A, Sauer DU. The influence of frequency containment reserve flexibilization on the economics of electric vehicle fleet operation. In: Journal of Energy Storage 2022. 53:105138. https://doi.org/10.1016/j.est.2022.105138.

[166] German TSOs. Platform for the auction of Control Reserve. https://www.regelleistung.net. [accessed March 08, 2022].

[167] Schäfer C. Regelleistung-Online: Die Analyseplattform für den Regelleistungsmarkt. 2023. https://www.regelleistung-online.de/. [accessed August 03, 2023].

[168] Bundesnetzagentur für Elektrizität, Gas, Telekommunikation und Eisenbahnen. Innovationsausschreibungen. 2020. https://www.bundesnetzagentur.de/DE/Fachthemen/ElektrizitaetundGas/Ausschreibungen/Innovation/start.html. [accessed January 14, 2022].

[169] Bundesministeriums der Justiz und für Verbraucherschutz. Gesetz für den Ausbau erneuerbarer Energien (ErneuerbareEnergien-Gesetz - EEG 2021). 2021.

[170] Bundesministerium für Wirtschaft und Energie. Verordnung zu den Innovationsausschreibungen (Innovationsausschreibungsverordnung - InnAusV). 2020.

[171] Koller M, Borsche T, Ulbig A, Andersson G. Defining a degradation cost function for optimal control of a battery energy storage system. In: 2013 IEEE Grenoble Conference. Grenoble: IEEE. 2013, p. 1–6. https://doi.org/10.1109/PTC.2013.6652329.

[172] 50Hertz Transmission GmbH, Amprion GmbH, TenneT TSO GmbH, TransnetBW GmbH. Szenariorahmen zum Netzentwicklungsplan Strom 2035, Version 2021: Entwurf der Übertragungs netzbetreiber. Deutsche Übertragungsnetzbetreiber. 2020. https://www.netzentwicklungsplan.de/archiv/netzentwicklungsplan-2035-2021. [accessed August 07, 2023].

[173] Ulbig A, Borsche TS, Andersson G. Analyzing Rotational Inertia, Grid Topology and their Role for Power System Stability. In: IFAC-PapersOnLine 2015. 48(30):541–7. https://doi.org/10.1016/j.ifacol.2015.12.436.

[174] Koltermann L, Drenker KK, Celi Cortés ME, Jacqué K, Figgener J, Zurmühlen S, Sauer DU. Potential analysis of current battery storage systems for providing fast grid services like synthetic inertia – Case study on a 6 MW system. In: Journal of Energy Storage 2023. 57:106190. https://doi.org/10.1016/j.est.2022.106190.

[175] Ulbig A, Galus MD, Chatzivasileiadis S, Andersson G. General frequency control with aggregated control reserve capacity from time-varying sources: The case of PHEVs. In: Bulk Power System Dynamics and Control (iREP) - VIII (iREP), 2010 iREP Symposium. IEEE. 2010, p. 1–14. https://doi.org/10.1109/IREP.2010.5563261.

[176] Tepe B, Figgener J, Englberger S, Sauer DU, Jossen A, Hesse H. Optimal pool composition of commercial electric vehicles in V2G fleet operation of various electricity markets. In: Applied Energy 2022. 308:118351. https://doi.org/10.1016/j.apenergy.2021.118351.

[177] Bloomberg New Energy Finance. Lithium-ion Battery Pack Prices Rise for First Time to an Average of $151/kWh. 2022. https://about.bnef.com/blog/lithium-ion-battery-pack-prices-rise-for-first-time-to-an-average-of-151-kwh/. [accessed August 03, 2023].

[178] pv magazine. Marktübersicht große Batteriespeicher. 2023. https://www.pv-magazine.de/marktuebersichten/grosse-batteriespeicher/. [accessed August 03, 2023].

[179] pv magazine. pv magazine Marktübersicht für Großspeicher aktualisiert. 2020. https://www.pv-magazine.de/2020/03/13/pv-magazine-marktuebersicht-fuer-grossspeicher-aktualisiert/. [accessed July 10, 2020].

[180] pv magazine. pv magazine Marktübersicht für Groß- und Gewerbespeicher aktualisiert: Preise sinken leicht. https://www.pv-magazine.de/2021/03/18/pv-magazine-marktuebersicht-fuer-gross-und-gewerbespeicher-aktualisiert-preise-sinken-leicht/. [accessed August 03, 2023].
[181] pv magazine. Marktübersicht Groß- und Gewerbespeicher. 2022. https://www.pv-magazine.de/2022/04/01/pv-magazine-marktuebersicht-zu-gross-und-gewerbespeicher-aktualisiert/. [accessed August 03, 2023].
[182] Bloomberg New Energy Finance. Energy Storage Cost Outlook 2022. 2023. https://www.bnef.com. [accessed August 03, 2023].
[183] Stenzel P, Kotzur L, Stolten D, Figgener J, Haberschusz D, Sauer DU, Gottke V, Valentin F, Velten A, Schäfer F, Zunft S. Energiespeicher - Batterien, Wasserstoff, Wärme. In: BWK - Brennstoff-Wärme-Kraft. 2021.
[184] Figgener J, van Ouwerkerk J, Haberschusz D, Bors J, Woerner P, Mennekes M, Hildenbrand F, Hecht C, Kairies K-P, Wessels O, Sauer DU. Multi-year field measurements of home storage systems and their use in capacity estimation. In: Nat Energy 2024. https://doi.org/10.1038/s41560-024-01620-9.
[185] Figgener J, Haberschusz D, Wessels O, Kai-Philipp Kairies, Bors J, van Ouwerkerk J, Sauer DU. Data for: Multi-year field measurements of home storage systems used for capacity estimation. In: Zenodo 2024. https://doi.org/10.5281/zenodo.12091223.
[186] Kairies K-P, Haberschusz D, Wessels O, Strebel J, van Ouwerkerk J, Magnor D, Sauer DU. Real-Life Load Profiles of PV Battery Systems from Field Measurements. In: Energy Procedia 2016. 99:401–10. https://doi.org/10.1016/j.egypro.2016.10.130.
[187] Bundesministeriums der Justiz sowie des Bundesamts für Justiz. Erneuerbare-Energien-Gesetz vom 21. Juli 2014 (BGBl. I S. 1066), das zuletzt durch Artikel 4 des Gesetzes vom 26. Juli 2023 (BGBl. 2023 I Nr. 202) geändert worden ist: EEG 2023. 2023.
[188] Angenendt G, Zurmühlen S, Mir-Montazeri R, Magnor D, Sauer DU. Enhancing Battery Lifetime in PV Battery Home Storage System Using Forecast Based Operating Strategies. In: Energy Procedia 2016. 99:80–8. https://doi.org/10.1016/j.egypro.2016.10.100.
[189] Weniger J, Bergner J, Tjaden T, Quaschning V. Bedeutung von prognosebasierten Betriebsstrategien für die Netzintegration von PV-Speichersystemen. HTW Berlin. 2014. https://solar.htw-berlin.de/wp-content/uploads/WENIGER-2014-Prognosebasierte-Betriebsstrategien-fuer-die-Netzintegration-von-PV-Speichersystemen.pdf. [accessed August 07, 2023].
[190] Kairies K-P. Auswirkungen dezentraler Solarstromspeicher auf Netzbetreiber und Energieversorger [Dissertation]. RWTH Aachen University. 2019. https://doi.org/10.18154/RWTH-2019-06706.

[191] Xu B, Zhao J, Zheng T, Litvinov E, Kirschen DS. Factoring the Cycle Aging Cost of Batteries Participating in Electricity Markets. In: IEEE Trans. Power Syst. 2018. 33(2):2248–59. https://doi.org/10.1109/TPWRS.2017.2733339.
[192] Xu B, Oudalov A, Ulbig A, Andersson G, Kirschen DS. Modeling of Lithium-Ion Battery Degradation for Cell Life Assessment. In: IEEE Trans. Smart Grid 2018. 9(2):1131–40. https://doi.org/10.1109/TSG.2016.2578950.
[193] Muenzel V, Hoog J de, Brazil M, Vishwanath A, Kalyanaraman S. A Multi-Factor Battery Cycle Life Prediction Methodology for Optimal Battery Management. In: Kalyanaraman S, Seetharam DP, Shorey R, Ramchurn S, Srivastava M, editors. Proceedings of the 2015 ACM Sixth International Conference on Future Energy Systems. New York, NY, USA: ACM. 2015, p. 57–66. https://doi.org/10.1145/2768510.2768532.
[194] Köhler M, Jenne S, Pötter K, Zenner H. Zählverfahren und Lastannahme in der Betriebsfestigkeit. Berlin, Heidelberg: Springer Berlin Heidelberg. 2012.
[195] Movassagh K, Raihan SA, Balasingam B. Performance Analysis of Coulomb Counting Approach for State of Charge Estimation. In: 2019 IEEE Electrical Power and Energy Conference (EPEC). Piscataway, NJ: IEEE. 2019, p. 1–6. https://doi.org/10.1109/EPEC47565.2019.9074781.
[196] Xu J, Cao B, Cao J, Zou Z, Mi CC, Chen Z. A Comparison Study of the Model Based SOC Estimation Methods for Lithium-Ion Batteries. In: 2013 IEEE Vehicle Power and Propulsion Conference (VPPC). IEEE. 2013, p. 1–5. https://doi.org/10.1109/VPPC.2013.6671653.
[197] Hossain Lipu MS, Hannan MA, Hussain A, Ayob A, Saad MH, Karim TF, How DN. Data-driven state of charge estimation of lithium-ion batteries: Algorithms, implementation factors, limitations and future trends. In: Journal of Cleaner Production 2020. 277:124110. https://doi.org/10.1016/j.jclepro.2020.124110.
[198] Birkl CR, McTurk E, Roberts MR, Bruce PG, Howey DA. A Parametric Open Circuit Voltage Model for Lithium Ion Batteries. In: J. Electrochem. Soc. 2015. 162(12):A2271-A2280. https://doi.org/10.1149/2.0331512jes.
[199] Ecker M, Nieto N, Käbitz S, Schmalstieg J, Blanke H, Warnecke A, Sauer DU. Calendar and cycle life study of $Li(NiMnCo)O_2$-based 18650 lithium-ion batteries. In: Journal of Power Sources 2014. 248:839–51. https://doi.org/10.1016/j.jpowsour.2013.09.143.
[200] Lewerenz M, Marongiu A, Warnecke A, Sauer DU. Differential voltage analysis as a tool for analyzing inhomogeneous aging: A case study for $LiFePO_4$|Graphite cylindrical cells. In: Journal of Power Sources 2017. 368:57–67. https://doi.org/10.1016/j.jpowsour.2017.09.059.
[201] Lewerenz M, Warnecke A, Sauer DU. Post-mortem analysis on $LiFePO_4$ |Graphite cells describing the evolution & composition of covering layer on anode and their impact on cell performance. In: Journal of Power Sources 2017. 369:122–32. https://doi.org/10.1016/j.jpowsour.2017.10.003.

[202] Liu S, Winter M, Lewerenz M, Becker J, Sauer DU, Ma Z, Jiang J. Analysis of cyclic aging performance of commercial $Li_4Ti_5O_{12}$-based batteries at room temperature. In: Energy 2019. 173:1041–53. https://doi.org/10.1016/j.energy.2019.02.150.

[203] Harlow JE, Ma X, Li J, Logan E, Liu Y, Zhang N, Ma L, Glazier SL, Cormier MM, Genovese M, Buteau S, Cameron A, Stark JE, Dahn JR. A Wide Range of Testing Results on an Excellent Lithium-Ion Cell Chemistry to be used as Benchmarks for New Battery Technologies. In: J. Electrochem. Soc. 2019. 166(13):A3031-A3044. https://doi.org/10.1149/2.0981913jes.

[204] Glazier SL, Li J, Louli AJ, Allen JP, Dahn JR. An Analysis of Artificial and Natural Graphite in Lithium Ion Pouch Cells Using Ultra-High Precision Coulometry, Isothermal Microcalorimetry, Gas Evolution, Long Term Cycling and Pressure Measurements. In: J. Electrochem. Soc. 2017. 164(14):A3545-A3555. https://doi.org/10.1149/2.0421714jes.

[205] Ma X, Harlow JE, Li J, Ma L, Hall DS, Buteau S, Genovese M, Cormier M, Dahn JR. Hindering Rollover Failure of $Li[Ni_{0.5}Mn_{0.3}Co_{0.2}]O_2$/Graphite Pouch Cells during Long-Term Cycling. In: J. Electrochem. Soc. 2019. 166(4):A711-A724. https://doi.org/10.1149/2.0801904jes.

[206] Severson KA, Attia PM, Jin N, Perkins N, Jiang B, Yang Z, Chen MH, Aykol M, Herring PK, Fraggedakis D, Bazant MZ, Harris SJ, Chueh WC, Braatz RD. Data-driven prediction of battery cycle life before capacity degradation. In: Nat Energy 2019. 4(5):383–91. https://doi.org/10.1038/s41560-019-0356-8.

[207] Preger Y, Barkholtz HM, Fresquez A, Campbell DL, Juba BW, Romàn-Kustas J, Ferreira SR, Chalamala B. Degradation of Commercial Lithium-Ion Cells as a Function of Chemistry and Cycling Conditions. In: J. Electrochem. Soc. 2020. 167(12):120532. https://doi.org/10.1149/1945-7111/abae37.

[208] Devie A, Baure G, Dubarry M. Intrinsic Variability in the Degradation of a Batch of Commercial 18650 Lithium-Ion Cells. In: Energies 2018. 11(5):1031. https://doi.org/10.3390/en11051031.

[209] Zhang Y, Tang Q, Zhang Y, Wang J, Stimming U, Lee AA. Identifying degradation patterns of lithium ion batteries from impedance spectroscopy using machine learning. In: Nat Commun 2020. 11(1):1706. https://doi.org/10.1038/s41467-020-15235-7.

[210] Lewerenz M, Fuchs G, Becker L, Sauer DU. Irreversible calendar aging and quantification of the reversible capacity loss caused by anode overhang. In: Journal of Energy Storage 2018. 18:149–59. https://doi.org/10.1016/j.est.2018.04.029.

[211] Schmalstieg J, Kabitz S, Ecker M, Sauer DU. From accelerated aging tests to a lifetime prediction model: Analyzing lithium-ion batteries. In: 2013 World Electric Vehicle Symposium and Exhibition (EVS27). IEEE. 2013 - 2013, p. 1–12. https://doi.org/10.1109/EVS.2013.6914753.
[212] Woody M, Arbabzadeh M, Lewis GM, Keoleian GA, Stefanopoulou A. Strategies to limit degradation and maximize Li-ion battery service lifetime - Critical review and guidance for stakeholders. In: Journal of Energy Storage 2020. 28:101231. https://doi.org/10.1016/j.est.2020.101231.
[213] Ecker M, Shafiei Sabet P, Sauer DU. Influence of operational condition on lithium plating for commercial lithium-ion batteries – Electrochemical experiments and post-mortem-analysis. In: Applied Energy 2017. 206:934–46. https://doi.org/10.1016/j.apenergy.2017.08.034.
[214] Lewerenz M, Münnix J, Schmalstieg J, Käbitz S, Knips M, Sauer DU. Systematic aging of commercial $LiFePO_4$|Graphite cylindrical cells including a theory explaining rise of capacity during aging. In: Journal of Power Sources 2017. 345:254–63. https://doi.org/10.1016/j.jpowsour.2017.01.133.
[215] Deline C, Sekulic W, Jenket D, Jordan D, DiOrio N, Smith K. Field-Aging Test Bed for Behind-the-Meter PV + Energy Storage. In: 2019 IEEE 46th Photovoltaic Specialists Conference (PVSC), Chicago, IL, USA 2019:1341–5. https://doi.org/10.1109/PVSC40753.2019.8980775.
[216] Benato R, Dambone Sessa S, Musio M, Palone F, Polito R. Italian Experience on Electrical Storage Ageing for Primary Frequency Regulation. In: Energies 2018. 11(8):2087. https://doi.org/10.3390/en11082087.
[217] ITP Renewables. Public Report 9: Lithium-ion Battery Testing. 2020. https://batterytestcentre.com.au/reports/. [accessed August 07, 2023].
[218] Dubarry M, Devie A, Stein K, Tun M, Matsuura M, Rocheleau R. Battery Energy Storage System battery durability and reliability under electric utility grid operations: Analysis of 3 years of real usage. In: Journal of Power Sources 2017. 338:65–73. https://doi.org/10.1016/j.jpowsour.2016.11.034.
[219] Dubarry M, Tun M, Baure G, Matsuura M, Rocheleau RE. Battery Durability and Reliability under Electric Utility Grid Operations: Analysis of On-Site Reference Tests. In: Electronics 2021. 10(13):1593. https://doi.org/10.3390/electronics10131593.
[220] Kubiak P, Cen Z, López CM, Belharouak I. Calendar aging of a 250 kW/500 kWh Li-ion battery deployed for the grid storage application. In: Journal of Power Sources 2017. 372:16–23. https://doi.org/10.1016/j.jpowsour.2017.10.063.
[221] Hund TD, Gates S. PV hybrid system and battery test results from Grasmere Idaho. In: IEEE 2002. https://doi.org/10.1109/PVSC.2002.1190876.

[222] Gustavsson M, Mtonga D. Lead-acid battery capacity in solar home systems—Field tests and experiences in Lundazi, Zambia. In: Solar Energy 2005. 79(5):551–8. https://doi.org/10.1016/j.solener.2004.10.010.

[223] Lansburg S, Brenier A, Boulais R. Passing the 10-year Mark - a Multi-Year, Multi-Technology Analysis of Ni-Cd Field Data. In: IEEE 2010. https://doi.org/10.1109/INTLEC.2010.5525695.

[224] Schaeck S, Karspeck T, Ott C, Weckler M, Stoermer AO. A field operational test on valve-regulated lead-acid absorbent-glass-mat batteries in micro-hybrid electric vehicles. Part I. Results based on kernel density estimation. In: Journal of Power Sources 2011. 196(5):2924–32. https://doi.org/10.1016/j.jpowsour.2010.09.034.

[225] Calearo L, Ziras C, Thingvad A, Marinelli M. Agnostic Battery Management System Capacity Estimation for Electric Vehicles. In: Energies 2022. 15(24):9656. https://doi.org/10.3390/en15249656.

[226] Kim SK, Cho KH, Kim JY, Byeon G. Field study on operational performance and economics of lithium-polymer and lead-acid battery systems for consumer load management. In: Renewable and Sustainable Energy Reviews 2019. 113:109234. https://doi.org/10.1016/j.rser.2019.06.041.

[227] Xu Z, Wang J, Lund PD, Zhang Y. Estimation and prediction of state of health of electric vehicle batteries using discrete incremental capacity analysis based on real driving data. In: Energy 2021. 225:120160. https://doi.org/10.1016/j.energy.2021.120160.

[228] Zhang Q, Li X, Zhou C, Zou Y, Du Z, Sun M, Ouyang Y, Yang D, Liao Q. State-of-health estimation of batteries in an energy storage system based on the actual operating parameters. In: Journal of Power Sources 2021. 506:230162. https://doi.org/10.1016/j.jpowsour.2021.230162.

[229] Abedi Varnosfaderani M, Strickland D, Ruse M, Brana Castillo E. Sweat Testing Cycles of Batteries for Different Electrical Power Applications. In: IEEE Access 2019. 7:132333–42. https://doi.org/10.1109/ACCESS.2019.2940846.

[230] Jannati M, Foroutan E. Analysis of power allocation strategies in the smoothing of wind farm power fluctuations considering lifetime extension of BESS units. In: Journal of Cleaner Production 2020. 266:122045. https://doi.org/10.1016/j.jclepro.2020.122045.

[231] Karoui F, Ha D-L, Delaplagne T, Bouaaziz M-F, Eudier V, Lévy M. Diagnosis and prognosis of complex energy storage systems: tools development and feedback on four installed systems. In: Energy Procedia 2018. 155:61–76. https://doi.org/10.1016/j.egypro.2018.11.066.

[232] Koller M, Borsche T, Ulbig A, Andersson G. Review of grid applications with the Zurich 1MW battery energy storage system. In: Electric Power Systems Research 2015. 120:128–35. https://doi.org/10.1016/j.epsr.2014.06.023.

[233] Münderlein J, Steinhoff M, Zurmühlen S, Sauer DU. Analysis and evaluation of operations strategies based on a large scale 5 MW and 5 MWh battery storage system. In: Journal of Energy Storage 2019. 24:100778. https://doi.org/10.1016/j.est.2019.100778.
[234] Li W, Sengupta N, Dechent P, Howey D, Annaswamy A, Sauer DU. Online capacity estimation of lithium-ion batteries with deep long short-term memory networks. In: Journal of Power Sources 2021. 482:228863. https://doi.org/10.1016/j.jpowsour.2020.228863.
[235] Xu J, Cao B, Chen Z, Zou Z. An online state of charge estimation method with reduced prior battery testing information. In: International Journal of Electrical Power & Energy Systems 2014. 63:178–84. https://doi.org/10.1016/j.ijepes.2014.06.017.
[236] How DN, Hannan MA, Hossain Lipu MS, Ker PJ. State of Charge Estimation for Lithium-Ion Batteries Using Model-Based and Data-Driven Methods: A Review. In: IEEE Access 2019. 7:136116–36. https://doi.org/10.1109/ACCESS.2019.2942213.
[237] Yu Q, Xiong R, Yang R, Pecht MG. Online capacity estimation for lithium-ion batteries through joint estimation method. In: Applied Energy 2019. 255:113817. https://doi.org/10.1016/j.apenergy.2019.113817.
[238] Kim T, Adhikaree A, Kang D, Kim M, Oh C-Y, Baek J. A real-time condition monitoring for lithium-ion batteries using a low-price microcontroller. In: 2017 IEEE Energy Conversion Congress and Exposition (ECCE). IEEE. 2017 - 2017, p. 5248–5253. https://doi.org/10.1109/ECCE.2017.8096881.
[239] Kim T, Adhikaree A, Pandey R, Kang D-W, Kim M, Oh C-Y, Baek J-W. An On-Board Model-Based Condition Monitoring for Lithium-Ion Batteries. In: IEEE Trans. on Ind. Applicat. 2019. 55(2):1835–43. https://doi.org/10.1109/TIA.2018.2881183.
[240] Wang Y, Gao G, Li X, Chen Z. A fractional-order model-based state estimation approach for lithium-ion battery and ultra-capacitor hybrid power source system considering load trajectory. In: Journal of Power Sources 2020. 449:227543. https://doi.org/10.1016/j.jpowsour.2019.227543.
[241] Li W, Fan Y, Ringbeck F, Jöst D, Han X, Ouyang M, Sauer DU. Electrochemical model-based state estimation for lithium-ion batteries with adaptive unscented Kalman filter. In: Journal of Power Sources 2020. 476:228534. https://doi.org/10.1016/j.jpowsour.2020.228534.
[242] Marcicki J, Todeschini F, Onori S, Canova M. Nonlinear Parameter Estimation for Capacity Fade in Lithium-Ion Cells Based on a Reduced-Order Electrochemical Model. In: American Control Conference 2012. https://doi.org/10.1109/ACC.2012.6315257.
[243] Doyle M, Fuller TF, Newman J. Modeling of Galvanostatic Charge and Discharge of the Lithium/Polymer/Insertion Cell. In: J. Electrochem. Soc. 1993. 140(6):1526–33. https://doi.org/10.1149/1.2221597.

[244] Fuller TF, Doyle M, Newman J. Simulation and Optimization of the Dual Lithium Ion Insertion Cell. In: J. Electrochem. Soc. 1994. 141(1):1–10. https://doi.org/10.1149/1.2054684.

[245] Richardson RR, Birkl CR, Osborne MA, Howey DA. Gaussian Process Regression for In Situ Capacity Estimation of Lithium-Ion Batteries. In: IEEE Trans. Ind. Inf. 2019. 15(1):127–38. https://doi.org/10.1109/TII.2018.2794997.

[246] Yang D, Zhang X, Pan R, Wang Y, Chen Z. A novel Gaussian process regression model for state-of-health estimation of lithium-ion battery using charging curve. In: Journal of Power Sources 2018. 384:387–95. https://doi.org/10.1016/j.jpowsour.2018.03.015.

[247] Wei J, Dong G, Chen Z. Remaining Useful Life Prediction and State of Health Diagnosis for Lithium-Ion Batteries Using Particle Filter and Support Vector Regression. In: IEEE Trans. Ind. Electron. 2018. 65(7):5634–43. https://doi.org/10.1109/TIE.2017.2782224.

[248] Klass V, Behm M, Lindbergh G. A support vector machine-based state-of-health estimation method for lithium-ion batteries under electric vehicle operation. In: Journal of Power Sources 2014. 270:262–72. https://doi.org/10.1016/j.jpowsour.2014.07.116.

[249] Chemali E, Kollmeyer PJ, Preindl M, Ahmed R, Emadi A. Long Short-Term Memory Networks for Accurate State-of-Charge Estimation of Li-ion Batteries. In: IEEE Trans. Ind. Electron. 2018. 65(8):6730–9. https://doi.org/10.1109/TIE.2017.2787586.

[250] Shen S, Sadoughi M, Chen X, Hong M, Hu C. A deep learning method for online capacity estimation of lithium-ion batteries. In: Journal of Energy Storage 2019. 25:100817. https://doi.org/10.1016/j.est.2019.100817.

[251] Chaoui H, Ibe-Ekeocha CC. State of Charge and State of Health Estimation for Lithium Batteries Using Recurrent Neural Networks. In: IEEE Trans. Veh. Technol. 2017. 66(10):8773–83. https://doi.org/10.1109/TVT.2017.2715333.

[252] dos Reis G, Strange C, Yadav M, Li S. Lithium-ion battery data and where to find it. In: Energy and AI 2021. 5(4):100081. https://doi.org/10.1016/j.egyai.2021.100081.

[253] Attia PM, Grover A, Jin N, Severson KA, Markov TM, Liao Y-H, Chen MH, Cheong B, Perkins N, Yang Z, Herring PK, Aykol M, Harris SJ, Braatz RD, Ermon S, Chueh WC. Closed-loop optimization of fast-charging protocols for batteries with machine learning. In: Nature 2020. 578(7795):397–402. https://doi.org/10.1038/s41586-020-1994-5.

[254] Saha B, Goebel K. Battery Data Set. 2007. http://ti.arc.nasa.gov/project/prognostic-data-repository. [accessed August 07, 2023].

[255] Center for Advanced Life Cycle Engineering. Battery Data. University of Maryland. https://calce.umd.edu/battery-data. [accessed August 07, 2023].

[256] Juarez Robles D, Jeevarajan JA, Mukherjee PP. Aging Test - Cylindrical Cell - Part 01 - Single Cells. In: Zenodo. https://doi.org/10.5281/zenodo.4443455.
[257] Catenaro E, Onori S. Experimental data of three lithium-ion batteries under galvanostatic discharge tests at different C-rates and operating temperatures. In: Mendeley Data. https://doi.org/10.17632/KXSBR4X3J2.2.
[258] Birkl C, Howey D. Oxford Battery Degradation Dataset 1. In: Oxford University Research Archive 2017. https://doi.org/10.5287/bodleian:KO2kdmYGg.
[259] Kollmeyer P. Panasonic 18650PF Li-ion Battery Data. In: Mendeley Data 2018. https://doi.org/10.17632/wykht8y7tg.1.
[260] Luzi M. Automotive Li-ion Cell Usage Data Set. In: IEEE DataPort. https://doi.org/10.21227/ce9q-jr19.
[261] Wang Y, Liu C, Pan R, Chen Z. Experimental data of lithium-ion battery and ultracapacitor under DST and UDDS profiles at room temperature. In: Data Brief 2017. 12:161–3. https://doi.org/10.1016/j.dib.2017.01.019.
[262] Pozzato G, Allam A, Pulvirenti L, Negoita GA, Paxton WA, Onori S. Real-world electric vehicle data: driving and charging. In: Mendeley Data. https://doi.org/10.17632/7vdkzpnjgj.2.
[263] Bole B, Kulkarni C, Daigle M. Randomized Battery Usage Data Set. In: NASA Prognostics Data Repository. https://www.nasa.gov/intelligent-systems-division/discovery-and-systems-health/pcoe/pcoe-data-set-repository/. [accessed August 07, 2023].
[264] Dubarry M. Graphite//LFP synthetic training diagnosis dataset. In: Mendeley Data. https://doi.org/10.17632/bs2j56pn7y.1.
[265] Dubarry M. Graphite//LFP synthetic training prognosis dataset. In: Mendeley Data. https://doi.org/10.17632/6s6ph9n8zg.1.
[266] Rücker F, Figgener J, Schoeneberger I, Sauer DU. Dataset to „Battery Electric Vehicles in Commercial Fleets: Use profiles, battery aging, and open-access data“. 2024. https://doi.org/10.18154/RWTH-2024-01907.
[267] Pozzato G, Allam A, Pulvirenti L, Negoita GA, Paxton WA, Onori S. Analysis and key findings from real-world electric vehicle field data. In: Joule 2023. https://doi.org/10.1016/j.joule.2023.07.018.
[268] Rücker F, Figgener J, Schoeneberger I, Sauer DU. Battery Electric Vehicles in Commercial Fleets: Use profiles, battery aging, and open-access data. In: Journal of Energy Storage 2024. 86:111030. https://doi.org/10.1016/j.est.2024.111030.
[269] KfW-Bank. Anlage zum Merkblatt: Erneuerbare Energien – Speicher. Technische Mindestanforderungen. 2018. https://www.kfw.de/PDF/Download-Center/F%C3%B6rderprogramme-%28Inlandsf%C3%B6rderung%29/PDF-Dokumente/6000003711_M_275_Anlage_TMA.pdf. [accessed June 07, 2018].

[270] Beck D, Dechent P, Junker M, Sauer DU, Dubarry M. Inhomogeneities and Cell-to-Cell Variations in Lithium-Ion Batteries, a Review. In: Energies 2021. 14(11):3276. https://doi.org/10.3390/en14113276.

[271] Li A, Pelissier S, Venet P, Gyan P. Fast Characterization Method for Modeling Battery Relaxation Voltage. In: Batteries 2016. 2(2):7. https://doi.org/10.3390/batteries2020007.

[272] Goldammer E, Kowal J. Determination of the Distribution of Relaxation Times by Means of Pulse Evaluation for Offline and Online Diagnosis of Lithium-Ion Batteries. In: Batteries 2021. https://doi.org/10.3390/batteries7020036.

[273] Jossen A. Fundamentals of battery dynamics. In: Journal of Power Sources 2006. 154(2):530–8. https://doi.org/10.1016/j.jpowsour.2005.10.041.

[274] Dahn JR, Burns JC, Stevens D. Importance of Coulombic Efficiency Measurements in R&D Efforts to Obtain Long-Lived Li-Ion Batteries. In: Electrochemical Society Interface 2016. https://doi.org/10.1149/2.F07163if.

[275] Dubarry M, Anseán D. Best practices for incremental capacity analysis. In: Front. Energy Res. 2022. 10. https://doi.org/10.3389/fenrg.2022.1023555.

[276] LYGTE. Battery test 18650: comparator. https://lygte-info.dk/review/batteries2012/Common18650comparator.php. [accessed August 07, 2023].

[277] Vermeer W, Chandra Mouli GR, Bauer P. A Comprehensive Review on the Characteristics and Modeling of Lithium-Ion Battery Aging. In: IEEE Trans. Transp. Electrific. 2022. 8(2):2205–32. https://doi.org/10.1109/TTE.2021.3138357.

[278] Diao W, Kim J, Azarian MH, Pecht M. Degradation modes and mechanisms analysis of lithium-ion batteries with knee points. In: Electrochimica Acta 2022. 431:141143. https://doi.org/10.1016/j.electacta.2022.141143.

[279] Chen K, Li X. Accurate determination of battery discharge characteristics – A comparison between two battery temperature control methods. In: Journal of Power Sources 2014. 247:961–6. https://doi.org/10.1016/j.jpowsour.2013.09.060.

[280] Figgener J, Bors J, Kuipers M, Hildenbrand F, Junker M, Koltermann L, Woerner P, Mennekes M, Haberschusz D, Kairies K-P, Sauer DU. Degradation mode estimation using reconstructed open circuit voltage curves from multi-year home storage field data. Preprint version 1. 2024. https://doi.org/10.48550/arXiv.2411.08025.

[281] Pastor-Fernández C, Uddin K, Chouchelamane GH, Widanage WD, Marco J. A Comparison between Electrochemical Impedance Spectroscopy and Incremental Capacity-Differential Voltage as Li-ion Diagnostic Techniques to Identify and Quantify the Effects of Degradation Modes within Battery Management Systems. In: Journal of Power Sources 2017. 360:301–18. https://doi.org/10.1016/j.jpowsour.2017.03.042.

[282] Wang X, Wei X, Zhu J, Dai H, Zheng Y, Xu X, Chen Q. A review of modeling, acquisition, and application of lithium-ion battery impedance for onboard battery management. In: eTransportation 2021. 7:100093. https://doi.org/10.1016/j.etran.2020.100093.
[283] Carkhuff BG, Demirev PA, Srinivasan R. Impedance-Based Battery Management System for Safety Monitoring of Lithium-Ion Batteries. In: IEEE Trans. Ind. Electron. 2018. 65(8):6497–504. https://doi.org/10.1109/TIE.2017.2786199.
[284] Ludwig S, Zilberman I, Horsche MF, Wohlers T, Jossen A. Pulse resistance based online temperature estimation for lithium-ion cells. In: Journal of Power Sources 2021. 490:229523. https://doi.org/10.1016/j.jpowsour.2021.229523.
[285] Rastegarpanah A, Hathaway J, Ahmeid M, Lambert S, Walton A, Stolkin R. A rapid neural network–based state of health estimation scheme for screening of end of life electric vehicle batteries. In: Proceedings of the Institution of Mechanical Engineers, Part I: Journal of Systems and Control Engineering. Sage Journal. 2021. 235(3):330–46. https://doi.org/10.1177/0959651820953254.
[286] Chung H-C. Charge and discharge profiles of repurposed $LiFePO_4$ batteries based on the UL 1974 standard. In: Sci Data 2021. 8(1):165. https://doi.org/10.1038/s41597-021-00954-3.
[287] Baghdadi I, Briat O, Gyan P, Vinassa JM. State of health assessment for lithium batteries based on voltage–time relaxation measure. In: Electrochimica Acta 2016. 194:461–72. https://doi.org/10.1016/j.electacta.2016.02.109.
[288] Aitio A, Howey DA. Predicting battery end of life from solar off-grid system field data using machine learning. In: Joule 2021. 5(12):3204–20. https://doi.org/10.1016/j.joule.2021.11.006.
[289] Li W, Chen J, Quade K, Luder D, Gong J, Sauer DU. Battery degradation diagnosis with field data, impedance-based modeling and artificial intelligence. In: Energy Storage Materials 2022. 53:391–403. https://doi.org/10.1016/j.ensm.2022.08.021.
[290] Zhu J, Huang Y, Knapp M, Liu X, Wang Y, Gopaluni RB, Cao Y, Heere M, Mühlbauer M, Mereacre L, Dai H, Senyshyn A, Wei X, Ehrenberg H. Data-driven lithium-ion battery capacity estimation from voltage relaxation 2021. https://doi.org/10.21203/rs.3.rs-770709/v1.
[291] Reichert M, Andre D, Rösmann A, Janssen P, Bremes H-G, Sauer DU, Passerini S, Winter M. Influence of relaxation time on the lifetime of commercial lithium-ion cells. In: Journal of Power Sources 2013. 239:45–53. https://doi.org/10.1016/j.jpowsour.2013.03.053.

[292] Fang Q, Wei X, Lu T, Dai H, Zhu J. A State of Health Estimation Method for Lithium-Ion Batteries Based on Voltage Relaxation Model. In: Energies 2019. https://doi.org/10.3390/en12071349.

[293] Ghodsi A. Dimensionality reduction: a short tutorial. Department of Statistics and Actuarial Science, Univ. of Waterloo, Ontario, Canada. https://www.math.uwaterloo.ca/~aghodsib/courses/f10stat946/readings/tutorial_stat890.pdf. [accessed August 07, 2023].

[294] Ghojogh B, Crowley M. Unsupervised and Supervised Principal Component Analysis: Tutorial. 2019. https://doi.org/10.48550/arXiv.1906.03148.

[295] Werner S, Rink JC, Riedel-Kruse IH, Friedrich BM. Shape mode analysis exposes movement patterns in biology: flagella and flatworms as case studies. In: PLoS One 2014. 9(11):e113083. https://doi.org/10.1371/journal.pone.0113083.

[296] Montgomery DC, Peck EA, Vining GG. Introduction to linear regression analysis. Hoboken, NJ: John Wiley & Sons, Inc. 2021.

[297] Goodfellow I, Bengio Y, Courville A. Deep learning. Cambridge, Massachusetts: The MIT Press. 2016.

[298] Hassan S, Attia S, Salama KN, Mostafa H. EANN: Energy Adaptive Neural Networks. In: Electronics 2020. 9(5):746. https://doi.org/10.3390/electronics9050746.

[299] Yu Q-Q, Xiong R, Wang L-Y, Lin C. A Comparative Study on Open Circuit Voltage Models for Lithium-ion Batteries. In: Chin. J. Mech. Eng. 2018. 31(1). https://doi.org/10.1186/s10033-018-0268-8.

[300] Ren Z, Du C, Wu Z, Shao J, Deng W. A comparative study of the influence of different open circuit voltage tests on model-based state of charge estimation for lithium-ion batteries. In: International Journal of Energy Research 2021. 45(9):13692–711. https://doi.org/10.1002/er.6700.

[301] Farmann A, Sauer DU. A study on the dependency of the open-circuit voltage on temperature and actual aging state of lithium-ion batteries. In: Journal of Power Sources 2017. 347:1–13. https://doi.org/10.1016/j.jpowsour.2017.01.098.

[302] Pastor-Fernández C, Yu TF, Widanage WD, Marco J. Critical review of non-invasive diagnosis techniques for quantification of degradation modes in lithium-ion batteries. In: Renewable and Sustainable Energy Reviews 2019. 109:138–59. https://doi.org/10.1016/j.rser.2019.03.060.

[303] Petzl M, Danzer MA. Advancements in OCV Measurement and Analysis for Lithium-Ion Batteries. In: IEEE Trans. Energy Convers. 2013. 28(3):675–81. https://doi.org/10.1109/TEC.2013.2259490.

[304] Dubarry M, Svoboda V, Hwu R, Yann Liaw B. Incremental Capacity Analysis and Close-to-Equilibrium OCV Measurements to Quantify Capacity Fade in Commercial Rechargeable Lithium Batteries. In: Electrochem. Solid-State Lett. 2006. 9(10):A454. https://doi.org/10.1149/1.2221767.

[305] Dubarry M, Liaw BY. Identify capacity fading mechanism in a commercial $LiFePO_4$ cell. In: Journal of Power Sources 2009. 194(1):541–9. https://doi.org/10.1016/j.jpowsour.2009.05.036.
[306] Plattard T, Barnel N, Assaud L, Franger S, Duffault J-M. Combining a Fatigue Model and an Incremental Capacity Analysis on a Commercial NMC/Graphite Cell under Constant Current Cycling with and without Calendar Aging. In: Batteries 2019. 5(1):36. https://doi.org/10.3390/batteries 5010036.
[307] Berecibar M, Dubarry M, Villarreal I, Omar N, van Mierlo J. Degradation Mechanisms Detection for HP and HE NMC Cells Based on Incremental Capacity Curves. In: 2016 IEEE Vehicle Power and Propulsion Conference (VPPC): Proceedings 17-20 October 2016, Hangzhou, China. Piscataway, NJ: IEEE. 2016, p. 1–5. https://doi.org/10.1109/VPPC.2016.7791648.
[308] Dubarry M, Truchot C, Cugnet M, Liaw BY, Gering K, Sazhin S, Jamison D, Michelbacher C. Evaluation of commercial lithium-ion cells based on composite positive electrode for plug-in hybrid electric vehicle applications. Part I: Initial characterizations. In: Journal of Power Sources 2011. 196(23):10328–35. https://doi.org/10.1016/j.jpowsour.2011.08.077.
[309] Han X, Ouyang M, Lu L, Li J, Zheng Y, Li Z. A comparative study of commercial lithium ion battery cycle life in electrical vehicle: Aging mechanism identification. In: Journal of Power Sources 2014. 251:38–54. https://doi.org/10.1016/j.jpowsour.2013.11.029.
[310] Maures M, Capitaine A, Delétage J-Y, Vinassa J-M, Briat O. Lithium-ion battery SoH estimation based on incremental capacity peak tracking at several current levels for online application. In: Microelectronics Reliability 2020. 114:113798. https://doi.org/10.1016/j.microrel.2020.113798.
[311] Dubarry M, Truchot C, Liaw BY. Synthesize battery degradation modes via a diagnostic and prognostic model. In: Journal of Power Sources 2012. 219:204–16. https://doi.org/10.1016/j.jpowsour.2012.07.016.
[312] Samadani E, Farhad S, Panchal S, Fraser R, Fowler M. Modeling and Evaluation of Li-Ion Battery Performance Based on the Electric Vehicle Field Tests. In: SAE International 2014. https://doi.org/10.4271/2014-01-1848.
[313] Weng C, Cui Y, Sun J, Peng H. On-board state of health monitoring of lithium-ion batteries using incremental capacity analysis with support vector regression. In: Journal of Power Sources 2013. 235:36–44. https://doi.org/10.1016/j.jpowsour.2013.02.012.
[314] Marongiu A, Sauer DU. On-board aging estimation using half-cell voltage curves for $LiFePO_4$ cathode-based lithium-ion batteries for EV applications. In: Int.J Automot. Technol. 2016. 17(3):465–72. https://doi.org/10.1007/s12239-016-0048-3.

[315] Marongiu A, Nlandi N, Rong Y, Sauer DU. On-board capacity estimation of lithium iron phosphate batteries by means of half-cell curves. In: Journal of Power Sources 2016. 324:158–69. https://doi.org/10.1016/j.jpowsour.2016.05.041.

[316] Tang X, Wang Y, Liu Q, Gao F. Reconstruction of the incremental capacity trajectories from current-varying profiles for lithium-ion batteries. In: iScience 2021. 24(10):103103. https://doi.org/10.1016/j.isci.2021.103103.

[317] Keil P, Jossen A. Calendar Aging of NCA Lithium-Ion Batteries Investigated by Differential Voltage Analysis and Coulomb Tracking. In: J. Electrochem. Soc. 2017. 164(1):A6066-A6074. https://doi.org/10.1149/2.0091701jes.

[318] Tian J, Xiong R, Yu Q. Fractional-Order Model-Based Incremental Capacity Analysis for Degradation State Recognition of Lithium-Ion Batteries. In: IEEE Trans. Ind. Electron. 2019. 66(2):1576–84. https://doi.org/10.1109/TIE.2018.2798606.

[319] He J, Wei Z, Bian X, Yan F. State-of-Health Estimation of Lithium-Ion Batteries Using Incremental Capacity Analysis Based on Voltage–Capacity Model. In: IEEE Trans. Transp. Electrific. 2020. 6(2):417–26. https://doi.org/10.1109/TTE.2020.2994543.

[320] Torai S, Nakagomi M, Yoshitake S, Yamaguchi S, Oyama N. State-of-health estimation of $LiFePO_4$/graphite batteries based on a model using differential capacity. In: Journal of Power Sources 2016. 306:62–9. https://doi.org/10.1016/j.jpowsour.2015.11.070.

[321] Tang X, Zou C, Yao K, Chen G, Liu B, He Z, Gao F. A fast estimation algorithm for lithium-ion battery state of health. In: Journal of Power Sources 2018. 396:453–8. https://doi.org/10.1016/j.jpowsour.2018.06.036.

[322] Tang X, Liu K, Lu J, Liu B, Wang X, Gao F. Battery incremental capacity curve extraction by a two-dimensional Luenberger–Gaussian-moving-average filter. In: Applied Energy 2020. 280:115895. https://doi.org/10.1016/j.apenergy.2020.115895.

[323] Dubarry M, Truchot C, Liaw BY, Gering K, Sazhin S, Jamison D, Michelbacher C. Evaluation of commercial lithium-ion cells based on composite positive electrode for plug-in hybrid electric vehicle applications. Part II. Degradation mechanism under 2C cycle aging. In: Journal of Power Sources 2011. 196(23):10336–43. https://doi.org/10.1016/j.jpowsour.2011.08.078.

[324] Dubarry M, Baure G, Devie A. Durability and Reliability of EV Batteries under Electric Utility Grid Operations: Path Dependence of Battery Degradation. In: J. Electrochem. Soc. 2018. 165(5):A773-A783. https://doi.org/10.1149/2.0421805jes.

[325] Eddahech A, Briat O, Vinassa J-M. Performance comparison of four lithium–ion battery technologies under calendar aging. In: Energy 2015. 84:542–50. https://doi.org/10.1016/j.energy.2015.03.019.

[326] Dubarry M, Svoboda V, Hwu R, Liaw BY. Capacity and power fading mechanism identification from a commercial cell evaluation. In: Journal of Power Sources 2007. 165(2):566–72. https://doi.org/10.1016/j.jpowsour.2006.10.046.
[327] Shafiei Sabet P, Warnecke AJ, Meier F, Witzenhausen H, Martinez-Laserna E, Sauer DU. Non-invasive yet separate investigation of anode/cathode degradation of lithium-ion batteries (nickel–cobalt–manganese vs. graphite) due to accelerated aging. In: Journal of Power Sources 2020. 449:227369. https://doi.org/10.1016/j.jpowsour.2019.227369.
[328] Goldammer MS, Kowal J. Investigation of degradation mechanisms in lithium-ion batteries by incremental open-circuit-voltage characterization and impedance spectra. In: 2020 IEEE Vehicle Power and Propulsion Conference (VPPC). IEEE. 2020, p. 1–8. https://doi.org/10.1109/VPPC49601.2020.9330948.
[329] Svens P, Behm M, Lindbergh G. Lithium-Ion Battery Cell Cycling and Usage Analysis in a Heavy-Duty Truck Field Study. In: Energies 2015. 8(5):4513–28. https://doi.org/10.3390/en8054513.
[330] Keil P, Schuster SF, Wilhelm J, Travi J, Hauser A, Karl RC, Jossen A. Calendar Aging of Lithium-Ion Batteries: I. Impact of the Graphie Anode on Capacity Fade. In: J. Electrochem. Soc. 2016. 163(9):A1872-A1880. https://doi.org/10.1149/2.0411609jes.
[331] Dubarry M, Beck D. Analysis of Synthetic Voltage vs. Capacity Datasets for Big Data Li-ion Diagnosis and Prognosis. In: Energies 2021. 14(9):2371. https://doi.org/10.3390/en14092371.
[332] Petzl M, Danzer MA. Nondestructive detection, characterization, and quantification of lithium plating in commercial lithium-ion batteries. In: Journal of Power Sources 2014. 254:80–7. https://doi.org/10.1016/j.jpowsour.2013.12.060.
[333] Dubarry M, Costa N, Matthews D. Data-driven direct diagnosis of Li-ion batteries connected to photovoltaics. In: Nat Commun 2023. 14(1):3138. https://doi.org/10.1038/s41467-023-38895-7.
[334] Dubarry M, Yasir F, Costa N, Matthews D. Data-Driven Diagnosis of PV-Connected Batteries: Analysis of Two Years of Observed Irradiance. In: Batteries 2023. 9(8):395. https://doi.org/10.3390/batteries9080395.
[335] Mao Z, Farkhondeh M, Pritzker M, Fowler M, Chen Z. Calendar Aging and Gas Generation in Commercial Graphite/NMC-LMO Lithium-Ion Pouch Cell. In: J. Electrochem. Soc. 2017. 164(14):A3469-A3483. https://doi.org/10.1149/2.0241714jes.
[336] Smith AJ, Svens P, Varini M, Lindbergh G, Lindström RW. Expanded In Situ Aging Indicators for Lithium-Ion Batteries with a Blended NMC-LMO Electrode Cycled at Sub-Ambient Temperature. In: J. Electrochem. Soc. 2021. 168(11):110530. https://doi.org/10.1149/1945-7111/ac2d17.

[337] Dubarry M, Anseán D. Synthetic data for Li-ion Batteries Degradation Maps with degradation example. In: Mendeley Data 2022. https://doi.org/10.17632/4k8f4t352y.1.
[338] Whitley E, Ball J. Statistics review 3: hypothesis testing and P values. In: Crit Care 2002. 6(3):222–5. https://doi.org/10.1186/cc1493.
[339] Meinert Lewerenz. Dissection and Quantitative Description of Aging of Lithium-Ion Batteries Using Non-Destructive Methods Validated by Post-Mortem-Analyses [Dissertation]. RWTH Aachen University. 2018. https://doi.org/10.18154/RWTH-2018-228663
[340] Li D, Danilov DL, Gao L, Yang Y, Notten PH. Degradation Mechanisms of the Graphite Electrode in $C_6/LiFePO_4$ Batteries Unraveled by a Non-Destructive Approach. In: J. Electrochem. Soc. 2016. 163(14):A3016-A3021. https://doi.org/10.1149/2.0821614jes.
[341] German Transmission System Operators: 50 Hertz, Amprion, Tennet, TransnetBW. Präqualifikationsverfahren für Regelreserveanbieter (FCR, aFRR, mFRR) in Deutschland ("PQ-Bedingungen"). 2020. https://www.regelleistung.net. [accessed March 15, 2023].
[342] Energy Storage Council. Global Energy Storage Market Overview & Regional Summary Report 2015. 2015. https://neca.asn.au/sites/default/files/media/state_nsw/News%20&%20Views/ESC%20Global%20Energy%20Storage%20Report_2015.pdf. [accessed July 20, 2019].
[343] Stenzel P, Linssen J, Robinius M, Stolten D, Gottke V, Teschner H, Velten A, Schäfer F. Energiespeicher. In: BWK 5 (2018). 2018.
[344] Stenzel P, Linssen J, Robinius M, Stolten D, Gottke V, Teschner H, Velten A, Schäfer F. Energiespeicher. In: BWK 2019(6):33-48.
[345] Kairies K-P, Haberschusz D, Magnor D, Leuthold M, Badeda J, Sauer DU. Wissenschaftliches Mess- und Evaluierungsprogramm Solarstromspeicher: Jahresbericht 2015. Institut für Stromrichtertechnik und Elektrische Antriebe, RWTH Aachen. 2015. https://www.researchgate.net/publication/314078160_Wissenschaftliches_Mess-_und_Evaluierungsprogramm_Solarstromspeicher_2015. [accessed June 01, 2023].
[346] Kairies K-P, Haberschusz D, van Ouwerkerk J, Strebel J, Wessels O, Magnor D, Badeda J, Sauer DU. Wissenschaftliches Mess- und Evaluierungsprogramm Solarstromspeicher: Jahresbericht 2016. Institut für Stromrichtertechnik und Elektrische Antriebe, RWTH Aachen. 2016. https://www.researchgate.net/publication/303817664_Wissenschaftliches_Mess-_und_Evaluierungsprogramm_Solarstromspeicher_Jahresbericht_2016. [accessed August 03, 2023].
[347] Figgener J, Kairies K-P, Haberschusz D, Wessels O, Sauer DU. Markt- und Technologieentwicklung von PV-Heimspeichern in Deutschland: BVES Pressekonferenz Energy Storage Europe. Institut für Stromrichtertechnik und Elektrische Antriebe, RWTH Aachen. 2019.

[348] Team Consult, Bundesverband Energiespeicher. Entwicklung und Perspektiven der Energiespeicherbranche in Deutschland. 2019. https://www.bves.de. [accessed July 06, 2019].
[349] Bundesverband Solarwirtschaft e.V. Statistische Zahlen der deutschen Solarstrombranche (Photovoltaik). 2019. https://www.solarwirtschaft.de. [accessed August 19, 2019].
[350] Bundesverband Solarwirtschaft e.V. und Intersolar Europe. Solarstromspeicher-Preismonitor Deutschland 2017. https://www.solarwirtschaft.de. [accessed August 19, 2019].
[351] Tan Z, Tan Q, Wang Y. A critical-analysis on the development of Energy Storage industry in China. In: J. of Energy Storage 2018(18):538–48. https://doi.org/10.1016/j.est.2018.05.013.
[352] McKinsey & Company. The new rules of competition in energy storage. 2018. https://www.mckinsey.com. [accessed October 09, 2019].
[353] Boston Consulting Group. Revisiting Energy Storage: There Is a Business Case. 2011. https://web-assets.bcg.com/img-src/BCG_Revisiting_Energy_Storage_Feb_11_tcm9-236611.pdf. [accessed October 09, 2019].
[354] AVICENNE. Energy Storage Systems: Grid to Behind the Meter 2017-2026 - 2018 edition. 2018. http://www.avicenne.com/reports_energy.php. [accessed October 10, 2019].
[355] AVICENNE. Worldwide Rechargeable: Battery Market 2017-2030 - 2018 edition. 2018. http://www.avicenne.com/reports_energy.php. [accessed October 10, 2019].
[356] Navigant Consulting. Country Forecasts for Utility-Scale Energy Storage. 2019. https://www.navigant.com/. [accessed October 10, 2019].
[357] Navigant Consulting. Market Data: Advanced Battery and Energy Storage Pricing Trends. 2019. https://www.navigant.com/. [accessed October 10, 2019].
[358] GTM Research/ESA. U.S. Energy Storage Monitor. 2019. https://www.woodmac.com/research/products/power-and-renewables/us-energy-storage-monitor/. [accessed October 05, 2019].
[359] Total Battery Consulting I. xEV Industry Insider Report. 2019. https://totalbatteryconsulting.com/. [accessed October 05, 2019].
[360] Mucherino A, Papajorgji PJ, Pardalos PM. Data mining in agriculture. Dordrecht, New York: Springer Verlag. 2009.
[361] Sreevalsan-Nair J. K-nearest Neighbors. In: Daya Sagar BS, Cheng Q, McKinley J, Agterberg F, editors. Encyclopedia of Mathematical Geosciences. Cham: Springer International Publishing. 2020, p. 1–3. https://doi.org/10.1007/978-3-030-26050-7_170-1.

[362] Schaeck S, Karspeck T, Ott C, Weirather-Koestner D, Stoermer AO. A field operational test on valve-regulated lead-acid absorbent-glass-mat batteries in micro-hybrid electric vehicles. Part II. Results based on multiple regression analysis and tear-down analysis. In: Journal of Power Sources 2011. 196(5):2933–8. https://doi.org/10.1016/j.jpowsour.2010.08.101.
[363] Henschel J, Horsthemke F, Stenzel YP, Evertz M, Girod S, Lürenbaum C, Kösters K, Wiemers-Meyer S, Winter M, Nowak S. Lithium ion battery electrolyte degradation of field-tested electric vehicle battery cells – A comprehensive analytical study. In: Journal of Power Sources 2020. 447:227370. https://doi.org/10.1016/j.jpowsour.2019.227370.

12 Related publications

Within this dissertation, several publications have been written. The content of these publications was partly integrated into this dissertation. This adheres to the current guidelines set forth by the faculty of Electrical Engineering and Information Technology at RWTH Aachen University and has received concurrence from Prof. Dirk Uwe Sauer, the primary supervisor overseeing this dissertation. Text elements, figures, or tables from these publications are not explicitly cited within the thesis, as far as I mainly created them. If the co-authors mainly created such elements in the listed publications, a direct link to the publication is given. The following publication list was written in September 2024.

Table 12-1: Publication overview status September 2024.

Type	Number
Peer-reviewed journal articles	31
Conference proceedings	6
Conference posters	5
Book chapters	3
Preprints and selected reports	9
Industry guidelines	3
Websites	2
Selected guest articles in mass media	21

12.1 Peer-reviewed journal articles (31)

Figgener J, van Ouwerkerk J, Haberschusz D, Bors J, Woerner P, Mennekes M, Hildenbrand F, Hecht C, Kairies K-P, Wessels O, Sauer DU. Multi-year field measurements of home storage systems and their use in capacity estimation. In: Nat Energy 2024. https://doi.org/10.1038/s41560-024-01620-9.

Figgener J, Tepe B, Rücker F, Schoeneberger I, Hecht C, Jossen A, Sauer DU. The influence of frequency containment reserve flexibilization on the economics of electric vehicle fleet operation. Journal of Energy Storage 2022. 53:105138. https://doi.org/10.1016/j.est.2022.105138.

Figgener J, Stenzel P, Kairies K-P, Linßen J, Haberschusz D, Wessels O, Robinius M, Stolten D, Sauer DU. The development of stationary battery storage systems in Germany – status 2020. Journal of Energy Storage 2021. 33:101982. https://doi.org/10.1016/j.est.2020.101982.

Figgener J, Stenzel P, Kairies K-P, Linßen J, Haberschusz D, Wessels O, Angenendt G, Robinius M, Stolten D, Sauer DU. The development of stationary battery storage systems in Germany – A market review. Journal of Energy Storage 2020. 29:101153. https://doi.org/10.1016/j.est.2019.101153.

Schulte J, **Figgener J (shared first authorship)**, Woerner P, Broering H, Sauer DU. Forecast-based charging strategy to prolong the lifetime of lithium-ion batteries in standalone PV battery systems in Sub-Saharan Africa. Solar Energy 2023. 258:130–42. https://doi.org/10.1016/j.solener.2023.03.029.

Aghsaee R, Hecht C, Schwinger F, **Figgener J**, Jarke M, Sauer DU. Data-Driven, Short-Term Prediction of Charging Station Occupation. Electricity 2023. 4(2):134–53. https://doi.org/10.3390/electricity4020009.

Angenendt G, Zurmühlen S, **Figgener J**, Kairies K-P, Sauer DU. Providing frequency control reserve with photovoltaic battery energy storage systems and power-to-heat coupling. Energy 2020. 194:116923. https://doi.org/10.1016/j.energy.2020.116923.

Gong J, Wasylowski D, **Figgener J**, Bihn S, Rücker F, Ringbeck F, Sauer DU. Quantifying the impact of V2X operation on electric vehicle battery degradation: An experimental evaluation. In: eTransportation 2024. 20:100316. https://doi.org/10.1016/j.etran.2024.100316.

Hecht C, Pournaghi A, Schwinger F, Spreuer KG, **Figgener J**, Jarke M, Sauer DU. Global electric vehicle charging station site evaluation and placement based on large-scale empirical data from Germany. In: eTransportation 2024. 22:100358. https://doi.org/10.1016/j.etran.2024.100358.

Hecht C, **Figgener J**, Sauer DU. Vehicle-to-Grid Market Readiness in Europe with a Special Focus on Germany. In: Vehicles 2023. 5(4):1452–66. https://doi.org/10.3390/vehicles5040079.

Hecht C, **Figgener J**, Li X, Zhang L, Sauer DU. Standard Load Profiles for Electric Vehicle Charging Stations in Germany Based on Representative, Empirical Data. Energies 2023. 16(6):2619. https://doi.org/10.3390/en16062619.

Hecht C, Spreuer KG, **Figgener J**, Sauer DU. Market Review and Technical Properties of Electric Vehicles in Germany. Vehicles 2022. 4(4):903–16. https://doi.org/10.3390/vehicles4040049.

Hecht C, **Figgener J**, Sauer DU. Simultaneity Factors of Public Electric Vehicle Charging Stations Based on Real-World Occupation Data. World Electr. Veh. J. 2022. 13(129). https://doi.org/ 10.3390/wevj13070129.

Hecht C, **Figgener J**, Sauer DU. Analysis of electric vehicle charging station usage and profitability in Germany based on empirical data. iScience 2022. 25(12):105634. https://doi.org/10.1016/j.isci.2022.105634.

Hecht C, **Figgener J**, Sauer DU. Predicting Electric Vehicle Charging Station Availability Using Ensemble Machine Learning. Energies 2021. 14(23):7834. https://doi.org/10.3390/en14237834.

Jacqué K, Koltermann L, **Figgener J**, Zurmühlen S, Sauer DU. The influence of frequency containment reserve on the cycles of a hybrid stationary large-scale storage system. Journal of Energy Storage 2022. 52:105040. https://doi.org/10.1016/j.est.2022.105040.

Jacqué K, Koltermann L, **Figgener J**, Zurmühlen S, Sauer DU. The influence of frequency containment reserve on the efficiency of a hybrid stationary large-scale storage system. Journal of Energy Storage 2022. 52:104961. https://doi.org/10.1016/j.est.2022.104961.

Jacqué K, Koltermann L, **Figgener J**, Zurmühlen S, Sauer DU. The Influence of Frequency Containment Reserve on the Operational Data and the State of Health of the Hybrid Stationary Large-Scale Storage System. Energies 2022. 15(4):1342. https://doi.org/10.3390/en15041342.

Kairies K-P, **Figgener J**, Haberschusz D, Wessels O, Tepe B, Sauer DU. Market and technology development of PV home storage systems in Germany. Journal of Energy Storage 2019. 23:416–24. https://doi.org/10.1016/j.est.2019.02.023.

Koltermann L, Celi Cortés M, **Figgener J**, Zurmühlen S, Sauer DU. Improved rule-based power distribution algorithm for hybrid battery storage systems and real-world validation. In: Journal of Energy Storage 2024. 86:111360. https://doi.org/10.1016/j.est.2024.111360.

Koltermann L, Celi Cortés M, **Figgener J**, Zurmühlen S, Sauer DU. Power curves of megawatt-scale battery storage technologies for frequency regulation and energy trading. Applied Energy 2023. 347:121428. https://doi.org/10.1016/j.apenergy.2023.121428.

Koltermann L, Drenker KK, Celi Cortés ME, Jacqué K, **Figgener J**, Zurmühlen S, Sauer DU. Potential analysis of current battery storage systems for providing fast grid services like synthetic inertia – Case study on a 6 MW system. Journal of Energy Storage 2023. 57:106190. https://doi.org/10.1016/j.est.2022.106190.

Koltermann L, Jacqué K, **Figgener J**, Zurmühlen S, Sauer DU. Operational Validation of a Power Distribution Algorithm for a Modular Megawatt Battery Storage System. Batteries & Supercaps 2023. https://doi.org/10.1002/batt.202200414.

Koltermann L, Jacqué K, **Figgener J**, Zurmühlen S, Sauer DU. Balancing group deviation & balancing energy costs due to the provision of frequency containment reserve with a battery storage system in Germany. International Journal of Electrical Power & Energy Systems 2022. 142:108327. https://doi.org/10.1016/j.ijepes.2022.108327.

Li X, Wang Z, Zhang L, Sun F, Cui D, Hecht C, **Figgener J**, Sauer DU. Electric vehicle behavior modeling and applications in vehicle-grid integration: An overview. Energy 2023. 268:126647. https://doi.org/10.1016/j.energy.2023.126647.

Rücker F, **Figgener J**, Schoeneberger I, Sauer DU. Battery Electric Vehicles in Commercial Fleets: Use profiles, battery aging, and open-access data. In: Journal of Energy Storage 2024. 86:111030. https://doi.org/10.1016/j.est.2024.111030.

Rücker F, Schoeneberger I, Wilmschen T, Sperling D, Haberschusz D, **Figgener J**, Sauer DU. Self-sufficiency and charger constraints of prosumer households with vehicle-to-home strategies. Applied Energy 2022. 317:119060. https://doi.org/10.1016/j.apenergy.2022.119060.

Rücker F, Schoeneberger I, Wilmschen T, Chahbaz A, Dechent P, Hildenbrand F, Barbers E, Kuipers M, **Figgener J**, Sauer DU. A Comprehensive Electric Vehicle Model for Vehicle-to-Grid Strategy Development. Energies 2022. 15(12):4186. https://doi.org/10.3390/en15124186.

Tepe B, Haberschusz D, **Figgener J**, Hesse H, Sauer DU, Jossen A. Feature-conserving gradual anonymization of load profiles and the impact on battery storage systems. Applied Energy 2023. 343:121191. https://doi.org/10.1016/j.apenergy.2023.121191.

Tepe B, **Figgener J**, Englberger S, Sauer DU, Jossen A, Hesse H. Optimal pool composition of commercial electric vehicles in V2G fleet operation of various electricity markets. Applied Energy 2022. 308:118351. https://doi.org/10.1016/j.apenergy.2021.118351.

van Ouwerkerk J, Celi Cortés M, Nsir N, Gong J, **Figgener J**, Zurmühlen S, Bußar C, Sauer DU. Quantifying benefits of renewable investments for German residential Prosumers in times of volatile energy markets. In: Nat Commun 2024. 15(1):8206. https://doi.org/10.1038/s41467-024-51967-6.

12.2 Conference proceedings (6)

Figgener J, Haberschusz D, Kairies K-P, Wessels O, Sauer DU. Alterung von PV-Heimspeichern im Feld: Kapazitätsverluste und Effizienzminderungen. 35. PV-Symposium 2020.

Figgener J, Haberschusz D, Wessels O, Kai-Philipp Kairies, Sauer DU. 5 Jahre KfW-Förderung: Markt- und Technologieentwicklung dezentraler Solarstromspeicher in Deutschland: Zusammenfassung. 2018.

Hecht C, Aghsaee R, Schwinger F, **Figgener J**, Jarke M, Sauer DU. Short-Term Prediction of Electric Vehicle Charging Station Availability Using Cascaded Machine Learning Models. 6th E-Mobility Power System Integration Symposium (EMOB 2022), 2022.

Kairies K-P, **Figgener J**, Magnor D, Axelsen H, Waffenschmidt E, Sauer DU. Analysis of Funded PV Battery Systems in Germany: Prices, Design Choices and Purchase Motivation. 7th International 100% Renewable Energy Conference, IRENEC 2017, 2017-05-18 – 2017-05-20, Istanbul, Turkey 2017.

Orth N, Weniger J, Tjaden T, Munzke N, Schwarz B, Büchle F, Messner C, **Figgener J**, Haberschusz D, Quaschning, V. Vergleich der Energieeffizienz verschiedener PV-Speichersystemkonzepte. PV-Symposium 2018.

Tepe B, **Figgener J**, Englberger S, Jossen A, Uwe Sauer DU, Hesse H. Analysis of optimally composed EV pools for the aggregated provision of frequency containment reserve and energy arbitrage trading. In: 5th E-Mobility Power System Integration Symposium (EMOB 2021). Institution of Engineering and Technology. 2021,175–180.

12.3 Conference posters (5)

Celi Cortés ME, Koltermann L, Nsir N, Zurmühlen S, **Figgener J**, Sauer DU. Optimal Multi-Use Operation of Utility-Scale Battery Systems: Techno-Economic Feasibility Study of the M5BAT Hybrid Storage in Aachen. Advanced Battery Power Conference 2023.

Gong J, **Figgener J**, Sauer DU. Optimizing the use of EV batteries with the dynamic stacking of multiple applications. Advanced Battery Power Conference 2023.

Koltermann L, Celi Cortés ME, Jacqué K, **Figgener J**, Zurmühlen S, Sauer DU. Rule-based Power Distribution Algorithm for a Modular Large-scale Battery Storage System. Advanced Battery Power Conference 2023.

Koltermann L, Jacqué K, **Figgener J**, Zurmühlen S, Sauer DU. Balancing group deviation & balancing energy costs due to the provision of frequency containment reserve with a battery storage system in Germany. Advanced Battery Power Conference 2022.

Schoeneberger I, Rücker F, **Figgener J**, Jakobowski S, Sauer DU. Electrical, Thermal and Aging Model of High-Energy Lithium-Ion Battery Pack for Simulation of V2G scenarios. Advanced Battery Power Conference 2019.

12.4 Book chapters (3)

Hecht C, **Figgener J**, Sauer DU. Lade- und Ladeinfrastruktur-Technologie. Chapter in Book: "Elektromobilität: Grundlagen einer Fortschrittstechnologie", hrsg. von Kampker A, Heimes H: Berlin: Springer Verlag. 2023.

Hecht C, **Figgener J**, Sauer DU. Ladeinfrastruktur im Status quo. Chapter in Book: "Elektromobilität: Grundlagen einer Fortschrittstechnologie", hrsg. von Kampker A, Heimes H: Berlin: Springer Verlag. 2023.

Hecht C, Luo B, **Figgener J**, Sauer DU. User Behaviour Analysis of Public Charging Infrastructure for Electric Vehicles. Chapter in Book: "Towards the New Normal in Mobility: Technische und betriebswirtschaftliche Aspekte" hrsg. von Heike Proff. Wiesbaden: Springer Fachmedien Wiesbaden. 2023.

12.5 Preprints and selected reports (9)

Figgener J, Bors J, Haberschusz D, Hildenbrand F, Kuipers M, Junker M, Koltermann L, Woerner P, Mennekes, M, Haberschusz D, Kairies K-P, Sauer DU. Degradation mode estimation using reconstructed open circuit voltage curves from multi-year home storage field data. 2024. https://doi.org/10.48550/arXiv.2411.08025.

Figgener J, Hecht C, Haberschusz D, Bors J, Spreuer KG, Kairies K-P, Stenzel P, Sauer DU. The development of battery storage systems in Germany: A market review (status 2023). 2023. http://arxiv.org/pdf/2203.06762v3.

Figgener J, Hecht C, Haberschusz D, Bors J, Spreuer KG, Kairies K-P, Stenzel P, Sauer DU. The development of battery storage systems in Germany: A market review (status 2022). 2022. http://arxiv.org/pdf/2203.06762v2.

Figgener J, Haberschusz D, Hecht C, Zurmühlen S, Sauer DU. Speichermonitoring BW 2.0 Schlussbericht (inhaltlicher Teil). 2022. http://dx.doi.org/10.13140/RG.2.2.17036.59528.

Figgener J, Haberschusz D, Zurmühlen S, Sauer DU. Speichermonitoring BW: Schlussbericht (inhaltlicher Teil). 2021. http://dx.doi.org/10.13140/RG.2.2.30516.37768.

Figgener J, Haberschusz D, Kairies K-P, Wessels O, Zurmühlen S, Sauer DU. Speichermonitoring BW: Jahresbericht 2019. 2019. http://dx.doi.org/10.13140/RG.2.2.16244.30088

Figgener J, Haberschusz D, Kairies K-P, Wessels O, Tepe B, Sauer DU. Wissenschaftliches Mess- und Evaluierungsprogramm Solarstromspeicher 2.0: Jahresbericht 2018. 2018. http://dx.doi.org/10.13140/RG.2.2.30057.19047.

Figgener J, Haberschusz D, Kairies K-P, Wessels O, Tepe B, Ebbert M, Herzog R, Sauer DU. Wissenschaftliches Mess- und Evaluierungsprogramm Solarstromspeicher 2.0: Jahresbericht 2017. http://dx.doi.org/10.13140/RG.2.2.16917.42727

Stenzel P, Kotzur L, Stolten D, **Figgener J**, Haberschusz D, Sauer DU et al. Energiespeicher – Batterien, Wasserstoff, Wärme. BWK – Brennstoff-Wärme-Kraft. 2021. http://hdl.handle.net/2128/30138.

12.6 Industry guideline contribution (3)

Bundesverband Energiespeicher e.V., Bundesverband Solarwirtschaft e. V. Effizienzleitfaden für PV-Speichersysteme 2.0. 2019. https://www.bves.de /publikation/effizienzleitfaden-fuer-pv-speichersysteme/. [accessed August 07, 2023].

VDI-Gesellschaft Energie und Umwelt. Planung und Integration von Energiespeichern in Gebäudeenergiesystemen – Elektrische Stromspeicher (ESS): VDI 4657 Blatt 3 – Entwurf. 2022. https://www.vdi.de/richtlinien/details/vdi-4657-blatt-3-planung-und-integration-von-energiespeichern-in-gebaeudeenergiesystemen-elektrische-stromspeicher-ess. [accessed August 07, 2023].

VDI-Gesellschaft Energie und Umwelt. Energiespeicher: Ökonomischer, ökologischer und systemischer Wert von netzgekoppelten Energiespeichern. 2022. https://www.vdi.de/ueber-uns/presse/publikationen/details/oekonomischer-oekologischer-und-systemischer-wert-von-netzgekoppelten-energiespeichern. [accessed August 07, 2023].

12.7 Websites (2)

Figgener J, Hecht C, Sauer DU. Battery Charts: Stationary battery storage registrations in Germany. 2022. www.battery-charts.de. [accessed August 07, 2024].

Hecht C, **Figgener J**, Sauer DU. Mobility Charts: Electric vehicle registrations in Germany. 2022. www.mobility-charts.de. [accessed August 07, 2024].

12.8 Selected guest articles in mass media (21)

Figgener J, Hecht C, Sauer DU. 250.000 neue Photovoltaik-Heimspeicher im ersten Halbjahr 2023. In: pv magazine, 2023. https://www.pv-magazine.de /2023/08/24/250-000-neue-photovoltaik-heimspeicher-im-ersten-halbjahr-2023/. [accessed September 09, 2023].

Figgener J, Hecht C, Sauer DU. Rekordjahr 2022 im Speichermarkt: Durchbruch der Batteriegroßspeicher. 2023. https://www.emw-online.com/artikel/233398/ rekordjahr-2022-im-speichermarkt. [accessed August 07, 2023].

Figgener J, Hecht C, Sauer DU. Mehr als 110.000 neue Heimspeicher im ersten Quartal 2023. In: pv magazine. 2023. https://www.pv-magazine.de/ 2023/05/26/mehr-als-110-000-neue-heimspeicher-im-ersten-quartal-2023/. [accessed August 07, 2023].

Figgener J, Hecht C, Sauer DU. ISEA veröffentlicht neue Plattform zur Marktentwicklung von Batteriespeichern: Zubau im ersten Halbjahr 2022 weiter auf Wachstumskurs. In: pv magazine. 2022. https://www.pv-magazine.de/2022/09/08/isea-veroeffentlicht-neue-plattform-zur-marktentwicklung-von-batterie speichern-zubau-im-ersten-halbjahr-2022-weiter-auf-wachstumskurs/. [accessed August 07, 2023].

Figgener J, Hecht C, Sauer DU. Rekordjahr im Gewerbespeichermarkt. In: pv magazine. 2022. https://www.pv-magazine.de/archiv/rekordjahr-im-gewerbespei chermarkt/. [accessed August 07, 2023].

Figgener J, Hecht C, Sauer DU. Rekordjahr im Speichermarkt: Privathaushalte tragen 2021 Gesamtzubau von rund 1,4 Gigawattstunden. In: pv magazine. 2022. https://www.pv-magazine.de/2022/03/15/rekordjahr-im-speichermarkt-priv athaushalte-tragen-2021-gesamtzubau-von-rund-14-gigawattstunden/. [accessed August 07, 2023].

Figgener J, Hecht C, Sauer DU. Wie lange leben Batterien? Zustandsbewertung und Lebensdauerprognose. In: RWTH THEMEN. 2022. https://www.rwth-aachen.de/global/show_document.asp?id=aaaaaaaabqxlbwf. [accessed August 07, 2023].

Figgener J, Hecht C. Gewerbespeichermarkt zieht an: 43 Megawattstunden für 2020 im Marktstammdatenregister gemeldet. In: pv magazine. 2021. https://www.pv-magazine.de/2021/04/28/gewerbespeichermarkt-zieht-an-43-megawattstunden-fuer-2020-im-marktstammdatenregister-gemeldet/. [accessed August 07, 2023].

Figgener J. Marktstammdatenregister beinhaltet Batteriespeicher mit einer Kapazität von insgesamt knapp 2.000 Megawattstunden. In: pv magazine. 2021. https://www.pv-magazine.de/2021/01/15/marktstammdatenregister-beinhaltet-batteriespeicher-mit-einer-kapazitaet-von-insgesamt-knapp-2-000-megawatt stunden/. [accessed August 07, 2023].

Hecht C, **Figgener J**, Sauer DU. Auto vs. Heimspeicher. In: pv magazine. 2023. https://www.pv-magazine.de/archiv/auto-vs-heimspeicher/. [accessed August 07, 2023].

Hecht C, **Figgener J**, Sauer DU. 6 Thesen zur Elektromobilität für 2023. In: pv magazine. 2023. https://www.pv-magazine.de/2023/01/27/6-thesen-zur-elektro mobilitaet-fuer-2023/. [accessed August 07, 2023].

Hecht C, **Figgener J**, Sauer DU. Elektromobilität für alle? Im geeigneten Strukturraum kein Problem. In: pv magazine. 2022. https://www.pv-magazine.de/2022/07/01/elektromobilitaet-fuer-alle-im-geeigneten-strukturraum-kein-problem/. [accessed August 07, 2023].

Hecht C, **Figgener J**, Sauer DU. ISEA veröffentlicht Datenpool zu Elektromobilität: Mobility Charts. In: pv magazine. 2022. https://www.pv-magazine.de/2022/05/24/isea-veroeffentlicht-datenpool-zu-elektromobilitaet-mobility-charts/. [accessed August 07, 2023].

Hecht C, **Figgener J**, Sauer DU. Bereits fast 40 Gigawattstunden an Batterien in 1,3 Millionen Elektroautos verbaut. In: pv magazine. 2022. https://www.pv-magazine.de/2022/03/15/bereits-fast-40-gigawattstunden-an-batterien-in-13-millionen-elektroautos-verbaut/. [accessed August 07, 2023].

Hecht C, **Figgener J**, Sauer DU. Maschinelles Lernen ist Schlüsselfaktor für intelligentes Laden. In: pv magazine. 2021. https://www.pv-magazine.de/2021/12/06/maschinelles-lernen-ist-schluesselfaktor-fuer-intelligentes-laden/. [accessed August 07, 2023].

Hecht C, **Figgener J**, Sauer DU. Nur geringer Anteil der Ladesäulen rechnet sich aktuell ohne Förderung. In: pv magazine 2021. https://www.pv-magazine.de/2021/07/07/nur-geringer-anteil-der-ladesaeulen-rechnet-sich-aktuell-ohne-foerderung/. [accessed August 07, 2023].

Hecht C, **Figgener J**. Wann und wie nutzen wir die Gigawattstunden in Elektroautobatterien? In: pv magazine. 2021. https://www.pv-magazine.de/2021/05/07/wann-und-wie-nutzen-wir-die-gigawattstunden-in-elektroautobatterien/. [accessed August 07, 2023].

Hecht C, **Figgener J**. Elektroauto-Boom 2020: Neuzulassungen mit 9 Gigawattstunden Batteriekapazität. 2021. https://www.pv-magazine.de/2021/03/12/elektroauto-boom-2020-neuzulassungen-mit-9-gigawattstunden-batteriekapazitaet/. [accessed August 07, 2023].

Kairies K-P, Haberschusz D, **Figgener J**. Energiespeicher im Gewerbe: Teil 2: Lastspitzenkappung an Beispielen und Batterielebensdauer. In: Elektropraktiker. 2019. https://www.elektropraktiker.de/fachartikel/detail/energiespeicher-im-gewerbe-1/. [accessed August 07, 2023].

Kairies K-P, **Figgener J**, Haberschusz D. Energiespeicher im Gewerbe: Teil 1: Überblick und Einsatzmöglichkeiten. In: Elektropraktiker. 2019. https://www.elektropraktiker.de/fachartikel/detail/energiespeicher-im-gewerbe/. [accessed August 07, 2023].

Kairies K-P, **Figgener J**, Haberschusz D. Market and technology development of stationary battery storage systems. In: PV Tech. 2019. https://www.pv-tech.org/technical-papers/market-and-technology-development-of-stationary-battery-storage-systems/. [accessed August 07, 2023].

13 Supervised students

During my dissertation, I defined the concept of student theses, supervised the conducted research closely, collaborated, and handed over existing datasets and methods I developed. Some of the topics are partial aspects of this dissertation and, therefore, part of this document. This adheres to the current guidelines set forth by the faculty of Electrical Engineering and Information Technology at RWTH Aachen University and has received concurrence from Prof. Dirk Uwe Sauer, the primary supervisor overseeing this dissertation. Corresponding contents are not explicitly referenced to these works. The theses are listed in reverse chronological order in their respective section. Student works not written under my supervision are cited like all other literature.

13.1 Bachelor theses

Constantin Schulte, „Development of a forecast-based operating strategy for home storage“, 03/2022 – 09/2022.

Aurélia Skrobacz, „Fire risk of electric vehicles: a techno-economic analysis“, 11/2021 – 03/2022.

Philipp Woerner, „Development of an online monitoring for PV home storage systems“, 04/2019 – 09/2019.

13.2 Master theses

Jasper Seitz-McIntyre, “Development of a Capacity Management System for Home Storage Systems”, 03/2022 – 08/2022.

Jakob Bors, “Online analysis of PV home storage OCV curves for determining battery aging in the field”, 12/2021 – 07/2022.

Philipp Woerner, „Battery aging and machine learning: a relaxation phase analysis of PV home storage systems“, 10/2021 – 03/2022.

Jonathan Schulte, “Development of Control Strategies for PV Battery Systems in African Off-Grid Energy Systems”, 10/2019 – 04/2020.

Marc Mennekes, “Ageing analysis of PV home storage systems”, 05/2019 – 11/2019.

Jonas van Ouwerkerk, „Development of software tools to estimate the SOH of stationary storage systems“, 10/2018 – 04/2019.

Benedikt Tepe, “Optimized Profile Combination of PV Battery Systems and Electric Vehicles for a Demand-Actuated Capacity Provision”, 03/2018 – 10/2018.

Markus Ebbert, “Development of a Tool for the Analysis of Innovative Business Models Based on Decentralized Photovoltaic Battery Systems”, 06/2017 – 12/2017.

13.3 Project thesis

Vishal Kaushik, “Load analysis of large electrical consumers in households”, 06/2019 – 07/2019.

13.4 Student assistants

Jakob Bors, Philipp Woerner, Marc Mennekes, Jonas van Ouwerkerk, Benedikt Tepe, Steffen Brenning, Adrien Christian, Daniel Dang

14 Acknowledgment

Measurements. I owe David Haberschusz, Kai-Philipp Kairies, and Oliver Wessels my deepest gratitude for introducing me to the field measurements of home storage systems. David has been the biggest help I could have asked for in terms of field measurements and database handling of any kind from the start to the end of my dissertation. Oliver was a great support in terms of field measurements and Kai-Philipp kindly introduced me to project management and presentations.

Publications. Thanks to Christopher Hecht, who was an enormous driver for publications and mass media science communication. In addition, I thank all co-authors, especially Kevin Jacqué, Lucas Koltermann, and Fabian Rücker for leading at least three excellent joint publications.

Discussions. Felix Hildenbrand, Matthias Kuipers, and Mark Junker helped me patiently to dive deeper into the field of battery aging. I appreciate the discussions on degradation modes and how to transfer laboratory knowledge to field data. In addition, many thanks to Sebastian Zurmühlen, Christian Bußar, Fabian Meishner, Philipp Dechent, and Florian Ringbeck for numerous helpful exchanges, and to Aniket Kapse for his feedback on spelling and grammar.

Students. Many thanks to all students who have worked with me. Special thanks go to Jakob Bors, Philipp Woerner, Marc Mennekes, Jonas van Ouwerkerk, and Benedikt Tepe. Your support was invaluable.

Supervision and assessment. I am very grateful to Professor Dirk Uwe Sauer for giving me the opportunity to do my doctorate. Despite a large university chair, he always took time for a professional exchange and provided valuable input in numerous discussions. I appreciate his trust in me to lead the Department of Grid Integration and Storage System Analysis for three years. I have been impressed by the support I have received in dealing with media and press inquiries. In my opinion, they represent an important task in science to communicate findings from research to society. In addition, I would like to sincerely thank Professor Andreas Ulbig for taking over the additional assessment of my thesis, his helpful feedback on the analyses, and the inspiring discussions about possible professional careers.

Funding. Parts of the results were obtained within the research projects “WMEP PV-Speicher” (funding number 0325666) and “WMEP PV-Speicher 2.0 (KfW 275)” (funding number 03ET6117)”, both funded by the German Federal Ministry for Economic Affairs and Climate Action (BMWK), and “Betterbat” (funding number 03XP0362B), funded by the Federal Ministry of Education and Research (BMBF). Other parts were obtained in the context of the research projects “Speichermonitoring BW 2.0” (funding number L75 21120) and “Speichermonitoring BW” (funding number L75 18006), both funded by the Ministry of Environment, Climate Protection and the Energy Sector, Baden-Württemberg (UMBW), as well as in the research projects.

15 Curriculum vitae

Personal details	
Name	Jan Figgener
Year, place of birth	1991, Bocholt (Germany)

Education	
2017 – 2024	**Dissertation on Battery Storage** RWTH Aachen University Supervisor: Prof. Dirk Uwe Sauer
2014 – 2016	**M.Sc. Business Administration and Engineering: Electrical Energy Technology** RWTH Aachen University
2010 – 2014	**B.Sc. Business Administration and Engineering: Electrical Energy Technology** RWTH Aachen University
2001 – 2010	**Abitur (High School Graduation)** St.-Josef-Gymnasium (school) in Bocholt

Employment	
Since 2024	**Senior Design Engineer** RWE Technology International GmbH, Essen
Since 2020	**Senior Battery Expert** ACCURE Battery Intelligence GmbH, Aachen
2021 – 2023	**Head of Grid Integration and Storage System Analysis** (Department at the Chair of Prof. Sauer) Institute for Power Electronics and Electrical Drives (ISEA), RWTH Aachen University and Institute for Power Generation and Storage Systems (PGS) at E.ON Energy Research Center (E.ON ERC), RWTH Aachen University Responsible for about 15 research scientists and 30 students

2017 – 2020	**Scientist and Project Manager** Institute for Power Electronics and Electrical Drives RWTH Aachen University
2014 – 2015	**Student Assistant** Institute for High Voltage Technology RWTH Aachen University
2013	**Intern** 50Hertz Transmission GmbH, Berlin
2013	**Intern** Westnetz GmbH, Bergheim

ABISEA Band 1
Eßer, Albert
Berührungslose, kombinierte Energie- und Informationsübertragung für bewegliche Systeme
1. Aufl. 1992, 129 S.
ISBN 3-86073-046-0

ABISEA Band 2
Vogel, Ulrich
Entwurf und Beurteilung von Verfahren zur Hochausnutzung des Rad-Schiene-Kraftschlusses durch Triebfahrzeuge
1. Aufl. 1992, 131 S.
ISBN 3-86073-060-6

ABISEA Band 3
Reckhorn, Thomas
Stromeinprägendes Antriebssystem mit fremderregter Synchronmaschine
1. Aufl. 1992, 128 S.
ISBN 3-86073-061-4

ABISEA Band 4
Ackva, Ansgar
Spannungseinprägendes Antriebssystem mit Synchronmaschine und direkter Stromregelung
1. Aufl. 1992, 137 S.
ISBN 3-86073-062-2

ABISEA Band 5
Mertens, Axel
Analyse des Oberschwingungsverhaltens von taktsynchronen Delta - Modulationsverfahren zur Steuerung von Pulsstromrichtern bei hoher Taktzahl
1. Aufl. 1992, 178 S.
ISBN 3-86073-069-X

ABISEA Band 6
Geuer, Wolfgang
Untersuchungen über das Alterungsverhalten von Blei-Akkumulatoren
1. Aufl. 1993, 97 S.
ISBN 3-86073-097-5

ABISEA Band 7
Langheim, Jochen
Einzelradantrieb für Elektrostraßenfahrzeuge
1. Aufl. 1993, 213 S.
ISBN 3-86073-123-8
(vergriffen)

ABISEA Band 8
Fetz, Joachim
Fehlertolerante Regelung eines Asynchron-Doppelantriebes für ein Elektrospeicherfahrzeug
1. Aufl. 1993, 136 S.
ISBN 3-86073-124-6
(vergriffen)

ABISEA Band 9
Schülting, Ludger
Optimierte Auslegung induktiver Bauelemente für den Mittelfrequenzbereich
1. Aufl. 1993, 126 S.
ISBN 3-86073-174-2
(vergriffen)

ABISEA Band 10
Skudelny, H.-Ch.
Stromrichtertechnik
4. Aufl. 1997, 259 S.
ISBN 3-86073-189-0

ABISEA Band 11
Skudelny, H.-Ch.
Elektrische Antriebe
3. Aufl. 1997, 124 S.
ISBN 3-86073-231-5

ABISEA Band 12
Schöpe, Friedhelm
Batterie-Management für Nickel-Cadmium Akkumulatoren
1. Aufl. 1994, 148 S.
ISBN 3-86073-232-3
(vergriffen)

ABISEA Band 13
v. d. Weem, Jürgen
Schmalbandige aktive Filter für Schienentriebfahrzeuge am Gleichspannungsfahrdraht
1. Aufl. 1995, 126 S.
ISBN 3-86073-233-1

ABISEA Band 14
Backhaus, Klaus
Spannungseinprägendes Direktantriebssystem mit schnelllaufender geschalteter Reluktanzmaschine
1. Aufl. 1995, 146 S.
ISBN 3-86073-234-X
(vergriffen)

ABISEA Band 15
Reinold, Harry
Optimierung dreiphasiger Pulsdauermodulationsverfahren
1. Aufl. 1996, 107 S.
ISBN 3-86073-235-8

ABISEA Band 16
Köpken, Hans-Georg
Regelverfahren für Parallelschwingkreisumrichter
1. Aufl. 1996, 125 S.
ISBN 3-86073-236-6

ABISEA Band 17
Mauracher, Peter
Modellbildung und Verbundoptimierung bei Elektrostraßenfahrzeugen
1. Aufl. 1996, 192 S.
ISBN 3-86073-237-4

ABISEA Band 18
Protiwa, Franz-Ferdinand
Vergleich dreiphasiger Resonanz-Wechselrichter in Simulation und Messung
1. Aufl. 1997, 178 S.
ISBN 3-86073-238-2

ABISEA Band 19
Brockmeyer, Ansgar
Dimensionierungswerkzeug für magnetische Bauelemente in Stromrichteranwendungen
1. Aufl. 1997, 175 S.
ISBN 3-86073-239-0

Aachener Beiträge des ISEA

ABISEA Band 20
Apeldoorn, Oscar
Simulationsgestützte Bewertung von Steuerverfahren für netzgeführte Stromrichter mit verringerter Netzrückwirkung
1. Aufl. 1997, 134 S.
ISBN 3-86073-680-9

ABISEA Band 21
Lohner, Andreas
Batteriemanagement für verschlossene Blei-Batterien am Beispiel von Unterbrechungsfreien Stromversorgungen
1. Aufl. 1998, 126 S.
ISBN 3-86073-681-7

ABISEA Band 22
Reinert, Jürgen
Optimierung der Betriebseigenschaften von Antrieben mit geschalteter Reluktanzmaschine
1. Aufl. 1998, 153 S.
ISBN 3-86073-682-5

ABISEA Band 23
Nagel, Andreas
Leitungsgebundene Störungen in der Leistungselektronik: Entstehung, Ausbreitung und Filterung
1. Aufl. 1999, 140 S.
ISBN 3-86073-683-3

ABISEA Band 24
Menne, Marcus
Drehschwingungen im Antriebsstrang von Elektrostraßenfahrzeugen - Analyse und aktive Dämpfung
1. Aufl. 2001, 169 S.
ISBN 3-86073-684-1

ABISEA Band 25
von Bloh, Jochen
Multilevel-Umrichter zum Einsatz in Mittelspannungs-Gleichspannungs-Übertragungen
1. Aufl. 2001, 137 S.
ISBN 3-86073-685-X

ABISEA Band 26
Karden, Eckhard
Using low-frequency impedance spectroscopy for characterization, monitoring, and modeling of industrial batteries
1. Aufl. 2002, 137 S.
ISBN 3-8265-9766-4

ABISEA Band 27
Karipidis, Claus-Ulrich
A Versatile DSP/ FPGA Structure optimized for Rapid Prototyping and Digital Real-Time Simulation of Power Electronic and Electrical Drive Systems
1. Aufl. 2001, 164 S.
ISBN 3-8265-9738-9

ABISEA Band 28
Kahlen, Klemens
Regelungsstrategien für permanentmagnetische Direktantriebe mit mehreren Freiheitsgraden
1. Aufl. 2002, 154 S.
ISBN 3-8322-1222-1

ABISEA Band 29
Inderka, Robert B.
Direkte Drehmomentregelung Geschalteter Reluktanzantriebe
1. Aufl. 2003, 182 S.
ISBN 3-8322-1175-6

ABISEA Band 30
Schröder, Stefan
Circuit-Simulation Models of High-Power Devices Based on Semiconductor Physics
1. Aufl. 2003, 123 S.
ISBN 3-8322-1250-7

ABISEA Band 31
Buller, Stephan
Impedance-Based Simulation Models for Energy Storage Devices in Advanced Automotive Power Systems
1. Aufl. 2003, 138 S.
ISBN 3-8322-1225-6

ABISEA Band 32
Schönknecht, Andreas
Topologien und Regelungsstrategien für das induktive Erwärmen mit hohen Frequenz-Leistungsprodukten
1. Aufl. 2004, 157 S.
ISBN 3-8322-2408-4

ABISEA Band 33
Tolle, Tobias
Konvertertopologien für ein aufwandsarmes, zweistufiges Schaltnetzteil zum Laden von Batterien aus dem Netz
1. Aufl. 2004, 148 S.
ISBN 3-8322-2676-1

ABISEA Band 34
Götting, Gunther
Dynamische Antriebsregelung von Elektrostraßenfahrzeugen unter Berücksichtigung eines schwingungsfähigen Antriebsstrangs
1. Aufl. 2004, 157 S.
ISBN 3-8322-2804-7

ABISEA Band 35
Dieckerhoff, Sibylle
Transformatorlose Stromrichterschaltungen für Bahnfahrzeuge am 16 2/3Hz Netz
1. Aufl. 2004, 147 S.
ISBN 3-8322-3094-7

ABISEA Band 36
Hu, Jing
Bewertung von DC-DC-Topologien und Optimierung eines DC-DC-Leistungsmoduls für das 42-V-Kfz-Bordnetz
1. Aufl. 2004, 148 S.
ISBN 3-8322-3201-X

ABISEA Band 37
Detjen, Dirk-Oliver
Characterization and Modeling of Si-Si Bonded Hydrophobie Interfaces for Novel High-Power BIMOS Devices
1. Aufl. 2004, 135 S.
ISBN 3-8322-2963-9

ABISEA Band 38
Walter, Jörg
Simulationsbasierte Zuverlässigkeitsanalyse in der modernen Leistungselektronik
1. Aufl. 2004, 121 S.
ISBN 3-8322-3481-0

ABISEA Band 39
Schwarzer, Ulrich
IGBT versus GCT in der Mittelspannungsanwendung - ein experimenteller und simulativer Vergleich
1. Aufl. 2005, 170 S.
ISBN 3-8322-4489-1

ABISEA Band 40
Bartram, Markus
IGBT-Umrichtersysteme für Windkraftanlagen: Analyse der Zyklenbelastung, Modellbildung, Optimierung und Lebensdauervorhersage
1. Aufl. 2006, 185 S.
ISBN 3-8322-5039-5

ABISEA Band 41
Ponnaluri, Srinivas
Generalized Design, Analysis and Control of Grid side converters with integrated UPS or Islanding functionality
1. Aufl. 2006, 163 S.
ISBN 3-8322-5281-9

ABISEA Band 42
Jacobs, Joseph
Multi-Phase Series Resonant DC-to-DC Converters
1. Aufl. 2006, 185 S.
ISBN 3-8322-5532-X

ABISEA Band 43
Linzen, Dirk
Impedance-Based Loss Calculation and Thermal Modeling of Electrochemical Energy Storage Devices for Design Considerations of Automotive Power Systems
1. Aufl. 2006, 185 S.
ISBN 3-8322-5706-3

ABISEA Band 44
Fiedler, Jens
Design of Low-Noise Switched Reluctance Drives
1. Aufl. 2007, 176 S.
ISBN 978-3-8322-5864-1

ABISEA Band 45
Fuengwarodsakul, Nisai
Predictive PWM-based Direct Instantaneous Torque Control for Switched Reluctance Machines
1. Aufl. 2007, 141 S.
ISBN 978-3-8322-6210-5

ABISEA Band 46
Meyer, Christoph
Key Components for Future Offshore DC Grids
1. Aufl. 2007, 187 S.
ISBN 978-3-8322-6571-7

ABISEA Band 47
Fujii, Kansuke
Characterization and Optimization of Soft-Switched Multi-Level Converters for STATCOMs
1. Aufl. 2008, 199 S.
ISBN 978-3-8322-6981-4

ABISEA Band 48
Carstensen, Christian
Eddy Currents in Windings of Switched Reluctance Machines
1. Aufl. 2008, 179 S.
ISBN 978-3-8322-7118-3

ABISEA Band 49
Bohlen, Oliver
Impedance-based battery monitoring
1. Aufl. 2008, 190 S.
ISBN 978-3-8322-7606-5

ABISEA Band 50
Thele, Marc
A contribution to the modelling of the charge acceptance of lead-acid batteries - using frequency and time domain based concepts
1. Aufl. 2008, 165 S.
ISBN 978-3-8322-7659-1

ABISEA Band 51
König, Andreas
High Temperature DC-to-DC Converters for Downhole Applications
1. Aufl. 2009, 154 S.
ISBN 978-3-8322-8489-3

ABISEA Band 52
Dick, Christian Peter
Multi-Resonant Converters as Photovoltaic Module-Integrated Maximum Power Point Tracker
1. Aufl. 2010, 182 S.
ISBN 978-3-8322-9199-0

ABISEA Band 53
Kowal, Julia
Spatially resolved impedance of nonlinear inhomogeneous devices: using the example of lead-acid batteries
1. Aufl. 2010, 203 S.
ISBN 978-3-8322-9483-0

ABISEA Band 54
Roscher, Michael Andreas
Zustandserkennung von LiFeP04-Batterien für Hybrid- und Elektrofahrzeuge
1. Aufl. 2011, 186 S.
ISBN 978-3-8322-9738-1

ABISEA Band 55
Hirschmann, Dirk
Highly Dynamic Piezoelectric Positioning
1. Aufl. 2011, 146 S.
ISBN 978-3-8322-9746-6

ABISEA Band 56
Rigbers, Klaus
Highly Efficient Inverter Architectures for Three-Phase Grid Connection of Photovoltaic Generators
1. Aufl. 2011, 244 S.
ISBN 978-3-8322-9816-9

ABISEA Band 57
Kasper, Knut
Analysis and Control of the Acoustic Behavior of Switched Reluctance Drives
1. Aufl. 2011, 205 S.
ISBN 978-3-8322-9869-2

Aachener Beiträge des ISEA

ABISEA Band 58
Köllensperger, Peter
The Internally Commutated Thyristor - Concept, Design and Application
1. Aufl. 2011, 214 S.
ISBN 978-3-8322-9909-5

ABISEA Band 59
Schoenen, Timo
Einsatz eines DC/DC-Wandlers zur Spannungsanpassung zwischen Antrieb und Energiespeicher in Elektro-und Hybridfahrzeugen
1. Aufl. 2011, 128 S.
ISBN 978-3-8440-0622-3

ABISEA Band 60
Hennen, Martin
Switched Reluctance Direct Drive with Integrated Distributed Inverter
1. Aufl. 2012, 141 S.
ISBN 978-3-8440-0731-2

ABISEA Band 61
van Treek, Daniel
Position Sensorless Torque Control of Switched Reluctance Machines
1. Aufl. 2012, 144 S.
ISBN 978-3-8440-1014-5

ABISEA Band 62
Bragard, Michael
The Integrated Emitter Turn-Off Thyristor. An Innovative MOS-Gated High-Power Device
1. Aufl. 2012, 164 S.
ISBN 978-3-8440-1152-4

ABISEA Band 63
Gerschler, Jochen B.
Ortsaufgelöste Modellbildung von Lithium-Ionen-Systemen unter spezieller Berücksichtigung der Batteriealterung
1. Aufl. 2012, 334 S.
ISBN 978-3-8440-1307-8

ABISEA Band 64
Neuhaus, Christoph R.
Schaltstrategien für Geschaltete Reluktanzantriebe mit kleinem Zwischenkreis
1. Aufl. 2012, 133 S.
ISBN 978-3-8440-1487-7

ABISEA Band 65
Butschen, Thomas
Dual-ICT- A Clever Way to Unite Conduction and Switching Optimized Properties in a Single Wafer
1. Aufl. 2012, 168 S.
ISBN 978-3-8440-1771-7

ABISEA Band 66
Plum, Thomas
Design and Realization of High-Power MOS Turn-Off Thyristors
1. Aufl. 2013, 113 S.
ISBN 978-3-8440-1884-4

ABISEA Band 67
Kiel, Martin
Impedanzspektroskopie an Batterien unter besonderer Berücksichtigung von Batteriesensoren für den Feldeinsatz
1. Aufl. 2013, 226 S.
ISBN 978-3-8440-1973-5

ABISEA Band 68
Brauer, Helge
Schnelldrehender Geschalteter Reluktanzantrieb mit extremem Längendurchmesserverhältnis
1. Aufl. 2013, 192 S.
ISBN 978-3-8440-2345-9

ABISEA Band 69
Thomas, Stephan
A Medium-Voltage Multi-Level DC/DC Converter with High Voltage Transformation Ratio
1. Aufl. 2014, 226 S.
ISBN 978-3-8440-2605-4

ABISEA Band 70
Richter, Sebastian
Digitale Regelung von PWM Wechselrichtern mit niedrigen Trägerfrequenzen
1. Aufl. 2014, 126 S.
ISBN 978-3-8440-2641-2

ABISEA Band 71
Bösing, Matthias
Acoustic Modeling of Electrical Drives - Noise and Vibration Synthesis based on Force Response Superposition
1. Aufl. 2014, 188 S.
ISBN 978-3-8440-2752-5

ABISEA Band 72
Waag, Wladislaw
Adaptive algorithms for monitoring of lithium-ion batteries in electric vehicles
1. Aufl. 2014, 232 S.
ISBN 978-3-8440-2976-5

ABISEA Band 73
Sanders, Tilman
Spatially Resolved Electrical In-Situ Measurement Techniques for Fuel Cells
1. Aufl. 2014, 126 S.
ISBN 978-3-8440-3121-8

ABISEA Band 74
Baumhöfer, Thorsten
Statistische Betrachtung experimenteller Alterungsuntersuchungen an Lithium-Ionen Batterien
1. Aufl. 2015, 157 S.
ISBN 978-3-8440-3423-3

ABISEA Band 75
Andre, Dave
Systematic Characterization of Ageing Factors for High-Energy Lithium-Ion Cells and Approaches for Lifetime Modelling Regarding an Optimized Operating Strategy in Automotive Applications
1. Aufl. 2015, 196 S.
ISBN 978-3-8440-3587-2

ABISEA Band 76
Merei, Ghada
Optimization of off-grid hybrid PV-wind-diesel power supplies with multi-technology battery systems taking into account battery aging
1. Aufl. 2015, 184 S.
ISBN 978-3-8440-4148-4

ABISEA Band 77
Schulte, Dominik
Modellierung und experimentelle Validierung der Alterung von Blei-Säure Batterien durch inhomogene Stromverteilung und Säureschichtung
1. Aufl. 2016, 165 S.
ISBN 978-3-8440-4216-0

ABISEA Band 78
Schenk, Mareike
Simulative Untersuchung der Wicklungsverluste in Geschalteten Reluktanzmaschinen
1. Aufl. 2016, 126 S.
ISBN 978-3-8440-4282-5

ABISEA Band 79
Wang, Yu
Development of Dynamic Models with Spatial Resolution for Electrochemical Energy Converters as Basis for Control and Management Strategies
1. Aufl. 2016, 188 S.
ISBN 978-3-8440-4303-7

ABISEA Band 80
Ecker, Madeleine
Lithium Plating in Lithium-Ion Batteries:
An Experimental and Simulation Approach
1. Aufl. 2016, 154 S.
ISBN 978-3-8440-4525-3

ABISEA Band 81
Zhou, Wei
Modellbasierte Auslegungsmethode von Temperierungssystemen für Hochvolt-Batterien in Personenkraftfahrzeugen
1. Aufl. 2016, 175 S.
ISBN 978-3-8440-4589-5

ABISEA Band 82
Lunz, Benedikt
Deutschlands Stromversorgung im Jahr 2050
Ein szenariobasiertes Verfahren zur vergleichenden Bewertung von Systemvarianten und Flexibilitätsoptionen
1. Aufl. 2016, 187 S.
ISBN 978-3-8440-4627-4

ABISEA Band 83
Hofmann, Andreas G.
Direct Instantaneous Force Control: Key to Low-Noise Switched Reluctance Traction Drives
1. Aufl. 2016, 228 S.
ISBN 978-3-8440-4715-8

ABISEA Band 84
Budde-Meiwes, Heide
Dynamic Charge Acceptance of Lead-Acid Batteries for Micro-Hybrid Automotive Applications
1. Aufl. 2016, 157 S.
ISBN 978-3-8440-4733-2

ABISEA Band 85
Engel, Stefan P.
Thyristor-Based High-Power On-Load Tap Changers Control under Harsh Load Conditions
1. Aufl. 2016, 156 S.
ISBN 978-3-8440-4986-2

ABISEA Band 86
Van Hoek, Hauke
Design and Operation Considerations of Three-Phase Dual Active Bridge Converters for Low-Power Applications with Wide Voltage Ranges
1. Aufl. 2017, 231 S.
ISBN 978-3-8440-5011-0

ABISEA Band 87
Diekhans, Tobias
Wireless Charging of Electric Vehicles - a Pareto-Based Comparison of Power Electronic Topologies
1. Aufl. 2017, 151 S.
ISBN 978-3-8440-5048-6

ABISEA Band 88
Lehner, Susanne
Reliability Assessment of Lithium-Ion Battery Systems with Special Emphasis on Cell Performance Distribution
1. Aufl. 2017, 184 S.
ISBN 978-3-8440-5090-5

ABISEA Band 89
Käbitz, Stefan
Untersuchung der Alterung von Lithium-Ionen-Batterien mittels Elektroanalytik und elektrochemischer Impedanzspektroskopie
1. Aufl. 2016, 258 S.
DOI: 10.18154/RWTH-2016-12094

ABISEA Band 90
Witzenhausen, Heiko
Elektrische Batteriespeichermodelle: Modellbildung, Parameteridentifikation und Modellreduktion
1. Aufl. 2017, 266 S.
DOI: 10.18154/RWTH-2017-03437

ABISEA Band 91
Münnix, Jens
Einfluss von Stromstärke und Zyklentiefe auf graphitische Anoden
1. Aufl. 2017, 171 S.
DOI: 10.18154/RWTH-2017-01915

ABISEA Band 92
Pilatowicz, Grzegorz
Failure Detection and Battery Management Systems of Lead-Acid Batteries for Micro-Hybrid Vehicles
1. Aufl. 2017, 212 S.
DOI: 10.18154/RWTH-2017-09156

ABISEA Band 93
Drillkens, Julia
Aging in Electrochemical Double Layer Capacitors:
An Experimental and Modeling Approach
1. Aufl. 2017, 179 S.
DOI: 10.18154/RWTH-2018-223434

Aachener Beiträge des ISEA

ABISEA Band 94
Magnor, Dirk
Globale Optimierung netzgekoppelter PV-Batteriesysteme unter besonderer Berücksichtigung der Batteriealterung
1. Aufl. 2017, 210 S.
DOI: 10.18154/RWTH-2017-06592

ABISEA Band 95
Iliksu, Merve
Elucidation and Comparison of the Effects of Lithium Salts on Discharge Chemistry of Nonaqueous Li-O_2 Batteries
1. Aufl. 2018, 160 S.
DOI: 10.18154/RWTH-2018-223782

ABISEA Band 96
Schmalstieg, Johannes
Physikalisch-elektrochemische Simulation von Lithium-Ionen-Batterien: Implementierung, Parametrierung und Anwendung
1. Aufl. 2017, 168 S.
DOI: 10.18154/RWTH-2017-04693

ABISEA Band 97
Soltau, Nils
High-Power Medium-Voltage DC-DC Converters: Design, Control and Demonstration
1. Aufl. 2017, 176 S.
DOI: 10.18154/RWTH-2017-04084

ABISEA Band 98
Stieneker, Marco
Analysis of Medium-Voltage Direct-Current Collector Grids in Offshore Wind Parks
1. Aufl. 2017, 144 S.
DOI: 10.18154/RWTH-2017-04667

ABISEA Band 99
Masomtob, Manop
A New Conceptual Design of Battery Cell with an Internal Cooling Channel
1. Aufl. 2017, 167 S.
DOI: 10.18154/RWTH-2018-223281

ABISEA Band 100
Marongiu, Andrea
Performance and Aging Diagnostic on Lithium Iron Phosphate Batteries for Electric Vehicles and Vehicle-to-Grid Strategies
1. Aufl. 2017, 222 S.
DOI: 10.18154/RWTH-2017-09944

ABISEA Band 101
Gitis, Alexander
Flaw detection in the coating process of lithium-ion battery electrodes with acoustic guided waves
1. Aufl. 2017, 109 S.
DOI: 10.18154/RWTH-2017-099519

ABISEA Band 102
Neeb, Christoph
Packaging Technologies for Power Electronics in Automotive Applications
1. Aufl. 2017, 132 S.
DOI: 10.18154/RWTH-2018-224569

ABISEA Band 103
Adler, Felix
A Digital Hardware Platform for Distributed Real-Time Simulation of Power Electronic Systems
1. Aufl. 2017, 156 S.
DOI: 10.18154/RWTH-2017-10761

ABISEA Band 104
Becker, Jan
Flexible Dimensionierung und Optimierung hybrider Lithium-Ionenbatteriespeichersysteme mit verschiedenen Auslegungszielen
1. Aufl., 2017, 157 S.
DOI: 10.18154/RWTH-2017-09278

ABISEA Band 105
Warnecke, Alexander J.
Degradation Mechanisms in NMC Based Lithium-Ion Batteries
1. Aufl. 2017, 158 S.
DOI: 10.18154/RWTH-2017-09646

ABISEA Band 106
Taraborrelli, Silvano
Bidirectional Dual Active Bridge Converter using a Tap Changer for Extended Voltage Ranges
1. Aufl. 2017, 94 S.
DOI: 10.18154/RWTH-2018-228242

ABISEA Band 107
Sarriegi, Garikoitz
SiC and GaN Semiconductors: The Future Enablers of Compact and Efficient Converters for Electromobility
1. Aufl. 2017, 106 S.
DOI: 10.18154/RWTH-2018-227548

ABISEA Band 108
Senol, Murat
Drivetrain Integrated Dc-Dc Converters utilizing Zero Sequence Currents
1. Aufl. 2017, 134 S.
DOI: 10.18154/RWTH-2018-226170

ABISEA Band 109
Kojima, Tetsuya
Efficiency Optimized Control of Switched Reluctance Machines
1. Aufl. 2017, 142 S.
DOI: 10.18154/RWTH-2018-226697

ABISEA Band 110
Lewerenz, Meinert
Dissection and Quantitative Description of Aging of Lithium-Ion Batteries Using Non-Destructive Methods Validated by Post-Mortem-Analyses
1. Aufl. 2018, 139 S.
DOI: 10.18154/RWTH-2018-228663

ABISEA Band 111
Büngeler, Johannes
Optimierung der Verfügbarkeit und der Lebensdauer von Traktionsbatterien für den Einsatz in Flurförderfahrzeugen
1. Aufl. 2018, 171 S.
DOI: 10.18154/RWTH-2018-226569

ABISEA Band 112
Wegmann, Raphael
Betriebsstrategien und Potentialbewertung hybrider Batteriespeichersysteme in Elektrofahrzeugen
1. Auflage 2018, 184 S.
DOI: 10.18154/RWTH-2018-228833

ABISEA Band 113
Nordmann, Hannes
Batteriemanagementsysteme unter besonderer Berücksichtigung von Fehlererkennung und Peripherieanalyse
1. Aufl. 2018, 222 S.
DOI: 10.18154/RWTH-2018-228763

ABISEA Band 114
Engelmann, Georges
Reducing Device Stress and Switching Losses Using Active Gate Drivers and Improved Switching Cell Design
1. Aufl. 2018, 195 S.
DOI: 10.18154/RWTH-2018-228973

ABISEA Band 115
Klein-Heßling, Annegret
Active DC-Power Filters for Switched Reluctance Drives during Single-Pulse Operation
1. Aufl. 2018, 166 S.
DOI: 10.18154/RWTH-2018-231030

ABISEA Band 116
Burkhart, Bernhard
Switched Reluctance Generator for Range Extender Applications - Design, Control and Evaluation
1. Aufl. 2018, 194 S.
DOI: 10.18154/RWTH-2019-00025

ABISEA Band 117
Biskoping, Matthias
Discrete Modeling and Control of a versatile Power Electronic Test Bench with Special Focus on Central Photovoltaic Inverter Testing
1. Aufl. 2018, 236 S.
DOI: 10.18154/RWTH-2019-03346

ABISEA Band 118
Schubert, Michael
High-Precision Torque Control of Inverter-Fed Induction Machines with Instantaneous Phase Voltage Sensing
1. Aufl. 2019, 221 S.
DOI: 10.18154/RWTH-2018-231364

ABISEA Band 119
Van der Broeck, Christoph
Methodology for Thermal Modeling, Monitoring and Control of Power Electronic Modules
1. Aufl. 2019, 290 S.
DOI: 10.18154/RWTH-2019-01370

ABISEA Band 120
Hust, Friedrich Emanuel
Physico-chemically motivated parameterization and modelling of real-time capable lithium-ion battery models – a case study on the Tesla Model S battery
1. Aufl. 2019, 203 S.
DOI: 10.18154/RWTH-2019-00249

ABISEA Band 121
Ralev, Iliya
Accurate Torque Control of Position Sensorless Switched Reluctance Drives
1. Aufl. 2019, 154 S.
DOI: 10.18154/RWTH-2019-03071

ABISEA Band 122
Ayeng'o, Sarah Paul
Optimization of number of PV cells connected in series for a direct-coupled PV system with lead-acid and lithium-ion batteries
1. Aufl. 2019, 114 S.
DOI: 10.18154/RWTH-2019-01843

ABISEA Band 123
Koschik, Stefan Andreas
Permanenterregte Synchronmaschinen mit verteilter Einzelzahnsteuerung - Regelkonzepte und Betriebsstrategien für hochintegrierte Antriebssysteme
1. Aufl. 2019, 158 S.
DOI: 10.18154/RWTH-2019-03446

ABISEA Band 124
Farmann, Alexander
A comparative study of reduced-order equivalent circuit models for state-of-available-power prediction of lithium-ion batteries in electric vehicles
1. Aufl. 2019, 214 S.
DOI: 10.18154/RWTH-2019-04700

ABISEA Band 125
Mareev, Ivan
Analyse und Bewertung von batteriegetriebenen, oberleitungsversorgten und brennstoffzellengetriebenen Lastkraftwagen für den Einsatz im Güterfernverkehr in Deutschland
1. Aufl. 2019, 158 S.
DOI: 10.18154/RWTH-2019-04698

ABISEA Band 126
Qi, Fang
Online Model-predictive Thermal Management of Inverter-fed Electrical Machines
1. Aufl. 2019, 154 S.
DOI: 10.18154/RWTH-2019-08304

ABISEA Band 127
Kairies, Kai-Philipp
Auswirkungen dezentraler Solarstromspeicher auf Netzbetreiber und Energieversorger
1. Aufl. 2019, 140 S.
DOI: 10.18154/RWTH-2019-06706

Aachener Beiträge des ISEA

ABISEA Band 128
Fleischer, Michael
Traction control for Railway Vehicles
1. Aufl. 2019, 162 S.
DOI: 10.18154/RWTH-2019-10570

ABISEA Band 129
Teuber, Moritz
Lifetime Assessment and Degradation Mechanisms in Electric Double-Layer Capacitors
1. Aufl. 2019, 150 S.
DOI: 10.18154/RWTH-2019-10071

ABISEA Band 130
Bußar, Christian
Investigation of Optimal Transformation Pathways towards 2050 for the Successful Implementation of a Sustainable Reduction of Carbon Emissions from Power Generation
1. Aufl. 2019, 204 S.
DOI: 10.18154/RWTH-2019-09975

ABISEA Band 131
Wienhausen, Arne Hendrik
High Integration of Power Electronic Converters enabled by 3D Printing
1. Aufl. 2019, 146 S.
DOI: 10.18154/RWTH-2019-08746

ABISEA Band 132
Kwiecien, Monika
Electrochemical Impedance Spectroscopy on Lead-Acid Cells during Aging
1. Aufl. 2019, 138 S.
DOI: 10.18154/RWTH-2019-09480

ABISEA Band 133
Titiz, Furkan Kaan
A Three-phase Low-voltage Grid-connected Current Source Inverter
1. Aufl. 2019, 128 S.
DOI: 10.18154/RWTH-2020-00458

ABISEA Band 134
Wünsch, Martin
Separation der Kathoden-alterung in Lithium-Ionen-Batteriezellen mittels elektrochemischer Impedanzspektroskopie
1. Aufl. 2019, 177 S.
DOI: 10.18154/RWTH-2019-11017

ABISEA Band 135
Badeda, Julia
Modeling and Steering of Multi-Use Operation with Uninterruptible Power Supply Systems - utilizing the example of lead-acid batteries
1. Aufl. 2020, 282 S.
DOI: 10.18154/RWTH-2020-05456

ABISEA Band 136
Kleinsteinberg, Björn
Energy Efficiency Increase of a Vanadium Redox Flow Battery with a Power-Based Model
1. Aufl. 2020, 163 S.
DOI: 10.18154/RWTH-2020-06092

ABISEA Band 137
Cai, Zhuang
Optimization of dimension and operation strategy for a wind-battery energy system in German electricity market under consideration of battery ageing process
1. Aufl. 2020, 144 S.
DOI: 10.18154/RWTH-2020-06525

ABISEA Band 138
Sabet, Pouyan Shafiei
Analysis of Predominant Processes in Electrochemical Impedance Spectra and Investigation of Aging Processes of Lithium-Ion Batteries with Layered Oxide Cathodes and Graphitic Anodes
1. Aufl. 2020, 136 S.
DOI: 10.18154/RWTH-2020-07683

ABISEA Band 139
Angenendt, Georg
Operation, Optimization and Additional Market Participation of Households with PV Battery Storage System and Power-to-Heat Application
1. Aufl. 2020, 221 S.
DOI: 10.18154/RWTH-2020-05200

ABISEA Band 140
Oberdieck, Karl Friedrich
Measurement and Mitigation of Electromagnetic Emissions of Propulsion Inverters for Electric Vehicles
1. Aufl. 2020, 181 S.
DOI: 10.18154/RWTH-2020-09215

ABISEA Band 141
Bubert, Andreas Martin
Optimierung des elektrischen Antriebsstrangs von Elektrofahrzeugen mit Betrachtung parasitärer Ströme innerhalb der elektrischen Maschine
1. Aufl. 2020, 215 S.
DOI: 10.18154/RWTH-2020-09556

ABISEA Band 142
Fleischer, Christian Georg
Model-Driven Software Development and Verification Solutions for Safety Critical Battery Management Systems
1. Aufl. 2021, 356 S.
DOI: 10.18154/RWTH-2021-00436

ABISEA Band 143
Arzberger, Arno
Thermografische Methoden zur zerstörungsfreien Messung der anisotropen Wärmeleitfähigkeit von Lithium-Ionen Zellen
1. Aufl. 2020, 131 S.
DOI: 10.18154/RWTH-2021-00479

ABISEA Band 144
Lange, Tobias
Oberwellenbasierte Modellierung, Regelung und Auslegung von Permanentmagnet- und Reluktanz-Synchronmaschinen
1. Aufl. 2020, S.
DOI: 10.18154/RWTH-2021-02537

ABISEA Band 145
Weiss, Claude
Fault Tolerant Switched Reluctance Machines with Distributed Inverters – Modeling and Control
1. Aufl. 2020, S.
DOI: 10.18154/RWTH-2021-02327

ABISEA Band 146
Huck, Moritz
Modelling the Transient Behaviour of Lead-Acid Batteries: Electrochemical Impedance of Adsorbed Species
1. Aufl. 2020, 151 S.
DOI: 10.18154/RWTH-2020-08362

ABISEA Band 147
Willenberg, Lisa
Volumenausdehnung und ihre Auswirkungen auf die Alterung einer zylindrischen Lithium-Ionen-Batterie
1. Aufl. 2020, S.
DOI: 10.18154/RWTH-2021-01906

ABISEA Band 148
Rogge, Matthias
Electrification of Public Transport Bus Fleets with Battery Electric Busses
1. Aufl. 2020, 161 S.
DOI: 10.18154/RWTH-2021-02146

ABISEA Band 149
Münderlein, Jeanette
Numerische Methodik zur Auslegung eines Hybriden Speichersystems mit Multinutzen“
1. Aufl. 2020, 221 S.
DOI: 10.18154/RWTH-2021-00867

ABISEA Band 150
Merten, Michael
Participation of Battery Storage Systems in the Secondary Control Reserve Market
1. Aufl. 2020, 187 S.
DOI: 10.18154/RWTH-2021-01029

ABISEA Band 151
Ge, Lefei
Performance Enhancement of Switched Reluctance Machines for High-speed Back-up Generators
1. Aufl. 2020, 152 S.
DOI: 10.18154/RWTH-2020-11546

ABISEA Band 152
Neubert, Markus
Modeling, Synthesis and Operation of Multiport-Active Bridge Converters
1. Aufl. 2020, 227 S.
DOI: 10.18154/RWTH-2020-10814

ABISEA Band 153
Schülting, Philipp
Optimierte Auslegung von hochintegrierten und bidirektionalen Onboard GaN-Ladegeräten
1. Aufl. 2020, 158 S.
DOI: 10.18154/RWTH-2020-09771

ABISEA Band 154
Sewergin, Alexander
Design Challenges and Solutions for the Practical Application of SiC Power Moduls – Exemplified by an Automotive DC-DC Converter. 1. Aufl. 2021, 154 S.
DOI: 10.18154/RWTH-2021-04498

ABISEA Band 155
Stippich, Alexander
Exploiting the Full Potential of Silicon Carbide Devices via Optimized Highly Integrated Power Modules
1. Aufl. 2021, 188 S.
DOI: 10.18154/RWTH-2021-08122

ABISEA Band 156
Gottschlich, Jan
Hilfsspannungsversorgungs konzepte für Mittelspannungs-DC/DC-Wandler
1. Aufl. 2021, 178 S.
DOI: 10.18154/RWTH-2021-11881

ABISEA Band 157
Hollstegge, Philipp
Injektion raumzeigerzerlegter Stromharmonischer zur Minderung tonaler Geräuschanteile in asymmetrisch sechsphasigen Permanentmagnetsynchronmaschinen
1. Aufl. 2021, 191 S.
DOI: 10.18154/RWTH-2021-11040

ABISEA Band 158
Grau, Vivien
Development of a Test Bench to Investigate the Impact of Steep Voltage Slopes on the Lifetime of Insulation Systems for Coil Windings
1. Aufl. 2021, 182 S.
DOI: 10.18154/RWTH-2021-09577

ABISEA Band 159
Ringbeck, Florian
Optimized Charging of Lithium-Ion Batteries with Physico-Chemical Models
1. Aufl. 2021, 174 S.
DOI: 10.18154/RWTH-2021-11038

ABISEA Band 160
Bank, Thomas
Performance and Aging Analysis of High-Power Lithium Titanate Oxide Cells for Low-Voltage Vehicle Applications
1. Aufl. 2021, 148 S.
DOI: 10.18154/RWTH-2021-10369

Aachener Beiträge des ISEA

ABISEA Band 161
Aupperle, Felix
Realizing High-Performance Silicon-Based Lithium-Ion Batteries
1. Aufl. 2022, 138 S.
DOI: 10.18154/RWTH-2022-05155

ABISEA Band 162
Schröer, Philipp A.
Entwicklung einer adaptiven Leistungsprognosefunktion für Starterbatterien mit Lithium-Titanat-Oxid-Anode als Grundlage zur sicheren Energieversorgung im Fahrzeug
1. Aufl. 2021, 187 S.
DOI: 10.18154/RWTH-2021-10819

ABISEA Band 163
Dechent, Philipp
Simulation and Real-Life assessment of cell-to-cell variation of ageing lithium-ion batteries
1. Aufl. 2022, 149 S.
DOI: 10.18154/RWTH-2022-09298

ABISEA Band 164
Li, Weihan
Battery Digital Twin with Physics-Based Modeling, Battery Data and Machine Learning
1. Aufl. 2022, 234 S.
DOI: 10.18154/RWTH-2022-02292

ABISEA Band 165
Thien, Tjark G. C.
Optimaler Betrieb von stationären Hybrid-Batterie-speichern am Beispiel des Projekts M5BAT
1. Aufl. 2022, 172 S.
DOI: 10.18154/RWTH-2022-00997

ABISEA Band 166
Lüdecke, Christoph
Compensating Asymmetries of Parallel-Connected SiC MOSFETs Using Intelligent Gate Drivers
1. Aufl. 2022, 166 S.
DOI: 10.18154/RWTH-2022-09587

ABISEA Band 167
Rahe, Christiane
Untersuchung von Batterieelektroden mit optischen Verfahren
1. Aufl. 2022, 214 S.
DOI: 10.18154/RWTH-2022-08794

ABISEA Band 168
Weber, Felix Martin
Stability of lithium electrolyte interphase enabling rechargeable lithium-metal batteries
1. Aufl. 2023, 168 S.
DOI: 10.18154/RWTH-2023-03565

ABISEA Band 169
Henn, Jochen
Gate Driver Integrated Closed-Loop Control for Electromagnetic Emissions and Switching Losses of Wide Bandgap Power Electronic Converters
1. Aufl. 2023, 169 S.
DOI: 10.18154/RWTH-2023-07726

ABISEA Band 170
Quabeck, Stefan
Modeling of Parasitic Currents and Fault Detection in Electrical Traction Drives
1. Aufl. 2023, 133 S.
DOI: 10.18154/RWTH-2023-10920

ABISEA Band 171
Hecht, Christopher
Usage overview, prediction, and siting optimization for electric vehicles public charging infrastructure with machine learning and big data methods
1. Aufl. 2023, 185 S.
DOI: 10.18154/RWTH-2024-01156

ABISEA Band 172
Kuipers, Matthias L. U.
Development of a Virtual Cell Design Tool for Objective Comparisons between State-of-the-Art Battery Cells and Next Generation Technologies
1. Aufl. 2023, 203 S.
DOI: 10.18154/RWTH-2023-11897

ABISEA Band 173
Brieske, Daniel Martin
Anwendungsbezogene Modellierung und Zustandsbestimmung von Lithium-Schwefel-Batterien
1. Aufl. 2023, 146 S.
DOI: 10.18154/RWTH-2023-10905

ABISEA Band 174
Teichert, Philipp
Einfluss der Degradation von nickelreichen $Li[Ni_xMn_yCo_z]O_2$ (NMC) Elektroden (mit $x \geq 0.6$) auf Vollzellalterung von Lithium-Ionen-Zellen
1. Aufl. 2023, 159 S.
DOI: 10.18154/RWTH-2024-01059

ABISEA Band 175
Kühnle, Hannes Sebastian
Optical and electrochemical investigations of fundamental lithium metal deposition processes on lithium surfaces
1. Aufl. 2023, S.
DOI:

ABISEA Band 176
Epp, Alexander
Multiphysical Models and Optimization for Conceptual Design of High-Voltage Battery Systems
1. Aufl. 2024, 256 S.
DOI: 10.18154/RWTH-2024-00430

Battery storage systems are a key technology for the energy transition. They can shift energy flexibly in time and thus balance out fluctuations in the presence of sun and wind. Home storage systems account for the largest share of grid-connected storage capacity in Germany, one of the pioneering markets worldwide. In the relatively young market, warranty periods of about ten years have become the norm. However, it is unknown whether these warranties can be maintained. To increase transparency, the European Union requires the provision of reliable information on the batteries' state of health.

As a contribution to research, this dissertation develops novel methods to estimate important warranty-relevant parameters of lithium-ion batteries, such as the remaining capacity or the internal resistance, based on operational data. The developed methods use the data generated during field measurements of 21 home storage systems in private households over a period of up to eight years. This corresponds to about 106 system years and 14 billion data points.

The analyzed storage systems show a decrease in usable capacity of around two to three percentage points per year. The batteries show an average system-specific resistance increase of around one to 25 percentage points per year. The dominant degradation mode observed is the loss of lithium inventory.

ISSN 1437-675X